

THESIS 97-014

**Thesis**

RAL-TH-97-009



# Measurements of $B_d^0 - \bar{B}_d^0$ Oscillations and the Inclusive $b$ Lifetime Using the Aleph Detector at LEP

F K Thomson

July 1997

© Council for the Central Laboratory of the Research Councils 1996

Enquiries about copyright, reproduction and requests for additional copies of this report should be addressed to:

The Central Laboratory of the Research Councils  
Library and Information Services  
Rutherford Appleton Laboratory  
Chilton  
Didcot  
Oxfordshire  
OX11 0QX  
Tel: 01235 445384 Fax: 01235 446403  
E-mail [library@rl.ac.uk](mailto:library@rl.ac.uk)

ISSN 1362-0215

Neither the Council nor the Laboratory accept any responsibility for loss or damage arising from the use of information contained in any of their reports or in any communication about their tests or investigations.

MEASUREMENTS OF  $B_d^0 - \bar{B}_d^0$   
OSCILLATIONS AND THE INCLUSIVE  $b$   
LIFETIME USING THE ALEPH DETECTOR  
AT LEP

Fiona Kirkwood Thomson

Department of Physics and Astronomy  
The University of Glasgow  
Glasgow, Scotland

*Thesis submitted for the degree of  
Doctor of Philosophy*

May, 1997

© F.K. Thomson, May 1997

## Abstract

Measurements of the  $B_d^0 - \bar{B}_d^0$  oscillation frequency and inclusive  $b$  hadron lifetime are presented, using a sample of approximately four million hadronic  $Z^0$  decays observed with the ALEPH detector.

An inclusive double jet-charge technique is used in order to maximise the statistical precision of the measurement. The method benefits from having approximately five times the statistics of other measurements. Events are  $b$ -tagged and decay lengths are reconstructed using inclusive vertexing procedures. A smearing procedure is applied to tracks in the Monte Carlo simulation in order to improve the agreement with data and hence control systematic uncertainties. A weighting procedure is used in reconstructing the  $b$  hadron momentum. The fitting procedures incorporate the effects of proper time resolution by means of folding matrices. A fit to the reconstructed proper time distribution yields a measurement of the inclusive  $b$  hadron lifetime :

$$\tau_b = 1.570 \pm 0.004 (\text{stat.}) \pm 0.013 (\text{syst.}) \text{ ps}$$

A jet-charge method is used to determine the states of  $B$  mesons at production and decay, based on the fact that the jet-charge for mixed mesons is different from that for unmixed mesons. A multi-parameter fit is performed to the product of the jet-charges in the two event hemispheres, plotted as a function of reconstructed proper time. This gives a measurement of the  $B_d$  oscillation frequency :

$$\Delta m_d = 0.441 \pm 0.026 (\text{stat.}) \pm 0.029 (\text{syst.}) \text{ ps}^{-1}$$

The result is compared with previous measurements and the potential for applying the method to the study of  $B_s$  oscillations is discussed.

## Preface

This thesis presents measurements of the time dependence of  $B_d^0 - \bar{B}_d^0$  oscillations and the inclusive  $b$  hadron lifetime, using ALEPH data collected at the LEP accelerator between 1991 and 1995.

Chapter 1 gives a brief overview of the Standard Model, with emphasis on the weak interaction and quark mixing. The CKM mixing matrix is discussed and current knowledge of its elements is reviewed. This leads to a discussion of  $B^0 - \bar{B}^0$  oscillations, which are an important way of constraining the matrix elements involving the top quark. Chapter 2 outlines the general requirements for a measurement of time dependent oscillations, demonstrating the effects of mistag fractions and proper time resolution on the sensitivity of the method. The motivation is given for the double jet-charge method which is used in this thesis and the expected sensitivity of the method relative to other analyses is presented.

A description of the ALEPH detector is given in Chapter 3, with emphasis on tracking performance, which is vital to this analysis. The event selection, vertex reconstruction and  $b$ -tagging procedures are described in Chapter 4 and the need for smearing the tracking resolution in the Monte Carlo simulation is highlighted. The smearing procedure is explained in some detail. Chapter 5 presents a discussion of the jet-charge method for measuring quark charges and explains how it can be used to give information on the  $B$  meson state at production and decay. The jet-charge method is optimised to give the best sensitivity to  $B^0 - \bar{B}^0$  oscillations.

The decay length and momentum reconstruction algorithms are described in Chapter 6, along with the matrix folding method which is used to account for detector resolution effects. A fit is performed to extract the inclusive  $b$  lifetime. The fitting procedure to extract the  $B_d^0 - \bar{B}_d^0$  oscillation frequency,  $\Delta m_d$ , is described in Chapter 7. The effects of the proper time reconstruction algorithms on the jet-charge are discussed and accounted for in the fit. The result for  $\Delta m_d$  is presented and compared with previous measurements.

The work of the ALEPH collaboration depends on the participation of many people over a long period of time. The author's contribution to the experiment included analysing data from the laser alignment system of the vertex detector (Appendix A), taking part in shifts during data taking and carrying out test-beam shifts during trials of the upgraded vertex detector.

The material presented in this thesis reflects the author's own individual analysis of the ALEPH data, developed as part of a small group of people. The  $B_d$  oscillation measurement was presented at the 'Frontiers in Contemporary Physics' conference, Nashville, in May 1997. No portion of the authors's work described in this thesis has been submitted in support of an application for another degree or qualification in this, or any other, institute of learning.

## Acknowledgements

So many people have helped me over the last few years that it would be impossible to name them all. Those I do not mention by name have not been forgotten.

I would like to thank my supervisor Jim Lynch, for his advice and support and for organising my visits to CERN, and Andy Halley for suggesting this analysis and for his enthusiasm and help in making it work. Thanks also to the Physics and Astronomy Department for giving me the opportunity to undertake this research and to the University of Glasgow for providing funding in the form of a Postgraduate Scholarship.

Among those who have helped me at Glasgow, I would like to thank Pedro and Stephen for many useful discussions and for their help with the momentum reconstruction, and Stan and Jason for their comments and suggestions. I am also indebted to Ian for providing valuable explanations and insight and to Catherine for all her kind help. I am particularly grateful to everyone who read this thesis - their comments were very welcome. Thanks also to the ALEPH Lifetime and Mixing group at CERN, for their advice and interest, and to the LEP *B* lifetime and oscillations working groups for Figures 6.29 and 7.22.

Life would have been dull had it not been for the company of Martin, Simon and Richard. They have done their best to keep me sane and happy over the last three years. Thanks also to Allan, Stephen, Lee, Evelyn and Matt for being thoroughly entertaining office mates, not forgetting Dougal for providing excellent times in Killin. I'd like to apologise to everyone who has been neglected these past few months and thank Debbie in particular, for being so understanding. Thanks also to Mark, simply for being there to share the ups and downs and for managing to grin his way through most of them.

Most important of all, I thank Mum, Dad and Catriona for their love and support, for encouraging me when things were difficult and for sharing in my excitement when things were going well. This thesis is dedicated to them.



# Contents

<b>1</b>	<b>Standard Model and <math>B^0 - \bar{B}^0</math> Oscillations</b>	<b>1</b>
1.1	The Standard Model . . . . .	1
1.2	Weak Interactions . . . . .	4
1.3	The Charged Weak Current for Quarks . . . . .	6
1.4	The CKM Matrix . . . . .	7
1.4.1	Parameterisation of the CKM Matrix . . . . .	7
1.4.2	The Unitarity Triangle . . . . .	8
1.4.3	Determination of the CKM Matrix Elements . . . . .	9
1.5	$B^0 - \bar{B}^0$ Oscillations . . . . .	10
1.5.1	Time Development of the $B^0 - \bar{B}^0$ System . . . . .	12
1.5.2	Evaluation of $\Delta m$ . . . . .	13
1.6	The Shape of the Unitarity Triangle . . . . .	15
1.7	Summary . . . . .	17
<b>2</b>	<b>Overview and Motivation</b>	<b>19</b>
2.1	Requirements for a Mixing Analysis . . . . .	19
2.1.1	Effect of Mistag Fraction on Mixing Signal . . . . .	20
2.1.2	Effect of Proper Time Resolution . . . . .	21
2.1.3	Significance of an Oscillation Signal . . . . .	23
2.2	Overview of Previous Oscillation Analyses . . . . .	24
2.2.1	Dilepton Method . . . . .	24
2.2.2	Lepton-Jet-Charge Method . . . . .	24
2.2.3	$D^*$ and Lepton or Jet-Charge . . . . .	25
2.2.4	Additional Methods for $B_s$ Oscillations . . . . .	25
2.3	Motivation for Double Jet-Charge Method . . . . .	26
2.3.1	Overview of Method . . . . .	26
2.3.2	Comparison with other Methods . . . . .	27
<b>3</b>	<b>The ALEPH Detector at LEP</b>	<b>29</b>
3.1	The LEP Collider . . . . .	29
3.2	Overview of the ALEPH Detector . . . . .	30
3.3	Tracking Detectors . . . . .	32
3.3.1	Vertex Detector (VDET) . . . . .	32
3.3.2	Inner Tracking Chamber (ITC) . . . . .	33
3.3.3	Time Projection Chamber (TPC) . . . . .	34



3.3.4	Overall Tracking Performance . . . . .	36
3.4	Calorimetry . . . . .	39
3.4.1	Electromagnetic Calorimeter (ECAL) . . . . .	39
3.4.2	Hadron Calorimeter (HCAL) . . . . .	40
3.5	Luminosity Monitors . . . . .	41
3.6	Trigger . . . . .	42
3.7	Event Reconstruction . . . . .	42
3.8	Summary . . . . .	43
<b>4</b>	<b>Event Selection and <math>b</math> Tagging</b>	<b>47</b>
4.1	Event Selection . . . . .	47
4.2	Vertex Reconstruction . . . . .	48
4.2.1	Primary Vertex Reconstruction . . . . .	48
4.2.2	Secondary Vertex Reconstruction . . . . .	49
4.2.3	$b$ Tagging . . . . .	50
4.3	Monte Carlo Simulation . . . . .	50
4.4	Discrepancies between Data and Monte Carlo . . . . .	51
4.5	Monte Carlo Track Smearing . . . . .	52
4.5.1	VDET Track Removal . . . . .	52
4.5.2	Track Impact Parameter Smearing . . . . .	54
4.5.3	Results of Monte Carlo Smearing . . . . .	60
4.6	Purities and Error Determination . . . . .	60
4.7	Summary . . . . .	63
<b>5</b>	<b>Charge Tagging</b>	<b>65</b>
5.1	Hadronisation . . . . .	65
5.2	Charge Tagging using Jet-Charge . . . . .	68
5.3	Choice of $\kappa$ for Best Average Mistag . . . . .	70
5.4	The $b$ Jet-Charge and Sensitivity to Mixing . . . . .	72
5.5	The Charge Correlation Function . . . . .	78
<b>6</b>	<b>Proper Time Measurement</b>	<b>81</b>
6.1	Introduction . . . . .	81
6.2	Measurement of Decay Length . . . . .	81
6.3	Momentum Reconstruction . . . . .	87
6.3.1	Charged Track Momentum and Track Weights. . . . .	88
6.3.2	Vertex Charge . . . . .	89
6.3.3	Neutral and Missing Energy Reconstruction . . . . .	92
6.3.4	Momentum Resolution . . . . .	94
6.3.5	Fragmentation Systematic Error . . . . .	94
6.4	Proper Time Resolution . . . . .	96
6.5	Measurement of the Inclusive $b$ Lifetime. . . . .	100
6.5.1	Outline of Fitting Procedure . . . . .	100
6.5.2	Resolution Folding . . . . .	100
6.5.3	Efficiency Corrections . . . . .	101

6.5.4	Construction of Theoretical Lifetime Distribution . . . . .	103
6.5.5	Results from Fit to Proper Time Distribution . . . . .	105
6.6	Summary . . . . .	109
<b>7</b>	<b>Measurement of <math>\Delta m_d</math></b>	<b>113</b>
7.1	Overview of Method . . . . .	113
7.2	Multiplicity Corrections . . . . .	115
7.2.1	Variation of Multiplicity with Proper Time . . . . .	115
7.2.2	Variation of Jet-Charge with Hemisphere Multiplicity . . .	119
7.3	Measurement of Average Jet-Charges . . . . .	124
7.4	Fitting for $\Delta m_d$ . . . . .	128
7.5	Parameters and Constraints in the $\Delta m_d$ Fit . . . . .	129
7.6	Results . . . . .	131
7.7	Errors on the $\Delta m_d$ Result . . . . .	134
7.8	Comparison with Previous Measurements . . . . .	137
<b>8</b>	<b>Summary and Conclusions</b>	<b>141</b>
<b>A</b>	<b>Study of the VDET Laser Data</b>	<b>143</b>
A.1	Introduction . . . . .	143
A.2	Outline of Laser Alignment System . . . . .	143
A.3	Analysis . . . . .	144
A.4	Results . . . . .	144
A.4.1	Possible Explanations for the Shift . . . . .	145
A.4.2	Interpretation of Spot Movements. . . . .	146
A.4.3	Addition of Laser Spot Analysis into DQUAL Program . . .	147
A.5	Improvements for LEP II . . . . .	148
A.6	Conclusions . . . . .	148
<b>B</b>	<b>Multi-parameter Fit Correlation Matrix</b>	<b>159</b>



# List of Figures

1.1	Feynman diagrams showing (a) electron-proton scattering and (b) beta decay. . . . .	4
1.2	One of the unitarity triangles (left) and its rescaled form (right) in the $\rho - \eta$ plane. . . . .	9
1.3	Box diagrams showing the transition $B_q^0 \rightarrow \bar{B}_q^0$ . . . . .	10
1.4	Intensities of $B^0$ (solid) and $\bar{B}^0$ (dashed) as a function of proper time from an initially pure $B^0$ state (the dotted line shows the total intensity). Plot (a) shows the $B_d^0$ case for $\Delta m_d = 0.467 \text{ ps}^{-1}$ and (b) shows the $B_s^0$ case with $\Delta m_s = 6 \text{ ps}^{-1}$ . . . . .	13
1.5	Constraints on the position of vertex A arising from measurement of $\left  \frac{V_{ub}}{V_{cb}} \right $ and $B_d^0 - \bar{B}_d^0$ oscillations. . . . .	16
1.6	Result of fit for position of vertex A. The triangle shows the best fit and the contour gives the 95% confidence level region. . . . .	16
2.1	The charge correlation in the Monte Carlo as function of proper time for the case of perfect charge tagging and proper time reconstruction for (a) $B_d$ mesons, (b) $B_s$ mesons and (c) all $b$ hadrons, where $\Delta m_d = 0.467 \text{ ps}^{-1}$ and $\Delta m_s = 3.33 \text{ ps}^{-1}$ . . . . .	21
2.2	The charge correlation function in the Monte Carlo for various total mistag rates. The mistag causes a reduction in the amplitude of the signal. . . . .	22
2.3	The charge correlation function in Monte Carlo for (a) perfect proper time resolution (b) 10% resolution and (c) 30% resolution. . . . .	23
2.4	Schematic diagram illustrating the dilepton method. . . . .	24
2.5	Schematic diagram illustrating the lepton-jet-charge method. . . . .	25
2.6	Schematic diagram illustrating some of the methods for investigating $B_s$ oscillations. . . . .	26
2.7	Schematic diagram illustrating the double jet-charge method. . . . .	26
2.8	Estimated signal/noise ratio for several $B_s$ oscillation analyses, as a function of the $B_s$ oscillation frequency. The parameters used for each analysis are given in Table 2.3. . . . .	28
3.1	The LEP collider. . . . .	30

3.2	Overall view of the ALEPH detector; (a) vertex detector, (b) inner tracking chamber, (c) time projection chamber, (d) electromagnetic calorimeter, (e) superconducting solenoid, (f) hadron calorimeter, (g) muon chambers. . . . .	31
3.3	Configuration of the silicon vertex detector. . . . .	32
3.4	Schematic of a double-sided silicon strip detector. . . . .	33
3.5	The ITC drift cells. . . . .	34
3.6	The time projection chamber. . . . .	35
3.7	Part of a TPC end-plate showing cathode pads for coordinate measurement alternating with trigger pads. . . . .	35
3.8	Definition of track helix parameters. . . . .	37
3.9	Impact parameter resolution in $r\phi$ and $z$ from dimuon events. . .	38
3.10	The electromagnetic calorimeter. . . . .	39
3.11	Detail of ECAL layer. . . . .	40
3.12	Distribution of the total energy calculated using the energy flow algorithm. . . . .	44
3.13	A $b$ event reconstructed in the ALEPH detector. . . . .	45
4.1	Comparison of [BTAG(hemi 1) + BTAG(hemi 2)] distributions in 1993 data and Monte Carlo. . . . .	51
4.2	The efficiency of the BTAG cut in 1993 data and Monte Carlo and the ratio of MC/data , prior to Monte Carlo smearing. The horizontal dotted lines indicate a disagreement of 5%. . . . .	52
4.3	Distributions of the QVSRCH decay length prior to any $b$ tagging for each data taking period (points) and corresponding unsmeared Monte Carlo sample (histogram). The final plot shows the ratio data/MC for the high statistics 1994 sample. . . . .	53
4.4	Fraction of (a) 0, (b) 1, and (c) 2 VDET hit tracks 'removed' in Monte Carlo as a function of $\cos\theta$ of the track. . . . .	55
4.5	Distributions of $d_0$ , $z_0$ , $d_0/\sigma_{d_0}$ and $z_0/\sigma_{z_0}$ in data (points) and unsmeared Monte Carlo (histogram). . . . .	56
4.6	Results of the multi-parameter fit to the $d_0/\sigma_{d_0}$ distribution in the 1992 data. The upper plot shows the central small values on a linear scale whereas the lower plot shows the full range of values on a logarithmic plot. . . . .	57
4.7	Comparison of data distributions of $d_0/\sigma_{d_0}$ and $z_0/\sigma_{z_0}$ with smeared and unsmeared Monte Carlo. The left-hand plots indicate the central regions and the right-hand plots show the tail region on a logarithmic scale. . . . .	59
4.8	Distributions of the QVSRCH decay length prior to any $b$ tagging for each data taking period (points) and corresponding smeared Monte Carlo sample (histogram). The final plot shows the ratio data/MC for the high statistics 1994 sample. . . . .	61

4.9	Ratio of the efficiency of the BTAG cut in the smeared Monte Carlo sample to that in data, for each of the data taking periods and corresponding Monte Carlo samples. The final plot shows the ratio obtained using the combined Monte Carlo sample and combined 1991–1995 data set. In each case the dotted lines represent $\pm 5\%$ .	62
4.10	Monte Carlo purities and efficiencies as a function of BTAG cut. . .	63
5.1	Schematic diagram of a hadronic $Z^0$ decay. . . . .	66
5.2	Schematic diagram of the string model. . . . .	66
5.3	The Peterson distribution (5.7) for the fraction of $(E + p_z)$ taken by hadrons containing $b$ and $c$ quarks. . . . .	68
5.4	Illustration of hierarchy of hadrons produced in fragmentation (from an original $b$ quark). . . . .	69
5.5	Monte Carlo jet-charge distributions for jets originating from $b$ (solid) and $\bar{b}$ (dotted) quarks for $\kappa = 0.5$ . . . . .	70
5.6	Signed jet-charge distributions for various $\kappa$ values, for Monte Carlo $b$ events. The shaded region represents the mistag fraction.	71
5.7	Variation of mistag with $\kappa$ for the various quark flavours. . . . .	72
5.8	The five possible fragmentation chains involving a $s\bar{s}$ pair (showing first two ranks only) from an initial (a) $u$ quark and (b) $d$ quark. .	72
5.9	Jet-charge contributions associated with a charged $B$ . . . . .	73
5.10	Jet-charge contributions for (a) unmixed and (b) mixed neutral $B$ mesons. . . . .	74
5.11	Monte Carlo momentum spectra for positively (solid circles) and negatively (open triangles) charged particles from (a) semi-leptonic, (b) two-body hadronic, (c) multi-body hadronic decays of neutral $B^0$ mesons (containing positively charged $\bar{b}$ quarks). . . . .	75
5.12	Initial quark signed jet-charge distributions for the different $b$ hadron classes ( $\kappa = 1.0$ ). . . . .	76
5.13	Sensitivity to mixing, as given by the difference between (initial state) mistags for mixed and unmixed mesons, as a function of $\kappa$ for $B_d$ and $B_s$ mesons. . . . .	78
6.1	Schematic diagram showing how the track significances are signed.	82
6.2	The ratio $\mathcal{R}_{sig}$ for tracks from Monte Carlo $b$ events. The shaded region indicates tracks from the decay of the $b$ hadron. . . . .	82
6.3	Comparison of the $\mathcal{R}_{sig}$ distribution for data and Monte Carlo. . .	83
6.4	The quality factor for revertexing as a function of the $\mathcal{R}_{sig}$ cut. The dotted line shows the quality factor obtained using the default QVSRCH vertexing. . . . .	84
6.5	Decay length resolution with revertexing (points) and without revertexing (histogram), plotted on a logarithmic scale in order to show the tail regions. . . . .	85
6.6	Decay length resolution, $(l_{reco} - l_{true})$ , for several slices in $l_{true}$ . . .	86

6.7	Reconstructed decay length distribution in data and Monte Carlo after a BTAG cut of 20. . . . .	87
6.8	Rapidity distribution for tracks from Monte Carlo $b$ events. . . . .	88
6.9	Track weights for $b$ events showing the distinction between $b$ hadron tracks and fragmentation tracks. . . . .	89
6.10	Track weights in data and Monte Carlo for all flavours of events (before applying BTAG cut). . . . .	90
6.11	Reconstructed charged momentum distribution for data and Monte Carlo, after a BTAG cut of 20. . . . .	90
6.12	Vertex charge distribution after a BTAG cut of 20. . . . .	91
6.13	Figure (a) shows the missing energy in the hemisphere as calculated using Equations (6.9) and (6.10). Figure (b) shows the missing energy which is added after taking resolution effects into account. . . . .	93
6.14	Reconstructed momentum distribution in data and Monte Carlo, after a BTAG cut of 20. . . . .	94
6.15	Momentum resolution in slices of true momentum. . . . .	95
6.16	Dependence of $\langle z \rangle$ upon the value of $\epsilon_b$ used to generate the Peterson fragmentation function. . . . .	96
6.17	Comparison of the reconstructed momentum distribution for various values of $\epsilon_b$ used in the Monte Carlo Peterson fragmentation function. . . . .	97
6.18	The reconstructed proper time distribution in data and Monte Carlo after a BTAG cut of 20. . . . .	98
6.19	The average proper time resolution for Monte Carlo $b$ events. . . . .	98
6.20	The proper time resolution, $(t_{reco} - t_{true})$ , in ps in slices of true proper time. . . . .	99
6.21	The proper time resolution matrix $\mathbf{R}$ . . . . .	101
6.22	Vertexing efficiency as a function of true proper time for Monte Carlo $b$ events. . . . .	102
6.23	Efficiency of a BTAG cut of 20, as a function of reconstructed proper time, for Monte Carlo $b$ events. . . . .	103
6.24	Average efficiency of BTAG cut in data and Monte Carlo as a function of reconstructed proper time. . . . .	103
6.25	Result of lifetime fit to combined Monte Carlo sample. . . . .	105
6.26	Results of the lifetime fit to the individual data years. The errors shown include statistical errors from data and Monte Carlo, combined with systematic uncertainties due to the flavour composition and efficiency corrections. The band shows the combined value and its total statistical and systematic error. . . . .	107
6.27	Reconstructed proper time distribution in data and the result of the fit. The bottom plot shows the ratio of the measured distribution to the fit. The errors shown include statistical errors from data and Monte Carlo and errors from the BTAG efficiency corrections. . . . .	108

6.28	Dependence of the measured $b$ lifetime on the sample purity. The results are indicated together with their uncorrelated statistical and systematic errors relative to the central value. . . . .	110
6.29	Summary of recent measurements of the inclusive $b$ lifetime. The error bars on the individual measurements indicate the size of the statistical error and total error on the result. The result from this analysis is not shown on the plot. . . . .	111
7.1	Schematic diagram showing the method for measuring $\Delta m_d$ . . . . .	113
7.2	Dependence of the mean signed jet-charge on reconstructed proper time for the various classes of $b$ hadrons. The points indicate the mean value observed in the Monte Carlo whereas the solid line represents the predicted dependence due to multiplicity variations (see Section 7.2.2). . . . .	116
7.3	Variation of the mean charged track multiplicity as a function of true proper time in Monte Carlo $b$ events (suppressed zero). . . . .	117
7.4	Variation of the mean charged track multiplicity as a function of true $B$ momentum in Monte Carlo $b$ events (suppressed zero). . . . .	117
7.5	Variation of the mean charged track multiplicity as a function of true $B$ decay length in Monte Carlo $b$ events (suppressed zero). . . . .	118
7.6	Variation of the mean charged track multiplicity as a function of reconstructed $B$ momentum in data and Monte Carlo (suppressed zero). . . . .	118
7.7	Variation of the mean charged track multiplicity as a function of reconstructed $B$ decay length in data and Monte Carlo (suppressed zero). . . . .	119
7.8	Variation of the mean charged track multiplicity as a function of reconstructed proper time in data and Monte Carlo simulation (suppressed zero). . . . .	119
7.9	Variation of signed jet-charge with hemisphere charged multiplicity for the different $b$ hadron classes. (Signed using initial quark charge). . . . .	121
7.10	Dependence of the opposite signed hemisphere charge on hemisphere charged track multiplicity in data and Monte Carlo simulation. . . . .	122
7.11	Variation of the hemisphere charged multiplicity as a function of reconstructed proper time in samples enhanced in (a) $B^0$ and (b) $B^\pm$ decays using a cut on the vertex charge (suppressed zero). . . . .	123
7.12	Dependence of the opposite signed hemisphere charge on hemisphere charged multiplicity in $B^0$ and $B^\pm$ enhanced samples of data and Monte Carlo events. . . . .	123
7.13	Dependence of the charged multiplicity in the 'opposite' hemisphere on reconstructed proper time in the 'same' hemisphere (suppressed zero). . . . .	124
7.14	Variation in data of $\langle -Q_{J_o}^\kappa Q_{J_s}^\kappa \rangle$ as a function of BTAG cut for $\kappa = 1.0$ and $\kappa = 0.5$ (suppressed zero). . . . .	125



7.15	Variation of $\langle -Q_{J_o}^\kappa Q_{J_s}^\kappa \rangle$ for (a) $b$ events, (b) $c$ events and (c) $uds$ events for $\kappa = 0.5$ and $\kappa = 1.0$ . . . . .	125
7.16	Schematic diagram showing the form of the covariance matrix used in the fit for $\langle Q_b^\kappa \rangle$ , $\langle Q_c^\kappa \rangle$ and $\langle Q_{uds}^\kappa \rangle$ ( $\kappa = 0.5, 1.0$ ). Details are given in the text. . . . .	127
7.17	Result of the fit to the charge correlation in Monte Carlo simulation. . . . .	131
7.18	The charge correlation as a function of measured proper time with the result of the fit shown as the solid line. The no mixing hypothesis is shown as a dotted line (suppressed zero). . . . .	132
7.19	The fitted distributions of $\langle -Q_{J_o}^\kappa Q_{J_s}^\kappa \rangle$ versus BTAG cut, for $\kappa = 1.0$ and $\kappa = 0.5$ (suppressed zero). . . . .	133
7.20	Summary of the $\Delta m_d$ fit results for the different data years, indicating their statistical uncertainties and systematic uncertainties arising from the fitted parameters. The value from the fit to the combined data-set is shown as the central band with its full statistical and systematic uncertainty. . . . .	134
7.21	$\Delta m_d$ dependence on the BTAG cut applied. The errors indicate the statistical uncertainties and systematic uncertainties from the fitted parameters. . . . .	137
7.22	Individual and combined measurements of $\Delta m_d$ at LEP. The error bars on the individual measurements indicate the size of the statistical error and total error on the result. . . . .	139
A.1	Diagram of the VDET laser system. . . . .	150
A.2	VDET faces projected onto the ALEPH XY plane, as viewed from side A. The face numbers are shown. Laser light is incident on the end wafers of faces 1, 4, 6, 9, 11 and 13 of the outer layer. . . . .	151
A.3	Numbering of VDET strips. . . . .	151
A.4	Pulse height against strip number for Z view spots. Note some spots are not seen, for example spot 8 on module A001. . . . .	152
A.5	Pulse height against strip number for XY view spots. Again note that some spots are not seen. . . . .	153
A.6	XY distribution of laser hits. . . . .	154
A.7	Deviation against run number for representative spots. Plot (a) shows the periods when the ALEPH detector was open and 'MD' refers to periods of LEP machine development. . . . .	155
A.8	Possible movements of VDET faces. . . . .	156
A.9	Laser plots of deviation vs. $\phi(\text{spot})$ . (Solid triangles - runs 28496–28608, open triangles - runs 29508–29540). . . . .	157
A.10	Laser plots of deviation distributions. . . . .	158

# List of Tables

1.1	The quarks and leptons of the Standard Model [2]. The $u$ , $d$ and $s$ quark masses are estimates of the ‘current’ quark masses. The $c$ and $b$ quark masses are estimated from charmonium, bottomonium, $D$ and $B$ masses. The top quark mass is obtained from the direct observation of top events by the CDF and D0 collaborations.	2
1.2	The gauge bosons of the four fundamental forces. . . . .	4
2.1	The possible charge contributions for an unmixed $B^0$ meson, taking mistag fractions into account. . . . .	20
2.2	Predicted signal/noise for measurement of $\Delta m_d$ using double jet-charge method, compared with ALEPH lepton-jet-charge and dilepton methods. $N$ is the number of events selected from approximately 4 million hadronic $Z^0$ decays, $\eta$ is the total mistag for the method and $\sigma_t$ is an estimate of the proper time resolution. . . . .	27
2.3	Properties of various methods for measuring $B_s$ oscillations. $N$ is the number of events, $p_s$ is the purity of $B_s$ mesons in the sample, $\eta$ is the total mistag and $\sigma_t$ is an estimate of the proper time resolution.	28
3.1	Momentum resolution of the ALEPH tracking devices. . . . .	37
3.2	Impact parameter resolution of ALEPH tracking devices. . . . .	38
4.1	Monte Carlo samples corresponding to each data taking period. . . . .	51
4.2	Amplitudes of the three Gaussians (G1, G2, G3) and the Student’s- $t$ distribution used to parameterise the $d_0/\sigma_{d_0}$ distribution in 1992 data and Monte Carlo. The widths of the distributions are determined from data and are fixed while fitting the Monte Carlo distribution. . . . .	58
4.3	Summary of selected events after each stage of event selection for the various data taking periods. . . . .	64
5.1	Meson and baryon fractions. . . . .	73
5.2	Time dependent and time integrated fractions for each of the $b$ hadron classes, where $\tau_{B^+}$ , $\tau_{\Lambda}$ , $\tau_{B_d}$ , $\tau_{B_s}$ are the lifetimes of $B^\pm$ , $b$ baryons, $B_d$ and $B_s$ respectively. . . . .	74
6.1	The effect of revertexing on the decay length resolution. G1, G2 and G3 are Gaussians 1,2 and 3 respectively. . . . .	85

6.2	Summary of Gaussian parameters from fit to negative side of missing energy distribution in data and Monte Carlo simulation. .	93
6.3	Results of a triple Gaussian fit to the average proper time resolution.	99
6.4	Summary of the lifetime fit results for the 1991–1995 data-taking periods. The errors include contributions from data statistics, Monte Carlo statistics, flavour composition and the effects of the BTAG efficiency correction. . . . .	106
6.5	Summary of the various contributions to the systematic error on $\tau_b$ .	107
6.6	Summary of the measured $b$ lifetime in samples of increasing $b$ purity. Errors include uncertainties from data and Monte Carlo statistics, flavour composition and efficiency corrections. The uncorrelated errors on the lifetime, relative to the central value, are indicated in brackets below the lifetime results. . . . .	109
7.1	Parameters and constraints used in the $\Delta m_d$ fit. . . . .	129
7.2	Fitted values for $b$ , $c$ and $uds$ mean jet-charges, for $\kappa = 0.5$ and $\kappa = 1.0$ . The Monte Carlo values are shown for comparison. . . .	133
7.3	Summary of the $\Delta m_d$ results for the individual data years including their statistical uncertainties, errors arising from correction factors and systematic uncertainties arising from the fitted parameters. .	134
7.4	Contributions to the systematic error on the $\Delta m_d$ result. The upper part of the table corresponds to the fitted parameters and the second column gives the Gaussian constraints which are used. The third column gives the values returned from the fit. The lower part of the table corresponds to ‘fixed’ parameters. The fourth column gives the contribution of each source to the systematic error on $\Delta m_d$ . . . . .	135
7.5	Measurements of $\Delta m_d$ by different methods used by ALEPH. . . .	138
A.1	Summary table of spot shifts. A positive shift indicates that the spot moved in the direction of increasing strip number (see Figures A.3, A.8). A * indicates an absent spot. . . . .	146
B.1	Correlation coefficients for multi-parameter fit. . . . .	160

# Chapter 1

## The Standard Model and $B^0 - \bar{B}^0$ Oscillations

Particle physics is the study of the ultimate constituents of matter and their interactions. Present knowledge has built up from many years of experimental discoveries and theoretical developments and is now formulated in the ‘Standard Model’ which describes processes involving elementary particles in terms of the interactions of their fields. In this chapter the Standard Model is briefly reviewed, with emphasis on the weak interaction and quark mixing. This leads to a presentation of the theory behind  $B^0 - \bar{B}^0$  oscillations, the measurement of which is the subject of this thesis.

### 1.1 The Standard Model

#### Quarks and Leptons

In the first half of this century there were few known, supposedly elementary, particles. The proton, neutron, electron and neutrino, together with the photon, seemed to describe the world around us. High energy experiments designed to study these particles in more detail, however, resulted in the discovery of a multitude of strongly interacting particles, labelled *hadrons*. In addition, deep inelastic scattering of electrons from protons showed the proton to have substructure.

From these discoveries emerged a simple model of matter. There are two kinds of fundamental, structureless, spin  $\frac{1}{2}$  fermions; *quarks* and *leptons*. There are six known types or *flavours* of quarks, three charged leptons and three neutral leptons (neutrinos) and they fall naturally into three *generations* which exhibit identical properties and differ only in their mass. Measurements of the  $Z^0$  line shape from LEP constrain the number of light neutrino generations to be three [1] which, in the framework of the Standard Model, also constrains the number of generations of quarks and leptons to be three. The quarks and leptons of the Standard Model are listed along with some of their properties in Table 1.1. Quarks carry fractional electric charge, the ‘up-type’ ( $u, c, t$ ) quarks having charge  $+\frac{2}{3}e$  and

Particle	Symbol	Charge (e)	Mass (GeV/ $c^2$ )
First Generation			
Up Quark	$u$	$+\frac{2}{3}$	$\sim 5 \times 10^{-3}$
Down Quark	$d$	$-\frac{1}{3}$	$\sim 8 \times 10^{-3}$
Electron Neutrino	$\nu_e$	0	$< 15 \times 10^{-9}$
Electron	$e^-$	-1	$0.51 \times 10^{-3}$
Second Generation			
Charm Quark	$c$	$+\frac{2}{3}$	$\sim 1.3$
Strange Quark	$s$	$-\frac{1}{3}$	$\sim 0.200$
Muon Neutrino	$\nu_\mu$	0	$< 0.17 \times 10^{-3}$
Muon	$\mu^-$	-1	0.106
Third Generation			
Top Quark	$t$	$+\frac{2}{3}$	$180 \pm 12$
Bottom Quark	$b$	$-\frac{1}{3}$	$\sim 4.5$
Tau Neutrino	$\nu_\tau$	0	$< 24 \times 10^{-3}$
Tau	$\tau^-$	-1	1.78

**Table 1.1:** The quarks and leptons of the Standard Model [2]. The  $u$ ,  $d$  and  $s$  quark masses are estimates of the ‘current’ quark masses. The  $c$  and  $b$  quark masses are estimated from charmonium, bottomonium,  $D$  and  $B$  masses. The top quark mass is obtained from the direct observation of top events by the CDF and D0 collaborations.

the ‘down-type’ ( $d$ ,  $s$ ,  $b$ ) quarks having charge  $-\frac{1}{3}e$ , while the  $e^-$ ,  $\mu^-$ ,  $\tau^-$  leptons have charge  $-e$ . Each particle has a corresponding antiparticle having the same mass but opposite electric charge, magnetic moment and fermion number.

All hadrons are made of quarks and fall into two categories. *Baryons* have half-integral spin and consist of three quarks (e.g.  $p = uud$ ,  $n = ddu$ ) and *mesons* have integral spin and are made from a quark-antiquark pair (e.g.  $\pi^+ = u\bar{d}$ ).

Quarks have an additional degree of freedom called *colour*, which was first introduced to explain the existence of the  $\Delta^{++}$  baryon. This particle consists of three identical  $u$  quarks in a symmetric spin state and so would be forbidden by Fermi statistics if it was not in an antisymmetric colour state. A quark can be one of three colours (Red, Green or Blue) and all objects observed in nature are colourless. This explains why allowed quark configurations are  $qqq$  (in state  $RGB = \text{white}$ ) and  $q\bar{q}$  (in state  $R\bar{R} + G\bar{G} + B\bar{B}$ ) and free quarks are not observed.

## Forces and Fields

There are four forces governing the universe : the strong force binds quarks to form hadrons and nucleons to form nuclei, the electromagnetic force acts on all charged particles, the weak force is responsible for processes like beta decay and the gravitational force acts on all bodies with mass. Classically, forces are described in terms of fields through which particles interact. In quantum theory

the equivalent view describes the force as being transmitted by the exchange of field quanta or *bosons*, of integral spin.

Combining Maxwell's ideas of electromagnetism with relativistic quantum mechanics gave rise to the theory of Quantum Electrodynamics (QED). This theory describes interactions between charged fermions as being due to the exchange of photons, the strength of the interaction being characterised by the coupling constant,  $\alpha = \frac{e^2}{4\pi\epsilon_0\hbar c} \sim \frac{1}{137}$ . QED is the simplest example of a *local gauge theory* which means that the theory is invariant under a local gauge (i.e. phase) transformation. It has the important property that infinities arising in the theory can be consistently eliminated (i.e. it is *renormalisable*) and its success at describing the magnetic moments of electrons and muons has meant that it has been used as a model for describing the other types of interaction.

The weak interaction was first postulated to describe the beta decay of nuclei and has been developed as a gauge theory in analogy to QED. The field quanta which transmit the weak force are the massive  $W^\pm$  and  $Z^0$  bosons. Glashow, Weinberg and Salam postulated that the electromagnetic and weak forces are different manifestations of the same *electroweak* force [3]. The slow rate of weak interactions is due to the gauge bosons having large mass giving rise to a smaller 'effective' coupling strength. The massive nature of the bosons also means that weak interactions have a short range since it requires a minimum energy fluctuation of  $M_W c^2$  to emit a virtual  $W$  which can then only travel a distance of  $\hbar/M_W c \approx 10^{-3}$  fm, limited by the uncertainty principle. The nature of weak interactions is discussed in more detail in Section 1.2.

Strong interactions are described by the gauge theory known as Quantum Chromodynamics (QCD). In this case the gauge bosons are massless *gluons* which couple to colour charge. Unlike QED, where the photons do not carry electric charge, gluons themselves carry colour charge and can therefore interact with each other in addition to interacting with quarks. The strong coupling constant,  $\alpha_s$ , is typically around one hundred times that of QED but appears to decrease at small distances as a result of the screening effect of gluon-gluon interactions. The potential between two quarks can be described by :

$$V_s = -\frac{4}{3} \frac{\alpha_s}{r} + kr \quad (1.1)$$

The first term, dominating at small  $r$ , arises from single gluon exchange and has the form of the Coulomb potential between charged particles. At large  $r$  ( $\mathcal{O}(1\text{ fm})$ ) the quarks are tightly bound by the exchange of many gluons. The colour lines of force between the quarks are pulled together due to gluon-gluon interactions and form a *flux tube* or *string* connecting the quark and antiquark. The potential increases linearly with separation and hence the quarks are *confined* within a hadron. Quarks and gluons are often referred to collectively as *partons*.

Lifetimes of strongly decaying particles are around  $10^{-23}$  s, electromagnetic lifetimes are around  $10^{-19}$  s and weak lifetimes are longer by around ten orders of magnitude.

Gravity is the weakest force and while it is important for objects with large

Force	Gauge Boson	Spin	Mass
Electromagnetic	photon ( $\gamma$ )	1	0
Weak	$W^\pm, Z^0$	1	$80.3 \text{ GeV}/c^2, 91.2 \text{ GeV}/c^2$
Strong	gluon ( $g$ )	1	0
Gravitational	graviton ( $G$ )	2	0

**Table 1.2:** The gauge bosons of the four fundamental forces.

mass, its effects can be neglected for the mass scales used in high energy physics. It is believed to be transmitted by massless, spin-2 *gravitons*, but there is currently no experimental evidence for such a particle. The four forces and their gauge bosons are summarised in Table 1.2.

## 1.2 Weak Interactions

The weak interaction was first proposed to explain processes such as beta decay which occur on much longer time scales than strong or electromagnetic decays.

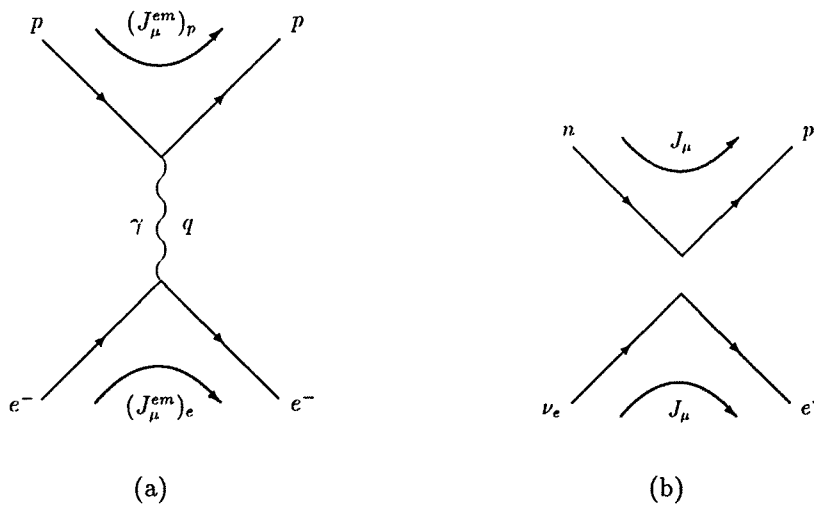


**Figure 1.1:** Feynman diagrams showing (a) electron-proton scattering and (b) beta decay.

Beta decay can be written as ;

$$n \rightarrow p + e^- + \bar{\nu}_e$$

which can also be expressed in terms of the constituent quarks ;

$$d \rightarrow u + e^- + \bar{\nu}_e$$

Fermi proposed a model for this type of interaction which was based on the structure of electromagnetic interactions. Consider electromagnetic electron proton scattering as shown in Figure 1.1(a). This can be described as the interaction of two currents,  $J_\mu^{em}$ , via the exchange of a single photon of momentum  $q$  and hence the matrix element is given by ;

$$\mathcal{M} = (e\bar{\psi}_p\gamma^\mu\psi_p) \left(\frac{1}{q^2}\right) (e\bar{\psi}_e\gamma_\mu\psi_e) = \frac{e^2}{q^2} (J^{em\mu})_p (J_\mu^{em})_e^\dagger \quad (1.2)$$

where the  $\psi$  are four component Dirac spinors and  $\gamma^\mu$  are the Dirac matrices [4]. The currents  $J_\mu^{em}$  transform as vectors under Lorentz transformations. By analogy Fermi proposed for beta decay (Figure 1.1(b)) ;

$$\mathcal{M} = G_F (\bar{\psi}_p \mathcal{O} \psi_n) (\bar{\psi}_e \mathcal{O} \psi_{\nu_e}) \quad (1.3)$$

where  $G_F$  is the Fermi coupling constant and  $\mathcal{O}$  is a matrix operator which Fermi chose to be vector in type, in analogy with electromagnetism. In this type of weak interaction, the matrix element is the product of a charge-raising and charge-lowering current. These are referred to as *charged current* interactions (CC) and do not conserve quark flavour.

Fermi's description was satisfactory until parity violation was discovered in 1957 when an asymmetry was observed in the angular distribution of electrons produced in the beta decay of polarised  $^{60}\text{Co}$  nuclei. It was observed, shortly after, that only 'left-handed' (i.e. negative helicity<sup>1</sup>) neutrinos ( $\nu_L$ ) and 'right-handed' (i.e. positive helicity) antineutrinos ( $\bar{\nu}_R$ ) are seen in nature. Under a parity ( $P$ ) transformation,  $\nu_L \rightarrow \nu_R$ , and under a charge conjugation ( $C$ ) transformation,  $\nu_L \rightarrow \bar{\nu}_L$ , so it is clear that both  $C$  and  $P$  are violated. The combined  $CP$  operation leaves the weak interaction invariant to a large degree and is discussed in more detail later.

A mixture of vector ( $\bar{\psi}\gamma^\mu\psi$ ) and axial vector ( $\bar{\psi}\gamma^5\gamma^\mu\psi$ ) currents violates parity and gives a suitable form for the weak interaction. Replacing the operator  $\mathcal{O}$  by  $\frac{1}{2}\gamma^\mu(1-\gamma^5)$  gives rise to the so-called  $V-A$  (vector-axial vector) structure. Since left and right handed states enter differently in the weak interaction it is often convenient to use left and right handed projections for all particles where ;

$$e_L = \frac{1}{2}(1-\gamma^5)e \quad e_R = \frac{1}{2}(1+\gamma^5)e \quad (1.4)$$

(denoting  $\psi_e$  by  $e$  for convenience). Charged current weak interactions have the form ;

$$\mathcal{M} = \frac{4G_F}{\sqrt{2}} J^{CC\mu} J_\mu^{CC\dagger} \quad (1.5)$$

where the charged current for *leptons* is ;

$$\begin{aligned} J^{CC\mu} &= \bar{\nu}_e\gamma^\mu\frac{1}{2}(1-\gamma^5)e + \bar{\nu}_\mu\gamma^\mu\frac{1}{2}(1-\gamma^5)\mu + \bar{\nu}_\tau\gamma^\mu\frac{1}{2}(1-\gamma^5)\tau \\ &= \bar{\nu}_e\gamma^\mu e_L + \bar{\nu}_\mu\gamma^\mu\mu_L + \bar{\nu}_\tau\gamma^\mu\tau_L \end{aligned} \quad (1.6)$$

<sup>1</sup>The helicity of a particle is defined as  $\hat{\sigma}\cdot\hat{p}$ , where  $\hat{\sigma}$  is the spin of the particle and  $\hat{p}$  is its momentum.



That is, the lepton charged current is constructed from the following pairs of left-handed states :

$$\begin{pmatrix} \nu_e \\ e^- \end{pmatrix}_L \quad \begin{pmatrix} \nu_\mu \\ \mu^- \end{pmatrix}_L \quad \begin{pmatrix} \nu_\tau \\ \tau^- \end{pmatrix}_L \quad (1.7)$$

The charged current for quarks is discussed below.

### Interpretation of $G_F$

The coupling strength  $G_F$  is the same for all types of processes described above, suggesting a single underlying explanation. Comparing (1.5) with the electromagnetic matrix element (1.2) it can be seen that  $G_F$  essentially replaces  $e^2/q^2$ . In QED, the  $e^2/q^2$  term comes from the coupling strength  $e$  at each vertex in Figure 1.1(a) and a photon *propagator*  $\sim \frac{1}{q^2}$ . Postulating that the weak force is mediated by the exchange of massive bosons [4] gives :

$$\mathcal{M} \sim \left( \frac{g}{\sqrt{2}} J^{CC\mu} \right) \frac{1}{M_W^2 - q^2} \left( \frac{g}{\sqrt{2}} J^{\mu CC\dagger} \right) \quad (1.8)$$

where  $g$  is a dimensionless weak coupling and  $q$  is the momentum carried by the  $W$  boson. In cases where  $q^2 \ll M_W^2$  then the propagator between the currents disappears (i.e. the interaction is at a point) and we can identify :

$$\frac{G_F}{\sqrt{2}} = \frac{g^2}{8M_W^2} \quad (1.9)$$

## 1.3 The Charged Weak Current for Quarks

The charged current for quarks may be expected to have the same structure as that for leptons (1.6) and be constructed from the doublets :

$$\begin{pmatrix} u \\ d \end{pmatrix}_L \quad \begin{pmatrix} c \\ s \end{pmatrix}_L \quad \begin{pmatrix} t \\ b \end{pmatrix}_L \quad (1.10)$$

This describes processes such as beta decay (involving a  $u \leftrightarrow d$  transition) and  $D^+ \rightarrow \bar{K}^0 l^+ \nu_l$  (involving a  $c \leftrightarrow s$  transition). However, processes such as  $K^+ \rightarrow \pi^0 \mu^+ \nu_\mu$  also occur, involving a  $s \leftrightarrow u$  transition. This *generation mixing* is not possible using the doublets in (1.10).

Instead, the charged current for quarks couples to 'rotated' quark states (the *weak eigenstates*), which for two generations are given by ;

$$\begin{pmatrix} u \\ d' \end{pmatrix}_L \quad \begin{pmatrix} c \\ s' \end{pmatrix}_L \quad (1.11)$$

where ;

$$\begin{pmatrix} d' \\ s' \end{pmatrix}_L = \begin{pmatrix} \cos \theta_c & \sin \theta_c \\ -\sin \theta_c & \cos \theta_c \end{pmatrix} \begin{pmatrix} d \\ s \end{pmatrix}_L \quad (1.12)$$

where  $\theta_c$  is the Cabibbo angle (measured to be  $\approx 13^\circ$  from experiment). Interactions involving quarks from the same generation occur with a coupling proportional to  $\cos \theta_c$  and are ‘Cabibbo favoured’, while those involving a generation mix are ‘Cabibbo suppressed’ (coupling  $\sim \sin \theta_c$ ). So for the case of beta decay described above,  $G_F$  should be replaced by  $G_F \cos \theta_c$ .

For three generations the rotation matrix is the  $3 \times 3$  Cabibbo-Kobayashi-Maskawa (CKM) matrix  $\mathbf{V}_{CKM}$  [5] :

$$\begin{pmatrix} d' \\ s' \\ b' \end{pmatrix}_L = \begin{pmatrix} V_{ud} & V_{us} & V_{ub} \\ V_{cd} & V_{cs} & V_{cb} \\ V_{td} & V_{ts} & V_{tb} \end{pmatrix} \begin{pmatrix} d \\ s \\ b \end{pmatrix}_L \quad (1.13)$$

The diagonal elements of  $\mathbf{V}_{CKM}$  represent couplings between quarks of the same generation and the smaller, off diagonal terms represent couplings between quarks of different generations. The charged current for quarks can be written as :

$$J^{CC\mu} = (\bar{u} \ \bar{c} \ \bar{t})_L \gamma^\mu \mathbf{V}_{CKM} \begin{pmatrix} d \\ s \\ b \end{pmatrix}_L \quad (1.14)$$

In the context of the Standard Model  $\mathbf{V}_{CKM}$  is a unitary matrix ( $\mathbf{V}^\dagger \mathbf{V} = \mathbf{1}$ ). This means that in neutral current interactions, involving the exchange of a  $Z^0$  boson, the only allowed transitions are  $d \leftrightarrow d$ ,  $s \leftrightarrow s$  etc. and transitions such as  $d \leftrightarrow s$  do not occur :

$$(\bar{d}' \ \bar{s}' \ \bar{b}') \begin{pmatrix} d' \\ s' \\ b' \end{pmatrix} = (\bar{d} \ \bar{s} \ \bar{b}) \mathbf{V}^\dagger \mathbf{V} \begin{pmatrix} d \\ s \\ b \end{pmatrix} = \bar{d}d + \bar{s}s + \bar{b}b \quad (1.15)$$

Flavour changing neutral currents can only occur at loop level, via charged currents. An example of this type of process is  $B^0 - \bar{B}^0$  mixing which is discussed in Section 1.5.

## 1.4 The CKM Matrix

The elements of the CKM matrix are not predicted by the Standard Model and the only theoretical constraint is that it is unitary. It is therefore necessary to measure the matrix elements experimentally and hence test unitarity constraints. In the following sections the parameterisation of the matrix is discussed and methods for determining its elements are outlined.

### 1.4.1 Parameterisation of the CKM Matrix

In the case of  $n$  generations,  $\mathbf{V}_{CKM}$  would be an  $n \times n$  matrix. In the most general case, the elements  $V_{ij}$  are complex giving  $2n^2$  parameters. However the unitarity condition  $\mathbf{V}^\dagger \mathbf{V} = \mathbf{1}$  imposes constraints. There are  $n$  constraints arising from the

diagonal terms and  $n(n-1)$  constraints arising from the off-diagonal terms leaving  $n^2$  free parameters. An orthogonal  $n \times n$  matrix has  $\frac{n}{2}(n-1)$  independent real parameters and so  $V_{CKM}$  has  $\frac{n}{2}(n-1)$  real parameters and  $n^2 - \frac{n}{2}(n-1) = \frac{n}{2}(n+1)$  complex phases. However, not all these parameters are physical and  $2n-1$  phases can be removed by redefining the quark fields. This leaves  $\frac{1}{2}(n-1)(n-2)$  independent phases. Therefore, whereas the original Cabibbo matrix for two generations was parameterised with a single real parameter (the Cabibbo angle), the  $3 \times 3$  CKM matrix of the Standard Model is complex and requires three real angles and one complex phase. A number of equivalent parameterisations of the CKM matrix exist [5] and for the discussion here it is convenient to use an approximate parameterisation suggested by Wolfenstein [6] which involves an expansion in terms of  $\lambda = \sin \theta_c \sim 0.22$  ;

$$V_{CKM} = \begin{pmatrix} 1 - \frac{\lambda^2}{2} & \lambda & A\lambda^3(\rho - i\eta) \\ -\lambda & 1 - \frac{\lambda^2}{2} & A\lambda^2 \\ A\lambda^3(1 - \rho - i\eta) & -A\lambda^2 & 1 \end{pmatrix} + \mathcal{O}(\lambda^4) \quad (1.16)$$

where  $A$ ,  $\rho$  and  $\eta$  are of order unity. This parameterisation clearly demonstrates the hierarchy in the couplings between generations. Quarks couple strongly to other quarks in the same generation and hence the diagonal elements are close to one. The further from the diagonal (i.e. the more generations crossed) the smaller the couplings.

### CP Violation

The presence of the imaginary part of the matrix is very important as it is necessary to describe  $CP$  violation in the Standard Model. The quark charged currents are only invariant under a  $CP$  transformation if  $V_{ij} = V_{ij}^*$  (i.e. the  $V_{ij}$  are real) [5]. It can be shown [7] that all  $CP$  violating amplitudes in the Standard Model are proportional to :

$$J_{CP} = |\text{Im} (V_{i\alpha} V_{j\beta} V_{i\beta}^* V_{j\alpha}^*)| \quad i \neq j, \alpha \neq \beta \quad (1.17)$$

Using the Wolfenstein parameterisation<sup>2</sup> it is found that  $J_{CP} \approx A^2 \eta \lambda^6 \approx \mathcal{O}(10^{-4})$  and hence  $CP$  violation is a small effect.

It should be noted that the Wolfenstein parameterisation is not invariant under redefinition of the quark fields by an arbitrary phase factor, however the moduli of the elements  $|V_{ij}|$  and the quantity  $J_{CP}$  are invariant quantities [7].

### 1.4.2 The Unitarity Triangle

A useful way of investigating the implications of unitarity is to represent the unitarity constraints  $\sum_i V_{ij} V_{ik}^* = 0$  ( $j \neq k$ ) as triangles in the complex plane.

<sup>2</sup>Care must be taken when making precise calculations of  $J_{CP}$  using the Wolfenstein approximation since the result is  $\mathcal{O}(\lambda^6)$ . However using  $i = u$ ,  $\alpha = d$ ,  $j = t$  and  $\beta = b$  in Equation (1.17) gives the correct result.

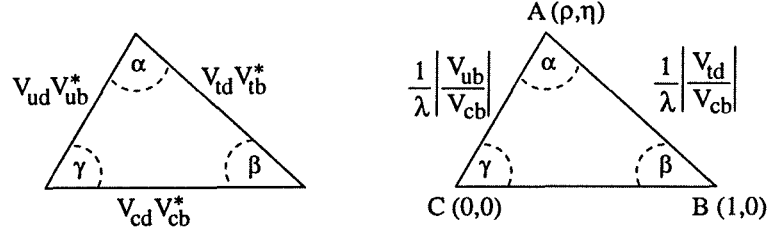


**Figure 1.2:** One of the unitarity triangles (left) and its rescaled form (right) in the  $\rho - \eta$  plane.

There are six triangles which can be shown to have the same area,  $A_{\Delta}$ , which is related to the measure of  $CP$  violation [7] :

$$|A_{\Delta}| = \frac{1}{2} J_{CP} \quad (1.18)$$

Without  $CP$  violation the triangles would collapse into lines along the real axis.

The unitarity constraint applied to columns 1 and 3 of  $\mathbf{V}_{CKM}$  involves the most poorly known CKM elements ;

$$V_{ud}V_{ub}^* + V_{cd}V_{cb}^* + V_{td}V_{tb}^* = 0 \quad (1.19)$$

and therefore gives the most useful triangle from a phenomenological point of view. Rescaling Equation (1.19) by  $|V_{cd}V_{cb}|$  gives a triangle in the  $\rho - \eta$  plane with coordinates at  $(0,0)$ ,  $(1,0)$ , and  $(\rho, \eta)$ . The triangle and its rescaled form are shown in Figure 1.2. The lengths of the sides of the rescaled triangle are given by the moduli of the CKM matrix elements :

$$|AC| = \frac{1}{\lambda} \left| \frac{V_{ub}}{V_{cb}} \right| \quad (1.20)$$

$$|AB| = \frac{1}{\lambda} \left| \frac{V_{td}}{V_{cb}} \right| = \frac{1}{\lambda} \left| \frac{V_{td}}{V_{ts}} \right| \quad (1.21)$$

and hence the shape of the triangle is invariant under quark phase redefinitions<sup>3</sup>. Determining the shape of the triangle is of great importance both to measure  $CP$  violation and to test the unitarity prediction. If the triangle does not close then this will be an indication of ‘new physics’, beyond the Standard Model.

### 1.4.3 Determination of the CKM Matrix Elements

The elements in rows one and two of the CKM matrix can be measured from tree level decays. Present knowledge of these elements is summarised below [2].

- $|V_{ud}|$  – From nuclear beta decay :  $|V_{ud}| = 0.9736 \pm 0.0010$ .
- $|V_{us}|$  – From Kaon decays ( $K^+ \rightarrow \pi^0 e^+ \nu_e$ ,  $K_L^0 \rightarrow \pi^- e^+ \nu_e$ ) and semileptonic hyperon decays ( $\Lambda \rightarrow p e^- \bar{\nu}_e$ ) :  $|V_{us}| = 0.2205 \pm 0.0018$ .

<sup>3</sup>The choice of a particular parameterisation simply changes the location of the triangle in the complex plane.

- $|V_{ub}|$  – The ratio  $|V_{ub}/V_{cb}|$  is obtained from the lepton energy spectrum for semileptonic  $B$  decays by looking at the spectrum beyond the endpoint for the  $b \rightarrow c$  transition. The result depends strongly on the theoretical model used to generate the lepton spectrum. Future measurements may use exclusive semileptonic charmless  $B$  decays (e.g.  $\bar{B}^0 \rightarrow \pi^+ \mu^- \bar{\nu}_\mu$ ,  $B^+ \rightarrow \rho^0 l^+ \nu_l$ ) but high statistics are required as the branching ratios for these decays are small. At present :  $|V_{ub}/V_{cb}| = 0.08 \pm 0.02$ .
- $|V_{cd}|$  – From charm production in deep inelastic neutrino(antineutrino)-nucleon scattering ( $\nu_\mu d \rightarrow \mu^- c$ ) :  $|V_{cd}| = 0.224 \pm 0.016$ .
- $|V_{cs}|$  – From decays of  $D$  mesons (e.g.  $D^+ \rightarrow \bar{K}^0 e^+ \nu_e$ ) :  $|V_{cs}| = 1.01 \pm 0.18$ .
- $|V_{cb}|$  – From exclusive decays such as  $B^+ \rightarrow \bar{D}^{*0} l^+ \nu_l$  and from the partial width of inclusive semileptonic  $B$  decays :  $|V_{cb}| = 0.041 \pm 0.003$ .

Information on CKM elements involving the top quark can be obtained from flavour changing processes which occur at the one loop level, for example, particle-antiparticle oscillations of neutral  $B$  mesons. This phenomenon is discussed in the following sections.

## 1.5 $B^0 - \bar{B}^0$ Oscillations

The states  $|B_q^0\rangle = |\bar{b}q\rangle$  and  $|\bar{B}_q^0\rangle = |b\bar{q}\rangle$  (where  $q = d, s$ ) are eigenstates of the flavour-conserving strong and electromagnetic interactions. They have the same mass but different quark flavours and are the correct basis states for describing the production of neutral  $B$  mesons by the strong interaction during fragmentation, and decays where quark flavours are tagged. They are not  $CP$  eigenstates, however, since applying the  $CP$  transformation,  $CP|\bar{b}q\rangle = |b\bar{q}\rangle$ , results in a different state.

Weak interactions do not conserve quark flavour and mix the  $|B^0\rangle$  and  $|\bar{B}^0\rangle$  states by the second order weak processes shown in Figure 1.3. An initially pure

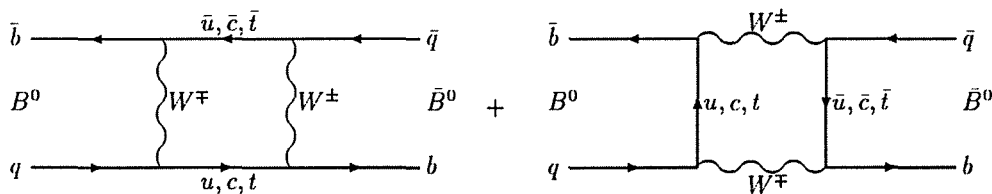


Figure 1.3: Box diagrams showing the transition  $B_q^0 \rightarrow \bar{B}_q^0$ .

$|B^0\rangle$  state, produced by a strong process at  $t = 0$ , will develop into a superposition of  $|B^0\rangle$  and  $|\bar{B}^0\rangle$  states. In the rest frame of the  $B$ , an arbitrary neutral meson

state can be written as a two-component wave function,  $a|B^0\rangle + b|\bar{B}^0\rangle$ , which obeys the time-dependent Schrödinger Equation<sup>4</sup> :

$$i\frac{\partial}{\partial t} \begin{pmatrix} a \\ b \end{pmatrix} = \mathbf{H} \begin{pmatrix} a \\ b \end{pmatrix} \quad (1.22)$$

The matrix  $\mathbf{H}$  is not hermitian since  $B$  mesons can decay and thus the system decays in time. The Hamiltonian can, however, be expressed in terms of hermitian mass and decay matrices :

$$\mathbf{H} = \left( \mathbf{M} - \frac{i}{2}\mathbf{\Gamma} \right) = \begin{pmatrix} M & M_{12} \\ M_{12}^* & M \end{pmatrix} - \frac{i}{2} \begin{pmatrix} \Gamma & \Gamma_{12} \\ \Gamma_{12}^* & \Gamma \end{pmatrix} \quad (1.23)$$

From  $CPT$  invariance, the diagonal elements of  $\mathbf{M}$  and  $\mathbf{\Gamma}$  are equal and the off-diagonal elements are related by complex conjugation [8]. If  $CP$  is also conserved then  $M_{12} = M_{12}^*$  and  $\Gamma_{12} = \Gamma_{12}^*$ .

The eigenvalues of the Hamiltonian  $\mathbf{H}$  are ;

$$\lambda_j = M_j - \frac{i}{2}\Gamma_j = M - \frac{i}{2}\Gamma \pm \sqrt{\left(M_{12} - \frac{i}{2}\Gamma_{12}\right) \left(M_{12}^* - \frac{i}{2}\Gamma_{12}^*\right)} \quad (1.24)$$

with eigenvectors ;

$$|B_j\rangle = \frac{1}{\sqrt{1+|p|^2}} \begin{pmatrix} p \\ \pm 1 \end{pmatrix} \quad p = \sqrt{\frac{M_{12} - \frac{i}{2}\Gamma_{12}}{M_{12}^* - \frac{i}{2}\Gamma_{12}^*}} \quad (1.25)$$

where  $j = H, L$  (Hheavy, Light) label the eigenvectors. These are the physical eigenstates of propagation (or 'weak eigenstates').

Neglecting  $CP$  violation,  $p = 1$ , and the weak eigenstates  $|B_H\rangle$  and  $|B_L\rangle$  are simply the  $CP$  eigenstates,  $|B_1\rangle$  and  $|B_2\rangle$  ;

$$\begin{aligned} |B_H\rangle = |B_1\rangle &= \frac{1}{\sqrt{2}} \left( |B^0\rangle + |\bar{B}^0\rangle \right) & CP = +1 \\ |B_L\rangle = |B_2\rangle &= \frac{1}{\sqrt{2}} \left( |B^0\rangle - |\bar{B}^0\rangle \right) & CP = -1 \end{aligned} \quad (1.26)$$

with eigenvalues ;

$$\begin{aligned} \lambda_H &= M_H - \frac{i}{2}\Gamma_H = (M + M_{12}) - \frac{i}{2}(\Gamma + \Gamma_{12}) \\ \lambda_L &= M_L - \frac{i}{2}\Gamma_L = (M - M_{12}) - \frac{i}{2}(\Gamma - \Gamma_{12}) \end{aligned} \quad (1.27)$$

The mass difference between the two eigenstates of propagation is denoted by  $\Delta m = M_H - M_L = 2M_{12}$  and the difference in width by  $\Delta\Gamma = \Gamma_H - \Gamma_L = 2\Gamma_{12}$ .

<sup>4</sup>Note that  $\hbar = c = 1$  is used throughout.

### 1.5.1 Time Development of the $B^0 - \bar{B}^0$ System

In order to discuss the time development of the  $B^0 - \bar{B}^0$  system, the physical eigenstates of propagation,  $|B_{H,L}\rangle$ , are used. Assuming  $CP$  is conserved, the time evolution of an initially pure  $|B^0\rangle$  state can be expressed as :

$$\begin{aligned}
 |B^0\rangle &= \frac{1}{\sqrt{2}} (|B_H\rangle + |B_L\rangle) && \text{time 0} \\
 &\rightarrow \frac{1}{\sqrt{2}} (e^{-i\lambda_H t}|B_H\rangle + e^{-i\lambda_L t}|B_L\rangle) && \text{time } t \\
 &= \frac{1}{2} (e^{-i\lambda_H t} + e^{-i\lambda_L t}) |B^0\rangle + \frac{1}{2} (e^{-i\lambda_H t} - e^{-i\lambda_L t}) |\bar{B}^0\rangle \\
 &\equiv A(t)|B^0\rangle + \bar{A}(t)|\bar{B}^0\rangle && (1.28)
 \end{aligned}$$

Hence, given an initially pure  $B^0$  state, the intensities of  $B^0$  and  $\bar{B}^0$  at a later time  $t$  are given by :

$$\begin{aligned}
 I(B^0 \rightarrow B^0)(t) &= |A(t)|^2 \\
 I(B^0 \rightarrow \bar{B}^0)(t) &= |\bar{A}(t)|^2
 \end{aligned} \tag{1.29}$$

That is :

$$\begin{aligned}
 I(B^0 \rightarrow B^0)(t) &= \frac{1}{4} \left| e^{-iM_H t - \frac{\Gamma_H}{2} t} + e^{-iM_L t - \frac{\Gamma_L}{2} t} \right|^2 \\
 &= \frac{1}{4} (e^{-\Gamma_H t} + e^{-\Gamma_L t} + 2e^{-\Gamma t} \cos(\Delta m t))
 \end{aligned} \tag{1.30}$$

Making the assumption that  $\Delta\Gamma \ll \Gamma$  [9] results in the following expressions :

$$\begin{aligned}
 I(B^0 \rightarrow B^0)(t) &= \frac{1}{2} e^{-\Gamma t} [1 + \cos(\Delta m t)] \\
 I(B^0 \rightarrow \bar{B}^0)(t) &= \frac{1}{2} e^{-\Gamma t} [1 - \cos(\Delta m t)]
 \end{aligned} \tag{1.31}$$

It is clear that the  $B^0$  and  $\bar{B}^0$  intensities oscillate with a frequency which is equal to the difference in mass between the two eigenstates of propagation. Figure 1.4 shows the intensities in (1.31) for the  $B_d$  and  $B_s$  cases, using  $\tau = 1/\Gamma = 1.5$  ps,  $\Delta m_d = 0.467$  ps $^{-1}$  and  $\Delta m_s = 6$  ps $^{-1}$ .

#### Time Integrated Mixing

If  $P_{mix}(t)$  is defined as the probability for a particle produced in state  $B^0$  (or  $\bar{B}^0$ ) to decay in the state  $\bar{B}^0$  (or  $B^0$ ) at time  $t$ , then it follows immediately from Equation (1.31) that :

$$P_{mix}(t) = \frac{1}{2} \Gamma e^{-\Gamma t} [1 - \cos(\Delta m t)] \tag{1.32}$$

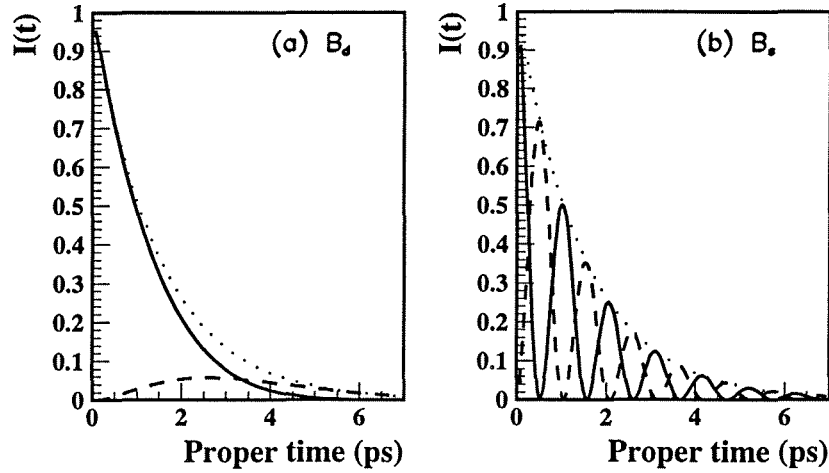


**Figure 1.4:** Intensities of  $B^0$  (solid) and  $\bar{B}^0$  (dashed) as a function of proper time from an initially pure  $B^0$  state (the dotted line shows the total intensity). Plot (a) shows the  $B_d^0$  case for  $\Delta m_d = 0.467 \text{ ps}^{-1}$  and (b) shows the  $B_s^0$  case with  $\Delta m_s = 6 \text{ ps}^{-1}$ .

From this, the time integrated probability for a ‘mixed’ decay,  $\chi$ , is given by :

$$\chi = \int_0^\infty P_{mix}(t) dt = \frac{x^2}{2(1+x^2)} \quad x = \frac{\Delta m}{\Gamma} \quad (1.33)$$

Here  $x$  can be interpreted as the number of oscillations occurring during an average lifetime. If  $\Delta m \ll \Gamma$  then the system will decay before a significant phase difference builds up between the  $|B_H\rangle$  and  $|B_L\rangle$  states and hence  $\chi \rightarrow 0$ . If  $x$  is large then  $\chi \rightarrow \frac{1}{2}$ .

### 1.5.2 Evaluation of $\Delta m$

The expression for  $\Delta m_q$  (where  $q = d, s$  for the  $B_d$  and  $B_s$  systems respectively) is derived by calculating the Feynman diagrams shown in Figure 1.3 [10]. The calculation yields a sum over the heavy quarks<sup>5</sup> in the loop and includes the relevant CKM coupling factors :

$$\Delta m_q = \frac{G_F^2}{6\pi^2} F_{B_q}^2 \mathcal{B}_{B_q} m_{B_q} M_W^2 \left[ \lambda_{c_q}^2 \eta_1 S(x_c) + \lambda_{t_q}^2 \eta_2 S(x_t) + 2\lambda_{c_q} \lambda_{t_q} \eta_3 S(x_c, x_t) \right] \quad (1.34)$$

with :

$$\lambda_{c_q} = |V_{cb}^* V_{cq}| \quad \lambda_{t_q} = |V_{tb}^* V_{tq}| \quad (1.35)$$

<sup>5</sup>The contribution from  $u$  quarks has been neglected since  $x_u$  is very small  $\sim \mathcal{O}(10^{-9})$ .



$$x_i = \frac{m_i^2}{M_W^2} \quad (1.36)$$

$$S(x_i) = x_i \left[ \frac{1}{4} + \frac{9}{4} \frac{1}{(1-x_i)} - \frac{3}{2} \frac{1}{(1-x_i)^2} \right] + \frac{3}{2} \left[ \frac{x_i}{x_i-1} \right]^3 \ln x_i \quad (1.37)$$

$$S(x_i, x_j) = x_i x_j \left[ \left( \frac{1}{4} + \frac{3}{2} \frac{1}{(1-x_j)} - \frac{3}{4} \frac{1}{(1-x_j)^2} \right) \frac{\ln x_j}{x_j - x_i} + (x_j \leftrightarrow x_i) - \frac{3}{4} \frac{1}{(1-x_i)(1-x_j)} \right] \quad (1.38)$$

where  $G_F$  is the Fermi coupling constant,  $m_{B_q}$  is the  $B_q$  meson mass,  $\eta_{1-3}$  are QCD correction factors,  $F_{B_q}$  is the decay constant for the  $B_q$  meson and  $\mathcal{B}_{B_q}$  is a confinement factor. The QCD corrections are discussed in more detail in the following sections.

The complicated expression for  $\Delta m_q$ , given in Equation (1.34), can be simplified by examining the relative importance of the terms in square brackets. The QCD corrections,  $\eta_{1-3}$ , are all of the same order of magnitude, and from the CKM matrix (1.16) the CKM factors for the  $B_d$  system are given by ;

$$\lambda_{cd} = |V_{cb}^* V_{cd}| \approx A\lambda^3 \quad \lambda_{td} = |V_{tb}^* V_{td}| \approx A\lambda^3 \quad (1.39)$$

and for the  $B_s$  system ;

$$\lambda_{cs} = |V_{cb}^* V_{cs}| \approx A\lambda^2 \quad \lambda_{ts} = |V_{tb}^* V_{ts}| \approx A\lambda^2 \quad (1.40)$$

So for each system the CKM factors are of the same order and hence the  $S(x_i)$  factors determine which term in (1.34) dominates. Since<sup>6</sup>  $x_c \approx 3 \times 10^{-4}$  and  $x_t \approx 5$  it is clear that the second term in Equation (1.34) is the dominant one. Terms resulting from the exchange of the lighter  $c$  quark can therefore be neglected giving the simplified expression for  $\Delta m_q$  :

$$\Delta m_q = \frac{G_F^2}{6\pi^2} F_{B_q}^2 \mathcal{B}_{B_q} m_{B_q} \eta_{QCD} M_W^2 S(x_t) |V_{tb}^* V_{tq}|^2 \quad (1.41)$$

where  $\eta_{QCD} \equiv \eta_2$ . Since  $V_{tb} \approx 1$  the above equation allows us to calculate  $|V_{td}|$  and  $|V_{ts}|$  from a measurement of  $\Delta m_d$  and  $\Delta m_s$ . It can be seen from Equations (1.39) and (1.40) that oscillations in the  $B_d$  system are suppressed with respect to the  $B_s$  system and we therefore expect  $\Delta m_s \approx \frac{1}{\lambda^2} \Delta m_d \approx 20 \Delta m_d$ . At present the world average for  $\Delta m_d$  is  $(0.459 \pm 0.018) \text{ ps}^{-1}$  [11] which suggests  $\Delta m_s \approx 10 \text{ ps}^{-1}$  and hence  $\chi_s \approx \frac{1}{2}$ . Thus while  $\Delta m_d$  can be measured from time integrated mixing,  $\Delta m_s$  must be determined by measuring the time dependence directly. At present only lower limits exist for  $\Delta m_s$ , with combined measurements from ALEPH giving  $\Delta m_s > 7.8 \text{ ps}^{-1}$  (at 95% C.L.) [12].

<sup>6</sup>Using  $m_c = 1.3 \text{ GeV}/c^2$ ,  $m_t = 180 \text{ GeV}/c^2$  and  $M_W = 80 \text{ GeV}/c^2$ .

### QCD Corrections and Theoretical Uncertainties

QCD corrections arise in the expression for  $\Delta m_q$  because, in reality, the box diagram is much more complicated than that shown in Figure 1.3, involving gluon exchange between the quarks. The QCD corrections are of two types.

(a) **Short distance effects**

The effective coupling constant  $\alpha_s(\mu)$  of QCD becomes small at short distances corresponding to large momentum transfer. Therefore at short distances lowest order diagrams involving one or two gluon exchanges dominate. These gluons have energies  $E > \mu$  where  $\mu$  is a renormalisation scale taken to be equal to  $m_b$ . The factor  $\eta_{QCD}$  accounts for these short distance corrections and has been calculated to next-to-leading order in  $\alpha_s$ , using perturbative techniques [14] giving  $\eta_{QCD} = 0.55 \pm 0.01$ .

(b) **Long distance effects**

At long distances the coupling becomes large and higher order diagrams involving the exchange of many soft gluons become important. These non-perturbative effects are responsible for the confinement of quarks within hadrons and are much harder to calculate. They are accounted for by the factors  $F_{B_q}$  and  $\mathcal{B}_{B_q}$ . Combining results from lattice QCD and QCD sum rules [13] gives  $\mathcal{B}_{B_d} = 1.0 \pm 0.2$  and  $F_{B_d} = (180 \pm 50) \text{ MeV}$ .

## 1.6 The Shape of the Unitarity Triangle

In order to determine the shape of the triangle, the position of vertex A in the  $\rho - \eta$  plane must be measured (Figure 1.2). This can be achieved by a direct measurement of the angles  $\alpha$ ,  $\beta$  and  $\gamma$  or by measuring the sides  $|AB|$  and  $|AC|$ . At present, experimental results only give information on the lengths of the sides. The angles of the triangle can be calculated using  $CP$  violating asymmetries in the decays of  $B^0(\bar{B}^0)$  mesons into  $CP$  eigenstates, for example  $B_d^0(\bar{B}_d^0) \rightarrow J/\psi K_s^0$ ,  $B_d^0(\bar{B}_d^0) \rightarrow \rho K_s^0$ . Measurements of this kind will be performed at future  $B$  factories.

Measurements of  $\lambda = |V_{us}|$  and the ratio  $|V_{ub}/V_{cb}|$  (Section 1.4.3) constrain vertex A to lie on a circle of radius  $|AC| = 0.36 \pm 0.09$  (Equation (1.20)) centred at  $C(0,0)$ . A measurement of  $\Delta m_d$  together with knowledge of  $|V_{cb}|$ , allows the length of side  $|AB|$  to be determined thus constraining vertex A to lie on a circle centred at  $B(1,0)$ . The length  $|AB|$  increases with decreasing top mass,  $m_t$ , and eventually the circle becomes so large that it completely encloses the  $|AC|$  circle and the two do not intersect. In this way, the first lower limit was set on the top quark mass ( $m_t > 50 \text{ GeV}/c^2$ ). Present measurements of  $\Delta m_d$  give  $|AB| = 0.99 \pm 0.22$  [15]. These two constraints are shown in Figure 1.5.

Another constraint can be obtained from a measurement of the indirect  $CP$  violation parameter<sup>7</sup>  $\epsilon_K$  in the  $K^0 - \bar{K}^0$  system. This constrains vertex A to lie

<sup>7</sup> $\epsilon_K$  is defined as the ratio  $\frac{Br(K_L \rightarrow (\pi\pi)_{I=0})}{Br(K_S \rightarrow (\pi\pi)_{I=0})}$ .

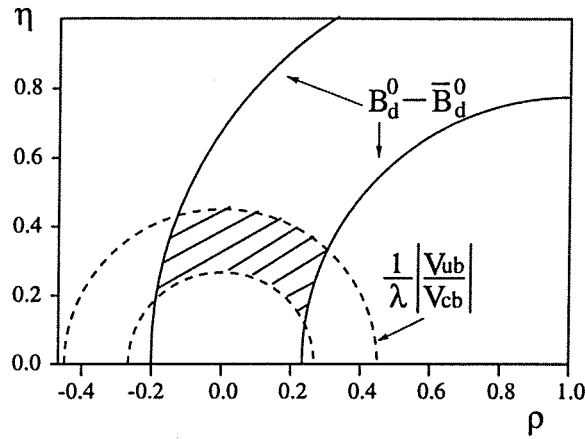


**Figure 1.5:** Constraints on the position of vertex A arising from measurement of  $\left| \frac{V_{ub}}{V_{cb}} \right|$  and  $B_d^0 - \bar{B}_d^0$  oscillations.

in the upper half plane on a hyperbola. A fit for the position of vertex A has been performed [16] using present experimental and theoretical knowledge and the result is shown in Figure 1.6 where the contour represents the 95% confidence level region.

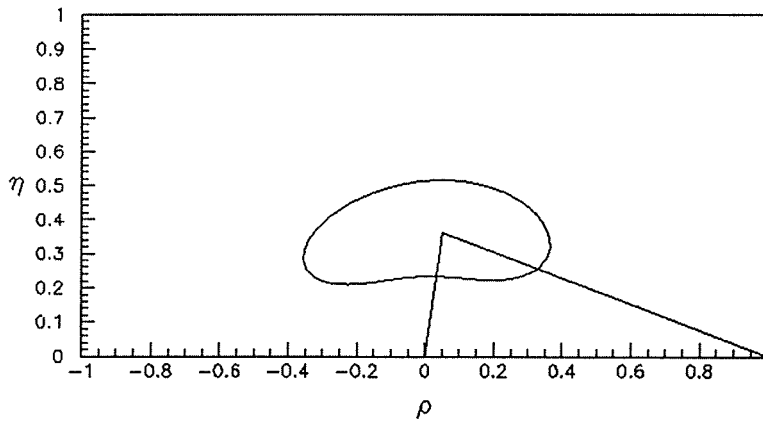


**Figure 1.6:** Result of fit for position of vertex A. The triangle shows the best fit and the contour gives the 95% confidence level region.

It can be seen that current knowledge of the shape of the triangle is rather poor, the uncertainties being largely theoretical. However measurements of both  $\Delta m_d$  and  $\Delta m_s$  allow a ratio to be constructed in which some of these uncertainties cancel :

$$\frac{\Delta m_s}{\Delta m_d} = \frac{m_{B_s} F_{B_s}^2 \mathcal{B}_{B_s}}{m_{B_d} F_{B_d}^2 \mathcal{B}_{B_d}} \left| \frac{V_{ts}}{V_{td}} \right|^2 \equiv \frac{m_{B_s}}{m_{B_d}} \xi_s^2 \left| \frac{V_{ts}}{V_{td}} \right|^2 \quad (1.42)$$

where  $\xi_s$  is estimated to be  $1.16 \pm 0.1$  [13]. All dependence on the top quark mass cancels, along with the  $\eta_{QCD}$  factors which are the same in both systems. The

remaining theoretical uncertainty is in the calculation of  $\xi_s$ . The ratio  $|V_{td}/V_{ts}|$  is directly related to  $|AB|$  (Equation (1.21)) and hence a measurement of  $\Delta m_d$  and  $\Delta m_s$  allows the length of this side to be determined with less theoretical uncertainty.

## 1.7 Summary

Charged current, weak interactions do not conserve quark flavour and allow transitions between the three generations of quarks. Generation mixing is described by the CKM matrix, which is predicted to be unitary by the Standard Model. Measurements of the CKM matrix elements are necessary in order to test unitarity constraints.

Particle-antiparticle oscillations of neutral mesons occur via second order weak processes. The oscillation frequency is determined from the difference in mass between the eigenstates of propagation (Section 1.5.1). Measurements of the oscillations of neutral  $B$  mesons yield constraints on the CKM matrix elements involving the top quark.



# Chapter 2

## Overview and Motivation

In this chapter the basic requirements for measurements of the time dependence of  $B^0 - \bar{B}^0$  oscillations are outlined. The effects of mistags and proper time resolution on the sensitivity of the measurement are shown. A number of methods for studying  $B_d$  and  $B_s$  oscillations are described and the motivation is given for the double jet-charge method used in this analysis.

### 2.1 Requirements for a Mixing Analysis

A measurement of time dependent oscillations requires the following basic components :

- An event sample selectively enriched in  $b$  events.
- The proper lifetime of the  $B$  meson, reconstructed from its decay length and momentum.
- The state of the meson ( $B^0$  or  $\bar{B}^0$ ) at production and decay, determined from the charge of the  $\bar{b}$  (or  $b$ ) quark in the meson at production and decay. A quantity which depends on the initial and final quark charges, referred to as the *charge correlation*, is measured as a function of proper time and fitted to extract the oscillation frequency.

The sensitivity of a mixing measurement depends on the size of the event sample, the fraction of quarks which have their charge wrongly identified (known as the *mistag* fraction) and the proper time resolution. Many different methods have been used for tagging the initial and final meson states and some of these are described in Section 2.2.

For the purpose of discussing the general form of an oscillation signal and showing how the significance of the signal is affected by the mistag fraction and the proper time resolution, a Monte Carlo study is performed on a pure sample of  $b$  events, where the charge correlation is simply defined as the product of the  $b$  quark charges in the meson at production ( $q_{ini}$ ) and decay ( $q_{fin}$ ) :

$$\text{charge correlation} = \langle q_{ini} \times q_{fin} \rangle(t) \quad (2.1)$$

$q_{ini}$	$q_{fin}$	Fraction	Charge correlation
+	+	$(1 - \eta_{ini})(1 - \eta_{fin})$	+
-	+	$\eta_{ini}(1 - \eta_{fin})$	-
+	-	$(1 - \eta_{ini})\eta_{fin}$	-
-	-	$\eta_{ini}\eta_{fin}$	+

**Table 2.1:** The possible charge contributions for an unmixed  $B^0$  meson, taking mistag fractions into account.

Unmixed events give a positive contribution to the charge correlation whereas mixed events give a negative contribution.

In the Monte Carlo sample, all  $b$  hadrons have an equal lifetime of  $\tau = 1.5$  ps, and the values  $\Delta m_d = 0.467$  ps<sup>-1</sup> and  $\Delta m_s = 3.33$  ps<sup>-1</sup> are used. Quark charges are taken as  $\pm 1$  for simplicity.

In the unphysical case, with perfect charge tagging and perfect proper time reconstruction, the charge correlation function defined in Equation (2.1) has a simple form consisting of a constant positive background term from charged  $B$  mesons and  $b$  baryons which do not mix, plus two cosine terms from neutral  $B_{d,s}$  mesons :

$$\langle q_{ini} \times q_{fin} \rangle(t) = f_\Lambda + f_u + f_d \cos(\Delta m_d t) + f_s \cos(\Delta m_s t) \quad (2.2)$$

where  $f_\Lambda$ ,  $f_u$ ,  $f_d$  and  $f_s$  are the relative fractions of baryons,  $B^\pm$ ,  $B_d$  and  $B_s$  as discussed in Section 5.4. In the Monte Carlo  $f_u = f_d \approx 40\%$ ,  $f_s \approx 10\%$  and  $f_\Lambda \approx 10\%$ . Figure 2.1(c) shows the form of this function (Figures (a) and (b) show the contributions from  $B_d$  and  $B_s$  mesons respectively).

### 2.1.1 Effect of Mistag Fraction on Mixing Signal

In a more realistic example, a fraction  $\eta_{ini}$  ( $\eta_{fin}$ ) of hadrons have their initial (final) state wrongly identified, causing a dilution of the mixing signal. As an example of this, consider the case of an initial  $B^0$  meson which decays in the same state as it was produced. If charge tagging is perfect,  $q_{ini}$  and  $q_{fin}$  are both positive, since the  $B^0$  meson contains a  $\bar{b}$  quark, resulting in a positive contribution to the charge correlation. However if mistags are introduced, a number of different outcomes are possible, as shown in Table 2.1. The total mistag rate,  $\eta$  is given by :

$$\eta = \eta_{ini}(1 - \eta_{fin}) + \eta_{fin}(1 - \eta_{ini}) \quad (2.3)$$

since this is the fraction of hadrons for which the contribution to the charge correlation has the wrong sign. The total contribution to the charge correlation from this unmixed  $B^0$  meson will therefore be  $(1 - \eta)(+1) + \eta(-1) = (1 - 2\eta)$ .

Hence the mistag fraction reduces the amplitude of the mixing signal by a factor of  $(1 - 2\eta)$  and Equation (2.2) becomes :

$$\langle q_{ini} \times q_{fin} \rangle(t) = (1 - 2\eta) [f_\Lambda + f_u + f_d \cos(\Delta m_d t) + f_s \cos(\Delta m_s t)] \quad (2.4)$$

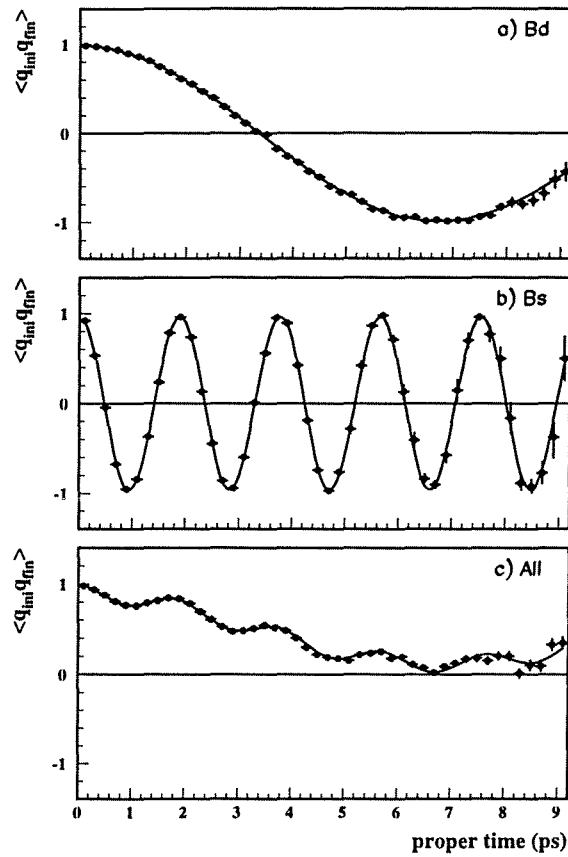


**Figure 2.1:** The charge correlation in the Monte Carlo as function of proper time for the case of perfect charge tagging and proper time reconstruction for (a)  $B_d$  mesons, (b)  $B_s$  mesons and (c) all  $b$  hadrons, where  $\Delta m_d = 0.467 \text{ ps}^{-1}$  and  $\Delta m_s = 3.33 \text{ ps}^{-1}$ .

Figure 2.2 shows the effect of various mistags on the charge correlation function<sup>1</sup>. The figure shows (a) perfect tagging, (b)  $\eta_{ini} = \eta_{fin} = 0.1$  ( $\eta = 0.18$ ), (c)  $\eta_{ini} = \eta_{fin} = 0.2$  ( $\eta = 0.32$ ) and (d)  $\eta_{ini} = \eta_{fin} = 0.3$  ( $\eta = 0.42$ ).

### 2.1.2 Effect of Proper Time Resolution

Detector resolution effects mean that a decay occurring at true time  $t$  will result in a measured decay time  $t_m$ . The proper time resolution function,  $R(t - t_m, \sigma_t)$ ,

<sup>1</sup>The mistag fraction is introduced into the Monte Carlo model by flipping the sign of the quark charge in a fraction of randomly selected events.



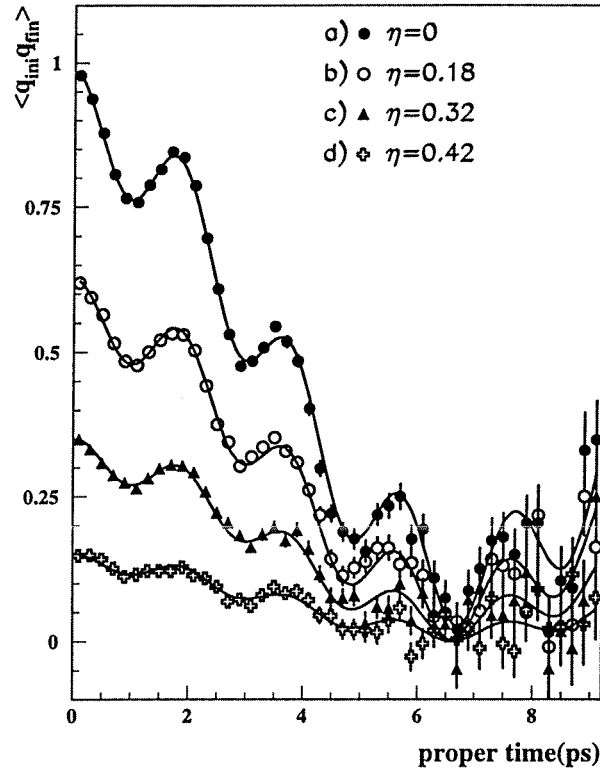


**Figure 2.2:** The charge correlation function in the Monte Carlo for various total mistag rates. The mistag causes a reduction in the amplitude of the signal.

can be described in terms of a Gaussian<sup>2</sup> of width  $\sigma_t$  :

$$R(t - t_m, \sigma_t) = \frac{1}{\sigma_t \sqrt{2\pi}} \exp\left(-\frac{(t - t_m)^2}{2\sigma_t^2}\right) \quad (2.5)$$

The effect of the proper time resolution results in the convolution of the true time distribution with the resolution function. This can be shown [17, 18] to reduce the amplitude of the oscillation signal by a damping factor,  $\exp\left(-\frac{\Delta m^2 \sigma_t^2}{2}\right)$ . The damping factor depends on the frequency,  $\Delta m$ , of the oscillation and hence the higher frequency  $B_s$  oscillations are damped more than the lower frequency  $B_d$  oscillations. The proper time resolution is a critical factor in determining the sensitivity of a method to  $B_s$  oscillations, while being relatively unimportant in the measurement of  $B_d$  oscillations.

The time resolution deteriorates as proper time increases (as discussed in Section 6.4). Figure 2.3 shows the comparison between (a) perfect resolution, (b) 10% resolution and (c) 30% resolution using the Monte Carlo study. The  $B_s$

<sup>2</sup>A sum of two or three Gaussians is a more realistic description of the proper time resolution. The widths also vary rapidly with proper time and this should strictly be taken into account for an accurate estimate of the mixing sensitivity. For this simple discussion, however, only a single Gaussian is considered.

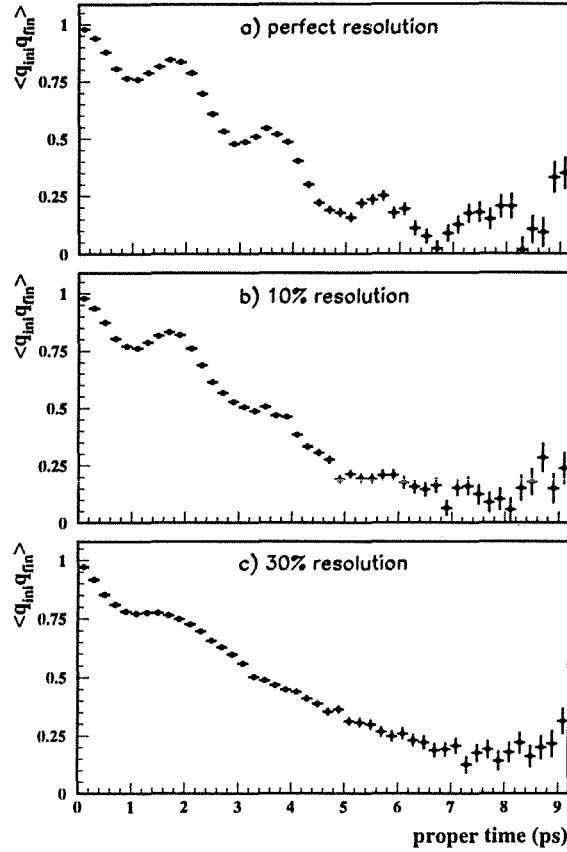


**Figure 2.3:** The charge correlation function in Monte Carlo for (a) perfect proper time resolution (b) 10% resolution and (c) 30% resolution.

oscillations are significantly damped out as the resolution deteriorates.

### 2.1.3 Significance of an Oscillation Signal

Combining the effects of mistag fractions and proper time resolution, along with factors arising from sample size and purity, gives an estimate of the statistical significance which can be achieved using a particular method. The signal/noise ratio is estimated as [17, 18] :

$$\text{signal/noise} \approx \sqrt{\frac{N}{2}} p_q (1 - 2\eta) \exp\left(-\frac{\Delta m_q^2 \sigma_t^2}{2}\right) \quad (2.6)$$

where  $N$  is the number of events in the sample,  $p_q$  is the purity of  $B_q$  mesons in the sample,  $\eta$  is the mistag fraction,  $\sigma_t$  is the proper time resolution in ps and  $\Delta m_q$  is the oscillation frequency for  $B_q$  mesons.

The remainder of this chapter is devoted to an overview of current methods for measuring time dependent oscillations. The motivation is given for the double

jet-charge method which is used in this analysis and comparisons are made with other analyses, based on the signal/noise equation.

## 2.2 Overview of Previous Oscillation Analyses

Methods for measuring time dependent oscillations fall into two general categories; inclusive methods and exclusive, or semi-exclusive, methods. Inclusive methods have the advantage of larger event samples but often mistag fractions are larger and the proper time resolution is worse. Exclusive methods have advantages in that the purity of  $B_s$  or  $B_d$  mesons is enhanced and the proper time resolution is better. However exclusive methods are limited by the small numbers of events. Some current LEP measurements are briefly described in this section.

### 2.2.1 Dilepton Method

The dilepton method [19, 20, 21, 22] is illustrated schematically in Figure 2.4. Hadronic  $Z^0$  decays containing two high transverse momentum leptons are

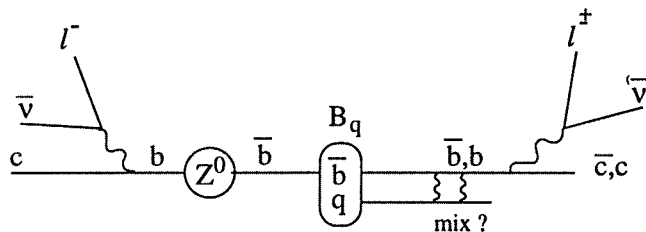
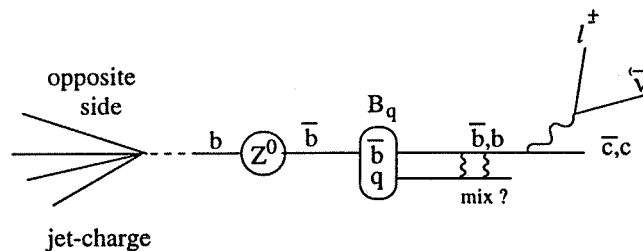


Figure 2.4: Schematic diagram illustrating the dilepton method.

selected. The particle/antiparticle state of the  $B^0$  meson is determined both at production and decay using the sign of the lepton charges. If either of the  $b$  hadrons is a  $B^0$  which oscillates to its antiparticle then the lepton charges will have the same sign. Events in which there has been no oscillation, and events where both mesons have oscillated, have opposite sign leptons. The fraction of dilepton events which have like-sign leptons is studied as a function of the proper time of the  $B^0$  decay. The total mistag fraction in this analysis is approximately 23% and comes largely from cascade decays ( $b \rightarrow c \rightarrow l^+$ , giving a lepton of the wrong sign). Dilepton methods have limited statistics since only about 20% of decays contain a lepton ( $e$  or  $\mu$ ) and hence only 4% of events contain two leptons. Dilepton methods are sensitive to both  $B_d$  and  $B_s$  oscillations.

### 2.2.2 Lepton–Jet-Charge Method

The lepton–jet-charge method [20, 23, 24, 25] is illustrated in Figure 2.5. Only one high momentum lepton is required in the event and its charge is used to tag the state of the  $B^0$  meson at decay. The initial meson state is inferred using



**Figure 2.5:** Schematic diagram illustrating the lepton-jet-charge method.

the ‘jet-charge’ on the opposite side of the event to the lepton. The jet-charge is the weighted sum of particle charges in the jet or hemisphere and reflects the sign of the quark which produced that jet. Charge tagging using the jet-charge is explained in detail in Chapter 5. The lepton-jet-charge method has approximately five times the statistics of the dilepton method since only one lepton is required, however the initial state mistag using the jet-charge method ( $\sim 33\%$ ) is higher than that for leptons giving rise to a total mistag fraction for the lepton-jet-charge method of around  $39\%$ . Like the dilepton analyses, the lepton-jet-charge analyses are sensitive to  $B_d$  and  $B_s$  mixing.

### 2.2.3 $D^*$ and Lepton or Jet-Charge

Many analyses [20, 26, 27, 28] identify  $B_d^0$  mesons by reconstructing the decay chain  $B_d^0 \rightarrow D^{*-} X$ ,  $D^{*-} \rightarrow \bar{D}^0 \pi^-$ , followed by the decay of the  $\bar{D}^0$  into one of  $K^- \pi^+$ ,  $K^- \pi^+ \pi^0$  or  $K^- \pi^+ \pi^+ \pi^-$ . The state of the  $B_d$  meson at decay is determined from the charge of the  $D^*$  and the state at production is determined using either a lepton or the jet-charge in the hemisphere opposite to the reconstructed  $D^*$ . If the  $D^*$  and lepton (or jet-charge) have unlike signs then this indicates that a mix has taken place. This method has advantages in that the  $B_d$  purity is higher than for inclusive analyses, however statistics are limited since only a few specific channels can be reconstructed. This method is not sensitive to  $B_s$  oscillations.

### 2.2.4 Additional Methods for $B_s$ Oscillations

In addition to the dilepton method and the lepton-jet-charge method, other more exclusive methods exist which are used to investigate  $B_s$  oscillations in particular. These methods involve the partial reconstruction of the  $B_s$  meson using either semileptonic decays involving a  $D_s$  meson,  $B_s \rightarrow D_s^{(*)-} l^+ \nu_l X$  [29, 30] or hadronic decays,  $B_s \rightarrow D_s^{(*)-} + \text{hadron}(s)$  [31]. A schematic diagram illustrating these methods is shown in Figure 2.6. The initial state of the  $B_s$  meson may be determined using the charge of a high momentum lepton in the opposite hemisphere if one is available, or by the jet-charge method, or by the charge of a fragmentation kaon which is produced along with the  $B_s$  meson. Some analyses [29, 31] use a combination of all these charge tagging methods to give an optimal tag. The final state of the  $B_s$  is determined using the charge of the

$D_s^\pm l^\mp$  or  $D_s^\pm h^\mp$  ( $h = \text{hadron track}$ ) combination. The  $B_s$  purity is around 67% in the  $D_s^\pm l^\mp$  samples and is around 25% in the  $D_s^\pm h^\mp$  samples, compared to the  $\sim 10\%$   $B_s$  production fraction. The proper time resolution is better than with inclusive methods. However, these methods suffer from a lack of statistics.

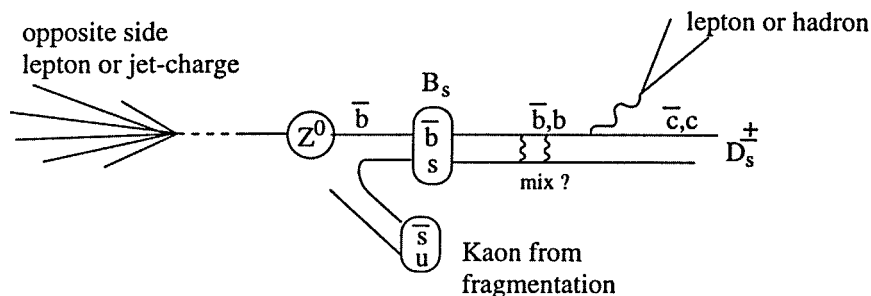


Figure 2.6: Schematic diagram illustrating some of the methods for investigating  $B_s$  oscillations.

## 2.3 Motivation for Double Jet-Charge Method

### 2.3.1 Overview of Method

The aim of the double jet-charge method which is used in this analysis is to obtain as large an event sample as possible, using inclusive tagging and vertexing techniques. The method, illustrated in Figure 2.7, is a generalisation of the lepton-jet-charge method, using the jet-charge to give information on the initial *and* final meson states. The method relies upon the fact that the jet-charge for hemispheres containing mixed mesons is different from that for hemispheres containing unmixed mesons, as explained in Chapter 5. The charge correlation is defined as the product of the jet-charges in the two hemispheres and is measured as a function of the reconstructed proper time in one of the hemispheres.

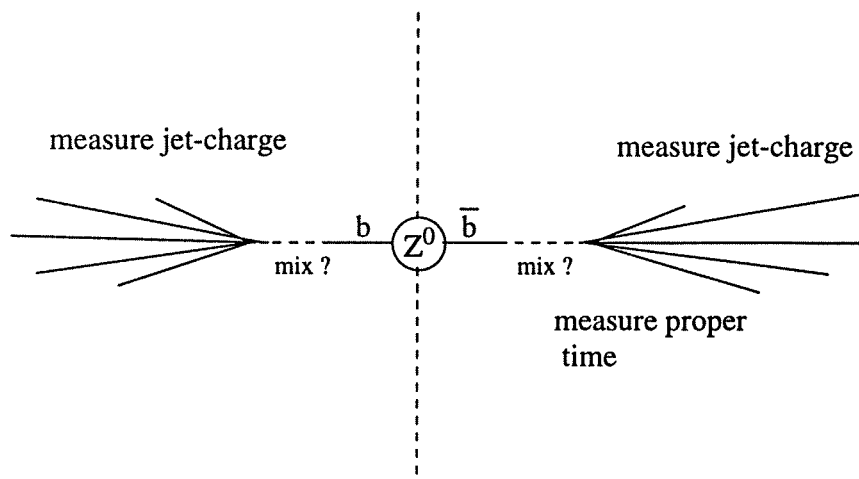


Figure 2.7: Schematic diagram illustrating the double jet-charge method.

The advantage of the double jet-charge method is that, since no lepton is required in the event, the number of events in the sample is expected to be around five times the number in lepton-jet-charge analyses. The disadvantage of the method is that the mistag fraction is higher. The initial and final state mistags for the jet-charge are both around 33% giving a total mistag fraction of 44%.

### 2.3.2 Comparison with other Methods

The statistical significance of the double jet-charge method is calculated using the signal/noise ratio given in Equation (2.6). Table 2.2 shows the expected signal/noise for a measurement of  $B_d$  oscillations using the double jet-charge method, compared to that for the ALEPH lepton-jet-charge and dilepton analyses [20]. The value of  $\Delta m_d$  has been taken as  $0.46 \text{ ps}^{-1}$  and the  $B_d$  purity is taken as 40%. Proper time resolution has a relatively small effect on the sensitivity to  $B_d$  oscillations but the values for each method are included for completeness. It can be seen from Table 2.2 that the double jet-charge method has a greater statistical sensitivity to  $B_d$  oscillations than either the lepton-jet-charge method or the dilepton method, despite the much higher mistag fraction.

Method	$N$	$\eta$	$\sigma_t$ (ps)	signal/noise
Double jet-charge	423169	0.44	$\sim 0.35$	$\sim 22$
Lepton-jet-charge	63131	0.39	$\sim 0.26$	$\sim 16$
Dilepton	9710	0.23	$\sim 0.30$	$\sim 15$

**Table 2.2:** Predicted signal/noise for measurement of  $\Delta m_d$  using double jet-charge method, compared with ALEPH lepton-jet-charge and dilepton methods.  $N$  is the number of events selected from approximately 4 million hadronic  $Z^0$  decays,  $\eta$  is the total mistag for the method and  $\sigma_t$  is an estimate of the proper time resolution.

An estimate of the signal/noise for measurements of  $B_s$  oscillations is shown as a function of  $\Delta m_s$  in Figure 2.8. The parameters used for the various analyses are given in Table 2.3. It can be seen from Figure 2.8 that in all cases the signal/noise decreases rapidly as the value of  $\Delta m_s$  increases due to the exponential damping factor in Equation (2.6). If the value of  $\Delta m_s$  is very high then the oscillations are not distinguishable from noise. Present methods have only succeeded in setting lower limits on the value of  $\Delta m_s$ . The double jet-charge method shows comparable sensitivity to the dilepton and lepton-jet-charge methods. The exclusive analyses, using  $D_s$  events, are inferior at low values of  $\Delta m_s$  due to the low statistics, however they become superior at higher frequencies due to the improved proper time resolution.

In this thesis, a measurement of the  $B_d$  oscillation frequency is presented. An investigation of  $B_s$  oscillations using this method will form part of a program of future work. The double jet-charge method is flexible since, with such a large event sample, tighter quality cuts can be made to improve the proper

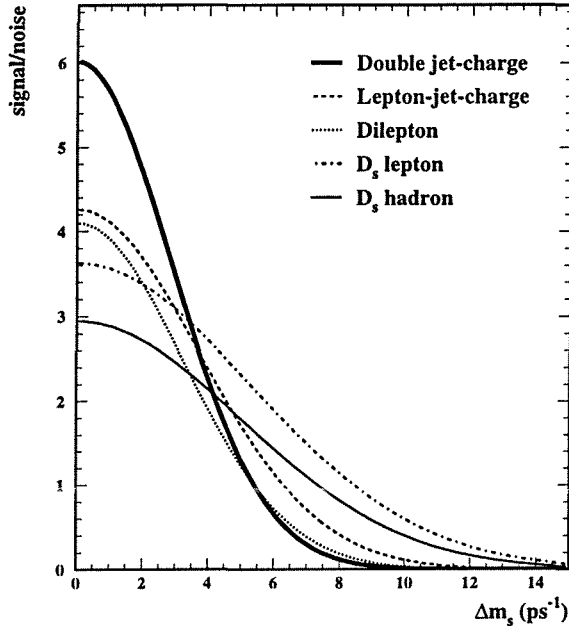


**Figure 2.8:** Estimated signal/noise ratio for several  $B_s$  oscillation analyses, as a function of the  $B_s$  oscillation frequency. The parameters used for each analysis are given in Table 2.3.

Method	$N$	$p_s$	$\eta$	$\sigma_t$ (ps)
Double jet-charge	423169	0.109	0.44	$\sim 0.35$
Lepton-jet-charge	63131	0.109	0.39	$\sim 0.26$
Dilepton	9710	0.109	0.23	$\sim 0.30$
$D_s - lepton$	277	0.67	0.27	$\sim 0.19$
$D_s - hadron$	1583	0.238	0.28	$\sim 0.2$

**Table 2.3:** Properties of various methods for measuring  $B_s$  oscillations.  $N$  is the number of events,  $p_s$  is the purity of  $B_s$  mesons in the sample,  $\eta$  is the total mistag and  $\sigma_t$  is an estimate of the proper time resolution.

time resolution and thus increase the sensitivity to  $B_s$  oscillations. Hence the sensitivity to  $B_s$  oscillations shown in Figure 2.8 should only be regarded as a rough guide since, in this thesis, no optimisation for  $B_s$  oscillations is performed.

# Chapter 3

## The ALEPH Detector at LEP

*“It may look like a big boiler but it’s actually a giant gun that fires bullets smaller than the smallest speck of dust. Scientists spend months studying those curly tracks looking for clues about the origins of the universe.”*

The Edinburgh Evening News (January 28, 1995)

### 3.1 The LEP Collider

ALEPH is one of four experiments which use the Large Electron Positron collider (LEP) at CERN, Geneva. The LEP collider is designed in order to allow detailed study of physics processes predicted by the Standard Model and to search for new phenomena. During the period from 1989 until 1995, electron-positron annihilations occurred at energies around the  $Z^0$  resonance (91.2 GeV) and approximately four million  $Z^0$  decays were detected by ALEPH. LEP has recently entered its second phase of operation at centre of mass energies around 160 GeV and the first  $W^+W^-$  pairs have been produced [32].

The 27 km LEP ring is the last in the chain of five accelerators which make up the CERN complex. The LEP ring and injection scheme are shown in Figure 3.1. Electrons are produced using a high intensity electron gun and accelerated by a 200 MeV linear accelerator (linac). Some of these electrons are then fired at a tungsten converter creating  $e^+e^-$  pairs. The positrons from the converter and the electrons from the linac are further accelerated by a 600 MeV linac and then accumulated in the Electron-Positron Accumulator (EPA) from which they are subsequently injected into the Proton Synchrotron (PS). The PS accelerates the electrons and positrons from 600 MeV to 3.5 GeV before injecting them into the Super Proton Synchrotron (SPS) which accelerates them to 20 GeV before finally injecting them into LEP.

Once inside LEP, dipole magnets around the ring keep the electrons and positrons in circular orbits and quadrupole magnets focus the beams to contain them within the beam pipe. The beams are accelerated by radio frequency (RF) cavities but energy is lost by synchrotron radiation. The energy losses



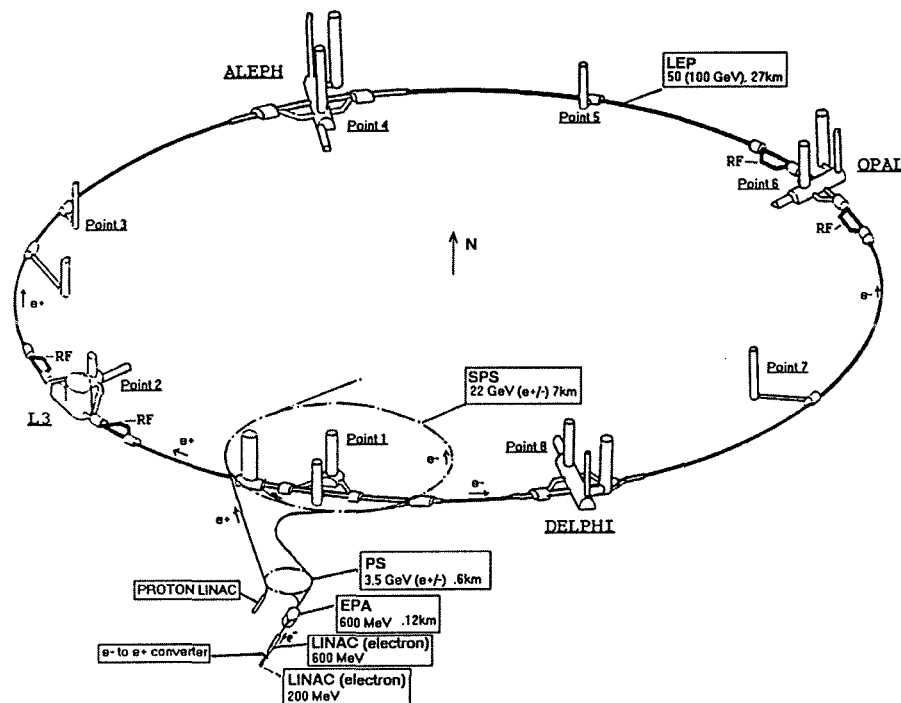


Figure 3.1: The LEP collider.

are proportional to  $E^4$ , where  $E$  is the beam energy, and inversely proportional to the radius of the beam orbit. This is the main reason for the large diameter of LEP. At each experimental collision point the beams are very tightly focused by means of superconducting quadrupoles to collide in an interaction region of transverse dimensions approximately  $10 \mu\text{m}$  by  $250 \mu\text{m}$ . Electrostatic separators are used at each collision point to keep the beams apart during injection and energy ramping.

## 3.2 Overview of the ALEPH Detector

The ALEPH detector is designed to cover all expected types of physics available in the LEP environment. The rate of events is low compared with hadron colliders and as much information as possible must be collected about each

event. The detector covers as much of the solid angle as possible, provides measurements of particle charges, momenta and energies, gives identification of leptons, photons and hadrons and allows measurement of the decay distances of short-lived particles such as  $b$  and  $c$  hadrons. It is sensitive to all  $Z^0$  decay products except neutrinos.

A cut-away view of the detector is shown in Figure 3.2. It forms a cylinder

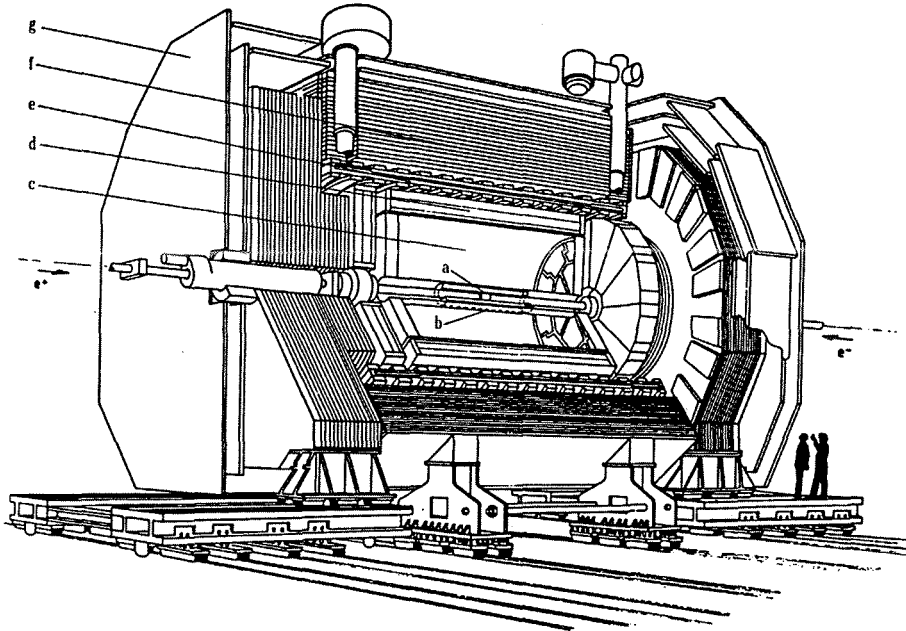


**Figure 3.2:** Overall view of the ALEPH detector; (a) vertex detector, (b) inner tracking chamber, (c) time projection chamber, (d) electromagnetic calorimeter, (e) superconducting solenoid, (f) hadron calorimeter, (g) muon chambers.

around the beam pipe with the interaction point at the centre. A superconducting solenoid provides an axial magnetic field of 1.5 T, enabling the charges and momenta of charged particles to be measured from the curvature of their tracks. Tracking detectors are situated closest to the beam pipe and are surrounded by an electromagnetic calorimeter. A hadron calorimeter is situated outside the superconducting coil and serves as a return yoke for the magnet. The coordinate system used by ALEPH has its origin at the beam crossing point. The positive  $z$  axis points along the  $e^-$  beam direction, the  $x$  axis is horizontal and points towards the centre of LEP and the  $y$  axis points upwards. The sides of the detector are referred to by the letters 'A' and 'B', where side 'A' is on the positive  $z$  side.

The remainder of this chapter aims to give a brief description of the main components of the ALEPH detector, concentrating on features which are of most relevance to the analysis of  $B^0 - \bar{B}^0$  oscillations presented in this thesis. The measurement of the time dependence of these oscillations relies on the ability to efficiently select events containing  $B$  mesons and accurately reconstruct their proper lifetimes. The tracking detectors, in particular the vertex detector,

play a vital role in enabling secondary vertices to be found and decay lengths measured. The tracking performance of ALEPH will therefore be emphasised. The electromagnetic and hadron calorimeters also play an important role in reconstructing the momenta of the  $B$  mesons. A more detailed description of the ALEPH detector can be found in [33, 34].

### 3.3 Tracking Detectors

#### 3.3.1 Vertex Detector (VDET)

The ALEPH silicon vertex detector was installed in 1991. Its purpose is to provide precise three dimensional tracking information close to the interaction point, enabling primary and secondary vertices to be accurately reconstructed. It

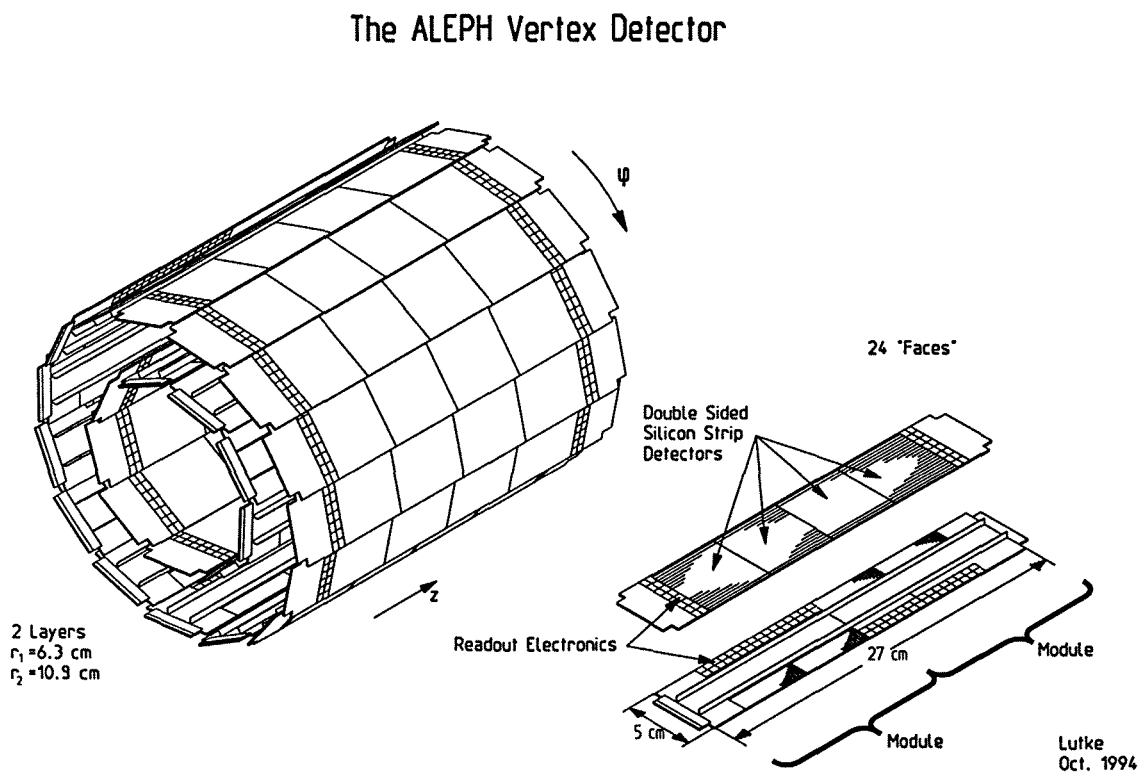


**Figure 3.3:** Configuration of the silicon vertex detector.

consists of two concentric cylindrical layers of double-sided silicon strip detectors at radii of 6.3 cm and 10.9 cm. A diagram of the VDET is shown in Figure 3.3. Each detector comprises a  $5.12$  cm  $\times$   $5.12$  cm  $\times$   $300$   $\mu$ m  $n$ -type silicon wafer onto which strips have been introduced on both sides (Figure 3.4). The strips on one side are  $p^+$  and function as rectifying junctions. The  $n^+$  strips on the other side are ohmic contacts and are separated by  $p$ -implantations in order to interrupt the

accumulation layer of electrons which forms at the Si-SiO<sub>2</sub> interface and would otherwise short-circuit all n<sup>+</sup> strips. A reverse bias voltage depletes the bulk volume and builds up an electric field. A charged particle passing through the detector creates electron-hole pairs which are transported by the electric field to the strips hence producing an electric signal. The strips on one side are parallel

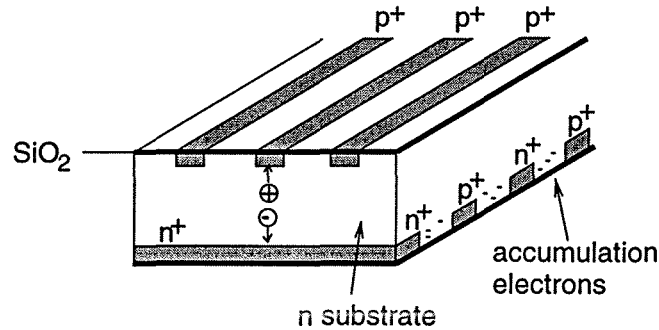


**Figure 3.4:** Schematic of a double-sided silicon strip detector.

to the beam direction and measure the azimuthal angle,  $\phi$ , while those on the other side are perpendicular to the beam and measure the  $z$  coordinate. Along with the radius of the detector layer  $r$  this gives three dimensional positional information for the particle hit.

Electronic units or 'modules' are constructed from two strip detectors. Each face is made up from two modules. The  $r\phi$  strips on neighbouring strip detectors within a module are connected together end-to-end and are read out at the ends of the detector while the  $z$  readout electronics are situated along the detector length.

Tracks with polar angle,  $\theta$ , greater than  $32^\circ$  will have one VDET hit while those with  $\theta > 47^\circ$  will have hits on both layers. The distance between p<sup>+</sup> strips on the  $r\phi$  side is  $25\ \mu\text{m}$  and the distance between n<sup>+</sup> strips on the  $z$  side is  $50\ \mu\text{m}$ . Not every strip is read out, however, the distance between readout strips being  $100\ \mu\text{m}$  on both sides of the detector. Capacitive charge division is used to interpolate the track impact point between readout strips. The spatial resolution achieved with the complete vertex detector is  $12\ \mu\text{m}$  in both the  $r\phi$  and  $z$  views [33, 35].

A new VDET was installed for the second phase of LEP operation. The new detector is approximately twice as long as the present detector, uses radiation-hard electronics, and has all the readout electronics situated at the ends of the detector, thus reducing the amount of passive material near the interaction point.

### 3.3.2 Inner Tracking Chamber (ITC)

The ITC is a cylindrical multiwire drift chamber which provides tracking in the radial region from 16 cm to 26 cm. It is 2 m long and consists of eight concentric layers of drift cells with wires running parallel to the beam direction. Each drift cell comprises six field wires surrounding a sense wire as detailed in Figure 3.5.

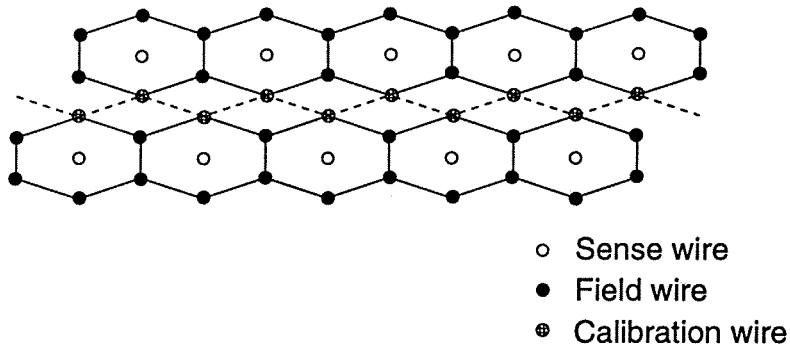


Figure 3.5: The ITC drift cells.

The sense wires are held at a positive potential between 1.8 and 2.5 kV and five of the six field wires are held at earth potential. The other field wire is insulated from earth and can be used to inject a calibration pulse into the chamber. The ITC gas is a mixture of 80% Argon, 20% Carbon Dioxide plus a small amount of Ethanol. The passage of a charged particle causes ionisation in the gas and the liberated electrons then drift towards nearby sense wires where they create secondary ionisation (the Townsend avalanche effect). The signal induced on the sense wire is mainly caused by the movement of positive ions away from it. The  $r\phi$  coordinate is found by measuring the drift time in the cell, giving an accuracy of around  $150\ \mu\text{m}$ . The  $z$  coordinate is obtained by measuring the difference in arrival times of the pulses at each end of the sense wire but the resolution ( $\sim 5\ \text{cm}$ ) is not sufficient for use in three dimensional tracking.

In addition to providing up to eight accurate  $r\phi$  coordinates, the ITC provides the only tracking information used in the level 1 trigger. The need for a fast trigger decision limits the size of the drift cells, the maximum drift distance being 6.5 mm. Two dimensional trigger information is available from the ITC within  $1\ \mu\text{s}$  of a beam crossing.

### 3.3.3 Time Projection Chamber (TPC)

The TPC is a large cylindrical drift chamber which provides up to 21 accurate three dimensional points for each track. It is 4.7 m long and extends radially from 0.31 to 1.8 m. A cut-away view of the TPC is shown in Figure 3.6. The central membrane is held at a potential of  $-27\ \text{kV}$  while the end-plates are grounded, giving rise to an axial electric field of  $11\ \text{kV/m}$ . The gas used in the TPC is 91% Argon and 9% Methane at atmospheric pressure. Ionisation electrons produced by charged particles drift towards one of the end-plates where their position and arrival time are measured. A schematic diagram of part of an end-plate is shown in Figure 3.7. An end-plate is formed from 18 wire chambers each of which comprises three layers of wires : a gating grid, cathode plane and sense wire plane. A plane of 21 radial rows of finely segmented cathode pads is situated approximately 4 mm behind the sense wires and between these rows are long pads which provide information for the second level trigger. Ionisation electrons cause

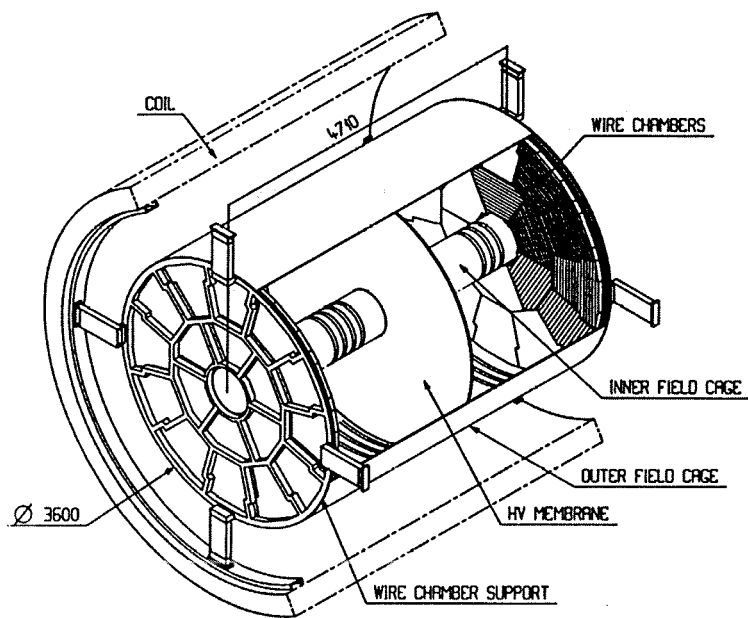


Figure 3.6: The time projection chamber.

avalanches around the sense wires, inducing signals on the nearby cathode pads. The  $\phi$  coordinate is measured by interpolating the signals induced on nearby

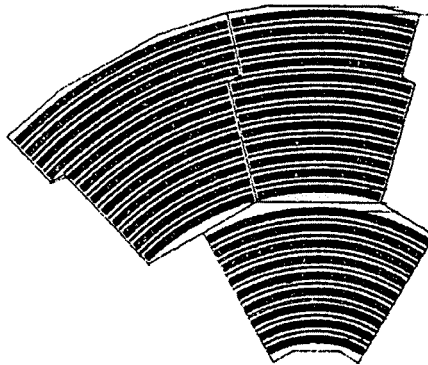


Figure 3.7: Part of a TPC end-plate showing cathode pads for coordinate measurement alternating with trigger pads.

pads and the  $r$  coordinate is given by the radial position of these pads. The  $z$  coordinate is obtained from the drift time and known drift velocity ( $\sim 5 \text{ cm}/\mu\text{s}$ ). The  $r\phi$  coordinate resolution depends on the drift length and the angles of the

track segment with respect to the wires and pads. When the pad crossing angle<sup>1</sup> is  $0^\circ$ , the typical single coordinate  $r\phi$  resolution is about  $180\ \mu\text{m}$ . The  $z$  coordinate resolution depends on the polar angle, being  $800\ \mu\text{m}$  for tracks with polar angle around  $90^\circ$  and becoming approximately twice as large at polar angles of  $20^\circ$ . These dependencies have been measured and parametrised using hadronic and leptonic  $Z^0$  decays and are used to calculate coordinate errors in the track fit. It is important to keep the electric field in the drift region as uniform as possible to avoid track distortions. A gating system is required to prevent positive ions produced during avalanches near the sense wires from entering the drift region and distorting the drift field. Remaining distortions are calibrated using collinear  $\mu$  pairs and a laser system which produces straight tracks. Any measured curvature in these tracks is used to correct the sagitta of particle tracks.

In addition to providing tracking information, the TPC measures the ionisation density,  $dE/dx$ , which can be used for particle identification. The  $dE/dx$  is determined from the pulse height on the sense wire and since the spacing of these wires is 4 mm, a track can have up to 338 sense wire pulses. A  $dE/dx$  estimator for the track is obtained by taking a truncated mean of these measurements.

### 3.3.4 Overall Tracking Performance

#### Track reconstruction

The solenoidal magnetic field causes all charged particles to follow a helical path inside the tracking volume. Track reconstruction begins in the TPC where ‘chains’ of hits are found which are consistent with the hypothesis of lying on the same helix. These chains are linked to form track candidates and are extrapolated to the inner detectors where consistent hits are assigned and the track fit repeated. The track helix is defined by five parameters: curvature ( $R$ ), polar angle ( $\theta$  or  $\lambda$ ), azimuthal angle ( $\phi_0$ ) and impact parameters ( $d_0$  and  $z_0$ ) (Figure 3.8). The  $d_0$  value of a track is signed such that it is positive if the particle has positive angular momentum about the  $z$  axis.

#### Alignment

Accurate determination of the track parameters relies on a precise knowledge of the alignment of the three tracking detectors. The relative alignment of the TPC, ITC and VDET is determined using isolated tracks from hadronic  $Z^0$  decays and the tracks from  $Z^0 \rightarrow \mu^+\mu^-$  events. Tracks are extrapolated back from the TPC to the inner detectors and the residuals between the measured and expected hit positions are analysed. Since the VDET resolution is much better than that of the outer trackers, its alignment does not rely solely on the outer tracking but makes use of self consistency constraints. Tracks which pass through the 5%

---

<sup>1</sup>The pad crossing angle is defined as the angle between the projected track segment and the radial direction. A large crossing angle indicates a large azimuthal spread of the charge cloud and hence poorer  $\phi$  resolution.

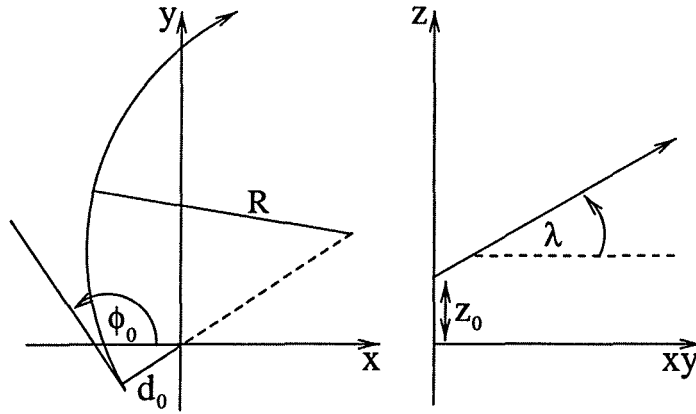


Figure 3.8: Definition of track helix parameters.

Detector	Momentum Resolution $\Delta P/P^2$ (GeV/c) <sup>-1</sup>
TPC only	$1.2 \times 10^{-3}$
TPC + ITC	$0.8 \times 10^{-3}$
TPC + ITC + VDET	$0.6 \times 10^{-3}$

Table 3.1: Momentum resolution of the ALEPH tracking devices.

overlap region of adjacent wafers in  $\phi$  are used to constrain the relative positions of those wafers. The alignment procedure is iterative with VDET constraints also being used to improve the alignment of the outer detectors.

A laser alignment system is also used to monitor relative movements between the VDET and the ITC. The VDET laser system is described in more detail in Appendix A, where an analysis of the laser data is presented.

### Momentum resolution

The transverse momentum of a particle,  $P_T$ , is obtained from its radius of curvature in the magnetic field. The resolution  $\Delta P_T$  is proportional to the resolution of the sagitta of the arc which is obtained by projecting the helix onto the  $r\phi$  plane :

$$\frac{\Delta P_T}{P_T} = 0.027 P_T \frac{\Delta s}{l^2 B}$$

where  $B$ (T) is the modulus of the magnetic field,  $\Delta s$ (mm) is the sagitta resolution and  $l$ (m) is the length of the projected trajectory. The relative error on the measured momentum,  $P$ , of a track arises from the error on the transverse momentum since the error on the polar angle is small ( $\Delta \tan \theta \approx 6 \times 10^{-4}$ ). The error on  $P_T$  has a  $\theta$  dependence since a track with large  $|\cos \theta|$  typically has fewer measured coordinates and a shorter projected trajectory. The momentum resolution for a 45 GeV particle traversing the full TPC radius is given in Table 3.1



Detector	Impact parameter resolution	
	$r\phi$ ( $\mu\text{m}$ )	$rz$ ( $\mu\text{m}$ )
TPC only	300	800
TPC + ITC	100	800
TPC + ITC + VDET	23	28

Table 3.2: Impact parameter resolution of ALEPH tracking devices.

for different sets of detectors [33]. Including the high precision VDET coordinates improves the momentum resolution by around 25%.

### Impact parameter resolution

The impact parameter ( $d_0, z_0$ ) resolution is important in this analysis since it has a direct effect on the resolution of a reconstructed decay length. The impact parameter resolution can be measured using the two tracks from  $Z^0 \rightarrow \mu^+\mu^-$  events. It is obtained from the distance between the two tracks at the interaction point projected into the  $r\phi$  and  $rz$  planes. Figure 3.9 shows the distributions

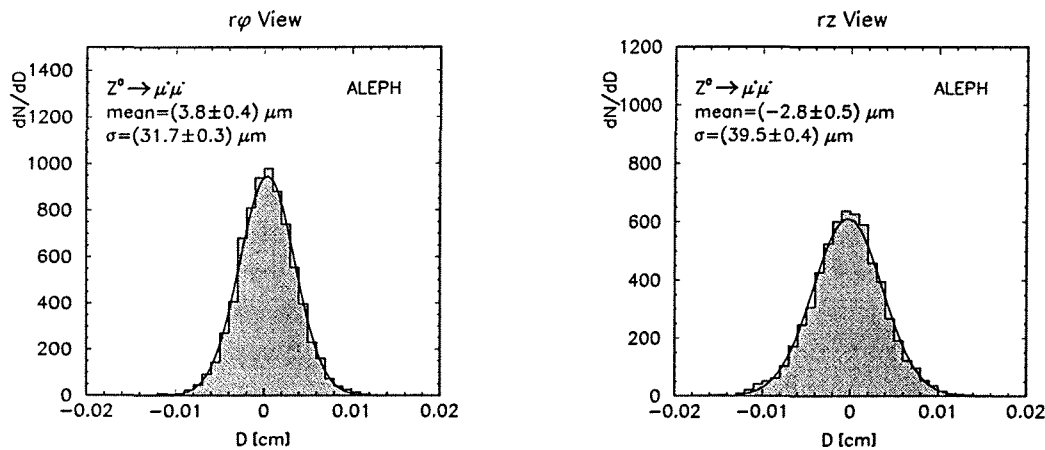


Figure 3.9: Impact parameter resolution in  $r\phi$  and  $z$  from dimuon events.

of these projected distances for events with VDET hits in both layers. Dividing the widths of these distributions by  $\sqrt{2}$  gives the single track impact parameter resolution in the respective direction [36]. The results are summarised in Table 3.2.

## 3.4 Calorimetry

### 3.4.1 Electromagnetic Calorimeter (ECAL)

The ECAL is a lead/proportional wire-chamber sampling calorimeter whose purpose is to identify and measure the position and energy of electrons, positrons and photons. It is situated inside the solenoid and consists of a barrel section extending radially from 1.85 to 2.25 m, plus two end-caps giving large solid angle coverage ( $0 < \phi < 2\pi$  and  $|\cos \theta| < 0.98$ ). A diagram of the ECAL is shown in Figure 3.10. The barrel and end-caps consist of 12 modules, each subtending

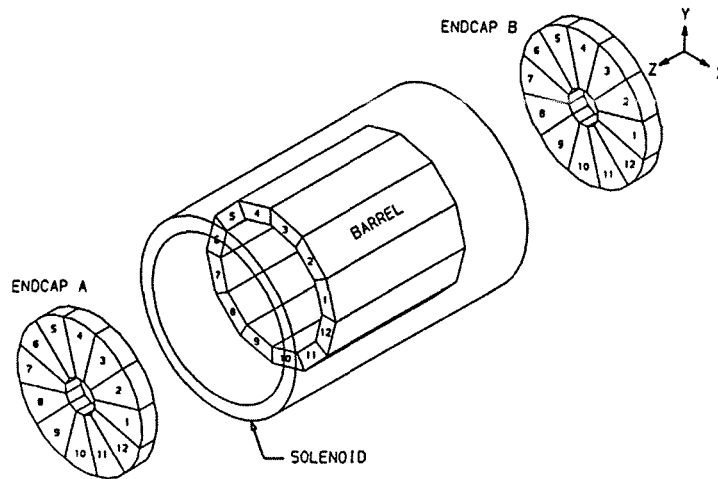


Figure 3.10: The electromagnetic calorimeter.

$30^\circ$  in azimuth. Each module is made up of 45 layers of lead/proportional tubes giving a total of 22 radiation lengths. Cracks between modules constitute about 2% of the barrel and 6% of the end-cap regions. The end-cap modules are rotated by  $15^\circ$  with respect to the barrel to ensure that the cracks do not overlap. The structure of an ECAL layer is shown in Figure 3.11. The lead sheets cause electrons, positrons and photons to produce showers of many electromagnetic particles through the processes of bremsstrahlung and pair-production. These showers cause ionisation avalanches around the anode wires and capacitively induce signals on finely segmented ( $\sim 30 \text{ mm} \times 30 \text{ mm}$ ) cathode pads. The cathode pads are connected together to form 'towers' which point towards the interaction point. The towers subtend an angle of  $0.9^\circ \times 0.9^\circ$  on average and are read out in three sections in depth, known as 'storeys', corresponding to 4, 9 and 9 radiation lengths. Signals are also available from the wires planes, providing information for the trigger. The direction ( $\theta, \phi$ ) of a shower is calculated from an energy weighted mean of the polar and azimuthal angles of the individual storeys in which energy deposits have been detected. The ECAL has an energy resolution of  $\sigma_E/E = 0.18/\sqrt{E/(\text{GeV})} + 0.009$  and an angular resolution of

$\sigma_{\theta,\phi} = (2.5/\sqrt{E/(\text{GeV})} + 0.25) \text{ mrad}$ . Particle identification is obtained using estimators based on the longitudinal and transverse shower shapes.

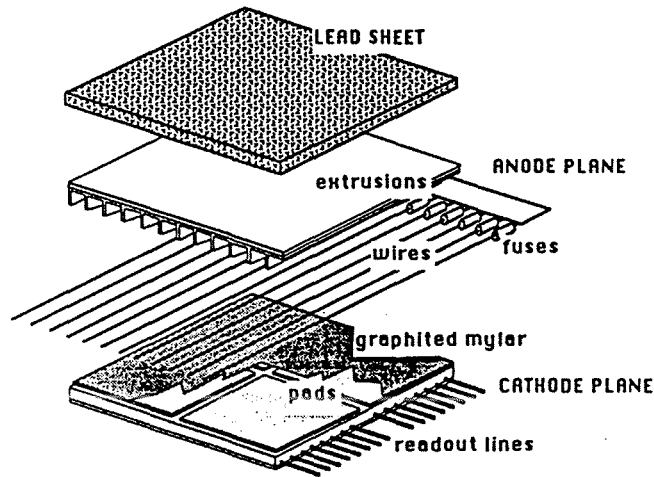


Figure 3.11: Detail of ECAL layer.

### 3.4.2 Hadron Calorimeter (HCAL)

The HCAL is situated outside the solenoid, extending to a radius of approximately 5 m and covering 93% of the solid angle. Its purpose is to absorb and provide information on all particles which pass through the ECAL (mainly hadrons and muons). It also carries the return flux of the magnetic field. It has a similar structure to ECAL, consisting of layers of active detectors sandwiched between layers of absorber. A total of 23 layers of iron are used as the absorber, corresponding to 7.16 interaction lengths at  $90^\circ$ . Streamer tubes are situated between the layers of iron and detect the hadronic showers. Streamer tubes are similar to proportional tubes but operate at a higher voltage which means that the size of signal produced is independent of the incident particle energy. Each streamer tube consists of eight cells which have a cross-section of  $0.9 \text{ cm} \times 0.9 \text{ cm}$  and a length of around 7 m in the barrel region. A  $100 \mu\text{m}$  wire runs along the centre of each cell and operates at 4 kV. The tubes provide three different kinds of signals. Cathode pads on one side of the tubes are used to measure the energy released in the shower. They are connected in projective towers subtending  $3.7^\circ$  in azimuth (one HCAL tower corresponding to around 14 ECAL towers). Aluminium strips (4 mm wide) on the other side of the tubes provide a digital signal if a tube has been fired at least once giving a two dimensional projection of the energy deposition which is used in muon identification. The third signal comes from the wires which give the energy deposited in single planes and is used for triggering. The energy resolution for pions at normal incidence is  $\sigma_E/E = 0.85/\sqrt{E/(\text{GeV})}$ .

### Muon Chambers

Outside the HCAL there are another two double layers of streamer tubes aimed at detecting muons which have passed through the iron layers. Each layer of tubes has cathode strips parallel to the wires on one side and orthogonal strips on the other side. The muon chambers are used as tracking devices and do not give energy information. The two layers are separated by 50 cm in the barrel region and 40 cm in the end-cap region allowing both the position and angle of a track to be measured. The angular resolution is approximately 10 – 15 mrad.

## 3.5 Luminosity Monitors

The integrated luminosity received by ALEPH is measured by determining the rate of elastic scattering (Bhabha) events at small scattering angles for which the cross section is well known<sup>2</sup>. The accuracy of the luminosity measurement depends on a precise measurement of the scattering angle since the cross section is a steep function of this angle. Good background rejection is also important.

The absolute luminosity is not important for the analysis described later, however the luminosity monitors also provide additional energy measurements which are used in calculations of missing energy.

### SICAL

Since 1992 the luminosity measurement has been performed using two silicon-tungsten sampling calorimeters (SICAL) which surround the beam-pipe at distances of  $\pm 2.5$  m from the interaction point, covering values of  $\theta$  between 24.3 and 57.7 mrad. Each calorimeter consists of 12 tungsten sheets alternating with layers of silicon giving a total of 23.4 radiation lengths. Each silicon layer is divided into 512 readout pads, corresponding to 16 radial pad rows of width 5.2 mm and 32 sectors in azimuth. The energy resolution of SICAL, for electrons, is  $\sigma_E/E = 0.33/\sqrt{E/(\text{GeV})}$ .

### LCAL

Prior to the installation of SICAL, the luminosity measurement was performed using a sampling calorimeter based on the design of ECAL. The LCAL consists of 38 layers of lead sheets and wire chambers.

### BCAL

Online luminosity measurement is provided by the very small angle luminosity monitor (BCAL) which consists of two pairs of rectangular detectors placed at distances of  $\pm 7.7$  m from the interaction point. Each calorimeter consists of 10

---

<sup>2</sup>In lowest order of  $\alpha$  ;  $\frac{d\sigma}{d\Omega} = \frac{4\alpha^2}{E^2} \frac{(\hbar c)^2}{\theta^4}$  where  $E$  is the electron energy.

layers of tungsten sheets alternating with layers of plastic scintillator. It covers the polar region  $5.1 \text{ mrad} < \theta < 9.0 \text{ mrad}$ .

## 3.6 Trigger

The purpose of the ALEPH trigger is to initiate readout of genuine  $e^+e^-$  events, reject as many background events as possible and keep the dead time of the detector to a minimum. It should also be sensitive to unforeseen events from 'new' physics.

A three level triggering system is used. The level 1 decision is reached within approximately  $5 \mu\text{s}$  of a bunch crossing and is based on one or more of the following conditions ;

- the energy deposited in the ECAL, HCAL or total detector is larger than a given threshold,
- there are track candidates in the ITC with a corresponding energy deposit in the ECAL or HCAL,
- there are back-to-back tracks in the ITC,
- there is a Bhabha event in SICAL.

A level 1 'NO' causes the detector to be reset in time for the next bunch crossing while a 'YES' decision initiates readout of the TPC.

The level 2 trigger uses information from the TPC trigger pads and hence the decision time is limited by the time required for all the ionisation to drift to the ends of the chamber. This takes about  $50 \mu\text{s}$ . A level 2 'YES' initiates a full read-out of the detector and a 'NO' causes the data acquisition to be cleared ready for the next event. The level 2 trigger rate is  $< 10 \text{ Hz}$ .

The level 3 decision is made by an analysis process which runs within the data acquisition system. Its purpose is to check the level 2 decision using the data from the whole detector and reject events which are not interesting. The level 3 trigger rate is  $1 - 2 \text{ Hz}$  which is an acceptable rate for data storage. The combined trigger efficiency is close to 100% for hadronic and leptonic  $Z^0$  decays and Bhabha events.

## 3.7 Event Reconstruction

In the event reconstruction process, signals from the individual subdetectors are turned into objects which are then used for physics analysis. There are two types of object; tracks and calorimeter clusters. Track reconstruction is outlined in Section 3.3.4. Calorimeter clusters are formed separately in ECAL and HCAL from groups of spatially connected storeys which each have an energy deposition of greater than  $30 \text{ MeV}$ . Two connected storeys must have at least one corner

in common [37]. An energy-flow algorithm is used to combine the track and calorimetric information.

### Energy Flow

The aim of the energy flow algorithm [36] is to improve energy resolution by combining tracking and calorimeter information. The basic idea is to use the tracking detectors to calculate charged particle energies and avoid double counting by masking out the expected energy in the calorimeters which is associated to those tracks. The energy flow is therefore derived from tracks plus unmasked calorimeter energy.

The first stage in the algorithm is a 'cleaning' process. A subset of good charged tracks is formed by requiring each track to have a minimum of four TPC hits and to originate from within a cylinder of length 20 cm and radius 2 cm which is coaxial with the beam and centred on the interaction point. This selection removes  $V^0$  candidates so these are searched for and recovered. Known noisy channels in the calorimeters are masked from the cluster finding and fake energy deposits from occasional noise are removed if the pad signal is incompatible with the signal measured on the wire plane.

After the cleaning process, charged tracks are extrapolated to the calorimeters. 'Calorimeter objects' are formed from associated tracks and calorimeter clusters. The energy associated with identified particles such as electrons, muons, photons and  $\pi^0$ s is masked in the calorimeter object. The remaining particles should be charged and neutral hadrons. The energy of the remaining charged tracks is calculated assuming that they are pions and is subtracted from the remaining calorimeter energy. Finally, the energy remaining in HCAL clusters is attributed to neutral hadrons if it is larger than 500 MeV. Neutrinos escape from the detector without being detected but their energy is inferred from the missing energy in the event.

The energy flow algorithm enables the energy of the whole event to be determined with an accuracy of around 7% as shown in Figure 3.12.

## 3.8 Summary

The ALEPH detector gives a good overall performance in the study of  $e^+e^-$  physics. The tracking detectors provide good momentum and impact parameter resolution which is important in the reconstruction of lifetimes and is vital for studying heavy flavour physics.

Figure 3.13 shows three views of a reconstructed  $b$  event. The top-left picture presents an end-on view of the ALEPH detector showing charged tracks and calorimeter deposits. The top-right picture is a magnified view of the the VDET and the bottom picture shows two reconstructed secondary vertices which have been identified as being from the decay of a  $\bar{B}_s^0$  meson and the subsequent decay of a  $D_s^+$  meson.

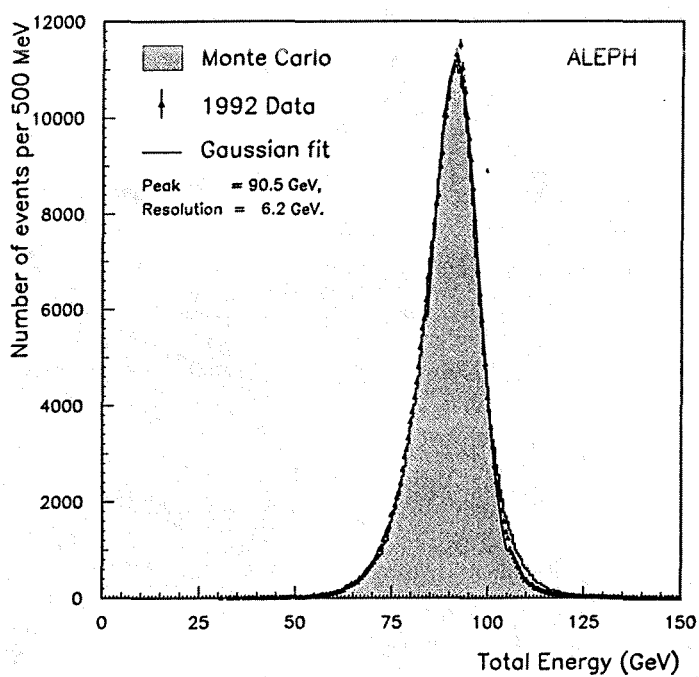


Figure 3.12: Distribution of the total energy calculated using the energy flow algorithm.

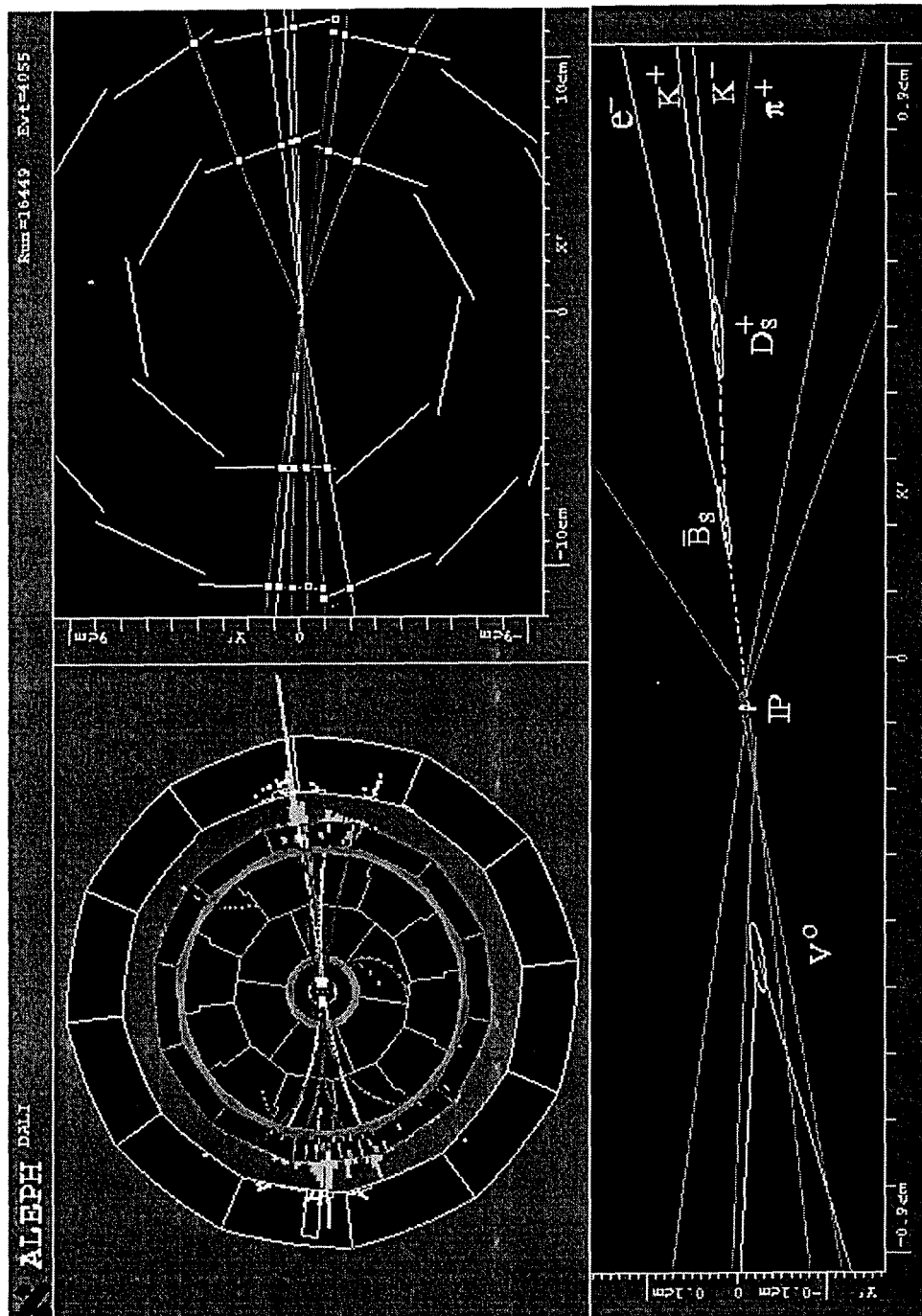


Figure 3.13: A  $b$  event reconstructed in the ALEPH detector.





# Chapter 4

## Event Selection and $b$ Tagging

This chapter describes the procedure for selecting candidate  $b$  events. The basic hadronic event selection is outlined and the procedures for reconstructing primary and secondary vertices are explained. The way in which the secondary vertex reconstruction package is used to enrich the event sample in  $b$  events is described. The need for smearing the track parameters in the Monte Carlo simulation is explained and the smearing procedure is outlined.

### 4.1 Event Selection

Hadronic events are selected from a total of approximately 4.1 million events collected between 1991 and 1995. The selection criteria are as follows :

- The high voltages for ECAL, HCAL and the tracking detectors are on.
- The event contains at least five ‘good’ charged tracks, where a ‘good’ track is defined to ;
  - (a) originate from a cylinder of radius 2 cm and length 20 cm around the interaction point,
  - (b) have at least four TPC hits,
  - (c) have  $|\cos \theta| < 0.95$ , where  $\theta$  is the angle of the track with respect to the beam axis.
- The total energy of all ‘good’ charged tracks must be more than 10% of the centre-of-mass energy.

For events which pass these basic selection cuts, the *thrust axis* is calculated. This is defined as the vector  $\hat{n}$  for which the quantity  $T = \frac{\sum_i |p_i \cdot \hat{n}|}{\sum_i |p_i|}$  is a maximum. A cut is made on the angle of the thrust axis with respect to the beam axis to ensure that events are well contained within the VDET acceptance (Section 3.3.1). Events with  $|\cos \theta_{thrust}| < 0.8$  are accepted and the others are discarded. This is essential for secondary vertex reconstruction. Each event is then separated into two *hemispheres* using the plane perpendicular to the thrust axis.

## 4.2 Vertex Reconstruction

### 4.2.1 Primary Vertex Reconstruction

The position and size of the beamspot are calculated by the ALEPH event reconstruction program using blocks of approximately 100 events. The size of the beamspot envelope is approximately  $150 \mu\text{m}$  in the  $x$  direction,  $3 \mu\text{m}$  in the  $y$  direction and  $\sim 1 \text{ cm}$  in the  $z$  direction [38]. The position of the beamspot is therefore not accurate enough to be used as a primary vertex position and so it is necessary to reconstruct the primary vertex on an event-by-event basis using information from the tracks in the event. It is very important that the reconstructed primary vertex position is not biased by the lifetime of heavy hadrons which may be present in the event. One method of primary vertex finding would be to identify tracks coming from the primary vertex and fit for a vertex position. In addition to being time consuming, this method opens up the possibility of including tracks with lifetime information in the primary vertex fit, hence biasing the primary vertex position.

In this analysis an alternative method is used which is relatively insensitive to hadron lifetimes. The QFNDIP package [39] removes lifetime information by projecting tracks onto a plane perpendicular to the direction of the nearest jet, this being an estimate of the direction of the decaying heavy hadron. The procedure is as follows :

- (1) Perform jet clustering using the JADE [40] algorithm with a  $y_{cut}$  of 0.02 and require at least two jets in the event.
- (2) Project all tracks onto a plane perpendicular to their nearest jet and situated at the origin.
- (3) Find the primary vertex position by minimising the  $\chi^2$  which includes all track information and the beamspot position ;

$$\chi^2 = \sum_{i=1}^3 \frac{(B_i - V_i)^2}{(\sigma_i^B)^2} + \sum_{j=1}^{N_{jet}} \sum_{k=1}^{N_{track}^j} \frac{(D_{\perp}^k)^2}{(\sigma_{\perp}^k)^2} \quad (4.1)$$

where ;

- $B_i$  = beam spot position in the  $i$  ( $x, y$  or  $z$ ) direction,
- $V_i$  = primary vertex position in the  $i$  direction,
- $\sigma_i^B$  = the size of the beam envelope in the  $i$  direction,
- $N_{jet}$  = number of jets,
- $N_{track}^j$  = number of tracks in jet  $j$ ,
- $D_{\perp}^k$  = distance between  $V$  and track  $k$   $\perp$  to jet,
- $\sigma_{\perp}^k$  = track  $k$  error  $\perp$  to jet.

- (4) Refine the vertex position by removing tracks from the calculation which have no relation to either the primary or secondary vertex (such as tracks

from photon conversions and tertiary decays). These tracks are removed if their contribution to the  $\chi^2$  is above a cut value.

- (5) Include the information *parallel* to the jet direction for tracks which have a *negative* projected distance along the jet direction and hence contain no lifetime information.

The procedure described above yields a resolution on the primary vertex of about  $75\ \mu\text{m}$  in  $z$  and  $80\ \mu\text{m}$  in  $x$  for  $b$  events, and  $50\ \mu\text{m}$  in  $z$  and  $60\ \mu\text{m}$  in  $x$  for  $uds$  events [41]. The resolution is better for  $uds$  events since there are more tracks originating from the primary vertex in  $uds$  events. The algorithm is 99.5% efficient and is largely unbiased by hadron lifetimes.

### 4.2.2 Secondary Vertex Reconstruction

The problem of reconstructing secondary vertices is a complex one. A  $b$  hadron produced in the  $Z^0$  decay will typically travel around 2mm before decaying into about five charged hadrons. There may also be a similar number of charged hadrons in that hemisphere coming from the primary vertex. It is time consuming at these high multiplicities to perform a search among all possible track combinations for the best secondary vertex.

In this analysis, secondary vertices are reconstructed using an inclusive pattern recognition package, QVSRCH [42], which is based on a search in coordinate space rather than a search amongst track combinations. Prior to using this algorithm, jet-finding is performed on all energy flow objects, using the JADE [40] algorithm with a  $y_{cut}$  of 0.02, identical to that of QFNDIP. Two jets are chosen as being those most likely to contain the  $b$  hadron decay vertices; the most energetic jet and the one which forms the highest invariant mass with it. The small fraction of events ( $\sim 0.06\%$ ) in which the two chosen jets are in the same hemisphere are rejected. The two jet directions and the primary vertex coordinates and its error are inputs to the QVSRCH algorithm. A quantity called  $\Delta\chi^2$  is defined as the difference between the  $\chi^2$  when all tracks are assigned to the primary vertex, and the sum of the primary and secondary vertex  $\chi^2$  values when some tracks are assigned to a possible secondary. The value of  $\Delta\chi^2$  is calculated for various secondary vertex positions on a grid extending  $\pm 1$  cm along the jet direction and  $\pm 500\ \mu\text{m}$  in the orthogonal direction. The point of maximum  $\Delta\chi^2$  is chosen as the secondary vertex position. This procedure is carried out for both jets therefore giving a secondary vertex position for each hemisphere. As long as there are usable tracks in the hemisphere a secondary vertex position will always be found and the significance of the vertex can be estimated by the size of  $\Delta\chi^2$ . In events with well separated vertices, the  $\chi^2$  will be greatly improved when a possible secondary vertex is introduced. Large values of  $\Delta\chi^2$  can therefore be used to tag  $b$  decays as discussed in the following section. The QVSRCH algorithm is approximately 99% efficient at finding secondary vertices, although the significance of the vertex varies.

After using QVSRCH, secondary vertices are refined by re-vertexing a subset of tracks. This improves the decay length resolution which is obtained and is discussed more fully in Section 6.2.

### 4.2.3 $b$ Tagging

The QVSRCH algorithm returns a variable for each hemisphere, called the BTAG, which is defined to be  $\Delta\chi^2/2$ . A cut on the BTAG value can be used to enrich the event sample in  $b$  events. Ideally, it would be desirable to cut on the BTAG in one hemisphere and reconstruct the proper time in the other hemisphere in an unbiased way. However, it is found that, due to correlations between hemispheres through the shared primary vertex, applying a cut on the BTAG in one hemisphere biases the proper time distribution in the other hemisphere. This bias must be taken into account in the fitting procedure. Therefore, since introducing a bias is unavoidable, an event tag is used, based on a cut on the sum of the BTAG variables in both hemispheres :

$$\text{BTAG}(\text{hemi } 1) + \text{BTAG}(\text{hemi } 2) > \text{BTAG cut} \quad (4.2)$$

Using a cut on the event as a whole has the advantage of being much more efficient than cutting on the BTAG in a single hemisphere. The bias introduced is taken into account in the fitting procedure.

## 4.3 Monte Carlo Simulation

Simulated events are used heavily in all lifetime and mixing analyses and similarly in several key areas of this analysis. In particular, Monte Carlo simulation is used in estimating the sample purity, modelling shapes of background distributions and accounting for the effects of detector resolution. It is vital that discrepancies between data and Monte Carlo simulation are understood and, where possible, reduced to a minimum.

Monte Carlo events are generated using version 7.4 of the JETSET program [43], with parameters tuned to ALEPH data [44]. The events are then passed through the detector simulation program, GALEPH, which converts the generated four-vectors into digitised pulses of the same format as those produced by the data acquisition system. The GALEPH program includes simulations of multiple-scattering, ionisation energy loss, electromagnetic processes and nuclear interactions. The events which are output from GALEPH are then reconstructed using the same reconstruction program, JULIA, as used for real data.

Simulated events corresponding to the 1992, 1993 and 1994 detector geometries are available. Table 4.1 shows the Monte Carlo samples which are used for each data taking period, as it is not possible to form a completely consistent set for each year.

Data year	MC simulation
1991	1992
1992	1992
1993	1993
1994	1994
1995	1994

Table 4.1: Monte Carlo samples corresponding to each data taking period.

## 4.4 Discrepancies between Data and Monte Carlo

Differences between data and Monte Carlo can be seen in the distribution of  $[\text{BTAG}(\text{hemi } 1) + \text{BTAG}(\text{hemi } 2)]$ , as shown in Figure 4.1 for 1993 data and Monte Carlo. This discrepancy gives rise to differences in the efficiency of the BTAG cut as shown in Figure 4.2 and implies differences between data and Monte Carlo in the flavour composition of the final sample. Discrepancies can also be seen in the distributions of reconstructed decay length returned from QVSRCH, as shown in Figure 4.3 for each data year and corresponding Monte Carlo sample.

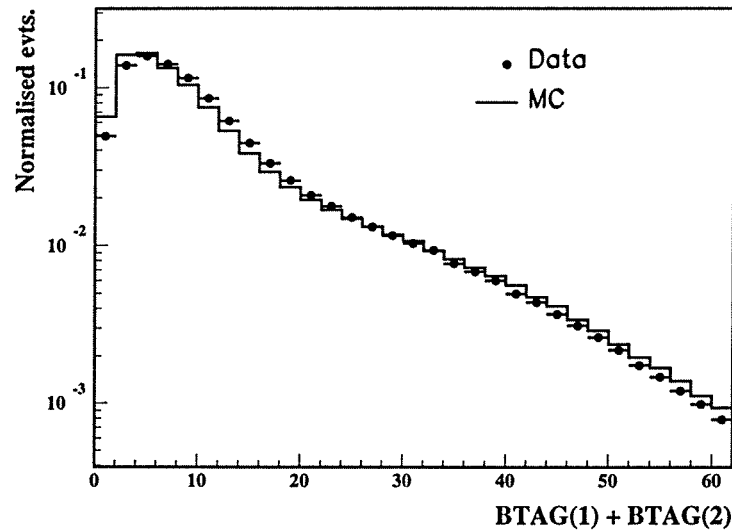
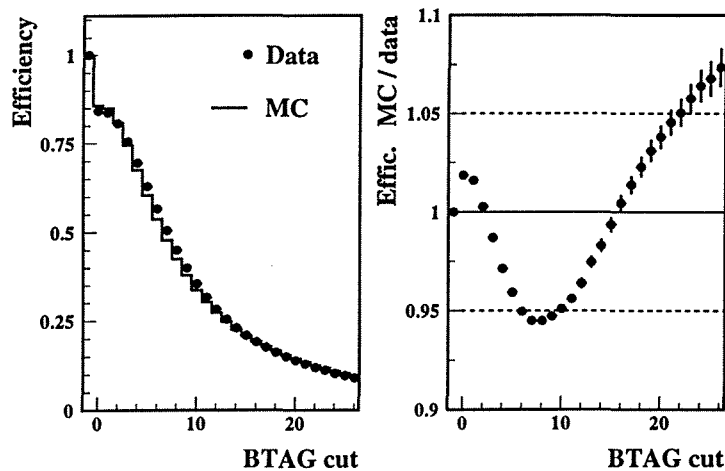


Figure 4.1: Comparison of  $[\text{BTAG}(\text{hemi } 1) + \text{BTAG}(\text{hemi } 2)]$  distributions in 1993 data and Monte Carlo.

The  $[\text{BTAG}(\text{hemi } 1) + \text{BTAG}(\text{hemi } 2)]$  distribution in Monte Carlo has more events with either very high or very low values and less in the intermediate region than the data. This is consistent with the hypothesis that the tracks in the simulation are more tightly clustered round the primary and secondary vertices, while in the data the tracking resolution is worse and the tracks are more spread out. The disagreement in the decay length distribution, especially in the negative tail, also indicates that the resolution in the simulation is better than in the data. The origin of both these discrepancies is a disagreement between data and



**Figure 4.2:** The efficiency of the BTAG cut in 1993 data and Monte Carlo and the ratio of MC/data, prior to Monte Carlo smearing. The horizontal dotted lines indicate a disagreement of 5%.

Monte Carlo in the fundamental track impact parameters,  $d_0$  and  $z_0$ , which are defined in Section 3.3.4. The agreement between data and simulation is improved by performing the Monte Carlo smearing procedure described in the following section.

## 4.5 Monte Carlo Track Smearing

Several precision measurements [45, 46, 47], such as the measurement of  $R_b$ , which rely on impact parameter information, have shown that there is a need for Monte Carlo track smearing. Two main causes of the discrepancy between ALEPH data and Monte Carlo have been identified. These are; (a) the VDET efficiency is incorrectly modelled in the Monte Carlo simulation, resulting in more tracks with VDET hits in the Monte Carlo than in the data and (b) differences exist in the track impact parameter distributions. The smearing procedure [48] described here tackles these problems by; (a) randomly ‘removing’ a fraction of Monte Carlo tracks from the primary and secondary vertexing procedures, depending on the number of VDET hits which are associated with the track and (b) smearing the  $d_0$  and  $z_0$  distributions by an amount determined from comparisons between data and Monte Carlo simulation.

### 4.5.1 VDET Track Removal

Differences in the behaviour of the vertex reconstruction algorithms between data and Monte Carlo can be partly attributed to differences in the numbers of VDET hits which are assigned to tracks. Monte Carlo simulation uses an efficiency

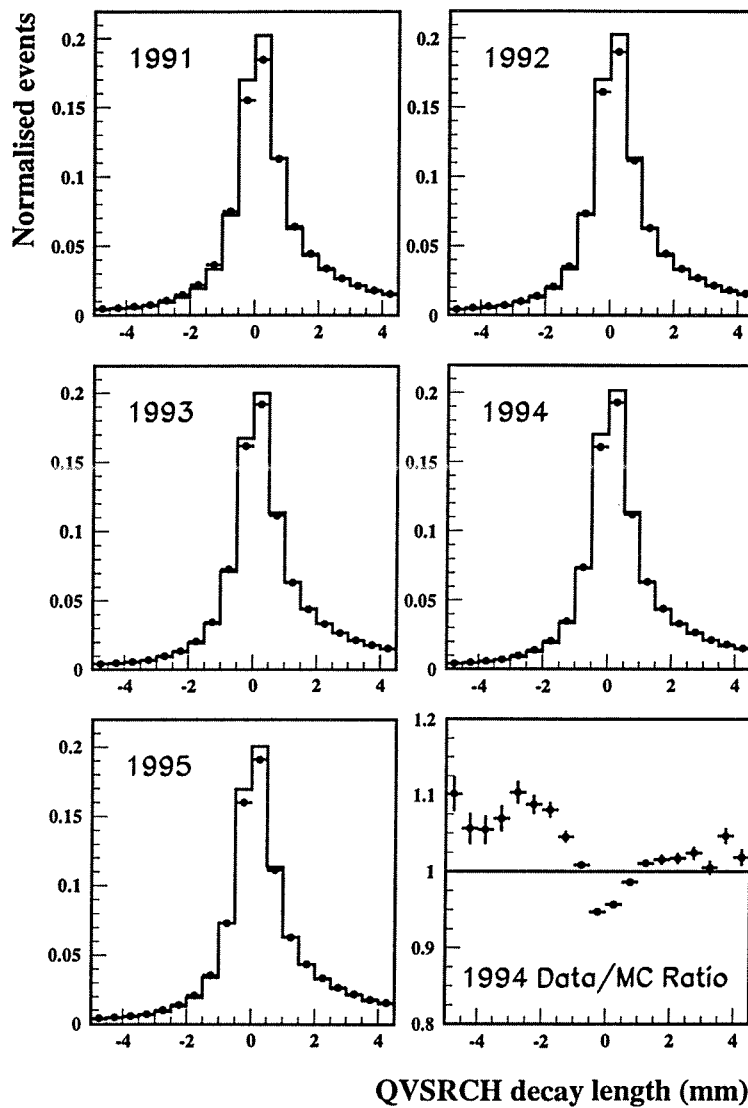


**Figure 4.3:** Distributions of the QVSRCH decay length prior to any  $b$  tagging for each data taking period (points) and corresponding unsmeared Monte Carlo sample (histogram). The final plot shows the ratio data/MC for the high statistics 1994 sample.

map of the vertex detector which reproduces inefficient regions and dead or noisy channels, however, some small discrepancies remain in the efficiency with which VDET hits are assigned to tracks. In general, there are more tracks with VDET hits in Monte Carlo than in data.

In order to correct for this, a small percentage of randomly selected tracks are temporarily removed from Monte Carlo events while primary and secondary vertexing is carried out. The percentage to be removed was calculated by comparing the numbers of tracks with 0, 1 or 2 VDET coordinates in each data



year with that in the corresponding Monte Carlo sample. The comparison was done in 10 equal bins of  $\cos \theta$ , where  $\theta$  is the angle of the track with respect to the beam axis, in order to allow for different data–Monte Carlo discrepancies in regions where there is coverage of either 0, 1 or 2 layers of silicon. The fraction of Monte Carlo tracks with  $n$  VDET coordinates and with  $\cos \theta$  in bin  $\Theta$ , which are to be removed, is given by  $\text{RTK}(\Theta, n)$  ;

$$\text{RTK}(\Theta, n) = \frac{F_{MC}^{\text{tracks}}(\Theta, n) - F_{\text{data}}^{\text{tracks}}(\Theta, n)}{F_{MC}^{\text{tracks}}(\Theta, n)} \quad (4.3)$$

where ;

$n$  = number of VDET coordinates (0, 1 or 2),

$\Theta = \cos \theta$  bin,

$F^{\text{tracks}}(\Theta, n)$  = fraction of tracks in bin  $\Theta$  which have  $n$  VDET hits.

In cases where there are more data tracks than Monte Carlo tracks in a particular bin, the RTK fraction is set to zero for that bin. Tracks are randomly removed from the vertexing procedures if the random number generated for that track is less than RTK for that track type. The RTK fractions used for the various data–Monte Carlo years are shown in Figure 4.4. The extent of the inner and outer layers of the VDET are marked on the plots. It is seen that for all data taking periods, Monte Carlo events have an excess of single and double hit tracks in the region with VDET coverage. The number of tracks to be ‘deleted’ in the 1992 Monte Carlo, in order to match to the 1991 data, is higher than any other year. This is because the VDET was commissioned in 1991 and was initially operated with high thresholds which resulted in lower efficiency than other years. For small track angles where there is no VDET coverage, any vertex detector ‘hits’ are due to noise and there is an excess of these in the data and so RTK is set to zero. Consequently, it can be seen that Monte Carlo track removal is only applied in the central region of the detector, at the level of a few percent. Monte Carlo tracks are only temporarily removed from the vertexing procedure so that properties of the event, such as multiplicity and jet-charge, are not affected.

### 4.5.2 Track Impact Parameter Smearing

The  $d_0$  and  $z_0$  distributions, and their significances ( $d_0/\sigma_{d_0}$ ,  $z_0/\sigma_{z_0}$ ), are shown in Figure 4.5 for data and Monte Carlo<sup>1</sup>. Discrepancies can be seen both in the central regions and in the tails. The track smearing procedure described here uses the shape of the data distributions of the impact parameter significances as a basis for modifying the Monte Carlo distributions. The discrepancies observed may be due to one, or a combination, of the following :

- (i) Physics scattering processes being incorrectly modelled in the simulation.

---

<sup>1</sup>The errors  $\sigma_{d_0}$  and  $\sigma_{z_0}$  are calculated from the track fit errors and are thus available for data and Monte Carlo.

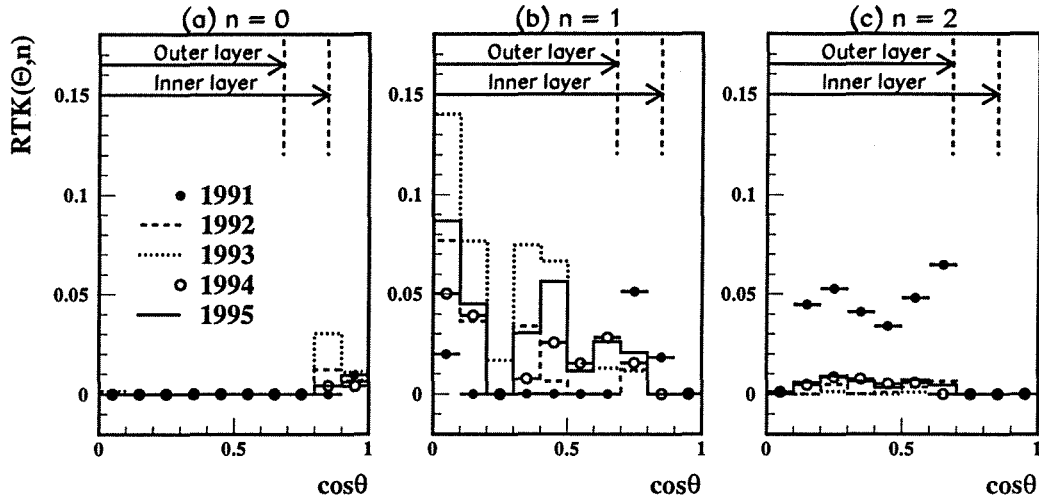


Figure 4.4: Fraction of (a) 0, (b) 1, and (c) 2 VDET hit tracks ‘removed’ in Monte Carlo as a function of  $\cos \theta$  of the track.

- (ii) The distribution of material being different in data and simulation.
- (iii) The amplitude of physics processes being incorrect in the simulation.

In order to perform the track smearing procedure, the data  $d_0 / \sigma_{d_0}$  and  $z_0 / \sigma_{z_0}$  distributions are first parameterised, using a combination of three Gaussians and a Student’s-t distribution. A Student’s-t distribution is given by [49] ;

$$f(t, n) = \frac{1}{\sqrt{n\pi}} \frac{\Gamma[(n+1)/2]}{\Gamma(n/2)} \left(1 + \frac{t^2}{n}\right)^{-(n+1)/2} \quad (4.4)$$

where  $n$  is a positive integer. The Student’s-t distribution resembles a Gaussian with wide tails. The tails diminish as  $n$  increases and the distribution approaches a Gaussian as  $n \rightarrow \infty$ . Student’s-t distributions with  $n = 3$  and  $n = 4$  were found to give the best fits to the  $d_0 / \sigma_{d_0}$  and  $z_0 / \sigma_{z_0}$  distributions respectively. Scaling factors were introduced to allow the width of the Student’s-t distribution to be varied in the fit, along with  $n$  and the amplitude. The parameterisation was found to yield a reasonable quality of fit to the data ( $\chi^2$  of 2 per degree of freedom). Contributions for each component of the parameterisations in data are illustrated in Figure 4.6 for the  $d_0 / \sigma_{d_0}$  case. An identical fitting procedure is applied to the Monte Carlo sample corresponding to each data-taking period. Significant differences are observed in the widths and relative magnitudes of each of the four functions used to parameterise data and Monte Carlo. As the discrepancy may be due to any of the several reasons stated previously, it is of interest to note whether it may be adequately explained by either the simulation yielding different widths or amplitudes in the fitted parameterisations.

It is observed that fitting the Monte Carlo using parameterisations with widths fixed to values determined from data, and allowing the Gaussian and Student’s-t

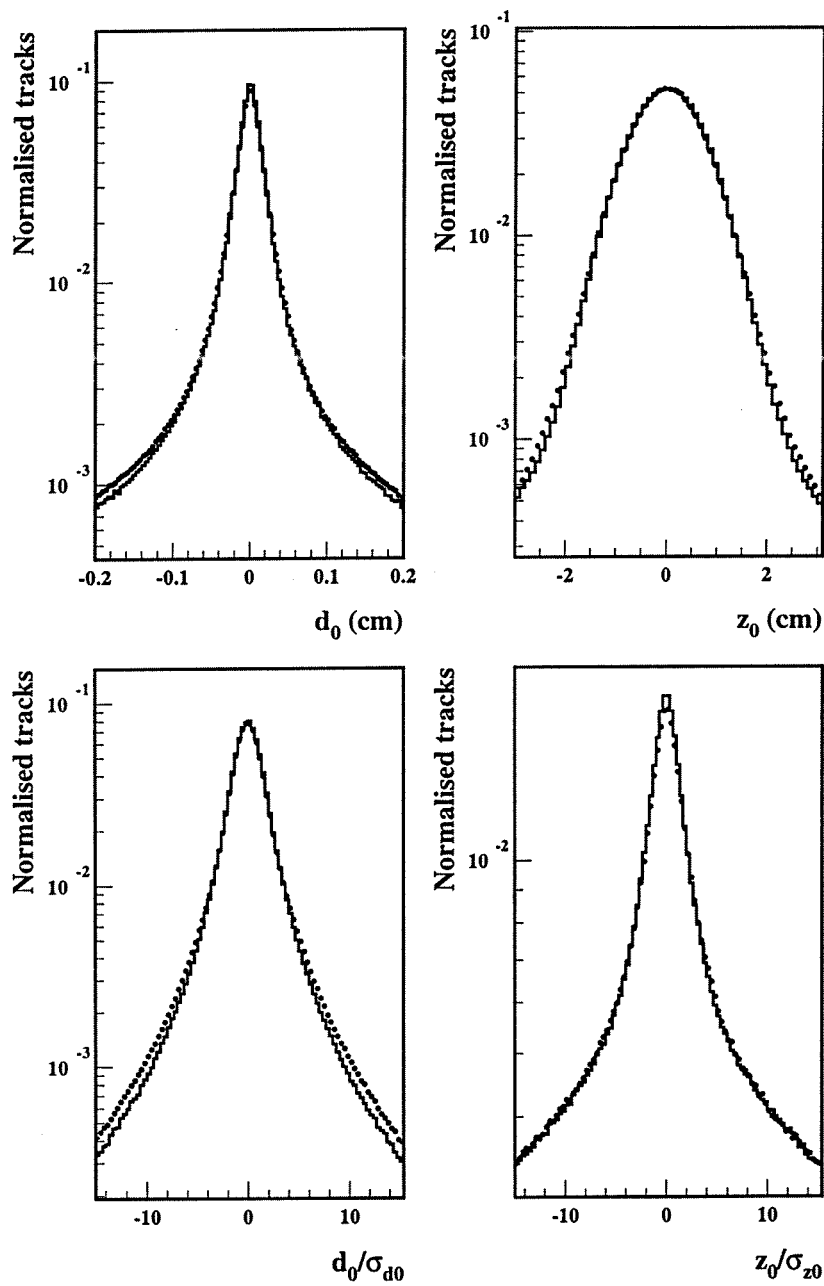


**Figure 4.5:** Distributions of  $d_0$ ,  $z_0$ ,  $d_0/\sigma_{d_0}$  and  $z_0/\sigma_{z_0}$  in data (points) and unsmeared Monte Carlo (histogram).

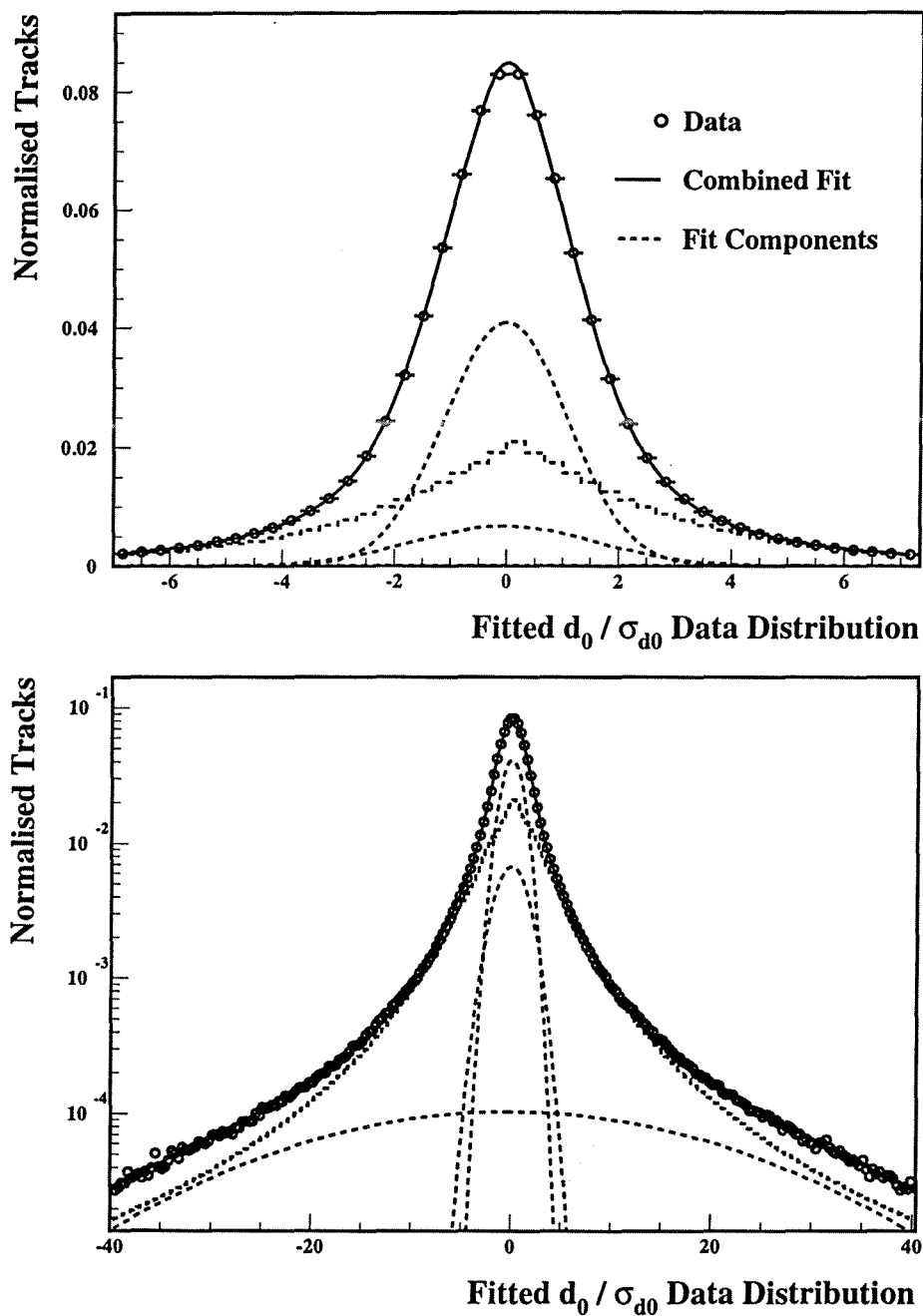


Figure 4.6: Results of the multi-parameter fit to the  $d_0 / \sigma_{d0}$  distribution in the 1992 data. The upper plot shows the central small values on a linear scale whereas the lower plot shows the full range of values on a logarithmic plot.

Function	G1 $\sigma = 1.07$	G2 $\sigma = 1.96$	G3 $\sigma = 21.3$	Student's-t $\sigma = 5.9$
Data	48.3%	11.9%	0.1%	39.7%
Monte Carlo	51.5%	13.4%	0.1%	35.0%

**Table 4.2:** Amplitudes of the three Gaussians (G1, G2, G3) and the Student's-t distribution used to parameterise the  $d_0/\sigma_{d_0}$  distribution in 1992 data and Monte Carlo. The widths of the distributions are determined from data and are fixed while fitting the Monte Carlo distribution.

amplitudes to float, yields a better  $\chi^2$  than the opposite case when the widths are varied. This implies that the discrepancy is most likely to be due to an incorrect modelling of the amplitudes for various scattering mechanisms. Hence, the Monte Carlo fits are performed with fixed widths and the amplitudes of the 4 functions used in the parameterisation are measured. The amplitudes obtained from fits to the  $d_0/\sigma_{d_0}$  distributions in 1992 data and Monte Carlo are given in Table 4.2. It can be seen that the narrowest Gaussians have greater amplitudes in the simulation while the Student's-t has a greater amplitude in data.

### Smearing Algorithm

Based upon the observations of the previous section, the smearing algorithm re-allocates Monte Carlo tracks from a point, on either the  $d_0/\sigma_{d_0}$  or  $z_0/\sigma_{z_0}$  axes, to a new position based upon that expected from the fitted data resolution functions. This is a stepwise approach which proceeds as follows :

- (1) For a given Monte Carlo track's  $d_0/\sigma_{d_0}$  or  $z_0/\sigma_{z_0}$ , the relative values of each of the 3 Gaussian and Student's-t distributions from the simulation are determined. A random number is then used to assign the track to one of the 4 parameterisations.
- (2) If the chosen parameterisation is noted to have a greater amplitude in Monte Carlo, compared to that in data, a second random number is used to reassign the excess fraction of tracks to one of the underpopulated parameterisations.
- (3) The underpopulated data parameterisation is then sampled and the position in  $d_0/\sigma_{d_0}$  or  $z_0/\sigma_{z_0}$  redistributed by firstly calculating the 'true' impact parameters,  $d_0^{true}$  and  $z_0^{true}$ , and then using :

$$\begin{aligned} d_0^{smear} &= d_0^{true} + \mathcal{G} \times \sigma_{d_0} \\ z_0^{smear} &= z_0^{true} + \mathcal{G} \times \sigma_{z_0} \end{aligned} \quad (4.5)$$

where  $\mathcal{G}$  is the sampled number of standard deviations from the data parameterisation. This redistributes simulated  $d_0$  and  $z_0$  significances, and hence their impact parameters, using a method which does not bias the actual value of

$d_0$  and  $z_0$ . The effects of the smearing algorithm on the  $d_0$ ,  $z_0$ ,  $d_0/\sigma_{d_0}$ , and  $z_0/\sigma_{z_0}$  distributions are shown in Figure 4.7. The agreement between data and smeared Monte Carlo is better. Clearly the result is not perfect, however the most important discrepancies in the densely populated central regions of the tracking distributions are almost entirely corrected. The improvement is most marked in the case of  $d_0$ .

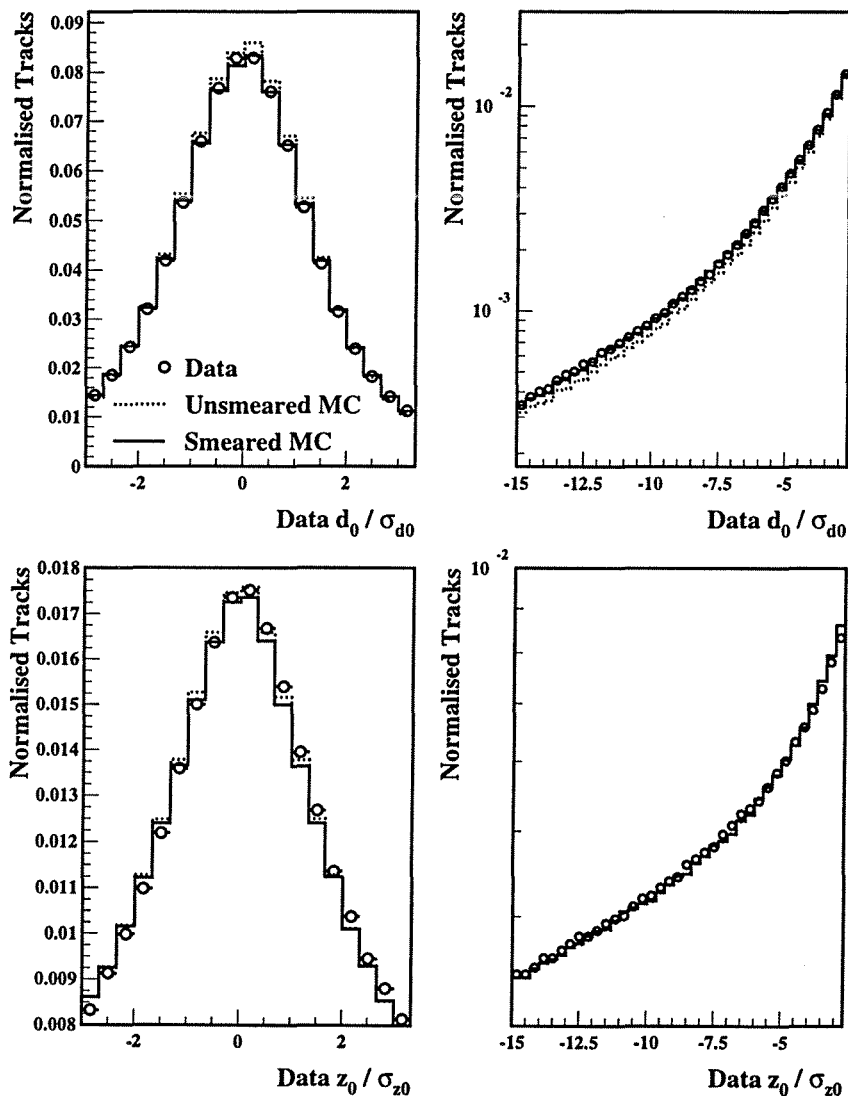


Figure 4.7: Comparison of data distributions of  $d_0/\sigma_{d_0}$  and  $z_0/\sigma_{z_0}$  with smeared and unsmeared Monte Carlo. The left-hand plots indicate the central regions and the right-hand plots show the tail region on a logarithmic scale.

### Re-weighting of Monte Carlo Charm Events

The charm decay tables used in the Monte Carlo simulation vary depending on the year of Monte Carlo production. In order to update Monte Carlo samples to bring them in line with the most recent charm measurements, a package of charm re-weighting algorithms is used. The package was first developed for the  $R_b$  measurements [45, 46]. It assigns both hemisphere and event weights according to the type and simulated lifetime of various charm branching modes. The weights are then used when filling all distributions. The net effect of the charm re-weighting is small.

After VDET track removal, impact-parameter smearing and charm re-weighting have been applied, primary and secondary vertex finding are performed.

### 4.5.3 Results of Monte Carlo Smearing

Prior to applying the track smearing and VDET track removal, significant discrepancies between data and Monte Carlo are observed in the decay length distribution and in the BTAG cut efficiency (see Figures 4.3 and 4.2). After applying the smearing procedure to each Monte Carlo sample, the agreement between each data year and its corresponding Monte Carlo sample is significantly improved. Figure 4.8 shows the decay length distributions obtained from QVSRCH (prior to any BTAG cut) after all Monte Carlo corrections have been applied. The bulk of the discrepancies are corrected, most importantly on the negative side of the distribution which is sensitive to detector resolution effects and relatively insensitive to lifetime contributions. The agreement in the BTAG cut efficiency is also improved, as shown in Figure 4.9 for each data-Monte Carlo year, although a discrepancy of a few percent remains. This discrepancy is used to assign an uncertainty to the flavour composition of the sample as described in the next section.

## 4.6 Purities and Error Determination

The flavour composition after applying a BTAG cut as described in Section 4.2.3 is estimated from the Monte Carlo simulation after smearing has been applied. The  $b$ ,  $c$  and  $uds$  purities and the  $b$  efficiency are shown in Figure 4.10 as a function of the BTAG cut which is applied. The first bin in the plot shows the purities before any cut is applied and the second bin shows the effects of the vertexing (and re-vertexing - Section 6.2) cuts alone. For this analysis a BTAG cut of 20 is used (unless otherwise stated) which gives a  $b$  purity of about 90% and a  $b$  efficiency of around 60%.

Uncertainties are assigned to the purities based on the level of agreement of the tagging efficiency in data and Monte Carlo, at the BTAG cut which is used. From Figure 4.9, the level of agreement at a BTAG cut of 20 is seen to be about 2–6%, depending on the year. In order to convert the error on the overall tagging efficiency into an error on the flavour purities,  $\mathcal{P}_f$ , two methods are considered.

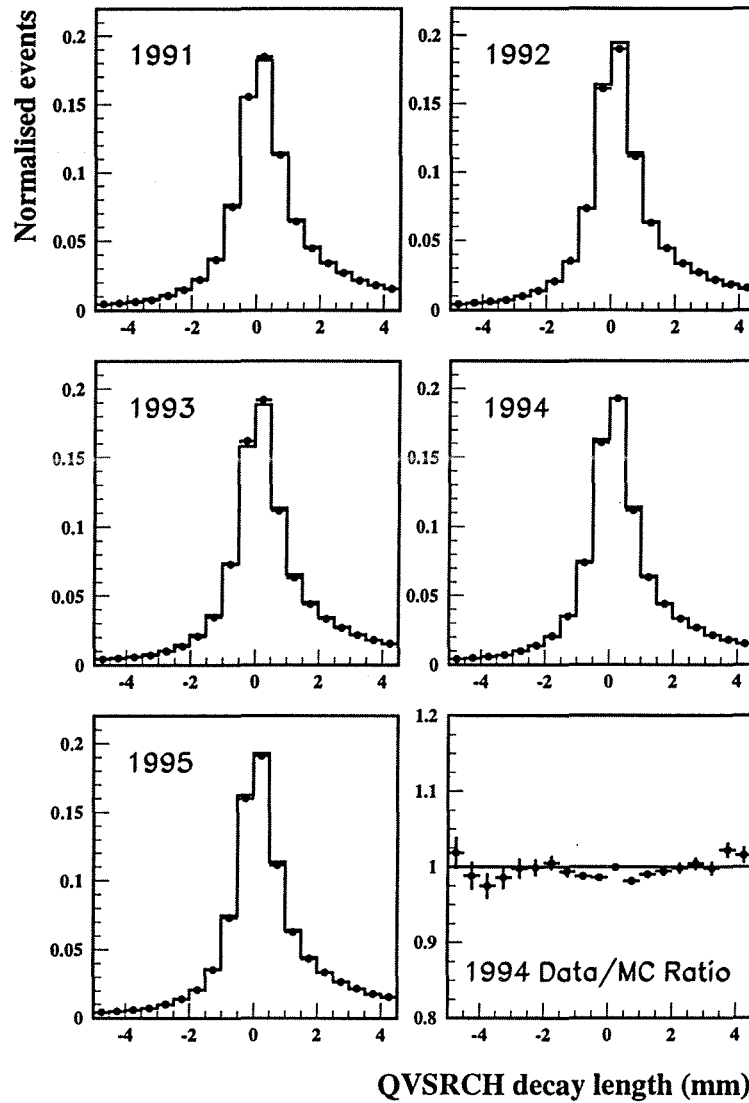


Figure 4.8: Distributions of the QVSRCH decay length prior to any  $b$  tagging for each data taking period (points) and corresponding smeared Monte Carlo sample (histogram). The final plot shows the ratio data/MC for the high statistics 1994 sample.

The errors on the flavour purities,  $\sigma_{\mathcal{P}_f}$  (where  $f = b, c, uds$ ), are related to the errors on the tagging efficiencies,  $\epsilon_f$ , for that flavour by :

$$\frac{\sigma_{\mathcal{P}_f}}{\mathcal{P}_f} = \frac{\sigma_{\epsilon_f}}{\epsilon_f} \quad (4.6)$$

One estimate assumes that the fractional error on the overall efficiency is the same as the fractional error on the flavour efficiency, hence :

$$\sigma_{\mathcal{P}_f} = \mathcal{P}_f \frac{\sigma_{\epsilon}}{\epsilon} \quad (4.7)$$



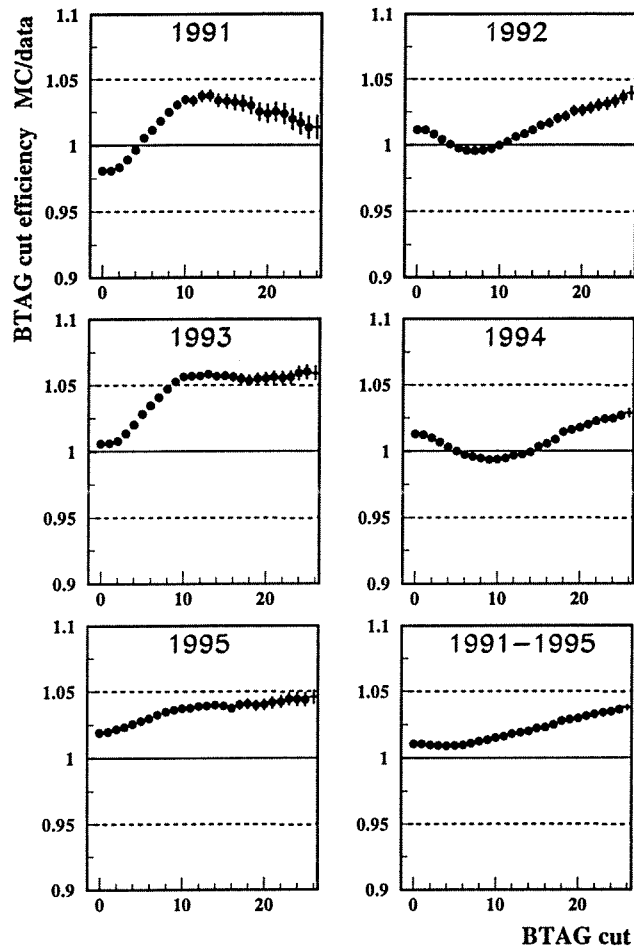


**Figure 4.9:** Ratio of the efficiency of the BTAG cut in the smeared Monte Carlo sample to that in data, for each of the data taking periods and corresponding Monte Carlo samples. The final plot shows the ratio obtained using the combined Monte Carlo sample and combined 1991–1995 data set. In each case the dotted lines represent  $\pm 5\%$ .

where  $\epsilon$  is the overall tagging efficiency at the chosen BTAG cut and  $\sigma_\epsilon$  is the error on the overall tagging efficiency which is taken to be the difference between the tagging efficiencies in data and Monte Carlo. This means that the error on the overall efficiency is ascribed to each flavour in proportion to the sample composition, the dominant error arising from *b* events with the contribution from *c* and *uds* events being negligible.

A second, more conservative estimate allows for the fact that large uncertainties in the *c* and *uds* backgrounds are as likely to give rise to the difference in the overall tagging efficiency as uncertainties in the *b* component. Assigning the total error on the overall tagging efficiency to each of the *b*, *c*, and *uds* components in

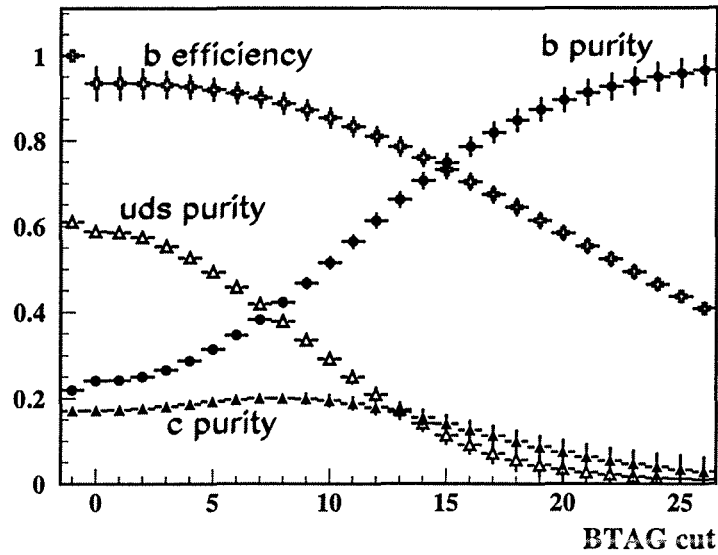


Figure 4.10: Monte Carlo purities and efficiencies as a function of BTAG cut.

turn gives :

$$\sigma_{p_f} = \frac{\sigma_\epsilon}{\epsilon} \quad (4.8)$$

Since this method is the more conservative of the two, it is used in this analysis. In the fit for the average  $b$  lifetime (Section 6.5) the  $b$  and  $c$  purities are allowed to vary in the fit, constrained to their Monte Carlo estimates within the errors given by Equation (4.8). The fitted purities and errors from the lifetime fit are then used in the fit for the mixing parameter,  $\Delta m_d$  (Section 7.5).

## 4.7 Summary

In summary, hadronic events are selected as described in Section 4.1. Monte Carlo events are then modified as described in Section 4.5 by smearing track impact parameters and temporarily ‘removing’ a fraction of tracks depending on their angle and number of associated VDET hits. By smearing in this way, Monte Carlo samples are obtained which are close representations of their corresponding data years. Primary and secondary vertices are found as described in Section 4.2 (after smearing in the Monte Carlo case). Refinement of the secondary vertices is then performed using a revertexing technique which is discussed fully in Section 6.2. The event sample is then enriched in  $b$  events by cutting on the sum of the BTAG values in the two event hemispheres. The statistics of the event selection are summarised in Table 4.3. After all cuts a total of 423169 events are selected from the 1991-1995 data set. In the following analysis, fits are performed on the combined 1991-1995 data set, using a Monte Carlo sample which is formed by combining the smeared Monte Carlo samples for each year in the same proportions

Selection Criteria	Year 1991	1992	1993	1994	1995
Hadronic selection	249352	680577	677501	1748950	749840
Thrust cut	183078	505953	505326	1297540	553560
QFNDIP, QVSRCH	180435	498622	498652	1280240	545771
Revertexing	153767	426895	425632	1097160	464975
BTAG cut = 20	24803	69972	70347	182246	75801
Total 1991-1995	423169				

**Table 4.3:** Summary of selected events after each stage of event selection for the various data taking periods.

as the data. This is referred to as the 'combined Monte Carlo sample'. Fits to individual data years, using their corresponding smeared Monte Carlo samples, are done as stability checks.

# Chapter 5

## Charge Tagging

In this chapter the method of determining quark charges by measuring the jet-charge is explained. In order to do this, the process of *hadronisation* is described, that is, how coloured quarks produced in  $Z^0$  decays are transformed into jets of hadrons which are measured in the detector.

### 5.1 Hadronisation

The decay of a  $Z^0$  boson into a fermion-antifermion pair results in two categories of events. Leptonic events ( $Z^0 \rightarrow l^+l^-$ ) are characterised by few, high momentum tracks while hadronic events ( $Z^0 \rightarrow q\bar{q}$ ) consist of collimated *jets* of particles. A typical hadronic event consists of about twenty charged particles and a similar number of neutral particles. The differences between leptonic and hadronic events arise because leptons are colourless and can exist as free particles whereas quarks are confined and can only exist inside colourless hadrons. The process whereby coloured quarks are transformed into hadrons is called *hadronisation* and consists of two main stages; a *parton shower* stage which is described using perturbation theory, followed by a *fragmentation* stage where perturbation theory breaks down and phenomenological models are used. A schematic diagram of a hadronic  $Z^0$  decay is shown in Figure 5.1.

#### Parton showers

The parton shower stage can be described using perturbative QCD since energies are high and  $\alpha_s$  is small. The shower structure is derived using only the leading terms in the perturbative expansion (the *leading logarithm approximation*) and can be viewed as a series of branchings of the type  $g \rightarrow gg$ ,  $g \rightarrow q\bar{q}$ ,  $q \rightarrow gq$ . The probability that a parton will branch is given by the Altarelli-Parisi equations [50]. The parton cascade continues until the effective mass of the branching parton falls below a cut-off value ( $\sim 1$  GeV). Beyond this cut-off,  $\alpha_s$  is too large and perturbation theory is no longer applicable.

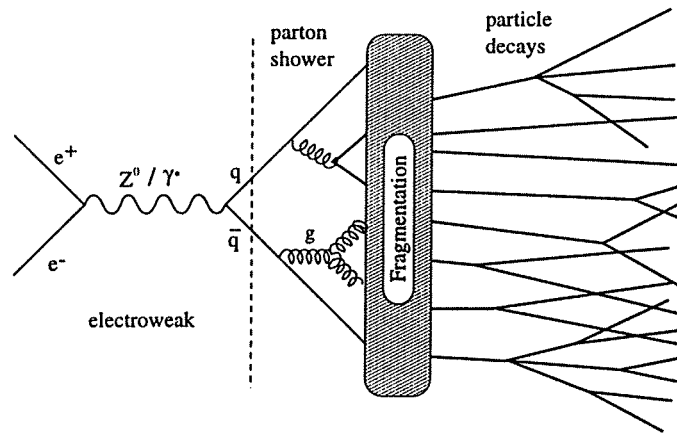


Figure 5.1: Schematic diagram of a hadronic  $Z^0$  decay.

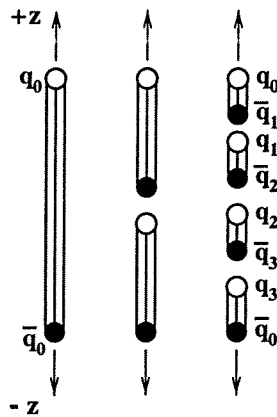


Figure 5.2: Schematic diagram of the string model.

## Fragmentation

As the distance between quarks increases, the strength of the QCD coupling increases and perturbation theory breaks down. A number of models have been created to try and understand the fragmentation process. The ALEPH Monte Carlo uses the ideas of *string fragmentation* in the form of the ‘Lund Model’ [43]. String fragmentation is based on the idea that, at long distances, quarks are confined by a linear potential (Equation (1.1)). The flux tube connecting the  $q$  and  $\bar{q}$  can be thought of as a one dimensional string having energy per unit length<sup>1</sup> (i.e. string constant)  $k$ . As the  $q$  and  $\bar{q}$  fly apart the energy in the string increases until it breaks with the production of another  $q\bar{q}$  pair (Figure 5.2). If the invariant mass of either of the new pieces of string is large enough, then further breaks will occur and the process continues until on-shell hadrons remain where each hadron is made of a small piece of string. The hadrons form collimated jets of particles travelling in approximately the same directions as the original quark and antiquark.

<sup>1</sup>The string constant is deduced to be  $\approx 1 \text{ GeV/fm}$  from hadron spectroscopy.

Partons produced during the shower stage complicate this picture slightly. High energy gluons create kinks in the string and  $q\bar{q}$  pairs produced in the shower will lead to more than one string being formed. In these cases the events may contain three or four (or more) jets.

The production of  $q_i\bar{q}_i$  pairs from the string relies on the idea of quantum mechanical tunnelling. The  $q_i$  and  $\bar{q}_i$  must be produced at a point in order to conserve local symmetries (charge, flavour etc.) however, classically, this can only happen if the  $q_i$  and  $\bar{q}_i$  have no *transverse mass*,  $m_\perp$ , where  $m_\perp^2 = m^2 + p_\perp^2$  and  $m$  and  $p_\perp$  are the quarks' masses and transverse momenta. Classically, if the  $q_i$  and  $\bar{q}_i$  had transverse mass then they would have to be produced some distance apart so that the energy in the string could be converted into the sum of the two transverse masses. Quantum mechanically, the quarks can be produced at a point and then tunnel into the classically allowed region. The tunnelling probability is given by :

$$\exp\left(-\frac{\pi m_\perp^2}{k}\right) = \exp\left(-\frac{\pi m^2}{k}\right) \exp\left(-\frac{\pi p_\perp^2}{k}\right) \quad (5.1)$$

It can be seen from this equation that the production of heavy quarks during fragmentation is strongly suppressed. The flavours of quarks are produced in the ratio :

$$u : d : s : c : b \approx 1 : 1 : 0.3 : 10^{-11} : \sim 0 \quad (5.2)$$

However, heavy quarks can be produced in the parton shower stage by gluon splitting. The string has no transverse modes of oscillation and hence the transverse momentum of quark  $q_i$  must balance that of its antiquark  $\bar{q}_i$ . The transverse momentum of the hadron formed from  $q_{i-1}$  and its neighbouring antiquark  $\bar{q}_i$  (Figure 5.2) is given by the sum of  $p_{\perp i-1}$  and  $p_{\perp i}$ .

The energy and longitudinal momentum (with respect to the initial quark directions) of each hadron is constrained by the transverse mass :

$$m_\perp^2 = E^2 - p_z^2 = (E + p_z)(E - p_z) \quad (5.3)$$

Assuming that the string breaks start at the quark end, the hadron  $q_0\bar{q}_1$  is formed, taking away a fraction  $z$  of the total available  $(E + p_z)$ , leaving reduced  $(E + p_z)$  and  $(E - p_z)$  given by :

$$(E + p_z)_{new} = (1 - z)(E + p_z)_{old} \quad (5.4)$$

$$(E - p_z)_{new} = (E - p_z)_{old} - \frac{m_\perp^2}{z(E + p_z)_{old}} \quad (5.5)$$

The new string behaves in the same way as the old string and further hadrons are formed by iterating the above process. The probability that a hadron takes a fraction  $z$  of the  $(E + p_z)$  of the string is given by a *fragmentation function*  $f(z)$ . Several forms have been tried for  $f(z)$  [43, 51]. The Lund Symmetric fragmentation function :

$$f(z) \sim \frac{1}{z} (1 - z)^a \exp\left(-\frac{bm_\perp^2}{z}\right) \quad (5.6)$$

with  $a = 0.5$  and  $b = 0.92$  [44], gives a good description of light quark ( $u, d, s$ ) fragmentation but suggests a harder spectrum for  $B$  mesons than is observed in data. The Peterson fragmentation function [52] gives a better description for  $b$  and  $c$  hadrons ;

$$f(z) \propto \frac{1}{z \left(1 - \frac{1}{z} - \frac{\epsilon_q}{1-z}\right)^2} \quad (5.7)$$

where the parameter  $\epsilon_q$  ( $q = b, c$ ) varies as  $1/m_q^2$ . The form of the Peterson function is shown in Figure 5.3 for the values  $\epsilon_b = 0.0045$ ,  $\epsilon_c = 0.03$  which are used in the 1994 Monte Carlo simulation. It can be seen that  $b$  and  $c$  hadrons are likely to take away a high fraction of the  $(E + p_z)$  of the string.

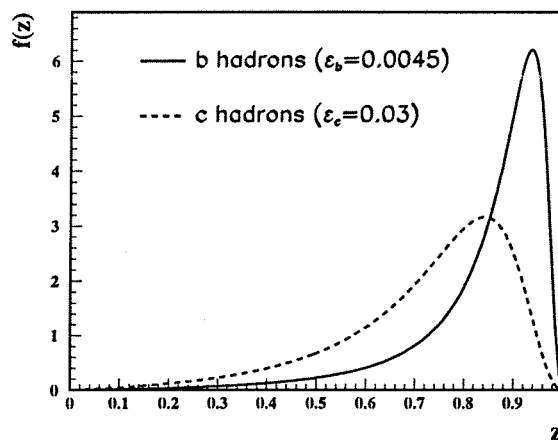


**Figure 5.3:** The Peterson distribution (5.7) for the fraction of  $(E + p_z)$  taken by hadrons containing  $b$  and  $c$  quarks.

The fragmentation process gives rise to an ordering of the final particles in their flavour relationships as shown in Figure 5.4 for the case of an initial  $b$  quark. The meson which contains the original quark (i.e. the *primary* meson) is given a *rank* of one, the neighbouring hadron is assigned rank two and so on down the chain. The decay products are assigned the same rank as their parents.

## 5.2 Charge Tagging using Jet-Charge

The jet-charge method has been used as a means of tagging initial quark charges in many analyses [24, 53, 54]. It is based on the fact that the particles produced during hadronisation retain some information about the charge of the quark which produced that jet [55]. This effect was first observed in neutrino and muon scattering experiments [56].

It can be appreciated from Figure 5.4 that if the primary meson is charged then the sum of charges of all rank one particles must have the same sign as the original quark. If the primary meson is neutral then the rank one particles

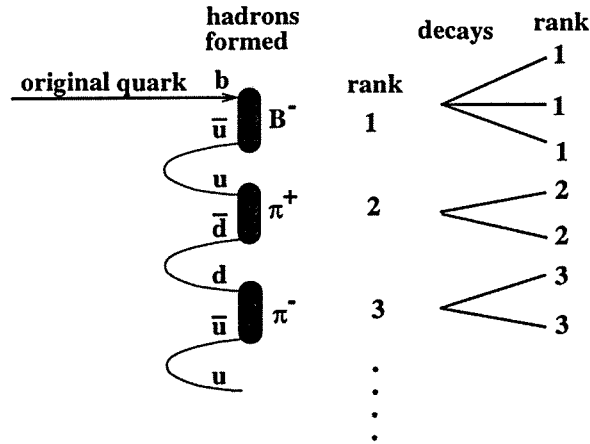


Figure 5.4: Illustration of hierarchy of hadrons produced in fragmentation (from an original  $b$  quark).

will have a total charge of zero but the information on the quark charge will be obtained from the charge of the rank two particles (unless this is also neutral in which case the information will be obtained from rank three etc.). The particles which are produced further down the chain with a high rank number retain almost no information about the charge of the original quark and only serve to add confusion. This gives some motivation for forming a *weighted* sum of particle charges in the jet or hemisphere, giving the particles which are more closely related to the original quark a higher weight than those produced further down the chain. In general the jet-charge is defined as ;

$$Q_J = \sum_i w_i q_i \quad (5.8)$$

where  $w_i$  is the weight given to track  $i$  with charge  $q_i$  and the sum is over all particles in the jet or hemisphere. The momentum of particles is expected to increase with decreasing rank number [55] and hence the longitudinal momentum,  $p_{\parallel i}$ , of a track  $i$ , with respect to the thrust axis, can be used as the weight. In this analysis the jet-charge is defined as ;

$$Q_J = \frac{\sum_{hemi} p_{\parallel i}^{\kappa} q_i}{\sum_{hemi} p_{\parallel i}^{\kappa}} \quad (5.9)$$

where  $\kappa$  is a positive constant. Choosing  $\kappa = 0$  means that  $Q_J$  is just the average charge in the hemisphere and as  $\kappa \rightarrow \infty$  only the fastest tracks in the hemisphere contribute. Figure 5.5 shows the jet-charge distributions for hemispheres containing initial  $b$  and  $\bar{b}$  quarks from a sample of Monte Carlo events using  $\kappa = 0.5$ . The overlap region indicates the fraction of hemispheres which would be wrongly tagged as  $b$  or  $\bar{b}$  using this method. The mistag fraction is defined as :

$$\text{mistag fraction} = \frac{\text{No. of wrongly tagged hemispheres}}{\text{No. of hemispheres}} \quad (5.10)$$



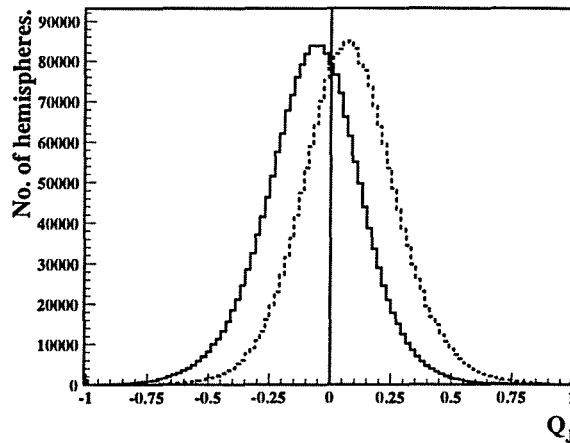


**Figure 5.5:** Monte Carlo jet-charge distributions for jets originating from  $b$  (solid) and  $\bar{b}$  (dotted) quarks for  $\kappa = 0.5$ .

For Monte Carlo it is useful to sign the jet-charge using the charge,  $q_{quark}$ , of the initial quark which produced the jet. The *quark signed jet-charge*,  $Q_{Jq}$ , is defined as :

$$Q_{Jq} = \text{sign}(q_{quark}) \times Q_J \quad (5.11)$$

This quantity has a positive mean and the fraction of hemispheres with  $Q_{Jq} < 0$  is equal to the mistag fraction. The signed jet-charge is shown in Figure 5.6 for various  $\kappa$  values and it can be seen that optimisation can be performed in order to obtain the  $\kappa$  value which gives the lowest mistag fraction.

### 5.3 Choice of $\kappa$ for Best Average Mistag

Figure 5.7 shows the variation of mistag fraction with  $\kappa$  for the various quark flavours. For each flavour, there is value of  $\kappa$  in the region 0.2–0.5 for which the mistag is at a minimum. It can be seen that the mistag fraction for  $u$  quarks is significantly lower than that for  $d$  quarks although their fragmentation is very similar. The reason for this is that  $u$  quark jets have a *higher* mean jet-charge and there is therefore less of an overlap region between the  $u$  and  $\bar{u}$  jet-charge distributions. This is not due to the  $u$  quark having a higher charge magnitude ( $\frac{2}{3}$ ) than the  $d$  quark ( $\frac{1}{3}$ ) as one might intuitively believe but is a consequence of the fact that only  $u\bar{u}$ ,  $d\bar{d}$  and  $s\bar{s}$  pairs are produced in the fragmentation process (see Equation(5.2)) [53]. An initial  $d$  quark can pair up with a  $\bar{d}$  or a  $\bar{s}$  to give a neutral meson whereas the suppression of  $c\bar{c}$  production means that an initial  $u$  quark can only form a neutral meson with a  $\bar{u}$ . This is illustrated in Figure 5.8 where the five possible fragmentation chains involving an  $s\bar{s}$  pair are shown for initial  $u$  and  $d$  quarks (showing only rank one and two mesons). It can be seen that fewer neutral states can be produced from an initial  $u$  quark. If  $u$  and  $d$  were the only two quark flavours then their jet-charges would be equal. This argument

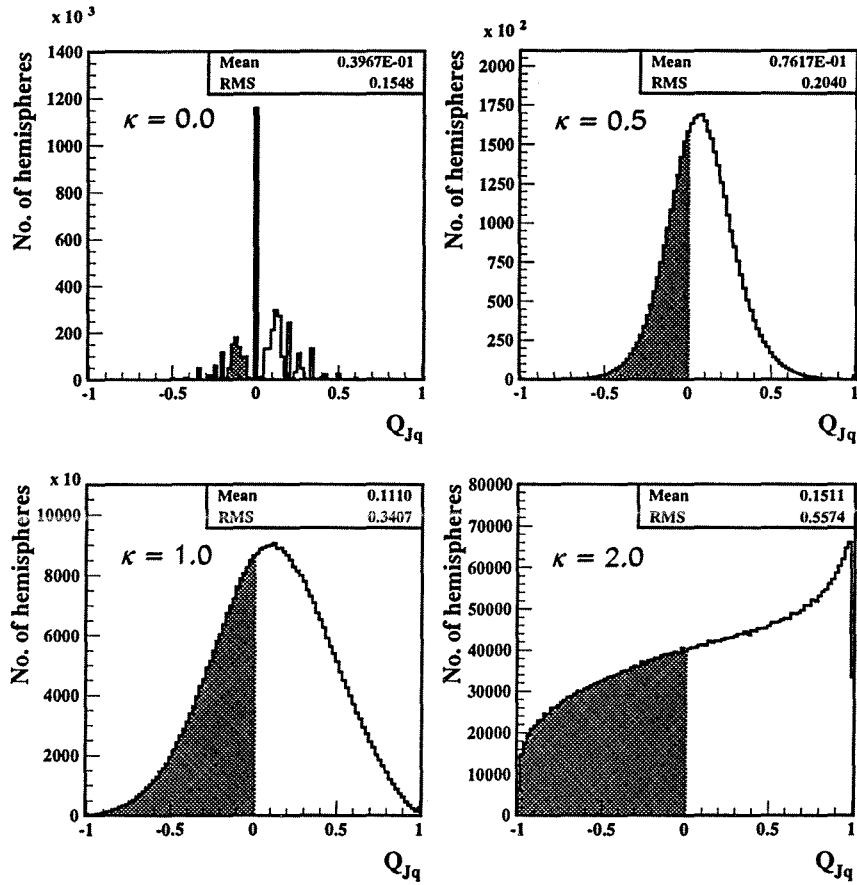


Figure 5.6: Signed jet-charge distributions for various  $\kappa$  values, for Monte Carlo  $b$  events. The shaded region represents the mistag fraction.

indicates that  $c$  quarks should also have a higher mean jet-charge and hence a lower mistag fraction. However,  $c$  quarks differ from  $u$  quarks in that they have more complicated decay chains which tend to obscure the charge of the original quark. For example, in the decay  $D^{*+} \rightarrow \pi^+ D^0$ , the pion which carries the the initial quark charge has low momentum and will therefore have a low weight in the jet-charge sum.

In order to tag the initial quark state,  $\kappa = 0.5$  is used since this gives the lowest initial state mistag for  $b$  events. In order to determine the sensitivity of the jet-charge method to  $B^0 - \bar{B}^0$  mixing (i.e. the *final* state) it is necessary to understand the contributions which the various types of  $b$  hadron make to the average  $b$  jet-charge.

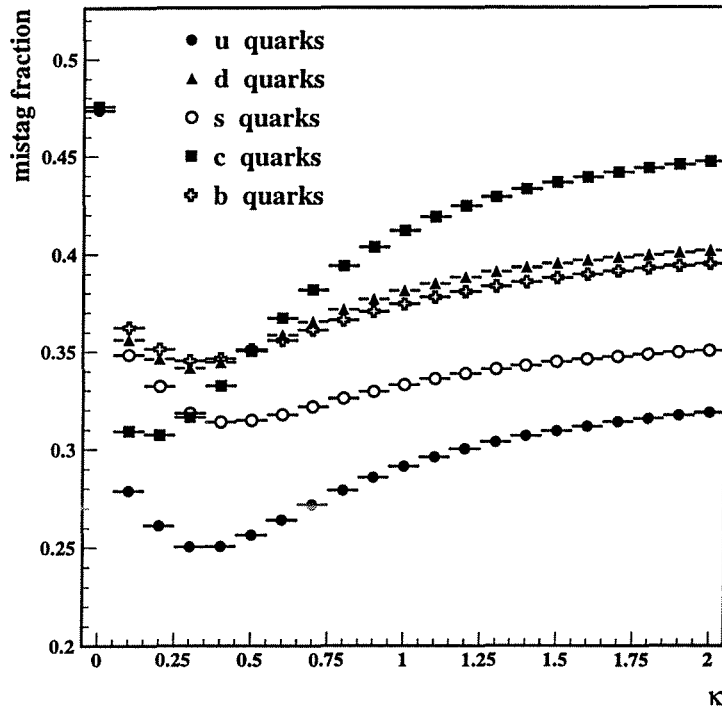


Figure 5.7: Variation of mistag with  $\kappa$  for the various quark flavours.

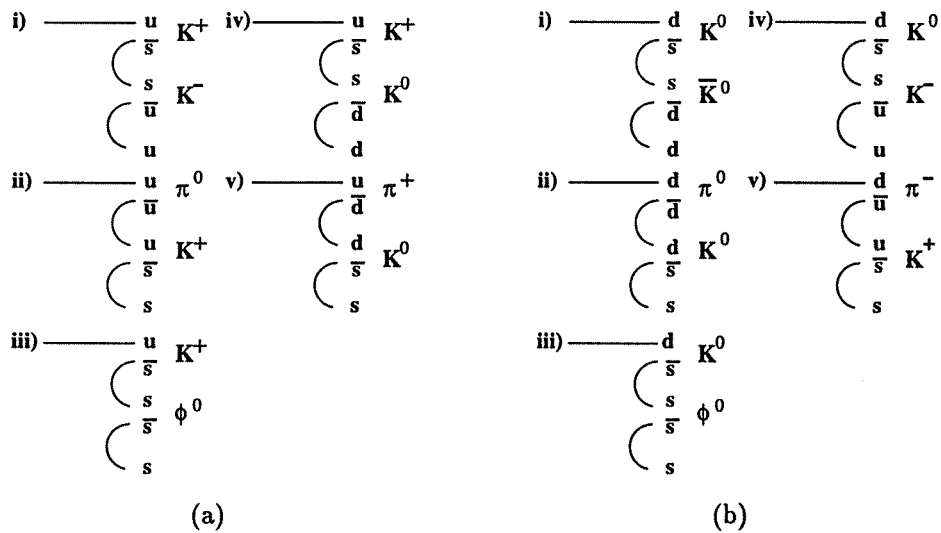
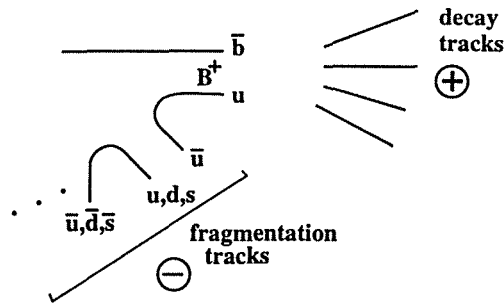


Figure 5.8: The five possible fragmentation chains involving a  $s\bar{s}$  pair (showing first two ranks only) from an initial (a)  $u$  quark and (b)  $d$  quark.

## 5.4 The $b$ Jet-Charge and Sensitivity to Mixing

The average  $b$  jet-charge receives contributions from the various types of  $b$  hadrons which are produced during fragmentation. The relative fractions of  $B^\pm$ ,  $B_d^0$  and

Figure 5.9: Jet-charge contributions associated with a charged  $B$ .

$B_s^0$  mesons which are produced are given by the probabilities to create  $u\bar{u}$ ,  $d\bar{d}$  and  $s\bar{s}$  pairs in the fragmentation process (Equation (5.2)). Baryon production is poorly understood, but one model suggests it arises when a diquark pair (i.e.  $qq\bar{q}\bar{q}$ ) is produced at a string break instead of the usual quark-antiquark pair. This requires more energy and hence the baryon fraction is small. The world average values [11] for the  $b$  baryon and meson fractions are shown in Table 5.1.

Fraction	Value
$f_u = BR(b \rightarrow B^\pm)$	$0.395 \pm 0.019$
$f_d = BR(b \rightarrow B_d^0)$	$0.395 \pm 0.019$
$f_s = BR(b \rightarrow B_s^0)$	$0.109 \pm 0.013$
$f_\Lambda = BR(b \rightarrow b \text{ baryon})$	$0.101 \pm 0.031$

Table 5.1: Meson and baryon fractions.

The different types of  $b$  hadron each give rise to different jet-charges. In each case, the jet-charge receives a contribution from the decay tracks of the  $b$  hadron (i.e. rank one tracks) and a contribution from the other particles produced during fragmentation (higher rank number tracks). This is shown in Figure 5.9 for the case of a  $B^+$  meson. The  $B^+$  decay tracks give a large positive contribution to the jet-charge, reflecting the sign of the  $\bar{b}$  charge, while the fragmentation tracks give a smaller negative contribution resulting in an overall positive jet-charge. The situation for neutral mesons is shown in Figure 5.10. The sensitivity of the jet-charge to mixing arises because the momentum weighted decay tracks of a  $B^0$  meson do not give a zero contribution to the jet-charge [54]. Figure 5.11 shows the Monte Carlo momentum spectra, in the  $B$  rest frame, for positively and negatively charged particles originating in (a) semi-leptonic decays, (b) two-body hadronic decays and (c) multi-body hadronic decays of  $B^0$  mesons. It can be seen that in all types of decay the positively charged particles have a harder momentum spectrum than the negatively charged particles. This is most obvious for semi-leptonic decays such as that shown in Figure 5.10. The high momentum lepton has the same sign as the  $b$  (or  $\bar{b}$ ) in the  $\bar{B}^0$  (or  $B^0$ ) meson when it decays, while the oppositely charged  $D$  meson shares its momentum between typically three or four decay tracks. The momentum weighted jet-charge contribution

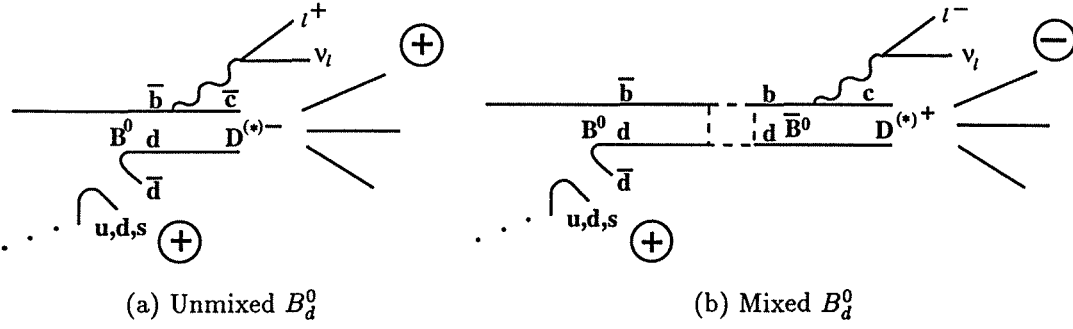


Figure 5.10: Jet-charge contributions for (a) unmixed and (b) mixed neutral  $B$  mesons.

from the decay tracks therefore reflects the sign of the  $b$  ( $\bar{b}$ ) quark at *decay*. The fragmentation tracks produced along with the neutral meson give a jet-charge contribution which, on average, has the same sign as the initial  $b$  quark. In the case of an unmixed  $B^0$  as shown in Figure 5.10(a), the contributions from decay and fragmentation tracks add to give a positive jet-charge. If the  $B^0$  mixes and decays as a  $\bar{B}^0$  (Figure 5.10(b)), then the contribution from the decay tracks flips sign and cancels the contribution from the fragmentation tracks to some extent, resulting in an average jet-charge which is closer to zero or possibly negative. Hence hemispheres containing mixed and unmixed mesons have different jet-charges and this is the basis of the method used in this analysis. The four *types* of  $b$  hadron ( $B^\pm, B_d^0, B_s^0$ , baryons) can be separated into six *classes* of hadron, each with its own characteristic jet-charge. The six classes are listed in Table 5.2 and their signed jet-charge distributions for  $\kappa = 1.0$  are shown in Figure 5.12

Class of hadron	Time dependent fraction	Time integrated fraction
$B^\pm$	$f_u \frac{e^{-t/\tau_{B^+}}}{\tau_{B^+}}$	$f_u$
baryons	$f_\Lambda \frac{e^{-t/\tau_\Lambda}}{\tau_\Lambda}$	$f_\Lambda$
$B_d$ unmixed	$f_d e^{-t/\tau_{B_d}} \frac{(1+\cos(\Delta m_d t))}{2\tau_{B_d}}$	$(1 - \chi_d) f_d$
$B_d$ mixed	$f_d e^{-t/\tau_{B_d}} \frac{(1-\cos(\Delta m_d t))}{2\tau_{B_d}}$	$\chi_d f_d$
$B_s$ unmixed	$f_s e^{-t/\tau_{B_s}} \frac{(1+\cos(\Delta m_s t))}{2\tau_{B_s}}$	$(1 - \chi_s) f_s$
$B_s$ mixed	$f_s e^{-t/\tau_{B_s}} \frac{(1-\cos(\Delta m_s t))}{2\tau_{B_s}}$	$\chi_s f_s$

Table 5.2: Time dependent and time integrated fractions for each of the  $b$  hadron classes, where  $\tau_{B^+}$ ,  $\tau_\Lambda$ ,  $\tau_{B_d}$ ,  $\tau_{B_s}$  are the lifetimes of  $B^\pm$ ,  $b$  baryons,  $B_d$  and  $B_s$  respectively.

(where the jet-charge has been signed using the *initial* quark charge). The effects of mixing cause the mean  $Q_{Jq}$  to be negative in the  $B_d$  case and significantly lower in the  $B_s$  case, than in the unmixed cases. The sensitivity of the jet-charge

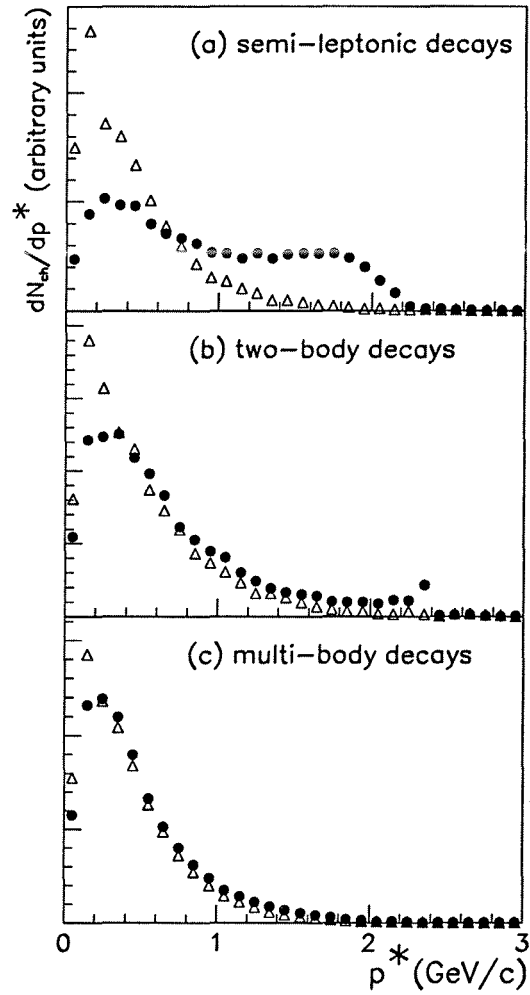


**Figure 5.11:** Monte Carlo momentum spectra for positively (solid circles) and negatively (open triangles) charged particles from (a) semi-leptonic, (b) two-body hadronic, (c) multi-body hadronic decays of neutral  $B^0$  mesons (containing positively charged  $\bar{b}$  quarks).

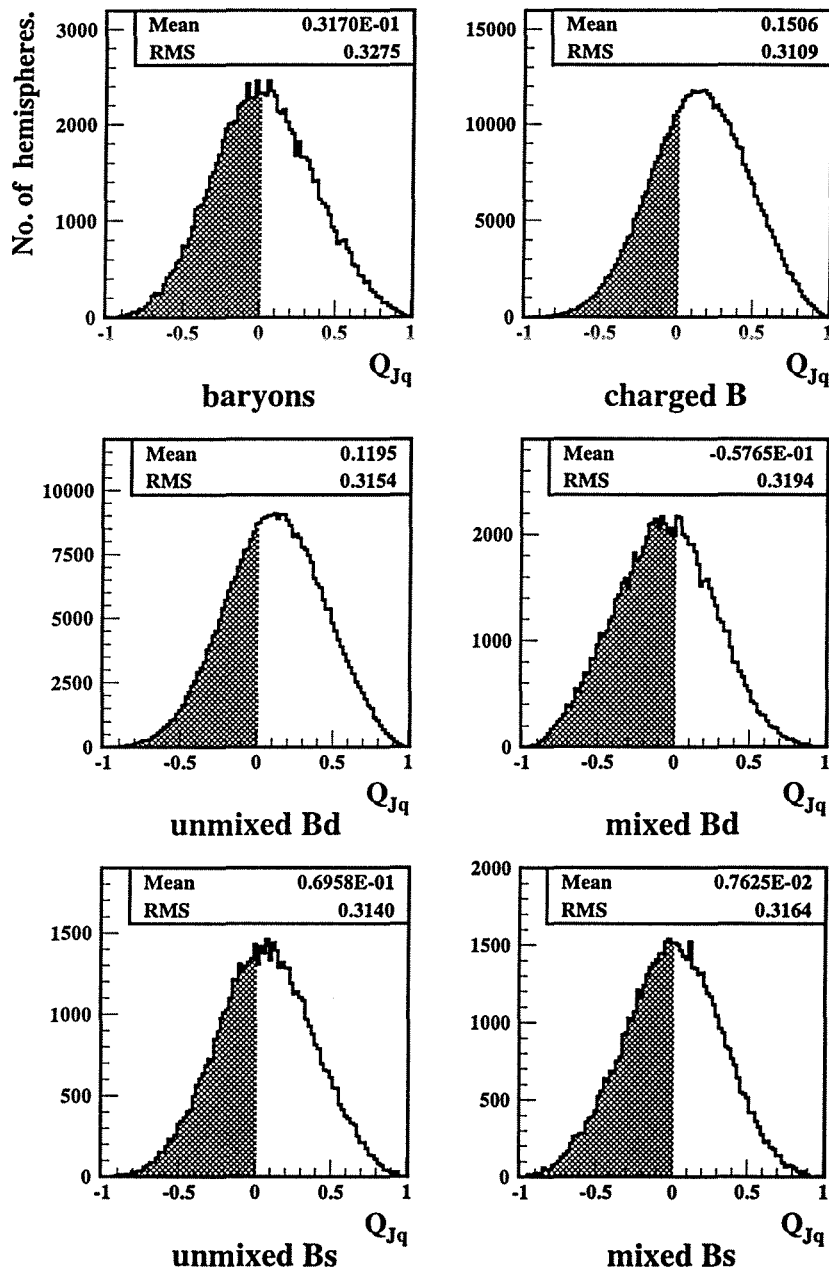


Figure 5.12: Initial quark signed jet-charge distributions for the different  $b$  hadron classes ( $\kappa = 1.0$ ).

to mixing depends on the relative weight given to the  $B$  decay tracks compared to the fragmentation tracks and therefore depends on the  $\kappa$  value used. Although  $\kappa = 0.5$  gives the best *average* mistag it does not necessarily provide the best sensitivity to mixing. Intuitively a higher  $\kappa$  value gives more weight to the  $B$  decay tracks and could give greater sensitivity, while  $\kappa = 0$  would be insensitive to mixing since the track charges from the neutral  $B$  would all sum to zero.

The value of the average jet-charge for  $b$  quarks changes as a function of proper time since the relative fractions of mixed and unmixed events is changing as a function of proper time (Equation(1.32)). For convenience, the time-dependent, average signed jet charge for  $b$  quarks,  $\langle Q_{Jq} \rangle_b(t)$ , is denoted by  $\langle Q_b \rangle(t)$ . An expression for  $\langle Q_b \rangle(t)$  is found by forming a sum of the jet-charges for each class of  $b$  hadron, weighted by their time-dependent fractions :

$$\langle Q_b \rangle(t) = \frac{\sum_{6 \text{ classes}} T_{\text{class}} \langle Q_{\text{class}} \rangle}{\sum_{6 \text{ classes}} T_{\text{class}}} \quad (5.12)$$

where  $T_{\text{class}}$  is the time-dependent fraction for that class (listed in Table 5.2) and  $\langle Q_{\text{class}} \rangle$  is the time-integrated signed jet-charge for that class. Rearranging Equation (5.12) and making the simplifying assumption that all  $b$  hadrons have equal lifetimes leads to the expression :

$$\begin{aligned} \langle Q_b \rangle(t) \approx & f_u \langle Q_{B^\pm} \rangle + f_\Lambda \langle Q_\Lambda \rangle + f_d \frac{\langle Q_{B_d^{\text{unmix}}} \rangle + \langle Q_{B_d^{\text{mix}}} \rangle}{2} \\ & + f_s \frac{\langle Q_{B_s^{\text{unmix}}} \rangle + \langle Q_{B_s^{\text{mix}}} \rangle}{2} + f_d \frac{\langle Q_{B_d^{\text{unmix}}} \rangle - \langle Q_{B_d^{\text{mix}}} \rangle}{2} \cos(\Delta m_d t) \\ & + f_s \frac{\langle Q_{B_s^{\text{unmix}}} \rangle - \langle Q_{B_s^{\text{mix}}} \rangle}{2} \cos(\Delta m_s t) \end{aligned} \quad (5.13)$$

The time-integrated, average  $b$  jet-charge, denoted by  $\langle Q_b \rangle$ , also contains mixing information through the time-integrating mixing probabilities,  $\chi_{d,s}$  :

$$\begin{aligned} \langle Q_b \rangle = & f_u \langle Q_{B^\pm} \rangle + f_\Lambda \langle Q_\Lambda \rangle + f_d \langle Q_{B_d^{\text{unmix}}} \rangle + f_s \langle Q_{B_s^{\text{unmix}}} \rangle \\ & + f_d \chi_d \left( \langle Q_{B_d^{\text{mix}}} \rangle - \langle Q_{B_d^{\text{unmix}}} \rangle \right) \\ & + f_s \chi_s \left( \langle Q_{B_s^{\text{mix}}} \rangle - \langle Q_{B_s^{\text{unmix}}} \rangle \right) \end{aligned} \quad (5.14)$$

In the above equations, the terms involving the mixing parameters are all multiplied by a  $(\langle Q_{B^{\text{unmix}}} \rangle - \langle Q_{B^{\text{mix}}} \rangle)$  factor and hence the maximum sensitivity to mixing is achieved by selecting the  $\kappa$  value which gives the largest significant separation between the means of the quark signed jet-charge distributions in Monte Carlo for mixed and unmixed mesons. This is equivalent to maximising the difference in initial state mistags for mixed and unmixed events as shown in Figure 5.13. For  $\kappa = 0$  the jet-charge distribution is unchanged by mixing and the difference between the mistags is zero. As  $\kappa$  is increased the sensitivity to mixing increases and reaches a maximum around  $\kappa = 1.0$  for both  $B_d$  and  $B_s$  mesons.



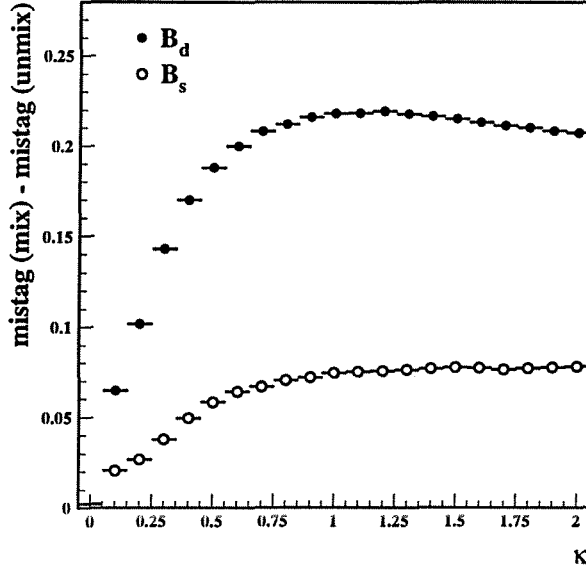


**Figure 5.13:** Sensitivity to mixing, as given by the difference between (initial state) mistags for mixed and unmixed mesons, as a function of  $\kappa$  for  $B_d$  and  $B_s$  mesons.

The different decay modes which are dominant in  $B_d$  and  $B_s$  decays give rise to differences in their jet-charges.  $B_d^0$  mesons decay predominantly via the decay chain :

$$B_d^0 \rightarrow D^{*-} X, \quad D^{*-} \rightarrow \bar{D}^0 \pi^- \quad (5.15)$$

The  $\pi^-$  has the opposite charge to the  $\bar{b}$  quark but has low momentum due to the small mass difference between the  $D^{*-}$  and  $\bar{D}^0$ . It will therefore have a low weight in the jet-charge sum and may escape detection altogether thus enhancing the positive jet-charge contribution from other tracks. In the  $B_s$  case, the corresponding decay chain is :

$$B_s^0 \rightarrow D_s^{*-} X, \quad D_s^{*-} \rightarrow D_s^- \gamma \text{ (or } D_s^- \pi^0) \quad (5.16)$$

There is no neutral  $D$  meson which contains an  $s$  quark and so the direct analogy to (5.15) is not possible, hence there is no charged pion to give an enhancement effect similar to that for  $B_d$  mesons. Consequently the jet-charge method is more sensitive to mixing for  $B_d$  mesons than for  $B_s$  mesons.

## 5.5 The Charge Correlation Function

The charge correlation function for data is defined as the product of the two hemisphere charges :

$$\text{charge correlation} = \langle -Q_{J_o}^{\kappa=0.5} Q_{J_s}^{\kappa=1.0} \rangle(t) \quad (5.17)$$

where ‘*s*’ refers to the hemisphere in which the proper time is measured, referred to as the ‘same’ hemisphere, and ‘*o*’ refers to the ‘opposite’ hemisphere. The charge correlation for a pure *b* sample (with perfect proper time resolution) can be written as :

$$\text{charge correlation} = \langle Q_{bo}^{0.5} \rangle \langle Q_{bs}^{1.0} \rangle (t) + \text{cov}(Q_{bo}, Q_{bs}) \quad (5.18)$$

where  $\langle Q_b \rangle$  and  $\langle Q_b \rangle (t)$  are defined in Equations (5.12) and (5.14) and  $\text{cov}(Q_{bo}, Q_{bs})$  is the covariance between the two hemisphere charges. The correlation between hemisphere charges arises due to ‘swapping’ of low momentum tracks from one hemisphere to the other [57], which occurs at the hemisphere boundaries<sup>2</sup>. The correlation is largest for low values of  $\kappa$ , where the contribution from low momentum tracks is greatest, and decreases rapidly as  $\kappa$  increases and the tracks in the core of the jet are given more weight. At the  $\kappa$  values used here, the correlation is approximately 1%. In the fitting procedure described in Chapter 7, these covariance terms are taken from Monte Carlo simulation.

The jet-charge in the ‘opposite’ hemisphere reflects, on average, the initial quark charge in that hemisphere and hence gives information on the initial charge in the ‘same’ hemisphere since initially a  $b\bar{b}$  pair are produced. The choice of  $\kappa = 0.5$  on the opposite side therefore gives the best initial state tag as discussed in Section 5.3. On the ‘same’ side, the best sensitivity to mixing is obtained using  $\kappa = 1.0$ . In most events, the two hemispheres will have opposite charges, and  $-Q_{Jo} Q_{Js}$  will be positive. In events where a single mix has taken place, the product of the charges will be smaller or negative. A full description of the fit to the charge correlation function is given in Chapter 7.

---

<sup>2</sup>This is partly due to the uncertainty in the definition of the hemispheres and partly due to charge conservation during hadronisation.



# Chapter 6

## Proper Time Measurement

### 6.1 Introduction

The proper lifetime of a  $b$  hadron is calculated using :

$$t = \frac{m_B}{p_B c} l \quad (6.1)$$

where  $m_B$  is the average mass of  $b$  hadrons (taken to be  $5.3 \text{ GeV}/c^2$ ),  $p_B$  is the reconstructed  $b$  hadron momentum and  $l$  is the reconstructed decay length. In this chapter, the algorithms for reconstructing the decay length and momentum of  $b$  hadrons are described. The resulting proper time resolution is shown and the fitting procedure which is used to extract the inclusive  $b$  lifetime,  $\tau_b$ , is described. An accurate value for the inclusive  $b$  lifetime is obtained which is in agreement with the world average. Measurement of the inclusive  $b$  lifetime serves as an important cross-check of the fitting procedures required to extract the  $B_d^0$  oscillation frequency and it is also a valuable measurement in its own right.

### 6.2 Measurement of Decay Length

A two stage process is used to calculate the decay length of the  $b$  hadron. Firstly, an initial secondary vertex position is found in each hemisphere, using the QVSRCH [42] reconstruction algorithm described in Section 4.2.2. A quantity, denoted by  $\mathcal{R}_{sig}$ , is then calculated for each track where :

$$\mathcal{R}_{sig} = \frac{\mathcal{S}_p}{\mathcal{S}_p + \mathcal{S}_s} \quad (6.2)$$

$\mathcal{S}_p$  and  $\mathcal{S}_s$  are the track significances<sup>1</sup> relative to the primary and secondary vertices respectively. The quantities  $\mathcal{S}_p$  and  $\mathcal{S}_s$  are signed relative to the jet-axis as shown in Figure 6.1.

---

<sup>1</sup>The track *significance* is the signed impact parameter (relative to the primary or secondary vertex) divided by its error.

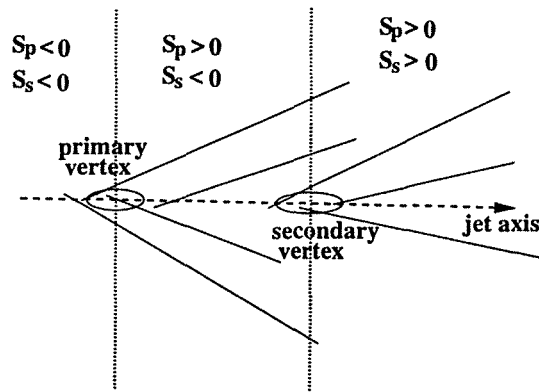


Figure 6.1: Schematic diagram showing how the track significances are signed.

The distribution of  $\mathcal{R}_{sig}$  for tracks from  $b$  events is shown in Figure 6.2 where the contributions from  $b$  decay tracks and fragmentation tracks are superimposed on the total. The ratio  $\mathcal{R}_{sig}$  is close to zero for tracks which pass through the

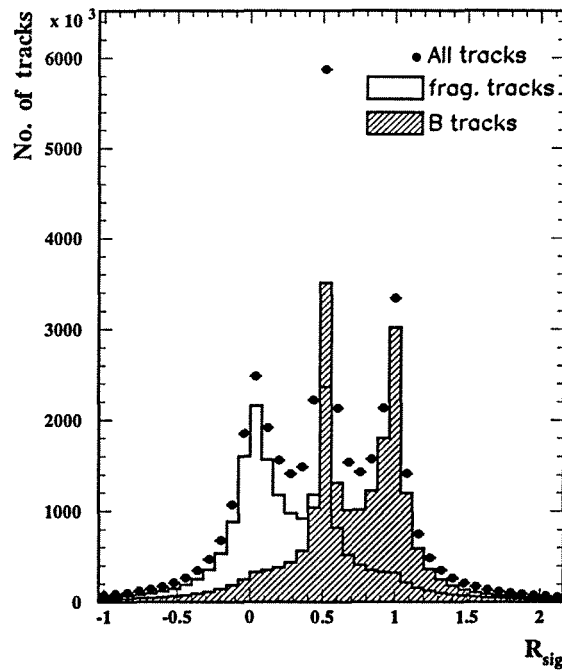


Figure 6.2: The ratio  $\mathcal{R}_{sig}$  for tracks from Monte Carlo  $b$  events. The shaded region indicates tracks from the decay of the  $b$  hadron.

primary vertex and is close to one for tracks which pass through the secondary vertex. There are a significant number of tracks which are far from both vertices or have no precision VDET information, and give a value of  $\mathcal{R}_{sig}$  which is close

to 0.5. Tracks which pass between the vertices (i.e. having  $\mathcal{S}_p$  positive and  $\mathcal{S}_s$  negative) populate the tails of the distribution. The  $\mathcal{R}_{sig}$  distributions for data and Monte Carlo (before applying the BTAG cut) are shown in Figure 6.3. The agreement between data and Monte Carlo is good, except in the region

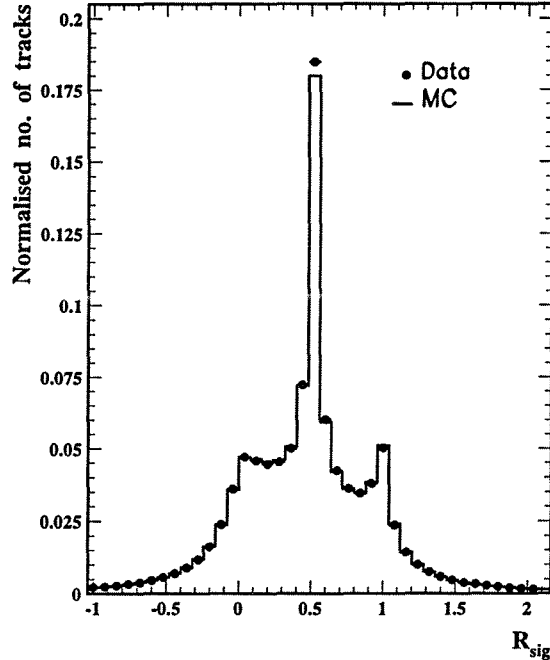


Figure 6.3: Comparison of the  $\mathcal{R}_{sig}$  distribution for data and Monte Carlo.

around  $\mathcal{R}_{sig} = 0.5$  where there are more tracks in the data than in the Monte Carlo. Since these are tracks which are far from both primary and secondary vertices, the excess in data is consistent with the fact that the tracking resolution is worse in data than in Monte Carlo. Smearing the Monte Carlo track resolution as described in Chapter 4 has improved the agreement around 0.5 but has not removed the discrepancy altogether.

It can be seen from Figure 6.2 that  $\mathcal{R}_{sig}$  provides a means of distinguishing between fragmentation tracks and those from the  $b$  hadron decay. Most fragmentation tracks have  $\mathcal{R}_{sig}$  smaller than  $\sim 0.5$  while  $b$  hadron tracks tend to have higher values of  $\mathcal{R}_{sig}$ . The decay length resolution is significantly improved by choosing a subset of tracks which have  $\mathcal{R}_{sig} > cut$  and fitting them to form a new secondary vertex using a vertex fitting routine, described in [58]. The re-fitted vertex is required to have a  $\chi^2$  probability of greater than 1%. The decay length is then given by the distance between the primary vertex and this revertexed secondary, signed relative to the jet direction.

The efficiency of the revertexing procedure decreases as the  $\mathcal{R}_{sig}$  cut increases, since less tracks are likely to pass the cut, whereas the decay length resolution

improves as the cut increases and hence there is an optimum cut which must be found. The best cut is found by optimising the sensitivity to  $B_d^0$  mixing by maximising the quality factor given by :

$$\text{Quality factor} = \sqrt{\epsilon} \exp^{-\frac{(\Delta m_d \sigma_l)^2}{2}} \quad (6.3)$$

This quality factor is derived from the signal/noise ratio given in Equation (2.6), taking only the decay length resolution into account. Here,  $\epsilon$  is the efficiency for at least one hemisphere to contain a ‘good’ revertexed secondary (a vertex is ‘good’ if the vertex fit succeeds and its  $\chi^2$  probability is greater than 1%) and  $\sigma_l$  is the decay length resolution (in millimetres) from the Monte Carlo, taken as the rms of the  $(l_{reco} - l_{true})$  distribution where  $l_{reco}$  is the reconstructed decay length and  $l_{true}$  is the true  $b$  hadron decay length. The quality factor is plotted

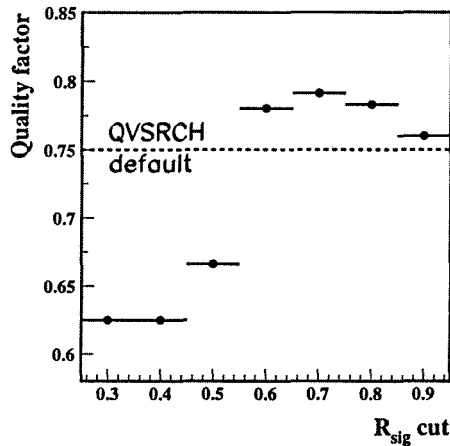


**Figure 6.4:** The quality factor for revertexing as a function of the  $\mathcal{R}_{sig}$  cut. The dotted line shows the quality factor obtained using the default QVSRCH vertexing.

in Figure 6.4 as a function of the  $\mathcal{R}_{sig}$  cut. A cut of at least 0.5 must be applied before the quality factor improves on that obtained using the original QVSRCH secondary vertex (i.e. without revertexing) and it can be seen that the best cut is at 0.7. From Monte Carlo  $b$  events it is determined that about 80% of tracks assigned to the secondary vertex by an  $\mathcal{R}_{sig}$  cut of 0.7 are  $b$  hadron tracks and the remaining 20% are fragmentation tracks.

The second stage of decay length reconstruction therefore consists of fitting all tracks with  $\mathcal{R}_{sig} > 0.7$  to a new secondary vertex and requiring that this vertex has a  $\chi^2$  probability of greater than 1%. If both hemispheres contain good revertexed secondary vertices, then the hemisphere containing the vertex with the highest  $\chi^2$  probability is chosen to be the side on which the proper time is measured (referred to as the ‘same’ side) and if there is only one good secondary vertex then that hemisphere is chosen as the ‘same’ side. Events in which neither

hemisphere contains a good secondary vertex are rejected. The resulting decay length reconstruction efficiency is approximately 85% on average and about 93% for  $b$  events. Any bias to the proper time distribution, arising from choosing a hemisphere in this way, is taken into account in the fitting procedure.

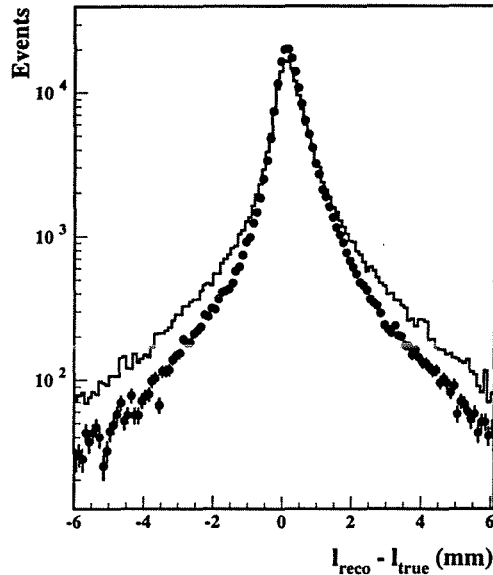


**Figure 6.5:** Decay length resolution with revertexing (points) and without revertexing (histogram), plotted on a logarithmic scale in order to show the tail regions.

Figure 6.5 shows the decay length resolution,  $(l_{reco} - l_{true})$ , after a BTAG cut of 20. The points show the resolution obtained after revertexing and the histogram shows the resolution obtained using the default QVSRCH vertex. Table 6.1 gives details of the resolutions obtained with and without revertexing. The first column shows the rms of the  $(l_{reco} - l_{true})$  distribution and the other three columns show the widths obtained when the resolution distribution is fitted with three Gaussians. It can be seen that revertexing gives a marked improvement.

Method	rms (mm)	G1 (75%) $\sigma$ (mm)	G2 (22%) $\sigma$ (mm)	G3 (3%) $\sigma$ (mm)
no revertexing	1.38	0.26	0.77	2.8
with revertexing	1.05	0.24	0.64	2.4

**Table 6.1:** The effect of revertexing on the decay length resolution. G1, G2 and G3 are Gaussians 1,2 and 3 respectively.

The distributions of  $(l_{reco} - l_{true})$  are shown in Figure 6.6 for several slices in  $l_{true}$ . It can be seen that the decay length resolution depends on  $l_{true}$  and tends to improve with increasing  $l_{true}$  as contamination of the secondary vertex, by tracks



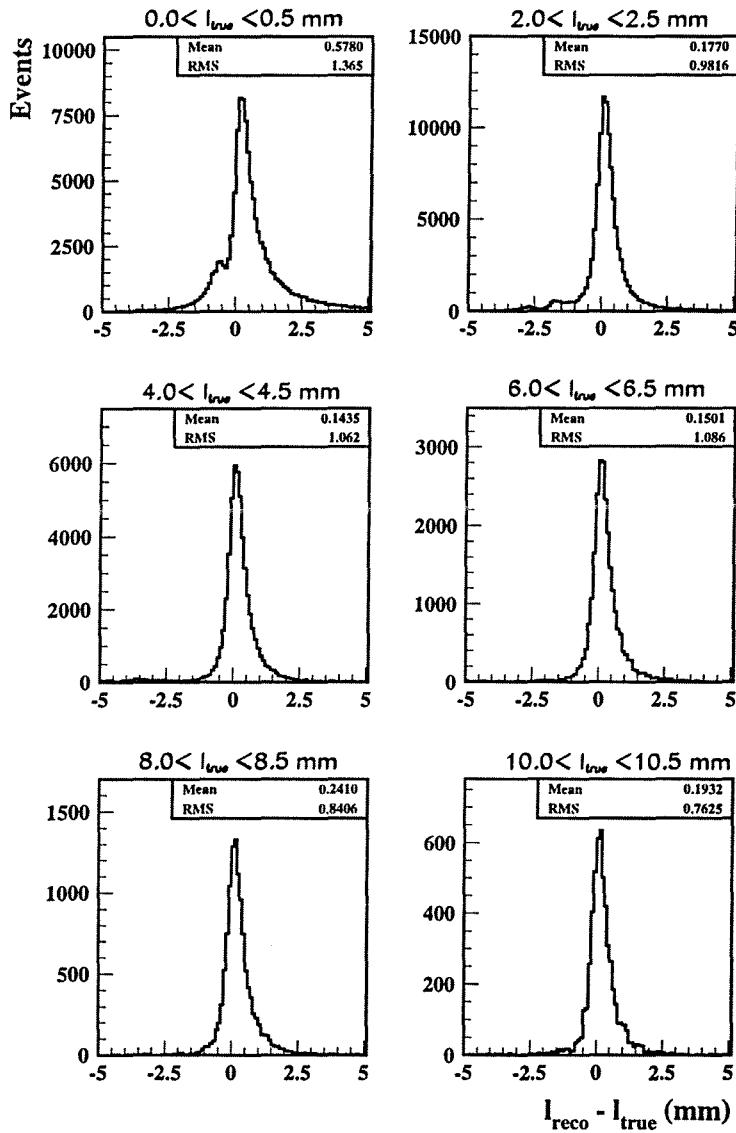


Figure 6.6: Decay length resolution,  $(l_{\text{reco}} - l_{\text{true}})$ , for several slices in  $l_{\text{true}}$ .

from the primary, decreases. All of the distributions have positive means, since in most cases the  $B$  meson decays to a  $D$  meson which travels some distance before decaying. Tracks from the  $D$  decay tend to pull the reconstructed vertex away from the true  $B$  vertex, giving larger decay lengths. This bias is taken into account using the folding procedure discussed in Section 6.5.2.

The reconstructed decay length distribution after a BTAG cut of 20 is shown in Figure 6.7 for data and Monte Carlo. Despite the Monte Carlo smearing which was performed, a significant discrepancy is seen between data and Monte Carlo, after  $b$  tagging, at low reconstructed decay lengths. This discrepancy is due to

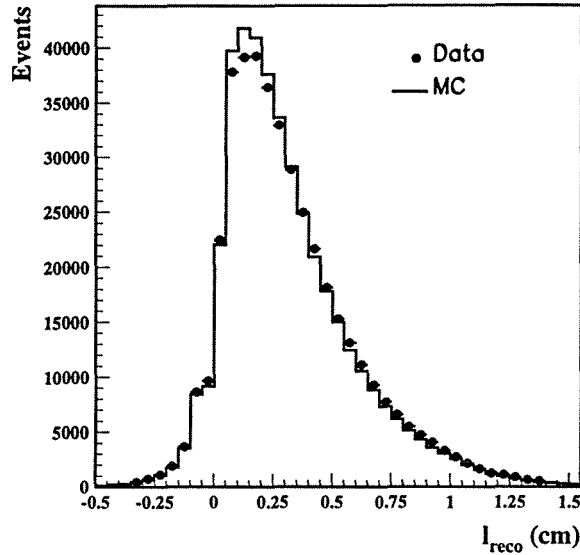


Figure 6.7: Reconstructed decay length distribution in data and Monte Carlo after a BTAG cut of 20.

differences between data and Monte Carlo in the efficiency of the BTAG cut and is discussed in more detail in Section 6.5.3.

## 6.3 Momentum Reconstruction

The momentum of the  $b$  hadron is composed of three contributions :

- Charged tracks from the  $b$  hadron decay, which contribute, on average, 60% of the total  $b$  hadron momentum.
- Neutral particles from the  $b$  decay, which constitute around 34% of the total  $b$  hadron momentum. These are particles such as  $\gamma$  and  $\pi^0$  which are detected in the ECAL and particles such as neutrons which are detected in HCAL.
- The third contribution comes from missing momentum which is carried by undetected neutrinos which may be produced in the  $b$  decay, contributing 6% on average.

The total  $b$  hadron momentum is reconstructed as the sum of these three components :

$$p_B = p_B^{ch} + p_B^{neu} + p_B^{miss} \quad (6.4)$$

The reconstruction of each component is described in the following sections.

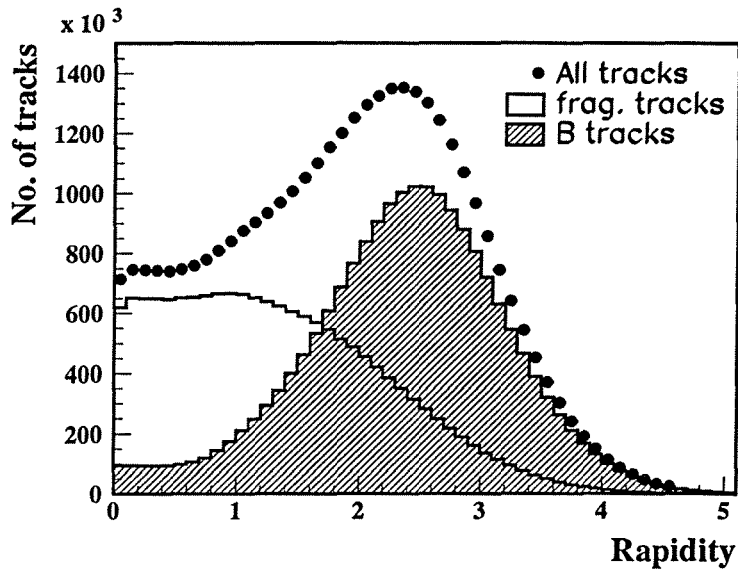


Figure 6.8: Rapidity distribution for tracks from Monte Carlo  $b$  events.

### 6.3.1 Charged Track Momentum and Track Weights.

In order to reconstruct the momentum contribution from charged tracks it is again necessary to distinguish between  $B$  decay tracks and fragmentation tracks. In order to do this the significance ratio,  $\mathcal{R}_{sig}$ , is used once more. However since there are a large number of tracks with  $\mathcal{R}_{sig} = 0.5$  which are either far from both the primary and secondary vertices or have no VDET information, a second quantity is needed to help discriminate between  $B$  and fragmentation tracks. The track rapidity,  $y$ , with respect to the secondary vertex direction is also used where  $y$  is given by :

$$y = \frac{1}{2} \ln \frac{E + p_{\parallel}}{E - p_{\parallel}} \quad (6.5)$$

where  $E$  is the energy of the track and  $p_{\parallel}$  is its momentum parallel to the vertex direction vector. The rapidity distribution for tracks from Monte Carlo  $b$  events can be seen in Figure 6.8, showing the contributions from  $b$  hadron tracks and fragmentation tracks.

The rapidity and  $\mathcal{R}_{sig}$  of a track are used to calculate a probability weight,  $w$ , that the track came from the decay of the  $b$  hadron. The weights are calibrated using Monte Carlo  $b$  events by plotting  $\mathcal{R}_{sig}$  against  $y$  on a two dimensional grid. The weight for a track in a particular  $(y, \mathcal{R}_{sig})$  bin is given by :

$$w(y, \mathcal{R}_{sig}) = \frac{\text{No. } B \text{ tracks in bin } (y, \mathcal{R}_{sig})}{\text{No. } B + \text{frag. tracks in bin } (y, \mathcal{R}_{sig})} \quad (6.6)$$

The distribution of track weights for  $b$  events is shown in Figure 6.9. A clear distinction can be seen between  $B$  tracks and fragmentation tracks. The weight

distributions for data and Monte Carlo are in good agreement, as shown in Figure 6.10 (prior to applying the BTAG cut). The unusual structure in the weight distribution is a consequence of the binning used in the calibration of the weights.

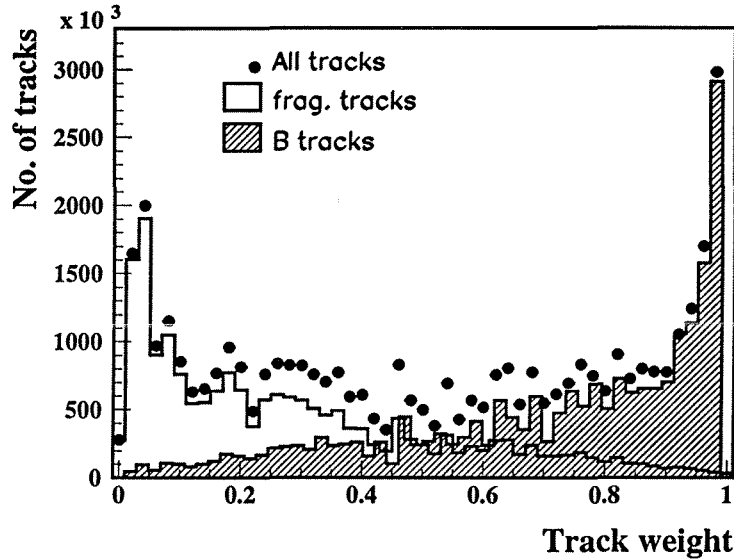


**Figure 6.9:** Track weights for  $b$  events showing the distinction between  $b$  hadron tracks and fragmentation tracks.

The charged contribution to the  $B$  momentum is found by summing the momenta of all charged tracks in the hemisphere, weighted by the probability that they are from the  $B$  decay :

$$p_B^{ch} = \sum_{i = \text{charged tracks}} w_i p_i \quad (6.7)$$

where  $w_i$  is the weight assigned to track  $i$  and  $p_i$  is the track momentum. Forming the weighted sum in this manner is more efficient than simply adding the momentum of all tracks having  $w_i$  passing a cut value. The reconstructed charged momentum distribution is shown in Figure 6.11 for data and Monte Carlo.

### 6.3.2 Vertex Charge

Since the track weights are high for  $b$  hadron decay tracks, it is interesting to use these weights to form a 'Vertex Charge',  $Q_{vert}$ , which should reflect the charge of the  $b$  hadron which decayed :

$$Q_{vert} = \sum_{hemi} w_i q_i \quad (6.8)$$

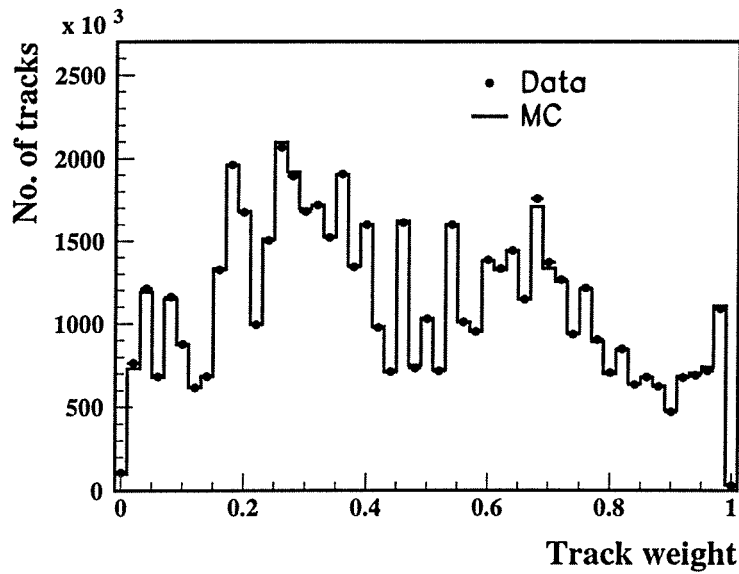


Figure 6.10: Track weights in data and Monte Carlo for all flavours of events (before applying BTAG cut).

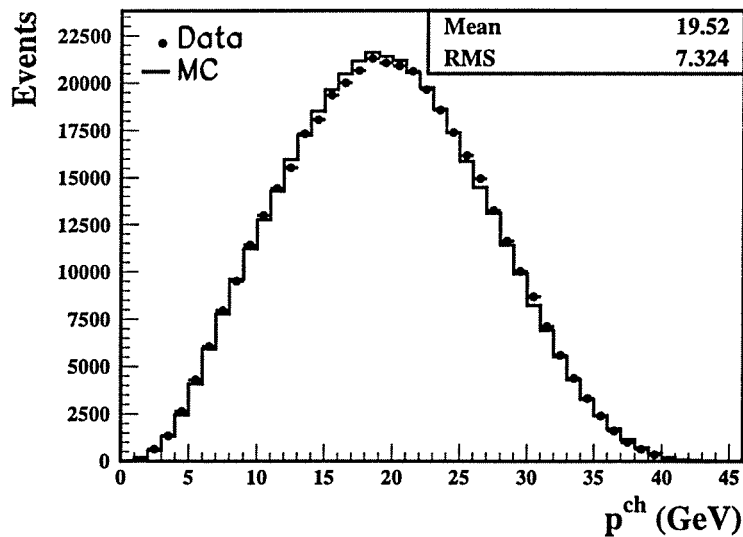


Figure 6.11: Reconstructed charged momentum distribution for data and Monte Carlo, after a BTAG cut of 20.

The vertex charge distribution does not lie between  $-1$  and  $+1$  as the standard jet-charge does, but tends to reflect the total charge at the secondary vertex. The vertex charge distribution is shown in Figure 6.12 where the contributions from charged and neutral  $B$  mesons are superimposed on the total. Definite

structure can be seen, with the distribution for  $B^\pm$  being more peaked at  $-1$  and  $+1$ , while the vertex charge for  $B^0$  mesons ( $B_d^0$  and  $B_s^0$ ) is closer to zero. By making a cut on the value of  $Q_{vert}$  for a hemisphere, it is possible to enhance the sample in charged or neutral mesons. For example, a sample of hemispheres with  $|Q_{vert}| < 0.6$  consists of approximately 58%  $B^0$  and 33%  $B^\pm$  compared to the production fractions of  $\sim 50\%$   $B^0$  and  $\sim 40\%$   $B^\pm$  (Table 5.1). The idea of cutting on  $|Q_{vert}|$  in this way is used in Section 7.2 to check the agreement between data and Monte Carlo distributions of jet-charges and hemisphere multiplicities in  $B^0$  and  $B^\pm$  enhanced samples.

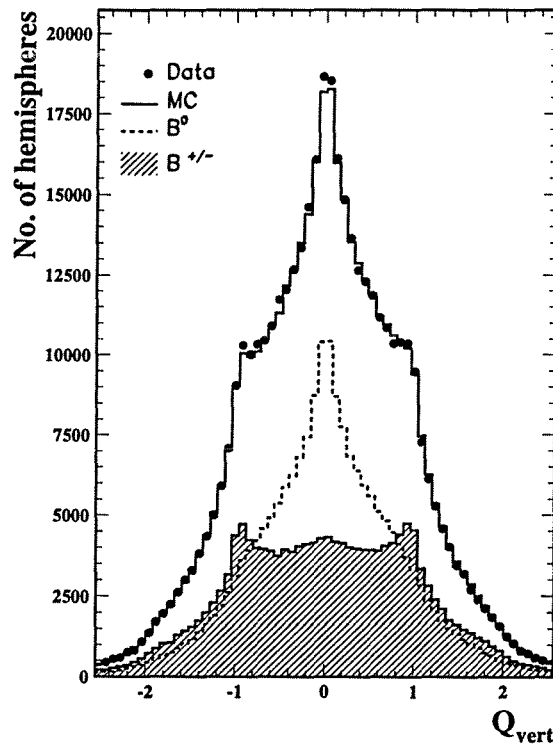


Figure 6.12: Vertex charge distribution after a BTAG cut of 20.

Although the vertex charge is useful for distinguishing between  $B^0$  and  $B^\pm$  mesons, it is not as sensitive to mixing as the standard jet-charge since the vertex charge for  $B^0$  mesons is close to zero and does not change significantly when a mix has occurred. While the mistag fraction for charged  $B$  mesons is better using the vertex charge ( $\sim 26\%$ ) than with the standard jet-charge ( $\sim 29\%$ ) it is worse for neutral  $B$  mesons ( $\sim 39\%$  compared with  $\sim 36\%$ ) and the overall mistag fraction is approximately the same as for the standard jet-charge. Consequently, the vertex charge is not used as a means of tagging the initial and final states of the  $B$  meson but is of use in obtaining  $B^0$  or  $B^\pm$  enhanced samples.

### 6.3.3 Neutral and Missing Energy Reconstruction

Assigning neutral energy to the  $B$  decay is slightly more difficult than calculating the contribution due to charged tracks. The procedure is as follows :

- Jet clustering is performed on all neutral and charged objects, using the JADE algorithm [40]. The algorithm loops over all pairs of tracks and merges pairs which satisfy  $(M/\sqrt{s})^2 < y_{cut}$  where  $M$  is the invariant mass of the track pair and  $\sqrt{s}$  is the centre-of-mass energy. The value of  $y_{cut}$  is chosen to be  $(5.3/\sqrt{s})^2$  corresponding to the average mass of the  $b$  hadron. On average 3–4 jets are found.
- The jet which is closest to the secondary vertex direction is chosen to be the  $B$  jet.
- If a neutral object is in the chosen jet, then its momentum component parallel to the vertex direction is included in the total  $B$  momentum. This serves to reduce the contribution from fragmentation neutrals since they have smaller longitudinal momenta than do neutrals from  $B$  decays. This differs from other analyses [19, 24] which multiply the neutral energy by a fixed scaling factor. On average, six neutral objects contribute to the  $B$  momentum.

#### Missing Energy Reconstruction

The missing energy due to undetected neutrinos is calculated by subtracting the visible energy in the hemisphere from the total energy in that hemisphere :

$$E_{hemi\ i}^{miss} = E_{hemi\ i}^{tot} - E_{hemi\ i}^{vis} \quad (6.9)$$

where the total energy in hemisphere 1,  $E_{hemi\ 1}^{tot}$  is calculated using conservation of energy and momentum :

$$E_{hemi\ 1}^{tot} = \frac{\sqrt{s}}{2} + \frac{m_{hemi\ 1}^2 - m_{hemi\ 2}^2}{2\sqrt{s}} \quad (6.10)$$

and  $m_{hemi\ 1,2}$  are the invariant masses of the two hemispheres. The missing energy distributions for data and Monte Carlo are shown in Figure 6.13(a). Negative missing energies are possible because of resolution fluctuations in the calorimeters. Noise fluctuations might mean that  $E^{vis}$  is greater than  $E^{tot}$  for that hemisphere. In order to estimate the missing energy resolution, the negative side of the missing energy distributions in data and Monte Carlo are fitted with Gaussians. The mean and widths of the Gaussians used for data and Monte Carlo are given in Table 6.2. It can be seen that the missing energy resolution is better in the Monte Carlo than in the data. Only a fraction of the missing energy,  $E_{added}^{miss}$ , is added to the  $B$  momentum, where :

$$E_{added}^{miss} = E^{miss} \times \left[ \text{erf} \left( \frac{E^{miss} - \tilde{\mu}}{\sqrt{2}\sigma} \right) \right] \quad (6.11)$$

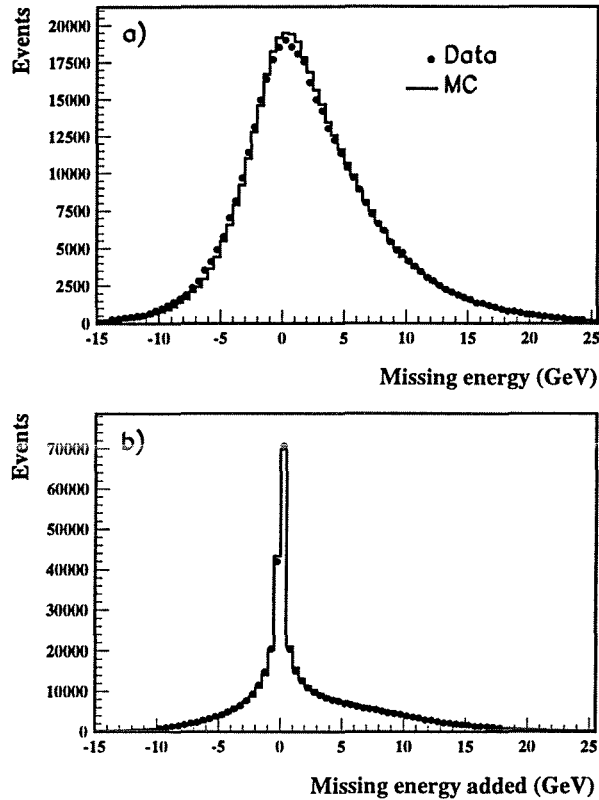


**Figure 6.13:** Figure (a) shows the missing energy in the hemisphere as calculated using Equations (6.9) and (6.10). Figure (b) shows the missing energy which is added after taking resolution effects into account.

Parameter	Data	Monte Carlo
$\tilde{\mu}$	0.780 GeV	0.678 GeV
$\sigma$	3.462 GeV	3.304 GeV

**Table 6.2:** Summary of Gaussian parameters from fit to negative side of missing energy distribution in data and Monte Carlo simulation.

where  $\text{erf}$  is the error function [2] and gives the fraction of the area of the resolution Gaussian which lies between  $\tilde{\mu} \pm E^{miss}$ . Hence for values of  $E^{miss}$  which lie outside the resolution Gaussian, the whole of  $E^{miss}$  is added, while for values of  $E^{miss}$  which lie within the resolution envelope, a fraction which is less than one is added. The distribution of  $E_{added}^{miss}$  is shown in Figure 6.13(b).



### 6.3.4 Momentum Resolution

The reconstructed momentum distribution is shown in Figure 6.14 after a BTAG cut of 20 has been applied. The momentum resolution is approximately 9% for 80% of events but is a strong function of  $p_{true}$  as shown in Figure 6.15 for four different ranges of true momentum. Low momentum  $b$  hadrons are much more poorly reconstructed and this is partly due to the poorer tracking information which implies less powerful track  $\mathcal{R}_{sig}$  values.

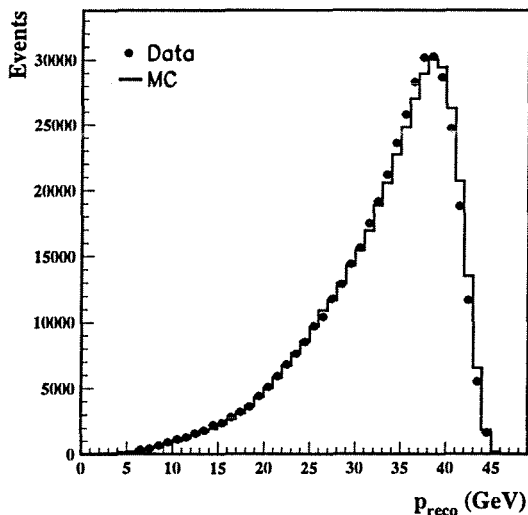


**Figure 6.14:** Reconstructed momentum distribution in data and Monte Carlo, after a BTAG cut of 20.

### 6.3.5 Fragmentation Systematic Error

The reconstructed momentum distributions in data and Monte Carlo are not in perfect agreement (see Figure 6.14). This disagreement may be partly due to the Peterson fragmentation function (Equation. (5.7)) which is used in Monte Carlo not being a perfect description of the fragmentation in data. Changes in the Monte Carlo fragmentation function will effect the reconstructed momentum distribution in Monte Carlo and consequently the reconstructed proper time distribution. Since the Monte Carlo simulation is used in the fitting procedure to account for resolution effects and efficiencies, it is important to investigate the effect that a variation in the fragmentation has on the final lifetime and mixing results.

Experimental measurements of  $b$  quark fragmentation are used to assign a systematic error contribution to  $b$  fragmentation. The Peterson fragmentation

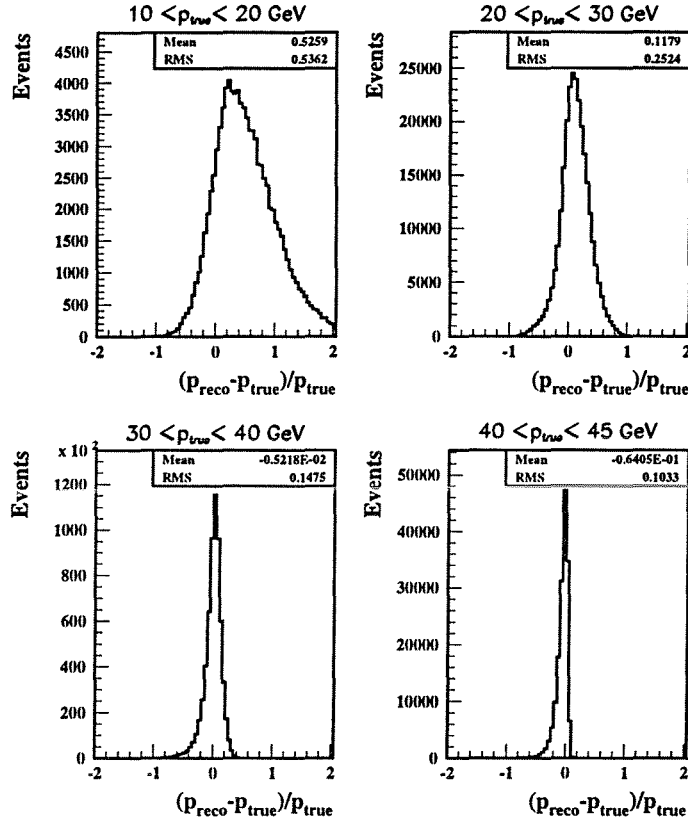


Figure 6.15: Momentum resolution in slices of true momentum.

function is defined in terms of the variable  $z$  as discussed in Section 5.1 ;

$$z = \frac{(E + p_z)_{\text{hadron}}}{(E + p)_{\text{quark}}} \quad (6.12)$$

where  $(E + p)_{\text{quark}}$  is the sum of the energy and momentum of the quark after accounting for initial state radiation, gluon bremsstrahlung and photon radiation in the final state and  $p_z$  is the momentum of the first hadron produced in the fragmentation chain, with respect to the quark direction. The  $z$  variable is not experimentally observable, however, so measurements of fragmentation functions are usually expressed in terms of the 'scaled energy',  $x_E^b$ , where :

$$x_E^b = \frac{E_{\text{hadron}}}{E_{\text{beam}}} \quad (6.13)$$

The  $x_E^b$  variable includes the effects of photon and hard gluon radiation in the denominator and hence the mean value of  $x_E^b$  is lower than the mean value of  $z$ . Combining experimental results from LEP [59, 60] gives :

$$\langle x_E^b \rangle = 0.702 \pm 0.008 \quad (6.14)$$

Assuming the fractional error on  $\langle z \rangle$  to be the same as the fractional error on  $\langle x_E^b \rangle$ , this can be used to estimate an error on the Peterson fragmentation parameter  $\epsilon_b$ . Figure 6.16 shows how the mean value of  $z$  depends on the value of  $\epsilon_b$ . The solid

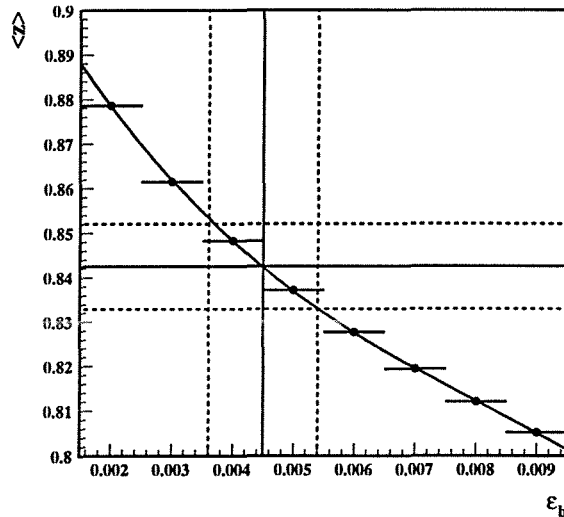


**Figure 6.16:** Dependence of  $\langle z \rangle$  upon the value of  $\epsilon_b$  used to generate the Peterson fragmentation function.

lines correspond to the value of  $\epsilon_b = 0.0045$  which is used in the 1994 Monte Carlo simulation and the dotted lines show the errors deduced from the measurement of  $\langle x_E^b \rangle$ . Hence the uncertainty on  $\epsilon_b$  is taken to be :

$$\epsilon_b = 0.0045 \pm 0.0009 \quad (6.15)$$

The systematic errors on the lifetime and mixing results were studied by re-weighting<sup>2</sup> the 1994 Monte Carlo to account for the spread in  $\epsilon_b$  values discussed above and then repeating the fitting procedures using the re-weighted Monte Carlo. This is discussed in more detail in Sections 6.5.5 and 7.7. The reconstructed momentum distributions corresponding to the different  $\epsilon_b$  values are shown in Figure 6.17.

## 6.4 Proper Time Resolution

The reconstructed proper time distribution which is obtained using the decay length and momentum algorithms described above is shown in Figure 6.18 for data and Monte Carlo, using a BTAG cut of 20. Perfect agreement is not expected on

<sup>2</sup>The Monte Carlo weights were calculated to be;  $w = \frac{f(z, \epsilon_b^{new})}{f(z, \epsilon_b^{old})}$  where  $f(z, \epsilon_b)$  is the Peterson fragmentation function (Eqn. (5.7)),  $\epsilon_b^{old}$  is the nominal value of 0.0045 and  $\epsilon_b^{new}$  is the new value of  $\epsilon_b$ .

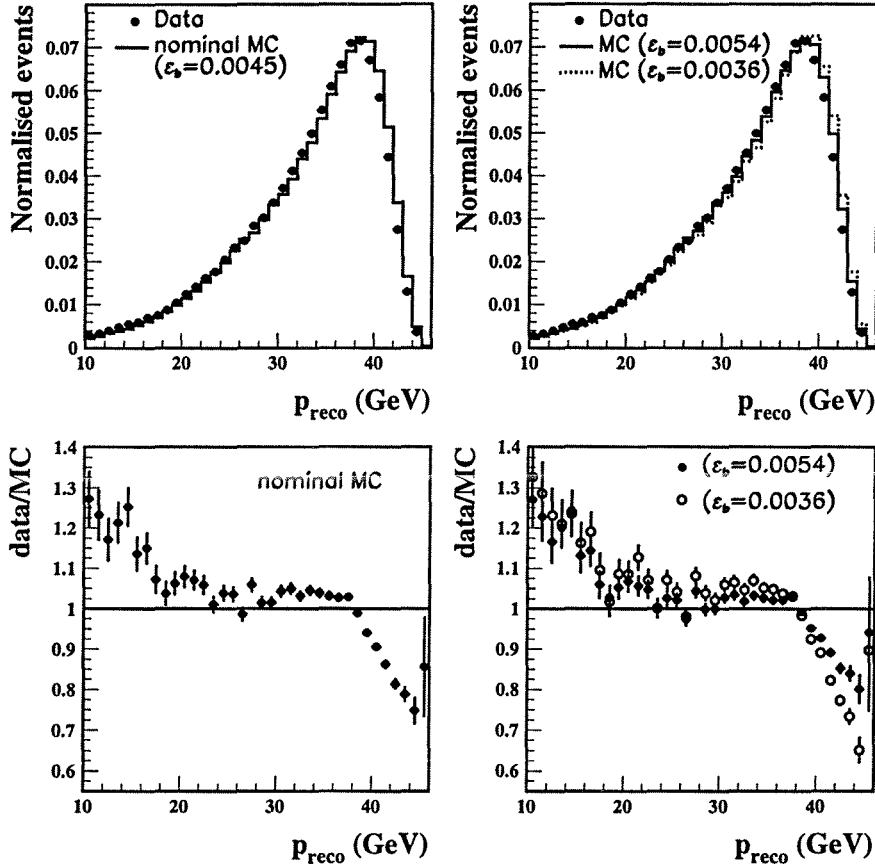


**Figure 6.17:** Comparison of the reconstructed momentum distribution for various values of  $\epsilon_b$  used in the Monte Carlo Peterson fragmentation function.

the positive side of the distribution since the average  $b$  lifetime in the Monte Carlo (1.5 ps) is lower than that expected in the data (world average  $\tau_b = 1.549 \pm 0.02$  ps [2]). The agreement is good in the negative tail indicating that the proper time resolution is well modelled in the Monte Carlo after smearing has been performed. A large discrepancy between data and Monte Carlo can be seen at low proper times and can also be seen in the decay length distribution (Figure 6.7). This discrepancy is due to differences between data and Monte Carlo in the way the BTAG cut affects the proper time distribution and is discussed in more detail in Section 6.5.3.

The average proper time resolution is shown in Figure 6.19 with the results of a triple Gaussian fit given in Table 6.3. The core 75% of events have a resolution of about 0.23 ps. Figure 6.20 shows the proper time resolution in eight slices of true proper time. The resolution deteriorates rapidly as  $t_{true}$  increases and at true proper times of 4 ps and above, a significant fraction of events appear to

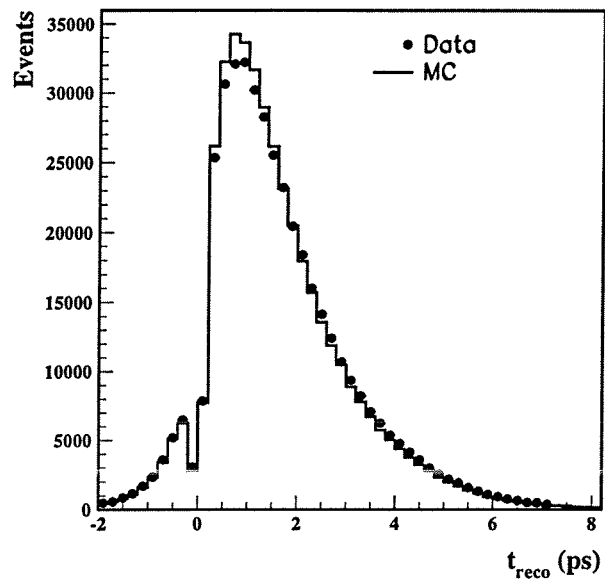


Figure 6.18: The reconstructed proper time distribution in data and Monte Carlo after a BTAG cut of 20.

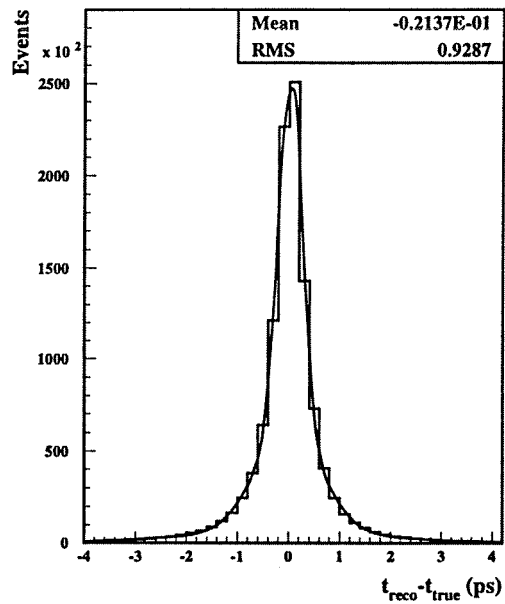


Figure 6.19: The average proper time resolution for Monte Carlo  $b$  events.

Parameter	Gaussian 1	Gaussian 2	Gaussian 3
Amplitude	75%	22%	3%
Mean (ps)	0.027	0.0002	-0.17
$\sigma$ (ps)	0.23	0.65	2.1

Table 6.3: Results of a triple Gaussian fit to the average proper time resolution.

be reconstructed at low proper times. This ‘bin-swapping’ must be taken into account in the fitting procedures which are used to extract  $\tau_b$  and  $\Delta m_d$ . The fitting procedures use a matrix folding method to incorporate resolution effects as discussed in the following sections. The greatest sensitivity to  $B_s^0$  oscillations is at low proper times where there are high statistics and the resolution is best.

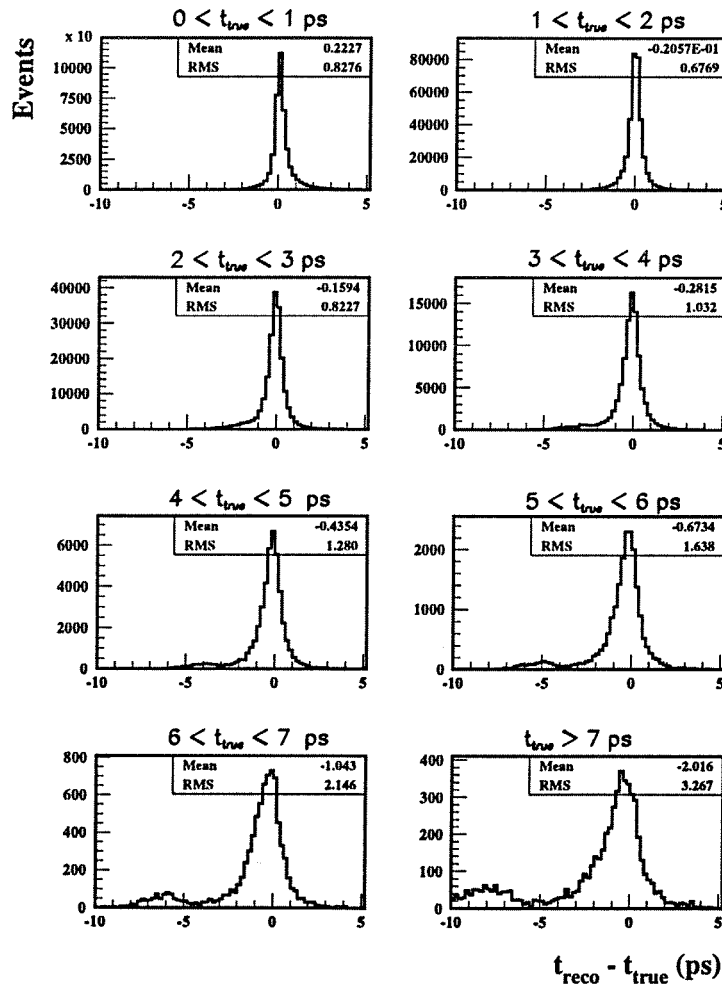


Figure 6.20: The proper time resolution,  $(t_{reco} - t_{true})$ , in ps in slices of true proper time.

## 6.5 Measurement of the Inclusive $b$ Lifetime.

A fit to the reconstructed proper time distribution is performed in order to extract the inclusive  $b$  lifetime,  $\tau_b$ . This is done primarily as a consistency check, to ensure that the effects of vertexing,  $b$  tagging, and proper time resolution are well modelled in the lifetime fit before fitting the more complicated charge correlation function. However, the lifetime measurement is of interest in its own right since the large event sample implies that a precise measurement of  $\tau_b$  can be obtained, provided systematic errors are not too large. There is much theoretical interest in measurements of the inclusive  $b$  lifetime as a way of constraining the individual  $b$  hadron lifetimes, in particular the  $b$  baryon lifetime.

### 6.5.1 Outline of Fitting Procedure

The lifetime fitting procedure consists of a MINUIT minimisation [61] of the  $\chi^2$  difference between the reconstructed proper time distribution in data and a ‘theoretical’ distribution which is constructed by folding detector resolution effects with a true  $b$  lifetime distribution and then adding background components. The basic structure of the lifetime fit is as follows :

- (a) Begin with the true  $b$  proper time distribution,  $e^{-t/\tau_b}/\tau_b$ .
- (b) Modify the true  $b$  distribution by the time dependent vertexing efficiency  $\epsilon^{vx}(t)$  which is taken from Monte Carlo.
- (c) Incorporate proper time resolution effects by folding the time distribution with the resolution matrix which is derived from Monte Carlo. This gives a ‘reconstructed’  $b$  proper time distribution, prior to the effects of the BTAG cut.
- (d) Modify this reconstructed distribution by the time dependent BTAG efficiency to obtain a final reconstructed distribution for  $b$  hadrons.
- (e) Add the contributions from  $c$  and  $uds$  backgrounds to obtain a ‘theoretical’ proper time distribution which is then fitted to data by varying the lifetime,  $\tau_b$ , in the true  $b$  proper time distribution.

### 6.5.2 Resolution Folding

The ‘bin swapping’ caused by the proper time resolution is included in the fit by means of a resolution folding matrix,  $\mathbf{R}$ , which is formed by plotting  $t_{reco}$  against  $t_{true}$  for  $b$  events and is obtained from the Monte Carlo. A schematic diagram of the matrix is shown in Figure 6.21(a) and Figure 6.21(b) shows the two dimensional plot of  $t_{reco}$  against  $t_{true}$  from which the matrix is derived. It can be seen that the plot is peaked along  $t_{reco} = t_{true}$  with the off-diagonal elements indicating the extent of the bin swapping. The matrix is filled after revertexing but before  $b$  tagging and is normalised to the total number of entries in each

'slice' of  $t_{true}$ . Hence  $R_{pq}$  is the fraction of events passing the revertexing cuts which have a true proper time in bin  $p$  and are reconstructed with a measured proper time in bin  $q$ .

An alternative method of folding would be to parameterise the time resolution in slices of true proper time [24], for example in terms of three or four Gaussians. These parameterisations are then convoluted with the true time distribution. This method has the disadvantage that the parameterisations often do not describe the resolution precisely, especially in the tails, leading to problems in the fit quality, especially considering the high statistical precision used here. Furthermore, the convolution process is mathematically complicated and can lead to instabilities in the fit. The matrix method of folding has advantages in that it is an exact description of the proper time resolution, at least in Monte Carlo, and it is mathematically very simple.

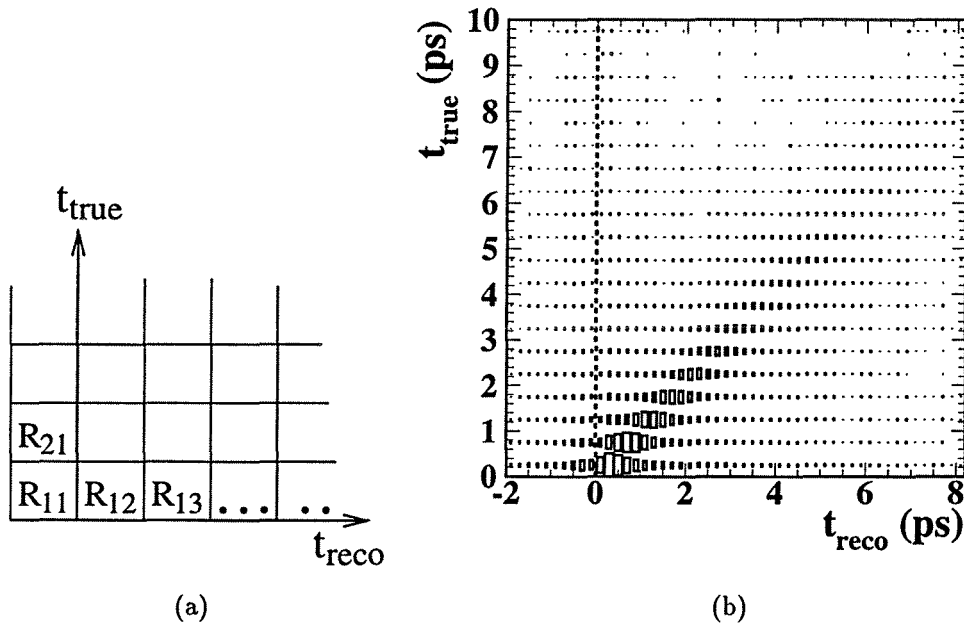


Figure 6.21: The proper time resolution matrix  $R$ .

### 6.5.3 Efficiency Corrections

The vertexing and BTAG cuts have efficiencies which depend on time. The cuts therefore modify the shape of the proper time distribution. These effects must be taken into account in the fitting procedure. The effects of vertexing and  $b$  tagging are treated separately in the fit since, while the time dependence of the vertexing efficiency is taken from Monte Carlo, the BTAG efficiency can be checked using data.



The vertexing efficiency for  $b$  events is shown in Figure 6.22 as a function of true proper time. It can be seen that events with intermediate proper times are reconstructed most efficiently. This is because at low proper times, less tracks pass the  $\mathcal{R}_{sig} > 0.7$  cut and so the vertexing is less efficient, while at high proper times, contamination of secondary tracks with those from the primary are more likely to cause the vertex to fail the  $\chi^2$  cut. The vertexing efficiency for  $b$  events is calculated by dividing the true proper time distribution, after vertexing cuts, by the true proper time distribution before cuts.

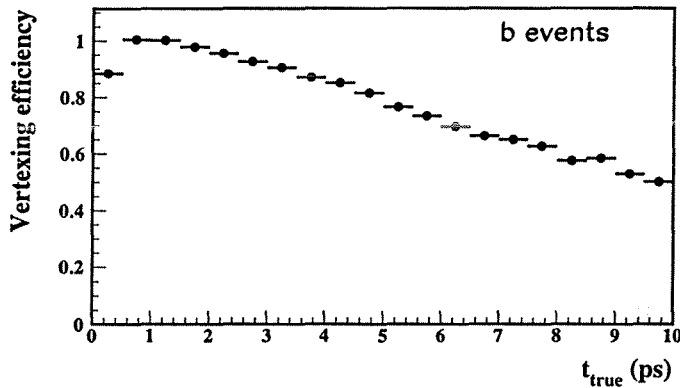


**Figure 6.22:** Vertexing efficiency as a function of true proper time for Monte Carlo  $b$  events.

After vertexing and momentum reconstruction have been performed, reconstructed proper time distributions are available and comparisons can be made between data and Monte Carlo. The time dependence of the BTAG cut efficiency is calculated as a function of  $t_{reco}$  and is shown in Figure 6.23 for Monte Carlo  $b$  events (for a BTAG cut of 20). The BTAG cut efficiency is calculated as a function of  $t_{reco}$  rather than  $t_{true}$  since the shape of the time dependence can then be checked by comparing the average BTAG efficiency in data and Monte Carlo. The average BTAG efficiency in data and Monte Carlo is shown in figure 6.24, along with the ratio data/MC. It can be seen that the BTAG cut is more efficient at low reconstructed proper times in Monte Carlo than in data. This is the most likely cause of the discrepancy at low proper times seen in Figure 6.18 and must be taken into account in the fit. Hence the time dependence of the BTAG efficiency for  $b$  events (Figure 6.23) is taken from Monte Carlo but is modified by a correction factor  $\mathcal{C}(t_{reco})$  which is equal to the ratio of data/MC shown in Figure 6.24. The only assumption made here is that the size of the discrepancy in the average efficiency is the same as that in a pure  $b$  sample. This is a reasonable assumption since the sample at a BTAG cut of 20 consists of 90%  $b$  events.

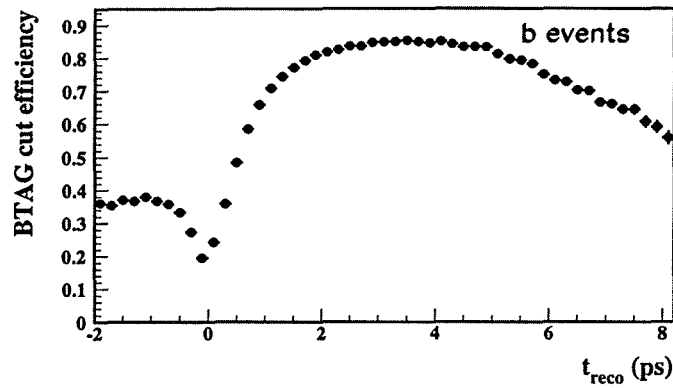


Figure 6.23: Efficiency of a BTAG cut of 20, as a function of reconstructed proper time, for Monte Carlo  $b$  events.

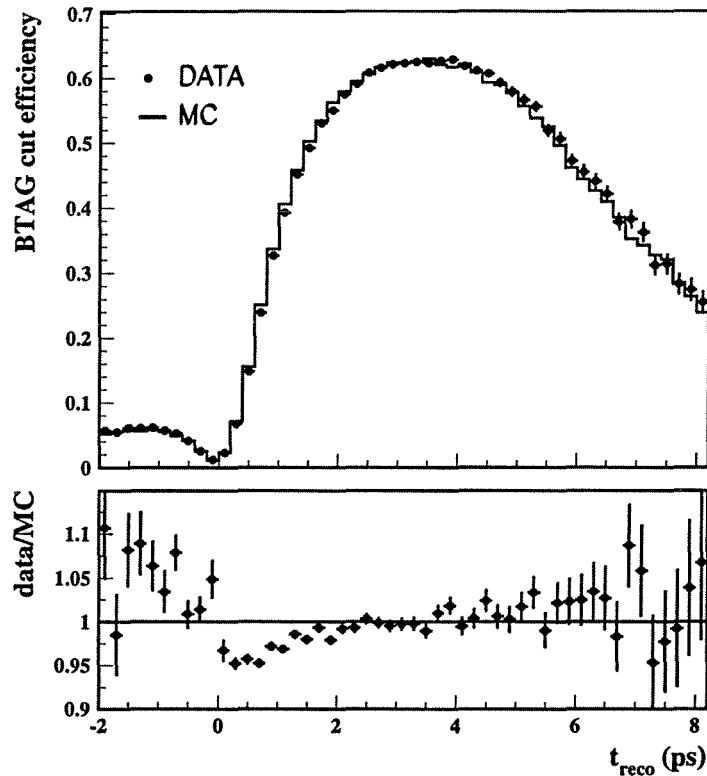


Figure 6.24: Average efficiency of BTAG cut in data and Monte Carlo as a function of reconstructed proper time.

#### 6.5.4 Construction of Theoretical Lifetime Distribution

The fraction of  $b$  events which are reconstructed in  $t_{reco}$  bin  $j$ , before tagging, is found by summing the contributions from each true bin  $i$  which have ended up

in bin  $j$  ;

$$f_j^b = \frac{\sum_i TT_i \epsilon_i^{vtx} R_{ij}}{\sum_i TT_i \epsilon_i^{vtx}} \quad (6.16)$$

where  $TT_i$  is the true theory for bin  $i$  and is given by ;

$$TT_i = \int_{\text{bin } i} \frac{e^{-t/\tau_b}}{\tau_b} dt \quad (6.17)$$

and  $\epsilon_i^{vtx}$  is the vertexing efficiency in true time bin  $i$  for  $b$  events shown in Figure 6.22. After  $b$  tagging, the fraction becomes ;

$$F_j^b = \frac{f_j^b \times \epsilon_{\text{BTAG}}^b(j) \times \mathcal{C}(j)}{\sum_j f_j^b \times \epsilon_{\text{BTAG}}^b(j) \times \mathcal{C}(j)} \quad (6.18)$$

where  $\epsilon_{\text{BTAG}}^b(j)$  is the bin-dependent efficiency for selecting  $b$  events by the BTAG cut, as shown in Figure 6.23. The bin dependent correction factors  $\mathcal{C}(j)$  are derived from the ratio plot in Figure 6.24 and take into account the discrepancies between data and Monte Carlo in the time dependence of the BTAG efficiency. Errors are assigned to the correction factors such that  $\sigma_{\mathcal{C}(j)} = \mathcal{C}(j) \times \text{ABS}(1.0 - \mathcal{C}(j))$  and are included in the errors on the final results.

The distribution for  $b$  events is then combined with that for charm and light-quark backgrounds and normalised to the total number of data events,  $N_{\text{dat}}$ , which pass all cuts. This gives a theoretical prediction,  $RT_j$ , for the number of events reconstructed in bin  $j$  :

$$RT_j = N_{\text{dat}} \times (\mathcal{P}_{uds} F_j^{uds} + \mathcal{P}_c F_j^c + \mathcal{P}_b F_j^b) \quad (6.19)$$

where  $\mathcal{P}_f$  are the flavour purities and :

$$\mathcal{P}_{uds} = 1 - \mathcal{P}_b - \mathcal{P}_c \quad (6.20)$$

The proper time distributions for backgrounds,  $F_j^c$  and  $F_j^{uds}$ , are taken from the Monte Carlo.

The inclusive  $b$  lifetime,  $\tau_b$ , is a free parameter in the lifetime fit and the  $b$  and  $c$  purities are allowed to vary within Gaussian constraints centred on the values estimated from the Monte Carlo. In this way, the systematic error arising from the knowledge of the flavour composition of the sample is automatically included in the error on  $\tau_b$  [62]. The  $\chi^2$  which is minimised by varying  $\tau_b$ ,  $\mathcal{P}_b$  and  $\mathcal{P}_c$  is given by :

$$\chi^2 = \sum_{pq \in \text{fit range}} \Delta_p \sigma_{pq}^{-1} \Delta_q + \frac{(\mathcal{P}_b^{\text{MC}} - \mathcal{P}_b)^2}{\sigma_{\mathcal{P}_b}^2} + \frac{(\mathcal{P}_c^{\text{MC}} - \mathcal{P}_c)^2}{\sigma_{\mathcal{P}_c}^2} \quad (6.21)$$

where  $\Delta_q = D_q - RT_q$  and  $D_q$  is the number of data events in bin  $q$ . The error matrix  $\sigma_{pq}$  is the sum of data and theory error matrices where the theory error matrix includes statistical errors due to the folding procedure, statistical errors on the shapes of the background distributions and errors due to the efficiency corrections,  $\mathcal{C}(t_{\text{reco}})$ . The constraints on the purities,  $\sigma_{\mathcal{P}_f}$ , are based on the size of the discrepancy between data and Monte Carlo in the overall tagging efficiency, as discussed in Section 4.6.

### 6.5.5 Results from Fit to Proper Time Distribution

In order to check that there is no bias in either the proper time reconstruction or fitting procedures, the whole analysis chain was first applied to the combined Monte Carlo sample<sup>3</sup>. The result of the fit is shown in Figure 6.25 and yields a value of  $\tau_b = (1.499 \pm 0.003)$  ps which is in good agreement with the value of 1.5 ps used in the Monte Carlo generation. The fitted purities are equal to the Monte Carlo values ( $\mathcal{P}_b = 89.3 \pm 0.4\%$ ,  $\mathcal{P}_c = 7.3 \pm 0.6\%$ ). The  $\chi^2/\text{n.d.f}$  of the fit is 0.8/49 and is very low as expected since the Monte Carlo is being used to fit itself. The results of the fit to Monte Carlo indicate that there are no additional biases which have not been accounted for in the fit.

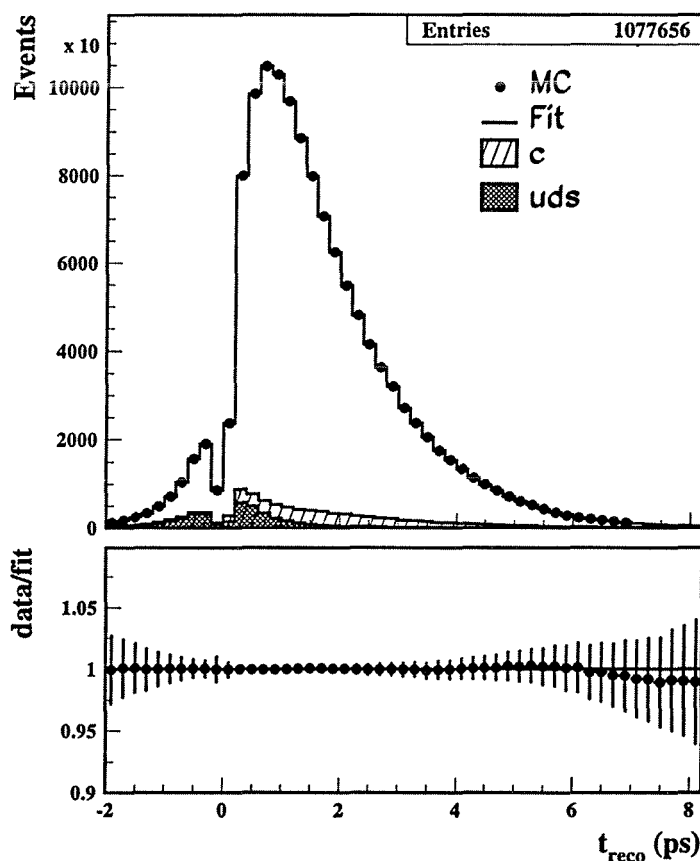


Figure 6.25: Result of lifetime fit to combined Monte Carlo sample.

As a stability check the lifetime fit was performed on each individual data year, using information from the corresponding Monte Carlo sample, to check that the results are all consistent. The results are given in Table 6.4 and are summarised in Figure 6.26. The errors include contributions from data and Monte Carlo statistics and the systematic errors due to flavour composition and the BTAG

<sup>3</sup>See Sections 4.3 and 4.7 for details of the Monte Carlo samples.

efficiency corrections,  $\mathcal{C}(t_{reco})$ . The central band shows the combined value and its full statistical and systematic error. The results are consistent with each other within the error. The fitted  $b$  and  $c$  purities are also shown in Table 6.4, along with the Monte Carlo expectations. It is clear that in all data taking periods, the fitting procedure requires a flavour composition which is slightly different from the Monte Carlo prediction. In general the data prefers a lower  $b$  purity and a higher  $c$  purity, as observed in other analyses [20]. Since  $c$  and  $uds$  events tend to be reconstructed at low proper times, the different flavour composition in data is a possible explanation for the discrepancies observed at low proper times in Figures 6.18 and 6.24.

Year	$\tau_b$ (ps)	$b$ Purity	$c$ Purity	$\chi^2/\text{n.d.f}$
1991	$1.602 \pm 0.026$	$0.875 \pm 0.012$ 0.882 (expected)	$0.089 \pm 0.018$ 0.074 (expected)	12/49
1992	$1.567 \pm 0.016$	$0.897 \pm 0.013$ 0.903 (expected)	$0.071 \pm 0.017$ 0.069 (expected)	18/49
1993	$1.543 \pm 0.019$	$0.851 \pm 0.020$ 0.884 (expected)	$0.136 \pm 0.030$ 0.077 (expected)	40/49
1994	$1.570 \pm 0.011$	$0.884 \pm 0.009$ 0.894 (expected)	$0.077 \pm 0.013$ 0.074 (expected)	15/49
1995	$1.601 \pm 0.016$	$0.898 \pm 0.017$ 0.894 (expected)	$0.068 \pm 0.025$ 0.073 (expected)	12/49

**Table 6.4:** Summary of the lifetime fit results for the 1991–1995 data-taking periods. The errors include contributions from data statistics, Monte Carlo statistics, flavour composition and the effects of the BTAG efficiency correction.

Performing the fit on the combined 1991 to 1995 data set, using the combined Monte Carlo sample gives the lifetime result :

$$\tau_b = 1.570 \pm 0.004(\text{stat.}) \pm 0.013(\text{syst.}) \text{ ps}$$

The fitted purities are determined to be :

$$\mathcal{P}_b = (87.5 \pm 1.2)\% \text{ (89.3\% expected)}, \quad \mathcal{P}_c = (9.8 \pm 1.8)\% \text{ (7.3\% expected)}$$

The result of the fit is shown in Figure 6.27. The  $\chi^2/\text{n.d.f}$  is 19/49 and is low since the errors include both contributions from statistics and from systematic errors arising from the BTAG efficiency corrections.

### Contributions to the error on $\tau_b$

The purely statistical error is determined by fixing the purities to their Monte Carlo values and only allowing  $\tau_b$  to vary in the fit. The errors due to Monte Carlo statistics and efficiency corrections are switched off by means of a series of flags in the fit and hence the resulting error on  $\tau_b$  is due to data statistics alone.

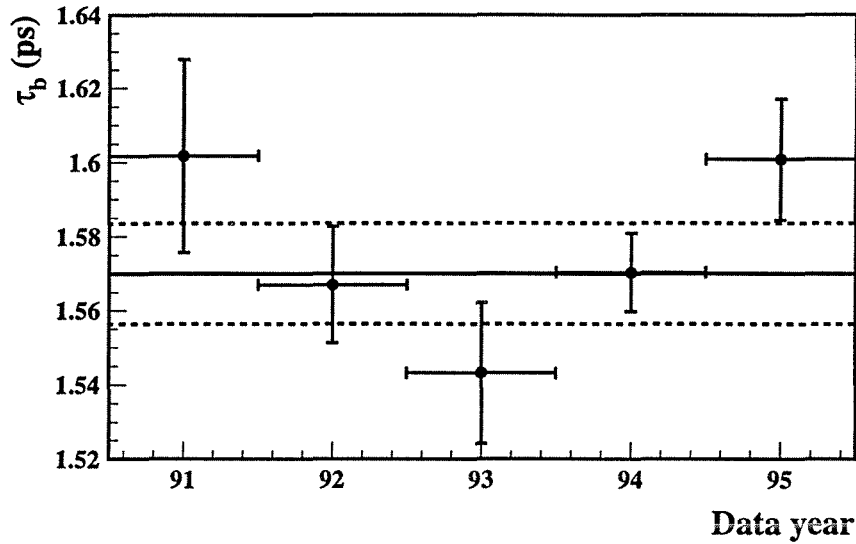


**Figure 6.26:** Results of the lifetime fit to the individual data years. The errors shown include statistical errors from data and Monte Carlo, combined with systematic uncertainties due to the flavour composition and efficiency corrections. The band shows the combined value and its total statistical and systematic error.

Error Source	$\sigma_{\tau_b}$ (ps)
Monte Carlo statistics	$\pm 0.002$
Efficiency corrections	$\pm 0.004$
Flavour composition	$\pm 0.006$
$b$ fragmentation	$\pm 0.010$
Total	$\pm 0.013$

**Table 6.5:** Summary of the various contributions to the systematic error on  $\tau_b$ .

Contributions to the systematic error on the inclusive lifetime are summarised in Table 6.5. The various contributions are determined as follows :

- **Monte Carlo Statistics :** Errors associated with the resolution folding matrix and the shape of the reconstructed proper time distributions for  $c$  and  $uds$  events are included by changing a flag in the fit. The contribution from these sources is found by subtracting in quadrature the errors with and without the Monte Carlo statistical error included.
- **Efficiency Corrections :** The error due to the BTAG efficiency corrections is calculated in the same way as the error due to the Monte Carlo statistics, by switching the  $\mathcal{C}(t_{reco})$  errors off and on in the fit and noting the change in the error on  $\tau_b$ .

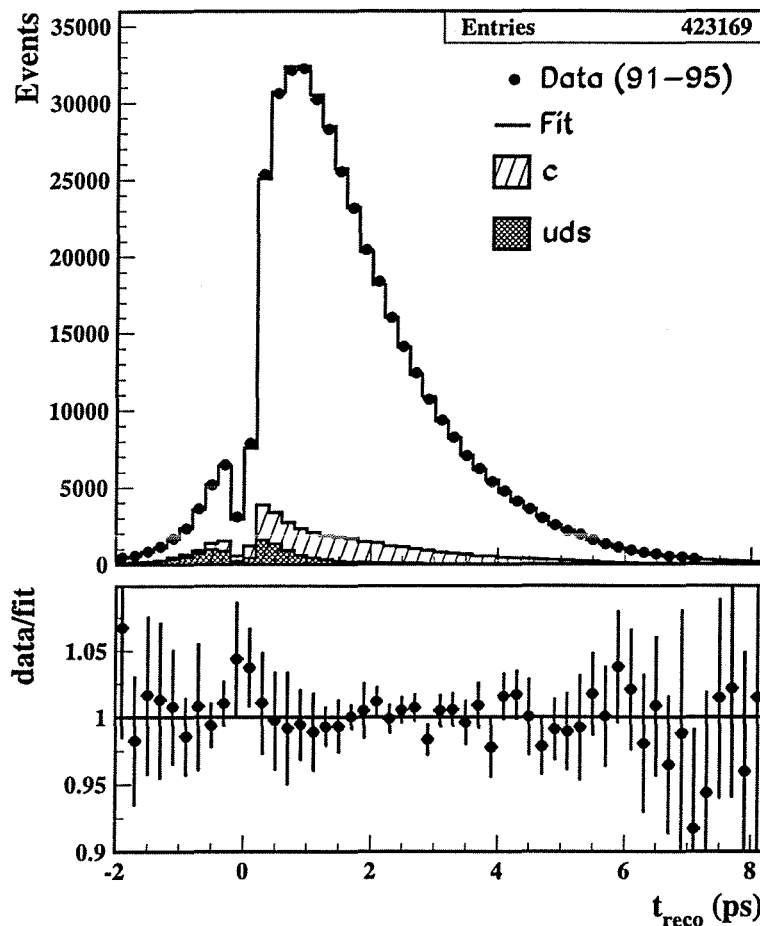


**Figure 6.27:** Reconstructed proper time distribution in data and the result of the fit. The bottom plot shows the ratio of the measured distribution to the fit. The errors shown include statistical errors from data and Monte Carlo and errors from the BTAG efficiency corrections.

- Flavour Composition :** The systematic error due to the flavour composition is determined by fixing the  $b$  and  $c$  purities and subtracting the resulting error on  $\tau_b$  in quadrature from the error obtained when the purities are allowed to vary within the constraints described in Section 6.5.4. This gives the error of 0.006 noted in the table. The shift in the actual value of  $\tau_b$  when the purities are fixed to their Monte Carlo values is 0.004 which is within the systematic error which has been assigned to the flavour composition.
- $b$  Fragmentation :** The error due to the knowledge of the  $b$  fragmentation function is estimated as explained in Section 6.3.5 by re-weighting the Monte Carlo using different values of the Peterson fragmentation parameter,  $\epsilon_b$ . Variations of  $\pm 0.0009$  were used about a central value of 0.0045. The re-weighting was performed on the 1994 Monte Carlo simulation alone and the

fit was repeated on the 1994 data. The shift observed in the fitted value of  $\tau_b$  is taken as the systematic error.

Additional cross-checks are performed to investigate the effect of the revertexing procedure described in Section 6.2 and the effect of varying the sample purity by changing the BTAG cut.

To study any possible bias introduced by the revertexing procedure, the analysis is repeated without using revertexing (i.e. using the default QVSRCH vertex) for the 1992 data set. This gives the value  $\tau_b^{no\ revtx} = (1.580 \pm 0.016)$  ps which is consistent, within errors, with the nominal 1992 value of  $\tau_b = (1.567 \pm 0.016)$  ps. Hence no additional systematic error is assigned to the revertexing procedure.

In order to vary the sample flavour composition, the analysis is performed in three bins of increasing  $b$  purity by varying the BTAG cut. Cuts of 15, 20 and 25 were used, corresponding to estimated Monte Carlo  $b$  purities of 75%, 89% and 96% respectively. The results of the fits are given in Table 6.6 and shown in Figure 6.28 (the systematic error due to fragmentation is not included here). There are many common events in the three samples since, for example, all events passing a cut of 25 will also pass a cut of 20. The statistical errors on the lifetimes obtained using cuts of 15 and 25 are scaled to take into account their correlations with the nominal value. These scaled errors are shown in brackets in the table. The results indicate that the measured  $b$  lifetime is stable within the uncorrelated statistical and systematic errors. This serves as a cross check that the systematic error assigned to the flavour composition has not been underestimated.

Cut	$\tau_b$ (ps)	$b$ Purity	$c$ Purity
15	$1.5761 \pm 0.006$ (0.0056)	$70.9 \pm 0.77\%$ (expect 74.7%)	$19.9 \pm 1.3 \%$ (expect 14.0%)
20	$1.5701 \pm 0.0086$	$87.5 \pm 1.2\%$ (expect 89.3%)	$9.8 \pm 1.8 \%$ (expect 7.3%)
25	$1.5592 \pm 0.013$ (0.0127)	$94.2 \pm 1.3\%$ (expect 95.7%)	$5.2 \pm 1.9 \%$ (expect 3.2%)

**Table 6.6:** Summary of the measured  $b$  lifetime in samples of increasing  $b$  purity. Errors include uncertainties from data and Monte Carlo statistics, flavour composition and efficiency corrections. The uncorrelated errors on the lifetime, relative to the central value, are indicated in brackets below the lifetime results.

## 6.6 Summary

Inclusive vertexing and momentum reconstruction techniques have been used to reconstruct the proper lifetimes of candidate  $b$  hadrons. Detector resolution effects have been taken into account by means of a folding matrix and cut efficiencies have been checked using the data as far as possible. A fit to the



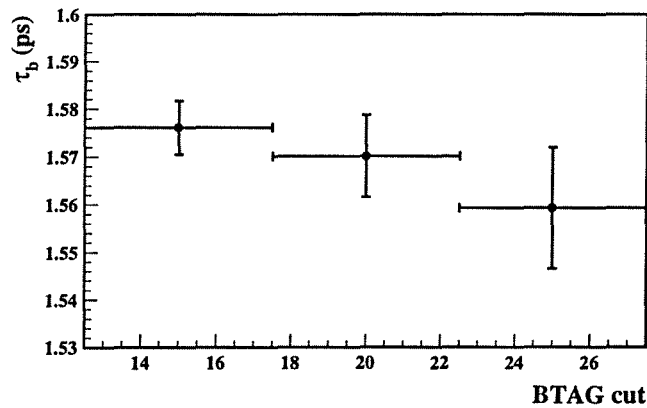


**Figure 6.28:** Dependence of the measured  $b$  lifetime on the sample purity. The results are indicated together with their uncorrelated statistical and systematic errors relative to the central value.

reconstructed proper time distribution for the full 1991–1995 data sample yields :

$$\tau_b = 1.570 \pm 0.004 (\text{stat.}) \pm 0.013 (\text{syst.}) \text{ ps}$$

where the systematic error is dominated by uncertainties in the  $b$  fragmentation function. The fit quality is good and the result is in agreement with the world average result of  $(1.549 \pm 0.020)$  ps [2], indicating that the effects of vertexing,  $b$  tagging and detector resolution are well modelled in the fit.

Some recent measurements of the inclusive  $b$  lifetime are shown in Figure 6.29 [63]. The world average including the new (unpublished) OPAL measurement [47] is shown. The precise OPAL value has raised the world average significantly. Due to the preliminary nature of the OPAL result, the world average is taken from reference [2] throughout this thesis.

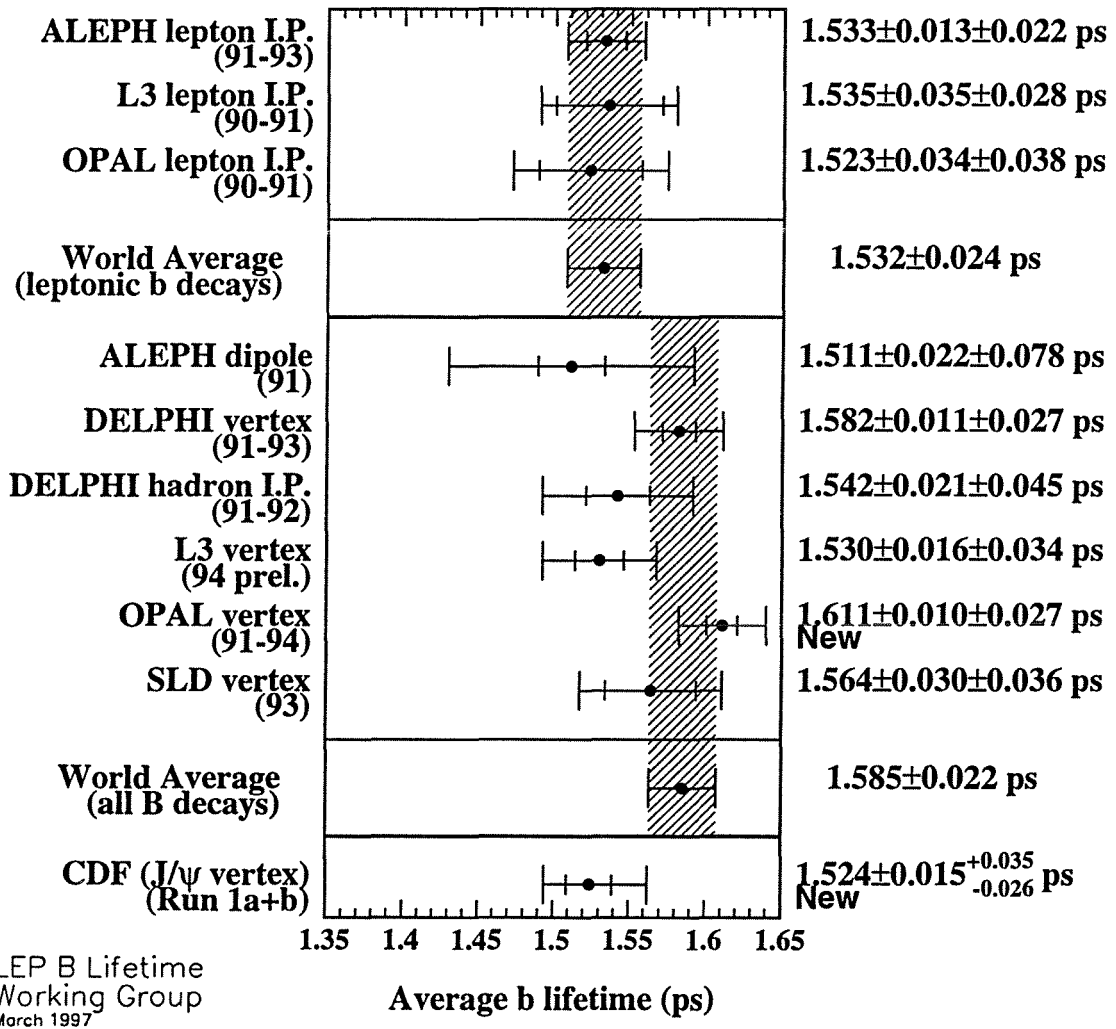


**Figure 6.29:** Summary of recent measurements of the inclusive  $b$  lifetime. The error bars on the individual measurements indicate the size of the statistical error and total error on the result. The result from this analysis is not shown on the plot.



# Chapter 7

## Measurement of $\Delta m_d$

In this chapter the fitting procedure for extracting the value of  $\Delta m_d$  is described. The method is briefly re-stated and the form of the fit is explained. Corrections to jet-charges due to effects of the reconstruction algorithms are described in Section 7.2. Results and systematic errors are presented in Sections 7.6 and 7.7 and comparisons made with other measurements in Section 7.8.

### 7.1 Overview of Method

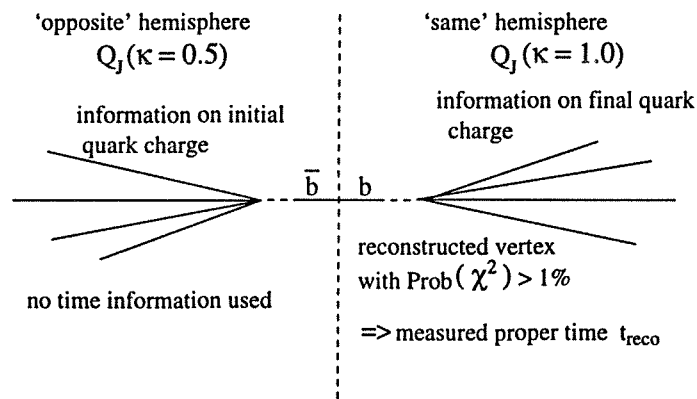


Figure 7.1: Schematic diagram showing the method for measuring  $\Delta m_d$ .

The method for measuring  $\Delta m_d$  is shown in Figure 7.1 and is summarised as follows :

- Proper time reconstruction is performed as described in Chapter 6. The hemisphere in which the proper time is reconstructed is referred to as the 'same' side. This is chosen as the hemisphere containing the secondary vertex with the highest  $\chi^2$  probability (see Section 6.2).
- Jet-charges are formed as described in Sections 5.2 and 5.4.

- The ‘charge correlation’ is defined as the product of the opposite and same side jet-charges as discussed in Section 5.5 :

$$\text{charge correlation} = \langle -Q_{J_o}^{\kappa=0.5} Q_{J_s}^{\kappa=1.0} \rangle(t)$$

where  $\kappa = 0.5$  is used on the ‘opposite’ side in order to obtain the lowest initial state mistag and  $\kappa = 1.0$  is used on the ‘same’ side to achieve the best sensitivity to mixing.

The charge correlation consists of contributions from the six classes of  $b$  hadrons listed in Table 5.2, plus contributions from  $c$  and  $uds$  backgrounds. Suppose, for example, there is a  $b$  baryon on the ‘same’ side. The contribution it makes to the charge correlation, denoted by  $\langle -QQ \rangle^\Lambda$ , is found by considering the various classes of  $b$  hadrons which it can ‘pair up’ with on the opposite side ;

$$\begin{aligned} \langle -QQ \rangle^\Lambda &= f_\Lambda \langle -Q_\Lambda^{0.5} Q_\Lambda^{1.0} \rangle + f_u \langle -Q_{B^\pm}^{0.5} Q_\Lambda^{1.0} \rangle + f_d (1 - \chi_d) \langle -Q_{B_d^{unmix}}^{0.5} Q_\Lambda^{1.0} \rangle \\ &+ f_d \chi_d \langle -Q_{B_d^{mix}}^{0.5} Q_\Lambda^{1.0} \rangle + f_s (1 - \chi_s) \langle -Q_{B_s^{unmix}}^{0.5} Q_\Lambda^{1.0} \rangle \\ &+ f_s \chi_s \langle -Q_{B_s^{mix}}^{0.5} Q_\Lambda^{1.0} \rangle \end{aligned} \quad (7.1)$$

which can be written as ;

$$\langle -QQ \rangle^\Lambda = \langle Q_b^{0.5} \rangle \langle Q_\Lambda^{1.0} \rangle + \text{covariance term} \quad (7.2)$$

where  $\langle Q_b^{0.5} \rangle$  is the time-integrated, average  $b$  jet-charge for  $\kappa = 0.5$  and  $\langle Q_\Lambda^{1.0} \rangle$  is the time-integrated jet-charge for baryons (for  $\kappa = 1.0$ ). Similarly, expressions can be found for the contributions from  $B^\pm$ ,  $B_d^{unmix}$  etc. and so in general :

$$\langle -QQ \rangle^{class} = \langle Q_b^{0.5} \rangle \langle Q_{class}^{1.0} \rangle + \text{covariance term} \quad (7.3)$$

These contributions, as they are written here, do not depend on time and the time dependence of the charge correlation comes from the variation in the relative fractions of the  $b$  hadron classes as a function of reconstructed proper time on the ‘same’ side. The procedure for fitting the charge correlation function reduces to a twofold problem :

- Find the contribution to the charge correlation from each class of  $b$  hadron and from backgrounds.
- Calculate the fraction of each class of  $b$  hadron and of backgrounds which is reconstructed in a particular proper time bin.

This is over simplified since, in reality, the contributions to the charge correlation from each  $b$  hadron class are not strictly independent of reconstructed proper time. The effect of the proper time reconstruction algorithms is such that it introduces a correlation between the hemisphere multiplicity and the reconstructed proper time and this, in turn, gives rise to a variation in the jet-charge as a function of reconstructed proper time due purely to the effect of the reconstruction

algorithms. It is essential that this effect is well understood and accounted for in the fit since it would mean that, even in the absence of any mixing, a time dependence of the charge correlation would be observed. This is discussed fully in Section 7.2. In performing stage (a) above, the data is used as much as possible to provide constraints and thus reduce the Monte Carlo dependence. The time-integrated, average jet-charges for  $b$ ,  $c$  and  $uds$  are extracted from the data by performing a fit to  $\langle -Q_{J_o}^\kappa Q_{J_s}^\kappa \rangle$  ( $\kappa = 0.5, 1.0$ ) as a function of BTAG cut (i.e. purity). This is explained in Section 7.3 [53].

Stage (b) is done in exactly the same way as in the lifetime fit (Section 6.5) with the modification that different classes of  $b$  hadrons are treated individually.

## 7.2 Multiplicity Corrections

The idea that the contributions to the charge correlation function (Equation (7.3)) are time-independent, with all the time dependence coming from the variation with time of the relative fractions of each  $b$  hadron class, is only strictly true in the case of perfect proper time reconstruction and charge tagging.

In reality, the vertexing and momentum reconstruction algorithms behave differently in the case of high and low charged multiplicity hemispheres, thus causing the mean hemisphere charged multiplicity to vary as a function of reconstructed proper time. This, in turn, causes the mean jet-charge to vary with reconstructed proper time such that, even in the absence of mixing, the charge correlation would show a time dependence. Figure 7.2 shows how the mean signed jet-charge,  $\langle Q_{class}^{1,0} \rangle$ , varies with reconstructed proper time for each  $b$  hadron class. It is clear that these distributions are not flat, with the jet-charges for  $B^\pm$  and unmixed  $B_d$  mesons (which constitute the majority of the sample) showing a significant rise in the region between 0 and 2 ps. This algorithm-induced time dependence must be well understood and accounted for in the fit for  $\Delta m_d$ .

### 7.2.1 Variation of Multiplicity with Proper Time

The mean charged multiplicity obtained from Monte Carlo  $b$  events is shown as a function of *true* proper time in Figure 7.3. The distribution shows that there is no dependence of hemisphere multiplicity on true proper time. However, the charged track multiplicity is seen to vary with true  $B$  momentum as shown in Figure 7.4 and with true  $B$  decay length as shown in Figure 7.5. Both these effects can be explained by considering the fragmentation process. If the  $b$  hadron takes a small fraction of the energy and momentum of the string then a large fraction is left over for the production of other fragmentation tracks and hence the hemisphere multiplicity is high, while if the  $b$  hadron has very high energy then there is little left over to create fragmentation tracks and so the hemisphere multiplicity will be close to the  $b$  multiplicity. Since the momentum and decay length are correlated, this gives the results as shown. In calculating the true proper time however, the high and low multiplicity hemispheres are distributed throughout all bins in true

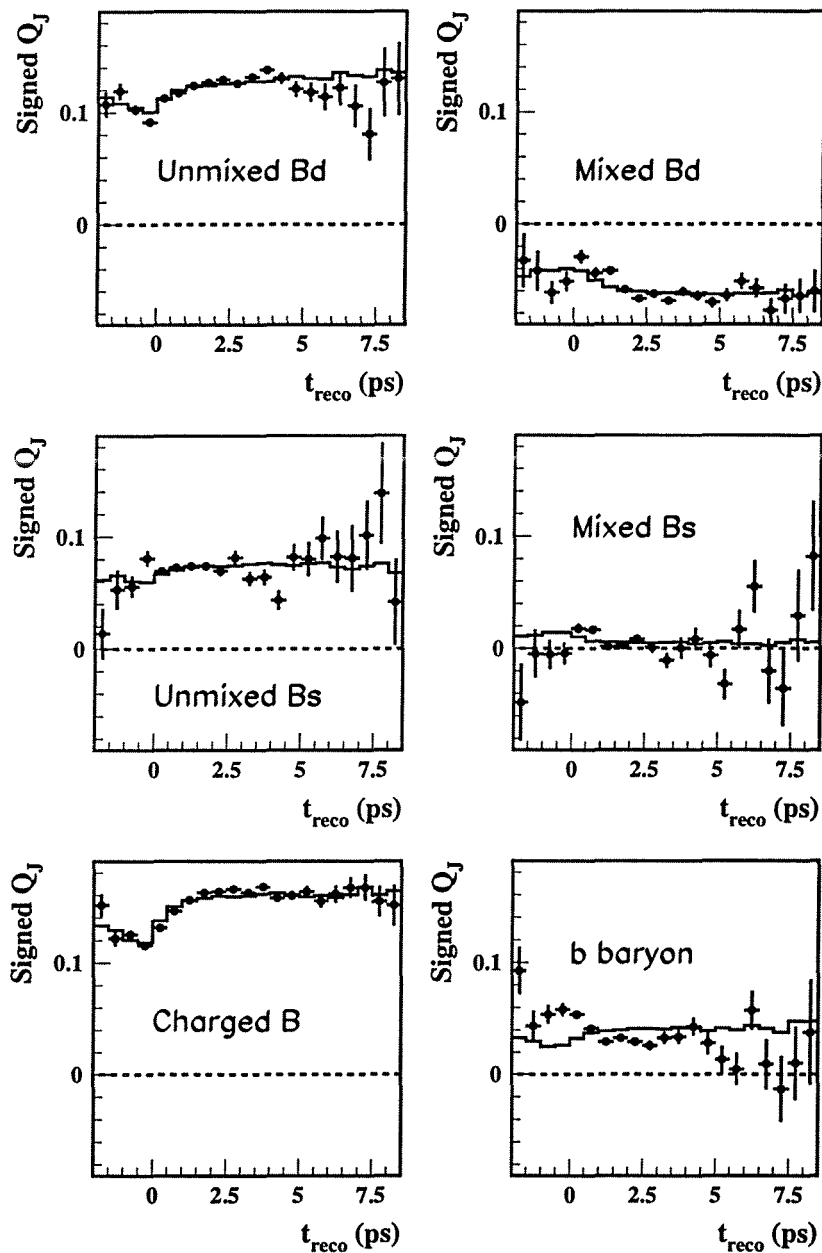


**Figure 7.2:** Dependence of the mean signed jet-charge on reconstructed proper time for the various classes of  $b$  hadrons. The points indicate the mean value observed in the Monte Carlo whereas the solid line represents the predicted dependence due to multiplicity variations (see Section 7.2.2).

proper time, giving the flat distribution in Figure 7.3.

The dependence of the hemisphere multiplicity on *reconstructed*  $B$  momentum

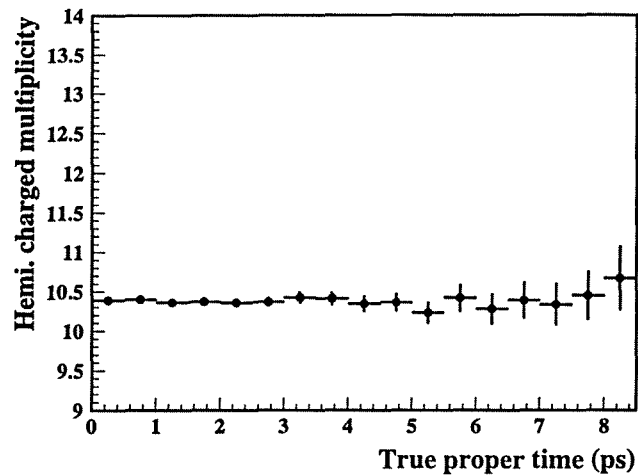


Figure 7.3: Variation of the mean charged track multiplicity as a function of true proper time in Monte Carlo  $b$  events (suppressed zero).

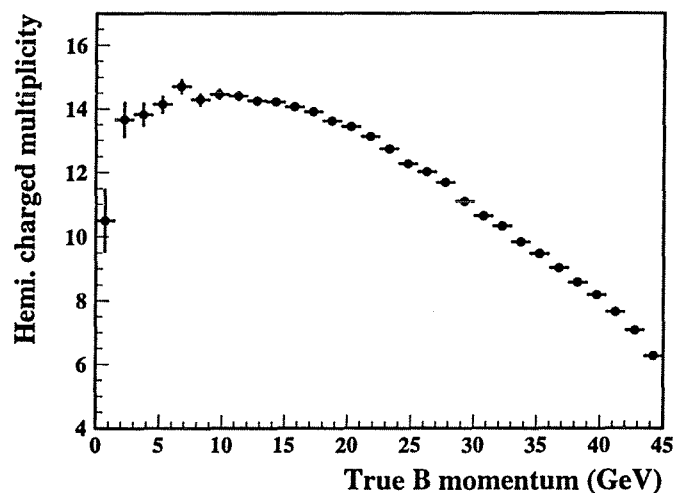
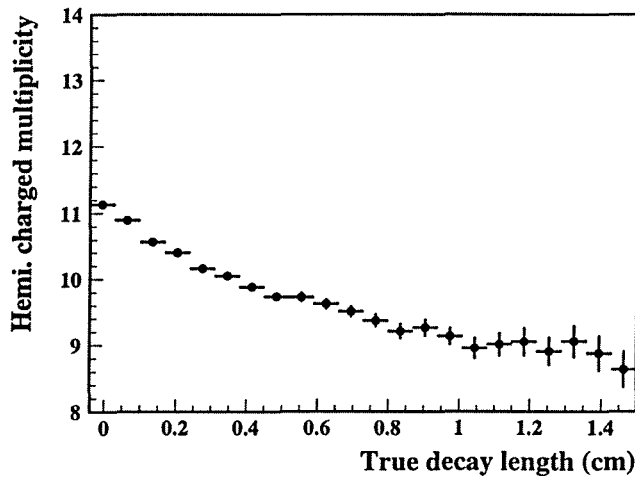


Figure 7.4: Variation of the mean charged track multiplicity as a function of true  $B$  momentum in Monte Carlo  $b$  events (suppressed zero).

and reconstructed  $B$  decay length is shown in Figures 7.6 and 7.7 for data and Monte Carlo. The shapes of the distributions are different from those obtained with the true momentum and decay length (Figures 7.4 and 7.5). This is due to the different behaviour of the decay length and momentum reconstruction algorithms and BTAG cut under conditions of low and high hemisphere multiplicities. It can be seen that the increase in hemisphere multiplicity at low reconstructed decay lengths (Figure 7.7) is more significant than in the true case (Figure 7.5). This is because hemispheres with high multiplicities are more likely





**Figure 7.5:** Variation of the mean charged track multiplicity as a function of true  $B$  decay length in Monte Carlo  $b$  events (suppressed zero).

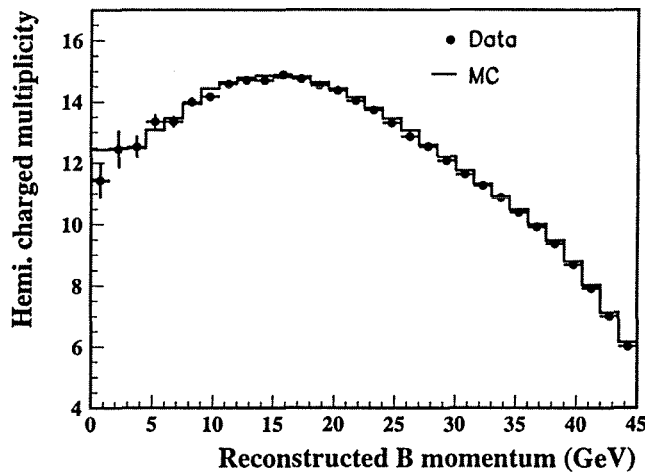


**Figure 7.6:** Variation of the mean charged track multiplicity as a function of reconstructed  $B$  momentum in data and Monte Carlo (suppressed zero).

to be those where a primary track is included in the secondary vertex calculation, thus ‘pulling’ the secondary vertex closer to the primary. The reconstruction algorithms produce a dependence of the average hemisphere charged multiplicity on reconstructed proper time. This is shown in Figure 7.8 for data and Monte Carlo simulation. The mean multiplicity at low proper times is approximately 20% greater than the average. The agreement between data and Monte Carlo is excellent.

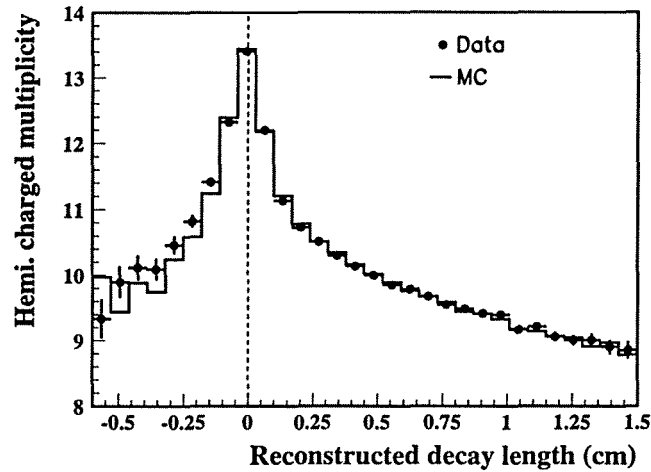


Figure 7.7: Variation of the mean charged track multiplicity as a function of reconstructed  $B$  decay length in data and Monte Carlo (suppressed zero).

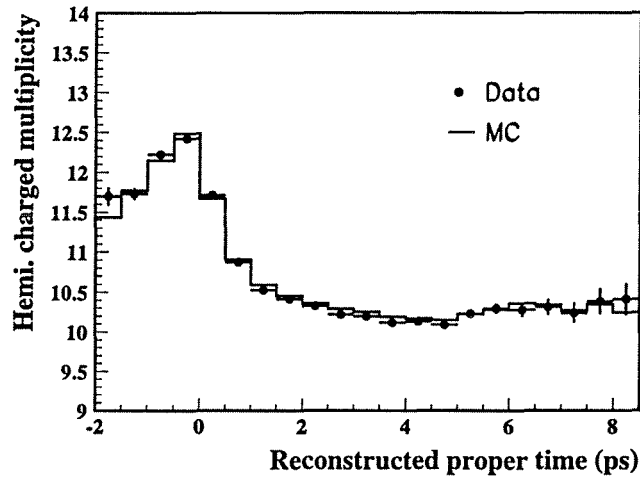


Figure 7.8: Variation of the mean charged track multiplicity as a function of reconstructed proper time in data and Monte Carlo simulation (suppressed zero).

### 7.2.2 Variation of Jet-Charge with Hemisphere Multiplicity

The jet-charge is sensitive to changes in the hemisphere multiplicity. In low multiplicity hemispheres, the quark charge information is contained within relatively few, high momentum tracks whereas in hemispheres containing a large number of tracks, the charge information is confused by the abundance of low momentum tracks. In high multiplicity hemispheres there is a higher probability that a

low momentum track will escape detection and charge information will be lost. The variation in Monte Carlo of the signed jet-charge with hemisphere charged multiplicity is shown in Figure 7.9 for the various  $b$  hadron classes. In all cases the charge information is ‘diluted’ as the number of charged tracks increases. Differences between the various  $b$  hadron classes arise because of the different contributions which fragmentation tracks make in each case (see Section 5.4). In the case of charged  $B$  mesons, the fragmentation tracks are of the opposite sign to the initial quark and so adding more fragmentation tracks quickly results in deterioration of the jet-charge. In the unmixed  $B^0$  case however, fragmentation tracks contain some useful information and so the deterioration is less rapid. An argument similar to that for charged  $B$  mesons can be applied to mixed  $B^0$  mesons since fragmentation tracks similarly give a contribution of the wrong sign. Hence the gradients of the graphs for mixed mesons are slightly steeper than for the corresponding unmixed mesons.

In order to study and confirm the multiplicity dependence of jet-charges in data the ‘opposite signed hemisphere charge’ is defined where :

$$\text{opposite signed hemisphere charge} = -\text{sign}(Q_{Jc}^{0.5}) \times Q_{Js}^{1.0} \quad (7.4)$$

This is an approximation to the signed jet-charge with the advantage that it is measurable in both data and Monte Carlo simulation. Figure 7.10 shows the dependence of the opposite signed hemisphere charge on the hemisphere multiplicity. The dependence seen in data is very similar to that of the signed jet-charge and is well modelled in the Monte Carlo simulation.

It is clear that the variation of jet-charges with multiplicity and the variation of multiplicity with reconstructed proper time accounts for a substantial component of the observed time-dependence of  $b$  hadron jet-charges observed in Figure 7.2. The multiplicity drops suddenly in the region from 0 to 2 ps, corresponding to the change in jet-charges in this region. In order to investigate whether this hypothesis is correct, distributions of signed  $Q_J$  versus multiplicity and multiplicity versus reconstructed proper time are combined to predict the behaviour of signed jet-charges as a function of reconstructed proper time for each  $b$  hadron class. This prediction is shown as the histograms superimposed on Figure 7.2. The prediction models the general behaviour reasonably well, especially in the case of  $B^\pm$  mesons and unmixed  $B_d$  mesons. The agreement for baryons is poorer since topologies of these decays are expected to differ more from the average, which is used to calculate the predictions shown.

### Time Dependent Jet-Charge Corrections

The multiplicity-induced time-dependence of the signed jet-charges for each  $b$  hadron class is taken from the Monte Carlo simulation and expressed as a time-dependent correction,  $\text{corr}_{mult}^{class}(t_{reco})$ , with respect to the time-integrated jet-charge for that hadron class :

$$\text{corr}_{mult}^{class}(t_{reco}) = \langle Q_{class}^{1.0} \rangle^{MC}(t_{reco}) - \langle Q_{class}^{1.0} \rangle^{MC} \quad (7.5)$$

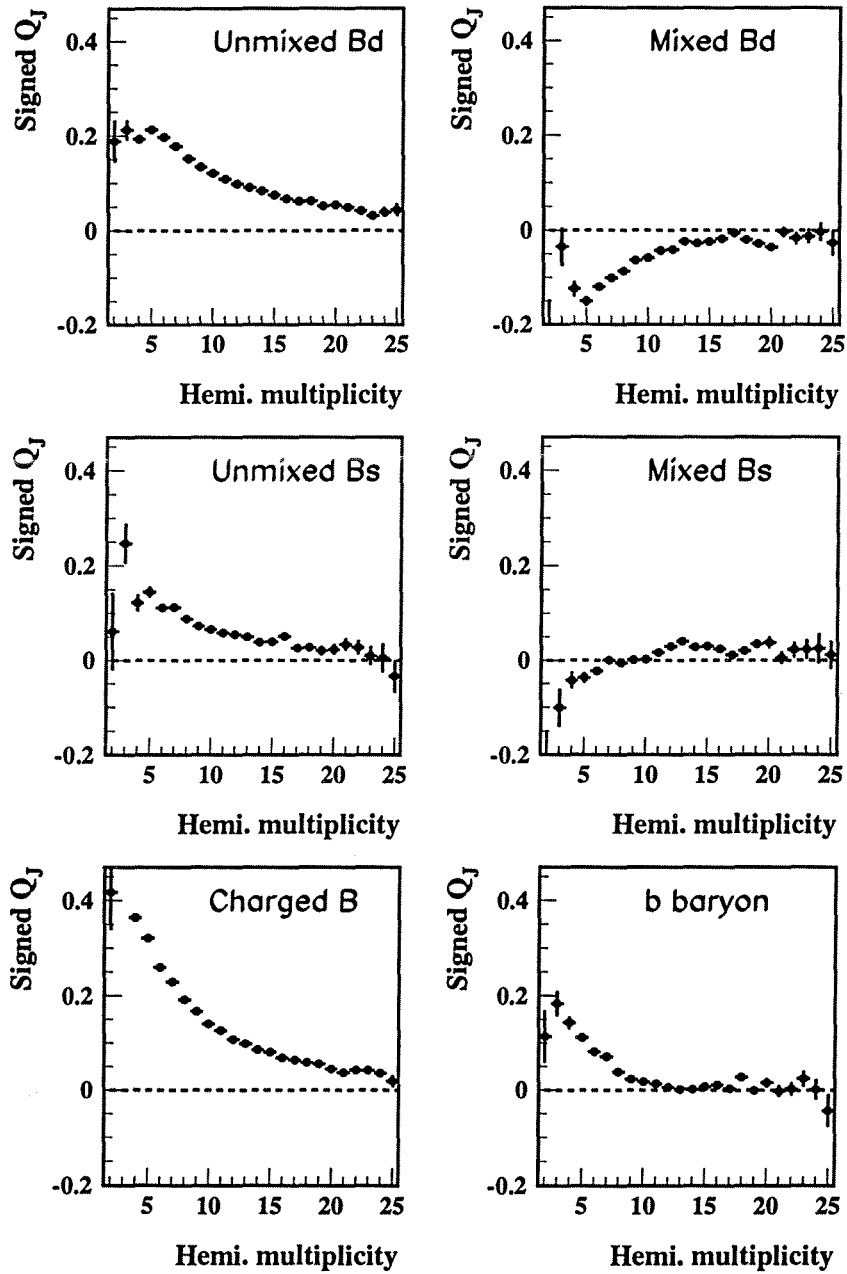


**Figure 7.9:** Variation of signed jet-charge with hemisphere charged multiplicity for the different  $b$  hadron classes. (Signed using initial quark charge).

The justification for taking these corrections from the Monte Carlo comes from the fact that :

- (a) The variation of mean hemisphere charged multiplicity with reconstructed

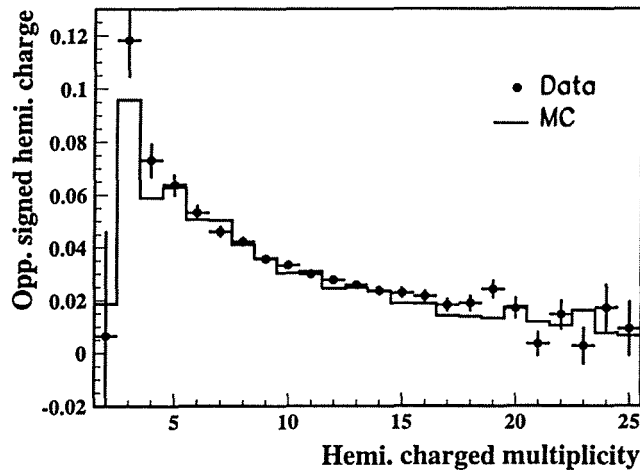


**Figure 7.10:** Dependence of the opposite signed hemisphere charge on hemisphere charged track multiplicity in data and Monte Carlo simulation.

proper time agrees closely in data and Monte Carlo (Figure 7.8).

- (b) The variation of ‘opposite signed hemisphere charge’ with charged multiplicity also agrees well in data and Monte Carlo (Figure 7.10).

These arguments are strengthened if the agreement between data and Monte Carlo is verified in samples with different mixtures of the  $b$  hadron classes. Using a cut on the vertex charge described in Section 6.3.2, samples enriched in  $B^0$  or  $B^\pm$  are obtained. Selecting hemispheres with  $|Q_{vert}| < 0.6$  is used to give  $B^0$  enhancement (50%  $\rightarrow$  58%) while cutting on  $|Q_{vert}| > 0.6$  gives  $B^\pm$  enhancement (40%  $\rightarrow$  50%). Figure 7.11 shows the variation of mean charged multiplicity with reconstructed proper time and Figure 7.12 shows the dependence of the opposite signed hemisphere charge on the hemisphere multiplicity for (a)  $B^0$  and (b)  $B^\pm$  enhanced samples. It can be seen that the dependence of the opposite signed hemisphere charge on multiplicity is much steeper in the  $B^\pm$  enhanced sample than in the  $B^0$  enhanced sample, as expected from Figure 7.9. The agreement between data and Monte Carlo is good in the enhanced samples, giving further indication that the Monte Carlo simulation gives a good description for the individual  $b$  hadron classes.

Percentage errors on the correction factors  $\text{corr}_{mult}^{class}(t_{reco})$ , are taken to be equal to the percentage difference between the mean hemisphere multiplicities in data and Monte Carlo for that  $t_{reco}$  bin, or the statistical error on the Monte Carlo value of  $\langle Q_{class} \rangle^{MC}(t_{reco})$ , whichever is largest.

As an additional cross check, the mean hemisphere multiplicity on the ‘opposite’ side of the event is plotted as a function of reconstructed proper time on the ‘same’ side (see Figure 7.13). This is done to verify that there is no bias on the opposite hemisphere jet-charge as a function of reconstructed proper time on

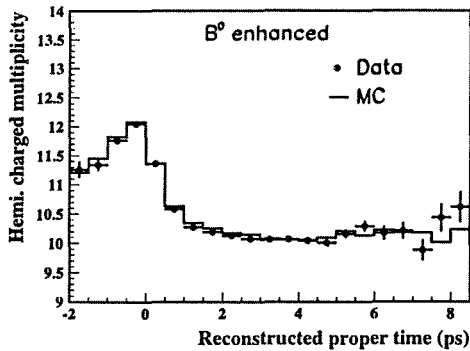
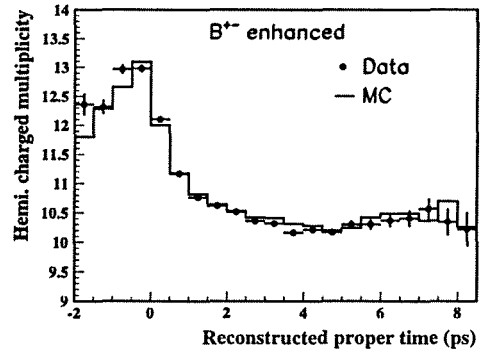
(a) Vertex charge  $B^0$  enhanced.(b) Vertex charge  $B^\pm$  enhanced.

Figure 7.11: Variation of the hemisphere charged multiplicity as a function of reconstructed proper time in samples enhanced in (a)  $B^0$  and (b)  $B^\pm$  decays using a cut on the vertex charge (suppressed zero).

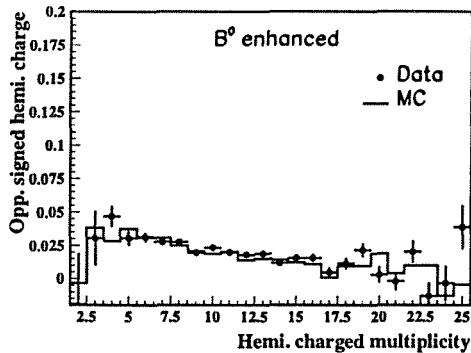
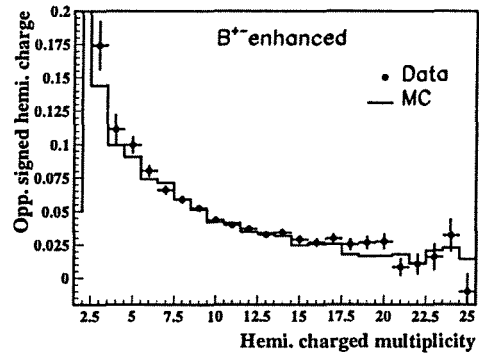
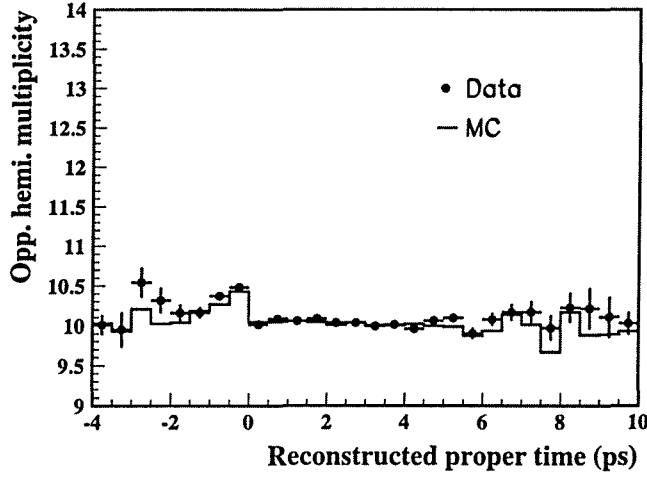
(a) Vertex charge  $B^0$  enhanced.(b) Vertex charge  $B^\pm$  enhanced.

Figure 7.12: Dependence of the opposite signed hemisphere charge on hemisphere charged multiplicity in  $B^0$  and  $B^\pm$  enhanced samples of data and Monte Carlo events.

the same side. This could arise due to correlations between hemispheres coming from the shared primary vertex. From Figure 7.13 it can be seen that negative reconstructed proper times are more probable when the opposite hemisphere multiplicity is high, however this effect is small and since there is no significant dependence for positive reconstructed proper times, any bias is neglected.



**Figure 7.13:** Dependence of the charged multiplicity in the ‘opposite’ hemisphere on reconstructed proper time in the ‘same’ hemisphere (suppressed zero).

### 7.3 Measurement of Average Jet-Charges

The values of  $\langle Q_b^\kappa \rangle$ ,  $\langle Q_c^\kappa \rangle$  and  $\langle Q_{uds}^\kappa \rangle$  for  $\kappa = 0.5$  and  $\kappa = 1.0$  are obtained, in this analysis, from a fit to the data distributions of  $\langle -Q_{J_o}^\kappa Q_{J_s}^\kappa \rangle$  as a function of BTAG cut.

The value of  $\langle -Q_{J_o}^\kappa Q_{J_s}^\kappa \rangle$  (where  $\kappa = 0.5$  or  $\kappa = 1.0$  and is the same in both hemispheres in this case) varies as a function of BTAG cut as shown in Figure 7.14 (the first bin is filled before vertexing or any BTAG cuts are performed and the second bin shows only the effect of vertexing cuts).

There are two reasons for the variation with BTAG cut :

- (1) The flavour composition is changing as a function of BTAG cut, as shown in Figure 4.10. As the jet-charge for  $u$  quarks is higher than that for  $c$  and  $b$  quarks, the value of  $\langle -Q_{J_o}^\kappa Q_{J_s}^\kappa \rangle$  tends to decrease as the  $uds$  contamination decreases with increasing BTAG cut.
- (2) The BTAG cut preferentially selects events with higher multiplicities and this affects the value of the jet-charges as explained in Section 7.2. This causes individual contributions from each flavour to vary with BTAG cut.

The value of  $\langle -Q_{J_o}^\kappa Q_{J_s}^\kappa \rangle$  after a BTAG cut in bin  $i$  is written as :

$$\begin{aligned} \langle -Q_{J_o}^\kappa Q_{J_s}^\kappa \rangle (i) &= \mathcal{P}_b(i) \langle -Q_{J_o}^\kappa Q_{J_s}^\kappa \rangle_b (i) + \mathcal{P}_c(i) \langle -Q_{J_o}^\kappa Q_{J_s}^\kappa \rangle_c (i) \\ &+ \mathcal{P}_{uds}(i) \langle -Q_{J_o}^\kappa Q_{J_s}^\kappa \rangle_{uds} (i) \end{aligned} \quad (7.6)$$

where  $\mathcal{P}_f(i)$  is the purity for flavour  $f$  at a BTAG cut  $i$ .

The contributions from each flavour vary due to the effect of the cut as described in (2) above. The variation of  $\langle -Q_{J_o}^\kappa Q_{J_s}^\kappa \rangle$  for each flavour is shown in

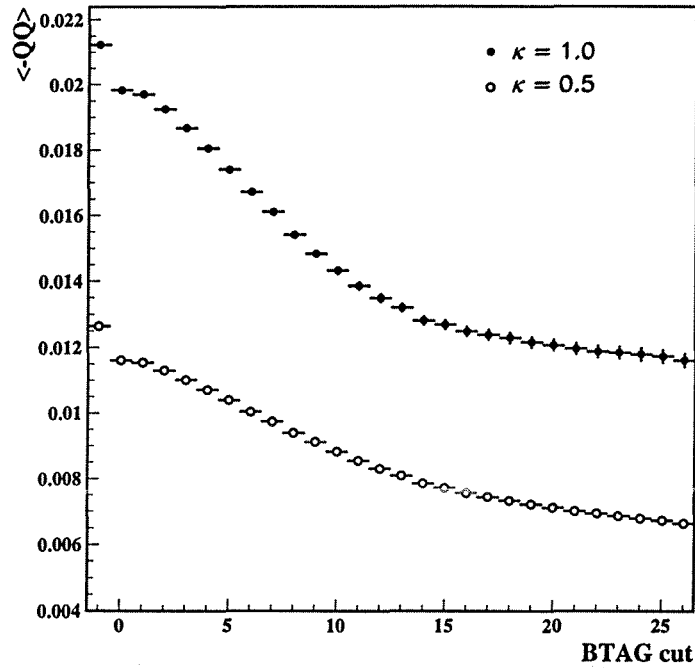


Figure 7.14: Variation in data of  $\langle -Q_{j_o}^\kappa Q_{j_s}^\kappa \rangle$  as a function of BTAG cut for  $\kappa = 1.0$  and  $\kappa = 0.5$  (suppressed zero).

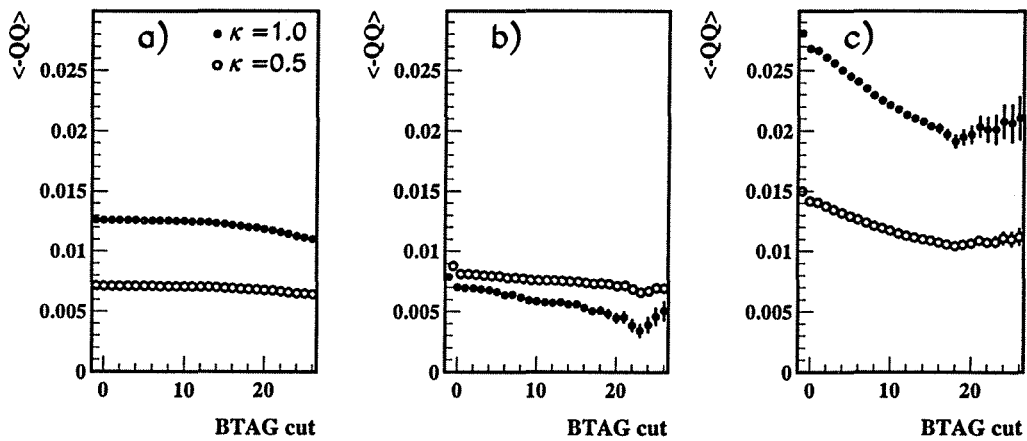


Figure 7.15: Variation of  $\langle -Q_{j_o}^\kappa Q_{j_s}^\kappa \rangle$  for (a)  $b$  events, (b)  $c$  events and (c)  $uds$  events for  $\kappa = 0.5$  and  $\kappa = 1.0$ .

Figure 7.15 for Monte Carlo events and is accounted for in the fit. It is convenient to express the variation caused by the BTAG algorithm as a correction,  $\text{corr}_f(i)$ , relative to the first bin, which is filled before the vertexing algorithm or any BTAG



cut is applied :

$$\text{corr}_f^\kappa(i) = \langle -Q_{J_o}^\kappa Q_{J_s}^\kappa \rangle_f(i) - \langle -Q_{J_o}^\kappa Q_{J_s}^\kappa \rangle_f(1) \quad (7.7)$$

Equation (7.6) can then be rewritten as :

$$\begin{aligned} \langle -Q_{J_o}^\kappa Q_{J_s}^\kappa \rangle(i) = & \mathcal{P}_b(i) [\langle -Q_{J_o}^\kappa Q_{J_s}^\kappa \rangle_b(1) + \text{corr}_b^\kappa(i)] + \\ & \mathcal{P}_c(i) [\langle -Q_{J_o}^\kappa Q_{J_s}^\kappa \rangle_c(1) + \text{corr}_c^\kappa(i)] + \\ & \mathcal{P}_{uds}(i) [\langle -Q_{J_o}^\kappa Q_{J_s}^\kappa \rangle_{uds}(1) + \text{corr}_{uds}^\kappa(i)] \end{aligned} \quad (7.8)$$

In the first BTAG bin, the two hemispheres of the event are equivalent since no vertexing or tagging has been done and so :

$$\langle -Q_{J_o}^\kappa Q_{J_s}^\kappa \rangle_f(1) = \langle Q_f^\kappa \rangle^2 + \text{cov}(Q_{f_o}^\kappa, Q_{f_s}^\kappa) \quad (7.9)$$

where  $\langle Q_f^\kappa \rangle$  is the time-integrated, average jet-charge for flavour  $f$  before vertexing or  $b$  tagging and  $\text{cov}(Q_{f_o}^\kappa, Q_{f_s}^\kappa)$  is the covariance between the same and opposite side jet-charges for flavour  $f$  and is taken from Monte Carlo simulation.

Hence by fitting data distributions of  $\langle -Q_{J_o}^{1.0} Q_{J_s}^{1.0} \rangle$  and  $\langle -Q_{J_o}^{0.5} Q_{J_s}^{0.5} \rangle$  as a function of BTAG cut, it is possible to extract the values for the time-integrated average jet-charges,  $\langle Q_b^\kappa \rangle$ ,  $\langle Q_c^\kappa \rangle$  and  $\langle Q_{uds}^\kappa \rangle$  ( $\kappa = 0.5, 1.0$ ). The  $\kappa = 0.5$  and  $\kappa = 1.0$  distributions are fitted simultaneously in order to take account of correlations between them.

### Treatment of Correlations

There are several sources of correlation which must be treated carefully in the fit. Different BTAG bins are statistically correlated since, for example, all events in bin  $j$  are also contained in bin  $i$  where  $i < j$ . The covariance between BTAG bins  $i$  and  $j$  ( $i < j$ ) of the  $\langle -Q_{J_o}^\kappa Q_{J_s}^\kappa \rangle$  versus BTAG plot is given by<sup>1</sup> :

$$\text{cov}(i^\kappa, j^\kappa) = \frac{N_j}{N_i} \sigma^2(j) \quad (7.10)$$

where  $\sigma^2(j)$  denotes the error on  $\langle -Q_{J_o}^\kappa Q_{J_s}^\kappa \rangle(j)$  and  $N_i$  is the number of events passing a cut value in bin  $i$ . It can be seen that the covariance between nearby bins is large ( $N_j \approx N_i$ ) and decreases as the number of shared events decreases.

In addition, there are large correlations ( $\sim 85\%$ ) between  $\langle -Q_{J_o}^{0.5} Q_{J_s}^{0.5} \rangle(i)$  and  $\langle -Q_{J_o}^{1.0} Q_{J_s}^{1.0} \rangle(i)$  since these products use much of the same information. The covariance between bin  $i$  of the  $\kappa = 0.5$  distribution and bin  $i$  of the  $\kappa = 1.0$  distribution is given by [64] :

$$\text{cov}(i^{0.5}, i^{1.0}) = \frac{1}{N_i} \left[ \langle Q_{J_o}^{0.5} Q_{J_s}^{0.5} Q_{J_o}^{1.0} Q_{J_s}^{1.0} \rangle(i) - \langle -Q_{J_o}^{0.5} Q_{J_s}^{0.5} \rangle(i) \langle -Q_{J_o}^{1.0} Q_{J_s}^{1.0} \rangle(i) \right] \quad (7.11)$$

<sup>1</sup>For a decreasing function.

and the covariance between bin  $i$  of the  $\kappa = 0.5$  distribution and bin  $j$  of the  $\kappa = 1.0$  distribution is given by :

$$\text{cov}(i^{0.5}, j^{1.0}) = \frac{N_j}{N_i} \text{cov}(j^{0.5}, j^{1.0}) \quad (7.12)$$

These covariances are calculated from data. A schematic diagram of the data covariance matrix is shown in Figure 7.16. A similar treatment is used in [53].

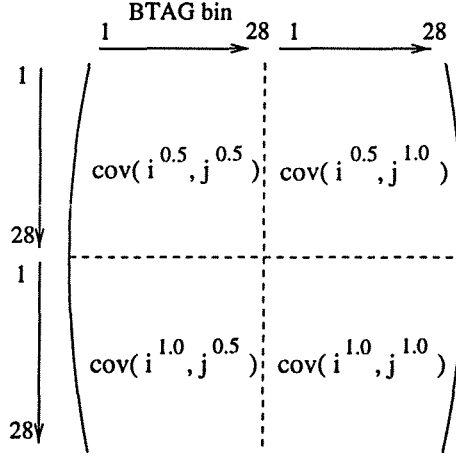


**Figure 7.16:** Schematic diagram showing the form of the covariance matrix used in the fit for  $\langle Q_b^\kappa \rangle$ ,  $\langle Q_c^\kappa \rangle$  and  $\langle Q_{uds}^\kappa \rangle$  ( $\kappa = 0.5, 1.0$ ). Details are given in the text.

The covariances for the Monte Carlo correction factors,  $\text{corr}_f$ , are calculated in the same way as described above and are used to construct a covariance matrix for the ‘theory’ prediction given in Equation (7.8). The purities,  $\mathcal{P}_f(i)$ , are taken from Monte Carlo simulation and their errors are taken as  $\sigma_\epsilon(i)/\epsilon(i)$ , as described in Section 4.6, where  $\epsilon(i)$  is the efficiency for a BTAG cut in bin  $i$  and  $\sigma_\epsilon(i)$  is the difference in tagging efficiencies between data and Monte Carlo for that BTAG cut. Purity errors are included in the diagonal terms of the theory covariance matrix.

A minimum  $\chi^2$  fit is performed by varying the values of the six average jet-charges :  $\langle Q_b^\kappa \rangle$ ,  $\langle Q_c^\kappa \rangle$  and  $\langle Q_{uds}^\kappa \rangle$  ( $\kappa = 0.5, 1.0$ ). This fit forms part of the global  $\Delta m_d$  fit as described in the next section.

The  $\chi^2$  sum runs over all bins in both the  $\langle -Q_{J_o}^{0.5} Q_{J_s}^{0.5} \rangle$  and  $\langle -Q_{J_o}^{1.0} Q_{J_s}^{1.0} \rangle$  distributions :

$$\chi_{\text{BTAG}}^2 = \sum_{ij=1,56} \Delta_i \sigma_{ij}^{-1} \Delta_j \quad (7.13)$$

where  $\sigma_{ij}$  is the sum of data and theory covariance matrices and has the form shown in Figure 7.16 and  $\Delta_i$  is the difference between the data value in bin  $i$  and the theory value predicted by Equation (7.8). Results from this fit are presented along with the  $\Delta m_d$  results in Section 7.6.

## 7.4 Fitting for $\Delta m_d$

The charge correlation in a reconstructed proper time bin  $j$  is given by a weighted sum of contributions from the various  $b$  hadron classes and from charm and light-quark backgrounds :

$$\langle -Q_{J_o}^{0.5} Q_{J_s}^{1.0} \rangle_j = \frac{\mathcal{P}_b \sum_{class} F_j^{class} \langle -QQ \rangle_j^{class} + \mathcal{P}_c F_j^c \langle -QQ \rangle_j^c + \mathcal{P}_{uds} F_j^{uds} \langle -QQ \rangle_j^{uds}}{\mathcal{P}_b \sum_{class} F_j^{class} + \mathcal{P}_c F_j^c + \mathcal{P}_{uds} F_j^{uds}} \quad (7.14)$$

The fraction of events of a particular class, reconstructed in bin  $j$ ,  $F_j^{class}$ , is calculated in the same way as in the fit for the inclusive  $b$  lifetime, using Equations (6.16)–(6.18), with the modification that the fraction is calculated separately for each  $b$  hadron class. The time-dependent fractions for each class are given in the second column of Table 5.2. For example, the true fraction of mixed  $B_d$  events in bin  $i$  is given by :

$$TT_i = \int_{\text{true bin } i} f_d e^{-t/\tau_{B_d}} \frac{(1 - \cos \Delta m_d t)}{2\tau_{B_d}} dt \quad (7.15)$$

These true fractions for each class are then folded with resolution matrices and modified by vertexing and BTAG efficiencies as in the inclusive  $b$  lifetime fit. Separate resolution folding matrices and efficiency corrections are used for the four different  $b$  hadron *types* (that is,  $B^\pm, B_d^0, B_s^0$ , baryons) to take into account differences due to different decay modes. Since the decay modes of  $B_s$  mesons are poorly known, the effect of using the  $B_d$  resolution matrix and efficiency corrections to calculate the  $B_s$  distributions is used as an estimate of its systematic error. The reconstructed proper time distributions for backgrounds,  $F_j^c$  and  $F_j^{uds}$ , are taken from the Monte Carlo, as in the lifetime fit.

The charge contribution from each  $b$  hadron class in reconstructed proper time bin  $j$  is given by a modified version of Equation (7.3) which takes into account the multiplicity variation and effects of  $b$  tagging :

$$\langle -QQ \rangle_j^{class} = \left[ \langle Q_b^{0.5} \rangle + \text{CBTAG}_b^{opp} \right] \left[ \langle Q_{class}^{1.0} \rangle + \text{corr}_{mult}^{class}(j) \right] + \text{covariance term} \quad (7.16)$$

Where  $\langle Q_b^{0.5} \rangle$  is the time-integrated, average  $b$  jet-charge ( $\kappa = 0.5$ ) before vertexing or  $b$  tagging and  $\text{CBTAG}_b^{opp}$  is a correction factor, taken from Monte Carlo, to account for the effect on the ‘opposite’ hemisphere jet-charge, of the vertexing algorithm and BTAG cut which is being used.  $\langle Q_{class}^{1.0} \rangle$  is the time-integrated jet-charge for this  $b$  hadron class after the effects of  $b$  tagging. A bin dependent correction,  $\text{corr}_{mult}^{class}(j)$ , takes into account the variation in jet-charges with reconstructed proper time due to the varying multiplicity (Section 7.2). The covariance terms are taken from Monte Carlo. The contributions to the charge correlation from backgrounds are constructed in a similar way. The contribution for  $c$  events is given by :

$$\langle -QQ \rangle_j^c = \left[ \langle Q_c^{0.5} \rangle + \text{CBTAG}_c^{opp} \right] \left[ \langle Q_c^{1.0} \rangle + \text{CBTAG}_c^{same} + \text{corr}_{mult}^c(j) \right] + \text{covariance term} \quad (7.17)$$

and similarly for  $uds$  events. The bin dependent multiplicity corrections,  $corr_{mult}^{c,uds}$ , for backgrounds are taken from Monte Carlo simulation and the effect of setting them to zero is taken into account as an estimate of their systematic error (Section 7.7).

## 7.5 Parameters and Constraints in the $\Delta m_d$ Fit

Parameter	Constraint
$\Delta m_d$	free
$\langle Q_b^{0.5} \rangle, \langle Q_c^{0.5} \rangle, \langle Q_{uds}^{0.5} \rangle$	free
$\langle Q_b^{1.0} \rangle, \langle Q_c^{1.0} \rangle, \langle Q_{uds}^{1.0} \rangle$	free
$\tau_{B_d}$	$1.56 \pm 0.06$ ps
$\tau_{B_s}$	$1.61 \pm 0.10$ ps
$\tau_{\Lambda}$	$1.14 \pm 0.08$ ps
$\tau_{B^+}$	$1.62 \pm 0.06$ ps
$\tau_b$	$1.570 \pm 0.014$ ps
$f_{\Lambda}$	$0.101 \pm 0.031$
$f_s$	$0.109 \pm 0.013$
$\langle Q_{\Lambda}^{1.0} \rangle$	$0.0317 \pm 10\%$
$\langle Q_{B^{\pm}}^{1.0} \rangle$	$0.1506 \pm 2\%$
$\langle Q_{B_d^{unmix}}^{1.0} \rangle$	$0.1195 \pm 2\%$
$\langle Q_{B_d^{mix}}^{1.0} \rangle$	$-0.0576 \pm 2\%$
$\langle Q_{B_s^{unmix}}^{1.0} \rangle$	$0.0696 \pm 10\%$
$\langle Q_{B_s^{mix}}^{1.0} \rangle$	$0.0076 \pm 10\%$
$\mathcal{P}_b$	$(87.5 \pm 1.2)\%$
$\mathcal{P}_c$	$(9.8 \pm 1.8)\%$

Table 7.1: Parameters and constraints used in the  $\Delta m_d$  fit.

In fitting to extract the values of  $\Delta m_d$ , systematic errors are reduced as far as possible by performing a multi-parameter fit to both the charge correlation function and the  $\langle -Q_{J_o}^{\kappa} Q_{J_s}^{\kappa} \rangle$  versus BTAG distributions, using many constraints from data. The parameters and constraints used in the fit are given in Table 7.1. They fall into the following categories :

- **Free Parameters** :  $\Delta m_d$  and the values of the time-integrated, average jet-charges,  $\langle Q_b^{\kappa} \rangle, \langle Q_c^{\kappa} \rangle$  and  $\langle Q_{uds}^{\kappa} \rangle$  ( $\kappa = 0.5, 1.0$ ), are free parameters in the fit.
- **$b$  Hadron Jet-Charges** : The time-integrated jet-charges for the various  $b$  hadron classes,  $\langle Q_{class}^{1.0} \rangle$ , are varied in the fit about a central Monte Carlo value within the Gaussian constraints given in Table 7.1. The average  $b$

jet-charge  $\langle Q_b^{1.0} \rangle$ , in data, agrees with the Monte Carlo value to a precision of 2%. This is used as a guide in assigning the constraints in Table 7.1. The jet-charges for  $B^\pm$  and  $B_d$  mesons are allowed to vary within a 2% constraint of their Monte Carlo values, while the more poorly known  $B_s$  and  $b$  baryon jet-charges are assigned a conservative 10% constraint. An additional constraint is imposed requiring that the weighted sum of the  $b$  hadron jet-charges is consistent with the time-integrated average  $b$  jet-charge ( $\kappa = 1.0$ ) for the BTAG cut value which is used ;

$$\begin{aligned} \left[ \langle Q_b^{1.0} \rangle + \text{CBTAG}_b^{\text{same}} \right] (\pm 3\%) = & f_u \langle Q_{B^\pm}^{1.0} \rangle + f_\Lambda \langle Q_\Lambda^{1.0} \rangle + \\ & f_d (1 - \chi_d) \langle Q_{B_d^{\text{unmix}}}^{1.0} \rangle + f_d \chi_d \langle Q_{B_d^{\text{mix}}}^{1.0} \rangle + \\ & f_s (1 - \chi_s) \langle Q_{B_s^{\text{unmix}}}^{1.0} \rangle + f_s \chi_s \langle Q_{B_s^{\text{mix}}}^{1.0} \rangle \end{aligned} \quad (7.18)$$

where the 3% constraint is taken from [53] as being the combined statistical and systematic uncertainty on  $\langle Q_b^{1.0} \rangle$ . In this way, the absolute values of all jet-charges are allowed to vary in the fit, taking only algorithm dependent corrections and covariance terms from Monte Carlo simulation.

- **Lifetimes** : The  $b$  hadron lifetimes are varied within Gaussian constraints around world average values [2] given in Table 7.1 whilst also requiring that their weighted average is consistent with the measurement of the inclusive  $b$  lifetime  $\tau_b$  given in Section 6.5.5 :

$$\tau_b (\pm \sigma_{\tau_b}) = f_d \tau_{B_d} + f_u \tau_{B^\pm} + f_s \tau_{B_s} + f_\Lambda \tau_\Lambda \quad (7.19)$$

- **$b$  Hadron Fractions** : The production fractions,  $f_u$  and  $f_d$ , are expressed in terms of the  $B_s$  fraction,  $f_s$ , and the baryon fraction  $f_\Lambda$  :

$$f_d = f_u = \frac{1}{2}(1 - f_s - f_\Lambda) \quad (7.20)$$

The fractions  $f_s$  and  $f_\Lambda$  are allowed to vary within Gaussian constraints [11] and are also constrained by Equations (7.18) and (7.19).

- **Purities** : The  $b$  and  $c$  purities are constrained within errors to the values obtained in the lifetime fit (Section 6.5.5).

The  $B_s$  oscillation frequency,  $\Delta m_s$ , is fixed at  $\infty$  and the possibility of non-maximal  $B_s$  mixing is taken into account in the systematic error.

In summary, a multi-parameter fit is performed simultaneously to the charge correlation function and the  $\langle -Q_{j_o}^\kappa Q_{j_s}^\kappa \rangle$  versus BTAG distributions by varying the parameters in Table 7.1 and minimising the combined  $\chi^2$  term :

$$\chi^2 = \chi_{\text{BTAG}}^2 + \chi_{\Delta m_d}^2 \quad (7.21)$$

where  $\chi_{\text{BTAG}}^2$  is defined in (7.13) and  $\chi_{\Delta m_d}^2$  incorporates the difference between the charge correlation in data and the theory prediction given in (7.14) plus additional terms for each of the constraints discussed above. The fit is well constrained since for each parameter that is allowed to vary, an additional constraint is added. The fit is structured such that each of the constrained parameters can be fixed in turn, to assess the individual contributions to the systematic error from each source.

## 7.6 Results

As in the lifetime fit, the fitting procedure is initially applied to the Monte Carlo sample. The result of the fit is shown in Figure 7.17 and gives the value of  $\Delta m_d = 0.465 \pm 0.026 \text{ ps}^{-1}$  with a  $\chi^2/\text{n.d.f}$  of 19/71. This is consistent with the Monte Carlo input value of  $0.467 \text{ ps}^{-1}$ . The fitted lifetimes, jet-charges and

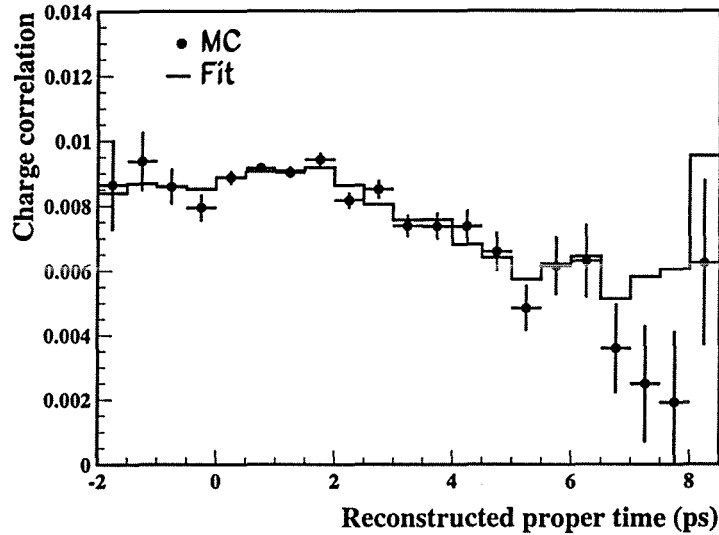


Figure 7.17: Result of the fit to the charge correlation in Monte Carlo simulation.

purities are all consistent with their input values.

The fit to the combined 1991 to 1995 data set gives the result :

$$\Delta m_d = 0.441 \pm 0.026 \text{ (stat.)} \pm 0.029 \text{ (syst.) ps}^{-1}$$

The shape of the time-dependent charge correlation function is shown in Figure 7.18 for large and small binning in reconstructed proper time<sup>2</sup>. The result of the fit is shown as a solid line and the expected distribution for a no-mixing hypothesis is shown as a dotted line. The fitted  $\langle -Q_{J_o}^\kappa Q_{J_s}^\kappa \rangle$  ( $\kappa = 0.5, 1.0$ ) versus BTAG distributions are shown in Figure 7.19 and the average jet-charge results are given in Table 7.2. The results are consistent with previous measurements [53]. The Monte Carlo values for the mean jet-charges are shown for comparison in the third column of Table 7.2. As mentioned previously in Section 7.5, the  $b$  jet-charges in data and Monte Carlo, for  $\kappa = 1.0$ , agree to within 2%.

The fitted values for the constrained parameters are given in the third column of Table 7.4. The fitted values are all consistent with their input values, within the constraints applied. The discussion of the various sources of systematic error is given in the following section.

<sup>2</sup>The result obtained using small binning is compatible within statistical errors.

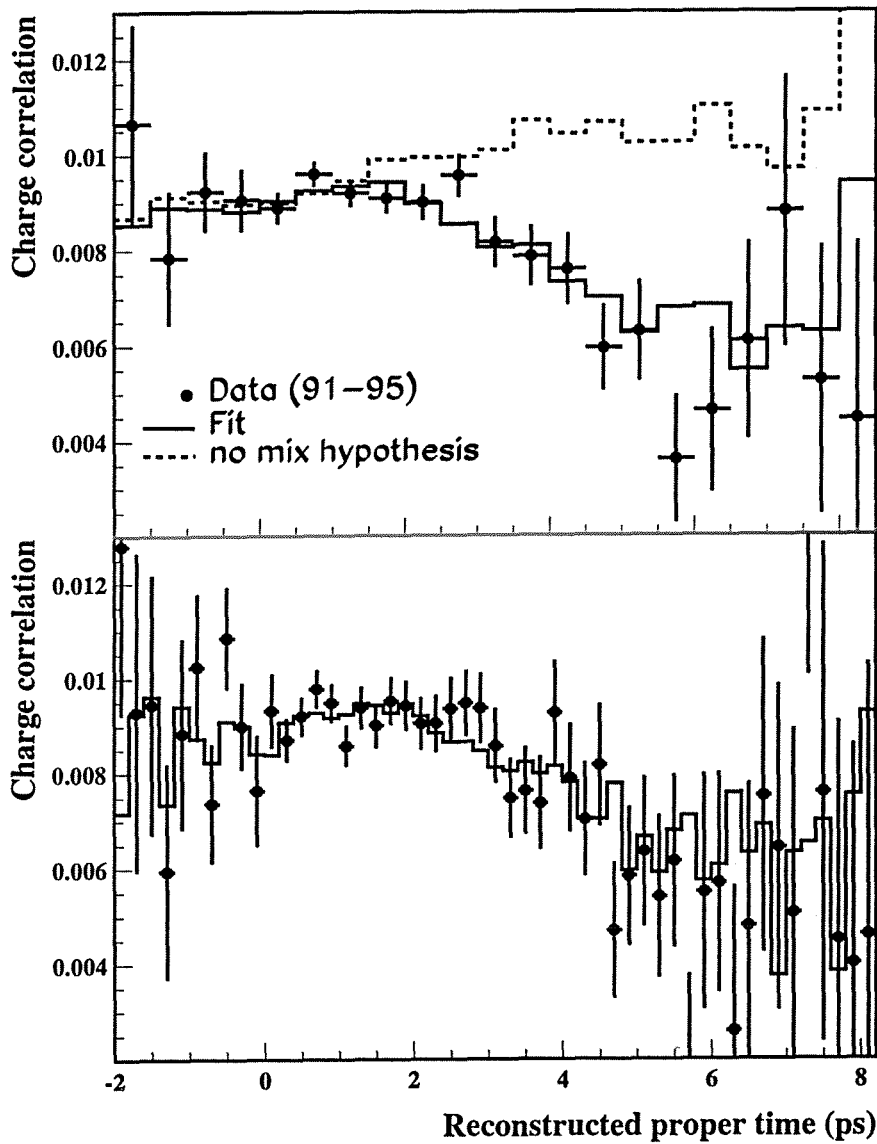


**Figure 7.18:** The charge correlation as a function of measured proper time with the result of the fit shown as the solid line. The no mixing hypothesis is shown as a dotted line (suppressed zero).

The fit is performed for each individual data year as a stability check and the results are given in Table 7.3 and shown in Figure 7.20. The central band on Figure 7.20 indicates the combined value and its full statistical and systematic error.

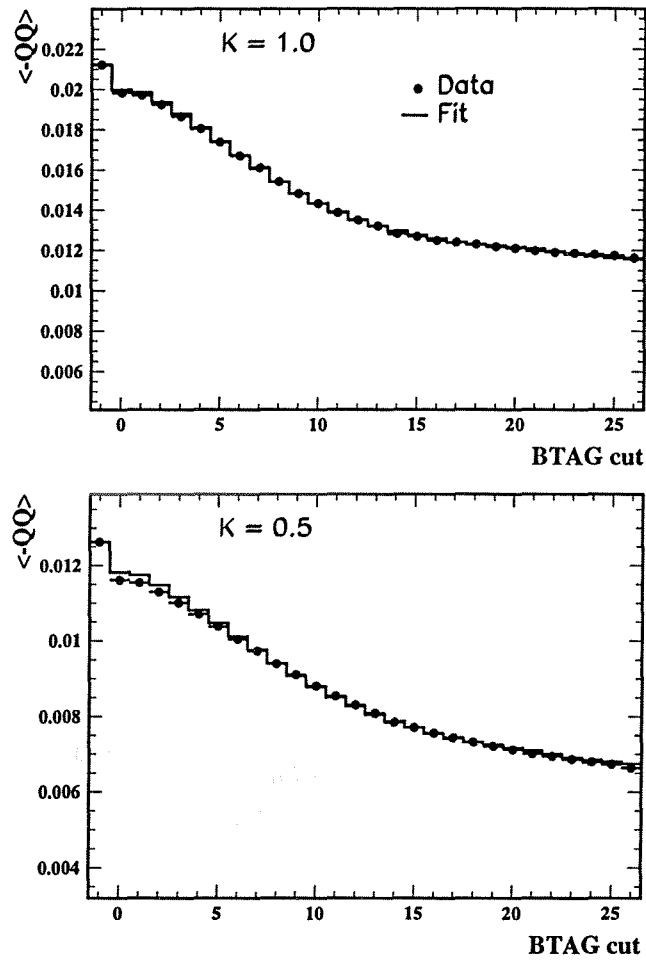


Figure 7.19: The fitted distributions of  $\langle -Q_{J_o}^\kappa Q_{J_s}^\kappa \rangle$  versus BTAG cut, for  $\kappa = 1.0$  and  $\kappa = 0.5$  (suppressed zero).

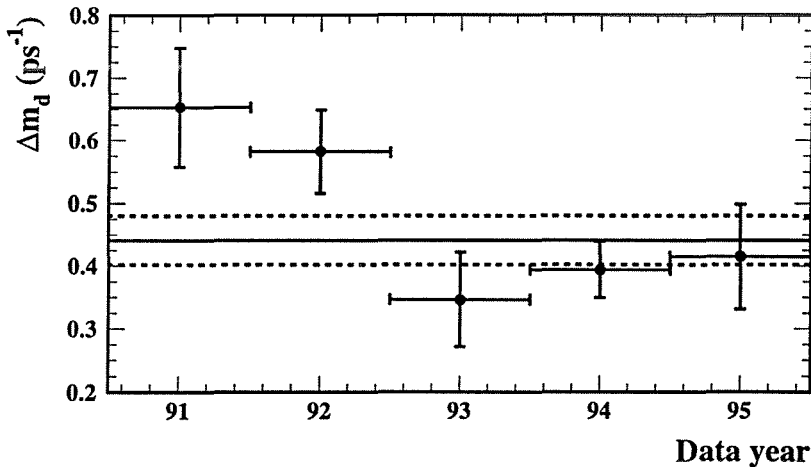
Parameter	Fitted Value	Monte Carlo Value
$\langle Q_b^{0.5} \rangle$	$0.0783 \pm 0.0013$	$0.0760 \pm 0.0002$
$\langle Q_c^{0.5} \rangle$	$0.0786 \pm 0.0080$	$0.0841 \pm 0.0002$
$\langle Q_{uds}^{0.5} \rangle$	$0.1153 \pm 0.0013$	$0.1117 \pm 0.0001$
$\langle Q_b^{1.0} \rangle$	$0.1136 \pm 0.0017$	$0.1112 \pm 0.0003$
$\langle Q_c^{1.0} \rangle$	$0.0888 \pm 0.0129$	$0.0859 \pm 0.0003$
$\langle Q_{uds}^{1.0} \rangle$	$0.1601 \pm 0.0016$	$0.1611 \pm 0.0002$

Table 7.2: Fitted values for  $b$ ,  $c$  and  $uds$  mean jet-charges, for  $\kappa = 0.5$  and  $\kappa = 1.0$ . The Monte Carlo values are shown for comparison.



Year	$\Delta m_d$ ( $\text{ps}^{-1}$ )	$\chi^2/\text{n.d.f}$
1991	$0.653 \pm 0.095$	43/71
1992	$0.582 \pm 0.067$	41/71
1993	$0.347 \pm 0.076$	20/71
1994	$0.394 \pm 0.045$	54/71
1995	$0.415 \pm 0.084$	25/71

**Table 7.3:** Summary of the  $\Delta m_d$  results for the individual data years including their statistical uncertainties, errors arising from correction factors and systematic uncertainties arising from the fitted parameters.



**Figure 7.20:** Summary of the  $\Delta m_d$  fit results for the different data years, indicating their statistical uncertainties and systematic uncertainties arising from the fitted parameters. The value from the fit to the combined data-set is shown as the central band with its full statistical and systematic uncertainty.

## 7.7 Errors on the $\Delta m_d$ Result

In order to determine the purely statistical error on the  $\Delta m_d$  result, all the parameters in Table 7.4 are fixed to their central values and only the free parameters in the upper part of Table 7.1 are allowed to vary.

Contributions to the systematic error are listed in Table 7.4. The systematic error due to each of the constrained parameters is determined by allowing each parameter to vary in turn, along with the free parameters, while fixing all others to their central values, and noting the new error on  $\Delta m_d$ . The systematic error for each parameter is found by subtracting the statistical error in quadrature from the new error which is obtained when that parameter is allowed to vary. The systematic error contributions from the fitted parameters are signed using the correlation matrix returned by the fit and given in Appendix B. Various sources

Parameter	Variation	Fitted Value	$\sigma_{sys}(\text{ps}^{-1})$
$\tau_{B_d}$	$1.56 \pm 0.06$ ps	$1.59 \pm 0.06$ ps	$\mp 0.0045$
$\tau_{B_s}$	$1.61 \pm 0.10$ ps	$1.61 \pm 0.10$ ps	$\mp 0.0022$
$\tau_{\Lambda}$	$1.14 \pm 0.08$ ps	$1.14 \pm 0.08$ ps	$\mp 0.003$
$\tau_{B^+}$	$1.62 \pm 0.06$ ps	$1.60 \pm 0.06$ ps	$\pm 0.004$
$\tau_b$	$1.570 \pm 0.014$ ps	$1.560 \pm 0.043$ ps	$\pm 0.0003$
$f_{\Lambda}$	$0.101 \pm 0.031$	$0.081 \pm 0.021$	$\mp 0.012$
$f_s$	$0.109 \pm 0.013$	$0.106 \pm 0.013$	$\mp 0.0093$
$\langle Q_{\Lambda}^{1,0} \rangle$	$0.0317 \pm 10\%$	$0.0319 \pm 0.0032$	$\pm 0.0025$
$\langle Q_{B^{\pm}}^{1,0} \rangle$	$0.1506 \pm 2\%$	$0.1510 \pm 0.0029$	$\pm 0.012$
$\langle Q_{B_d^{unmix}}^{1,0} \rangle$	$0.1195 \pm 2\%$	$0.1199 \pm 0.0023$	$\pm 0.0063$
$\langle Q_{B_d^{mix}}^{1,0} \rangle$	$-0.0576 \pm 2\%$	$-0.0577 \pm 0.0011$	$\pm 0.0015$
$\langle Q_{B_s^{unmix}}^{1,0} \rangle$	$0.0696 \pm 10\%$	$0.0699 \pm 0.0069$	$\pm 0.004$
$\langle Q_{B_s^{mix}}^{1,0} \rangle$	$0.0076 \pm 10\%$	$0.0076 \pm 0.0008$	$\pm 0.0006$
sample composition	$\mathcal{P}_b = (87.5 \pm 1.2)\%$ $\mathcal{P}_c = (9.8 \pm 1.8)\%$	$(87.4 \pm 1.1)\%$ $(8.9 \pm 1.2)\%$	$\pm 0.004$
$\Delta m_s$	$\infty \rightarrow 6 \text{ ps}^{-1}$		$+0.0001$
set $\mathbf{R}(B_s) = \mathbf{R}(B_d)$			$-0.0022$
$\langle -QQ \rangle^{c,uds}$ time depend.	off		$-0.005$
$\epsilon_{\text{BTAG}}^b$ correction, $\mathcal{C}(j)$	off		$+0.0002$
multiplicity correction			$\pm 0.008$
$b$ fragmentation	$\epsilon_b = 0.0045 \pm 0.0009$		$\mp 0.015$
MC statistics			$\pm 0.001$
Total			$\pm 0.029$

**Table 7.4:** Contributions to the systematic error on the  $\Delta m_d$  result. The upper part of the table corresponds to the fitted parameters and the second column gives the Gaussian constraints which are used. The third column gives the values returned from the fit. The lower part of the table corresponds to ‘fixed’ parameters. The fourth column gives the contribution of each source to the systematic error on  $\Delta m_d$ .

of systematic uncertainty are separated into the following general categories :

- **Lifetimes :** The  $b$  hadron fractions and lifetimes are allowed to vary in the fit within the Gaussian constraints given in Table 7.1, as discussed in Section 7.5. The fit has also been performed using the current world average value of  $\tau_b = 1.549 \pm 0.02$  ps as the constraint in (7.19) instead of the value obtained from the fit to the proper time distribution given in Section 6.5.5. This results in a shift of  $3 \times 10^{-5} \text{ ps}^{-1}$  in the fitted value of  $\Delta m_d$  and hence is safely neglected.

The charged  $B$  lifetime,  $\tau_{B^+}$ , is positively correlated with  $\Delta m_d$  and may be intuitively understood since an increase in  $\tau_{B^+}$  implies a larger fraction

of  $B^\pm$  at long proper times. This would increase the value of the charge correlation at long proper times and so  $\Delta m_d$  must increase to compensate and so fit the data. Similar reasoning explains why  $\tau_{B_d}$ ,  $\tau_{B_s}$  and  $\tau_\Lambda$  are anti-correlated with  $\Delta m_d$ .

- **$b$  Hadron Jet-Charges** : The combined statistical and systematic error on the fitted average  $b$  jet-charge,  $\langle Q_b^{1,0} \rangle$ , is used to constrain the sum of the individual  $b$  hadron components as described in Equation (7.18). The errors ascribed to the individual  $b$  hadron jet-charges account for possible conspiracies between the less well-known  $b$  hadron classes such as  $B_s$  and  $b$  baryons. The systematic error arising from the  $B^\pm$  jet-charge is relatively large since this jet-charge shows the largest dependence on multiplicity and hence the largest variation with reconstructed proper time (Figures 7.2 and 7.9). All of the  $b$  hadron jet-charges are positively correlated with  $\Delta m_d$  since an increase in any of the jet-charges means that  $\Delta m_d$  has to increase in order to fit the data.
- **Sample Composition** : The values of  $\mathcal{P}_b$  and  $\mathcal{P}_c$  obtained from the fit to data for  $\tau_b$  are used together with their associated errors. The  $b$  hadron fractions,  $f_s$  and  $f_\Lambda$ , are varied within Gaussian constraints [11]. The systematic error associated with the  $b$  baryon fraction is relatively large since it is poorly known and, although the baryon fraction itself is small, a variation in  $f_\Lambda$  implies a variation in  $f_d$  and  $f_u$  via Equation (7.20).
- **$b$  Fragmentation** : The effect of varying the  $b$  fragmentation is studied in two ways. These are : (a) varying the fragmentation function by re-weighting the Monte Carlo, using the range of  $\epsilon_b$  values discussed in Section 6.3.5 and (b) using the  $B_d$  folding matrix and efficiency corrections in calculating the  $B_s$  distributions, to take into account the current lack of knowledge about  $B_s$  decays.
- **Multiplicity Corrections** : Errors associated with corrections to the  $b$  hadron jet-charges,  $corr_{mult}^{class}(t_{reco})$ , are discussed in Section 7.2 and are passed through, bin-by-bin, in  $t_{reco}$ .
- **Background Jet-Charges** : The effect of the corrections applied to the  $uds$  and  $c$  jet-charges to take into account their multiplicity induced time-dependence is estimated by turning the time-dependence on and off in the fit and observing the effect on the value of  $\Delta m_d$ .
- **$\Delta m_s$**  : The effects of varying the input value of  $\Delta m_s$  between  $\infty$  and  $6 \text{ ps}^{-1}$  is taken as an additional systematic error.

Allowing all parameters to vary simultaneously in the fit gives an error of  $\pm 0.035$  on the value of  $\Delta m_d$ . This corresponds to a statistical error of  $\pm 0.026$  in quadrature with an error of  $\pm 0.023$  arising from the fitted parameters, corresponding to the sum of the contributions from the fitted parameters listed in the upper part of Table 7.4.

The dominant systematic uncertainty is currently due to the knowledge of the fragmentation function for  $b$  quarks. The relative fractions of  $b$  hadrons assumed in the sample, and the average jet-charge for  $B^\pm$  mesons are also significant.

The analysis is repeated without applying the revertexing algorithm after the initial QVRSCH vertexing. This is done in order to check that no bias has been introduced by revertexing. Based upon the 1992 data alone, the value obtained without revertexing is  $\Delta m_d^{novervx} = 0.593 \pm 0.074 \text{ ps}^{-1}$  which is consistent with the nominal 1992 value given in Table 7.3. The gain in signal/noise obtained using the re-vertexing procedure is approximately equal to that expected from Figure 6.4.

As a further cross check the fit is performed for BTAG cuts of 15, 20 and 25, giving the results shown in Figure 7.21 (errors shown are due to statistical uncertainties and systematic uncertainties arising from the fitted parameters). The results are stable as expected, since the systematic error due to the flavour composition is small.

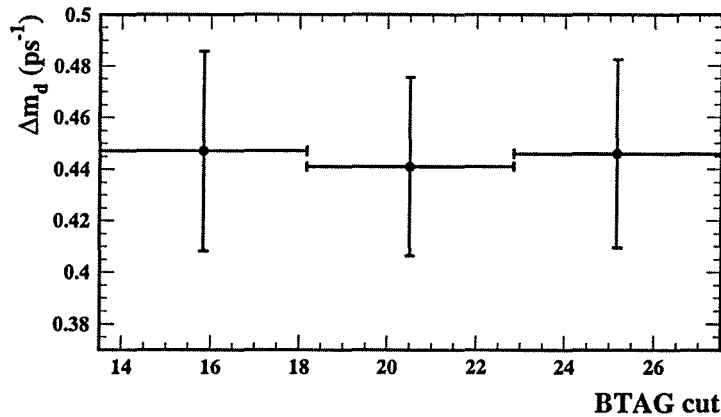


**Figure 7.21:**  $\Delta m_d$  dependence on the BTAG cut applied. The errors indicate the statistical uncertainties and systematic uncertainties from the fitted parameters.

## 7.8 Comparison with Previous Measurements

The value for  $\Delta m_d$  obtained using this ( $Q_{Jet}/Q_{Jet}$ ) method is compared with other measurements from ALEPH in Table 7.5, where (prel.) denotes the most recent preliminary results. Combining the result obtained in this analysis with the three other most recent results in the lower part of Table 7.5, assuming statistical

Method	No. $Z^0$ ( $\times 10^6$ )	$\Delta m_d$ ( $\text{ps}^{-1}$ )
Dileptons [19]	0.98	$0.51^{+0.07}_{-0.06}$ (stat.) $^{+0.11}_{-0.10}$ (syst.)
$D^*/\text{lepton}$ [26]	0.9	$0.52^{+0.10}_{-0.11}$ (stat.) $^{+0.04}_{-0.03}$ (syst.)
(prel.) Lepton/ $Q_{Jet}$ [20]	3.3	$0.396^{+0.046}_{-0.044}$ (stat.) $^{+0.026}_{-0.028}$ (syst.)
(prel.) $D^*/l, Q_{Jet}$ [20]	3.3	$0.482 \pm 0.044$ (stat.) $\pm 0.024$ (syst.)
(prel.) Dileptons [20]	3.3	$0.426 \pm 0.039$ (stat.) $\pm 0.052$ (syst.)
(prel.) $Q_{Jet}/Q_{Jet}$	4.1	$0.441 \pm 0.026$ (stat.) $\pm 0.029$ (syst.)

Table 7.5: Measurements of  $\Delta m_d$  by different methods used by ALEPH.

correlations of 20% with the lepton analyses and 5% with the  $D^*/Q_{Jet}$  analysis [65], yields the following preliminary ALEPH result :

$$\Delta m_d(\text{combined}) = 0.434 \pm 0.029 \text{ ps}^{-1}$$

For comparison, the combined ALEPH result, excluding the result from this analysis, is  $\Delta m_d(\text{combined}) = 0.436 \pm 0.033 \text{ ps}^{-1}$ .

The ALEPH results for  $\Delta m_d$  (including the result from this analysis) are shown in Figure 7.22 along with recent results from the other LEP experiments [66]. The LEP average value is shown as a central band on the plot.

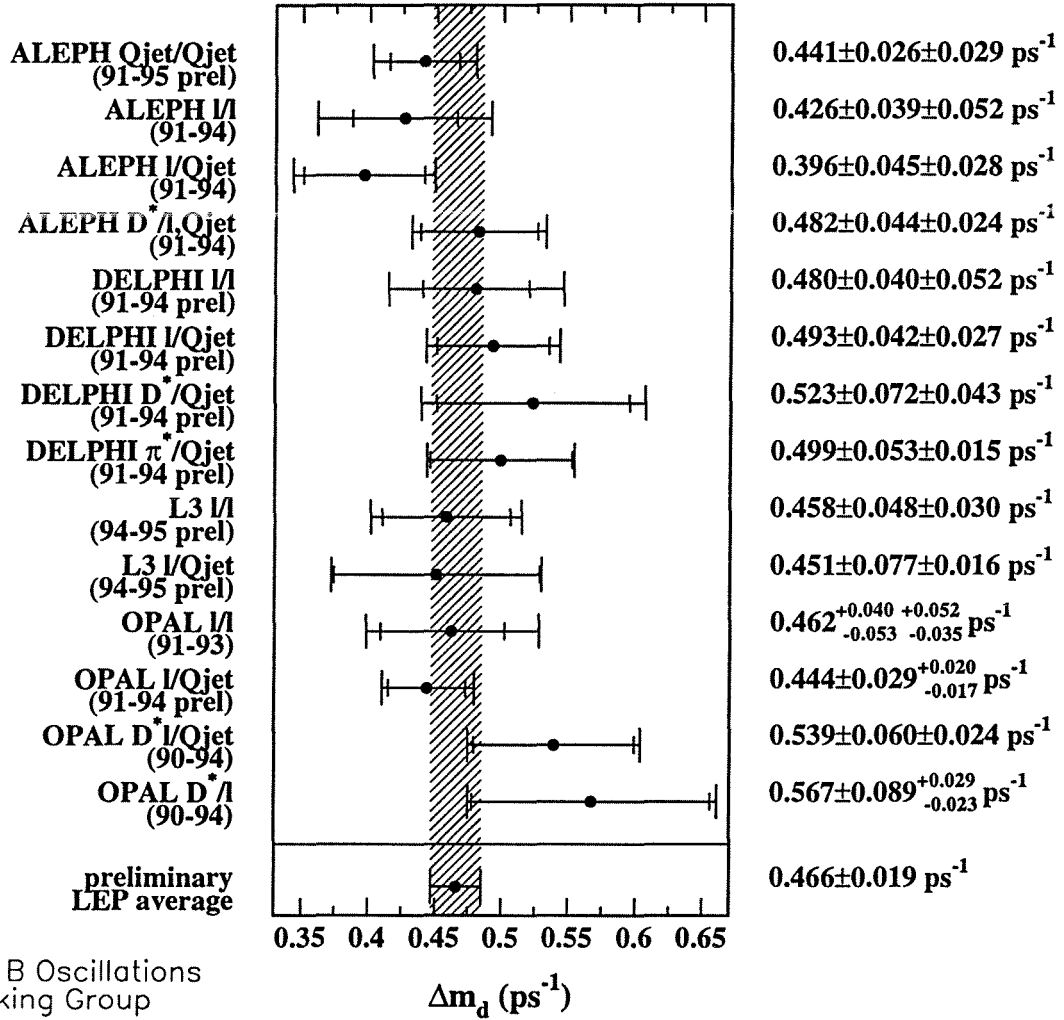


Figure 7.22: Individual and combined measurements of  $\Delta m_d$  at LEP. The error bars on the individual measurements indicate the size of the statistical error and total error on the result.



# Chapter 8

## Summary and Conclusions

The time dependence of  $B_d^0 - \bar{B}_d^0$  oscillations has been studied using an inclusive double jet-charge method, using data taken with the ALEPH detector between 1991 and 1995. The method relies on the fact that the jet-charge for hemispheres containing mixed mesons differs from the jet-charge for hemispheres containing unmixed mesons, as described in Chapter 5. Since no lepton is required in the event, and no exclusive cuts are made, the double jet-charge method benefits from having at least five times the statistics of existing analyses.

The inclusive nature of this analysis places demands on the control of systematic uncertainties arising from backgrounds and detector resolution, which are estimated using the Monte Carlo. In order to keep discrepancies between data and Monte Carlo to a minimum and hence reduce systematic errors, a smearing procedure was developed and applied to the Monte Carlo (Chapter 4).

An inclusive vertexing technique followed by a re-vertexing procedure is used to reconstruct the decay length of the  $b$  hadron. Track probability weights are calculated, based on the significance of the track to the primary and secondary vertices and the rapidity of the track. These weights are used in the reconstruction of the charged part of the  $b$  hadron momentum. The decay length and momentum are used to calculate the proper lifetime of the  $b$  hadron. The proper time resolution is taken into account in the fitting procedure by means of folding matrices. Biases to the proper time distribution arising from the vertexing procedure and  $b$  tagging cut are also taken into account in the fitting procedure and are checked using the data as much as possible (Chapter 6).

### Measurement of the Inclusive $b$ Lifetime

From around 4.1 million hadronic  $Z^0$  decays collected during 1991–1995, a total of 423169 events pass all vertexing and  $b$  tagging cuts. A fit to the reconstructed proper time distribution for this data sample gives a result for the inclusive  $b$  lifetime :

$$\tau_b = 1.570 \pm 0.004(\text{stat.}) \pm 0.013(\text{syst.}) \text{ ps}$$

The systematic error is dominated by uncertainties in the  $b$  fragmentation function. The fit quality is good and the result is in agreement with the world



average value of  $(1.549 \pm 0.020)$  ps, indicating that the effects of vertexing,  $b$  tagging and detector resolution are well modelled in the fit.

### Measurement of the $B_d^0 - \bar{B}_d^0$ Oscillation Frequency

A multi-parameter fit has been constructed in order to extract the value of  $\Delta m_d$ , using constraints from data where possible in order to control systematic errors. Variations in the jet-charges due to the effects of the reconstruction algorithms are well understood (Section 7.2) and have been included in the fitting procedure. The average values for all jet-charges are allowed to vary in the fit, taking only the algorithm dependent corrections and covariance terms from the Monte Carlo.

The fit to the 1991–1995 data sample gives the  $\Delta m_d$  result :

$$\Delta m_d = 0.441 \pm 0.026 \text{ (stat.)} \pm 0.029 \text{ (syst.) ps}^{-1}$$

The dominant contributions to the systematic uncertainty are due to the knowledge of the fragmentation function for  $b$  quarks, the relative fractions of  $b$  hadrons assumed in the sample, and the average jet-charge for  $B^\pm$  mesons. The result is in good agreement with the world average value [11] of  $\Delta m_d = 0.459 \pm 0.018 \text{ ps}^{-1}$ .

### Future Developments

The tools developed for this analysis have not yet been exploited to their full potential and hence it is possible that improvements can be made in the sensitivity to  $B_d$  and  $B_s$  oscillations and in the control of systematic errors. The methods used here can also be extended to enable new measurements to be made. Future developments can be made in the following areas :

- It is possible to improve the statistical sensitivity to both  $B_d$  and  $B_s$  oscillations by making use of the vertex charge described in Section 6.3.2 to calculate a probability weight for each hemisphere which can be used to enhance the contribution from neutral  $B$  mesons.
- The vertex charge can also be used to obtain samples of events with varying  $b$  hadron compositions. Performing the lifetime fit on the various samples will allow tighter constraints to be placed on the individual  $b$  hadron lifetimes.
- The analysis has yet to be optimised to give maximum sensitivity to  $B_s$  oscillations. The large event sample means that tighter vertex quality cuts can be implemented, albeit at the expense of a drop in efficiency, in order to obtain improved proper time resolution.

# Appendix A

## Study of the VDET Laser Data

### A.1 Introduction

The purpose of the VDET Laser Alignment System is to help maintain the tracking quality by monitoring relative movements between the VDET and the ITC. The laser system provides online information to the shift crew and laser events are also written to tape to allow further analysis to be carried out. In this section, results from the analysis of VDET laser data taken during 1994 are presented [67]. This analysis was motivated by a deterioration in the tracking quality which was discovered after the ALEPH detector was opened for maintenance in June 1994, around run number 26600. One possible suggestion for the cause of this deterioration was that the VDET had moved [68]. A total of 650 runs were analysed from June to November 1994 and the results are presented.

### A.2 Outline of Laser Alignment System

A diagram of the system is shown in Figure A.1. Two kapton foils are glued onto the inner carbon-fibre tube of the ITC, each foil covering a half cylinder. Six sets of pairs of prisms are mounted on each foil, three sets at each end giving twelve pairs in total. In each set, one of the prisms delivers light perpendicular to the wafer and the other is orientated to deliver light at a  $30^\circ$  angle of incidence. Thus, for example, any radial motion of the wafers would cause changes in the distance between the two spots. There are two semiconductor infrared lasers, one at each end of the detector, and light is transmitted to the prism sets via optical fibres. The lasers are fired by an oscillator which sends an independent signal to the ALEPH trigger at the same time. There are approximately 100 laser events per run. Light is pulsed onto the end wafers, 1 and 4, of faces 1, 4, 6, 9, 11 and 13 of the outer layer. The numbering of VDET faces is shown in Figure A.2 (more detailed information on the VDET geometry can be found in Section 3.3.1 and elsewhere [69]). Each wafer should have two spots making 24 in total, and each spot has a Z view and an XY view which are treated separately giving 48 'spots' in total. The spots are numbered such that spots 1-24 correspond to the Z view

and 25-48 correspond to the XY view. Plots of pulse height versus strip number are shown in Figure A.4 for the Z view and Figure A.5 for the XY view. The numbering of the strips is shown in Figure A.3. It can be seen that some of the spots are missing or are very weak. This is due to misalignment of the prisms or poor contact between the optical fibres and the prisms. Modules B001, B006 and A009 are the only ones which have two good spots in both views. Most of the other modules have one good spot seen in both views, except module A006 which has no spots at all. Figure A.6 shows the XY distribution of hits for laser events. The laser spots can be seen along with some noise hits.

### A.3 Analysis

The analysis was performed on approximately 650 runs taken between June and November 1994. The positions of the laser spots were determined and monitored as follows :

- A threshold level was set for each module in order to eliminate the background which can be seen on some modules, for example A013, B004, and B001 (see Figures A.4 and A.5). This overcomes the problem of fake hit positions being found from background.
- 'Clusters' are formed from strips with pulse height above the threshold value and the exact hit position is found using a centre-of-gravity technique.
- For each spot, a nominal position was determined. This was taken as being the mean hit position found using 200 laser events. Windows centred on each spot were then set to allow each hit to be associated with a certain spot number. For most spots the width of this window was set at  $600 \mu\text{m}$  (ie. 6 readout strips), to allow for movements of that size. In the case of two very close spots, for example spots 13 and 14 in Figure A.4, a smaller window was chosen.
- Deviations from the nominal positions were calculated on an event by event basis and history plots were produced showing the run-averaged deviation as a function of run number.

### A.4 Results

Figure A.7 shows the run-averaged spot deviation as a function of run number for representative spots. It can be seen that until around run 29400 the spots are stable within approximately  $3 \mu\text{m}$ . Around run 29400 however, all the spots show a significant shift. The size of the shift varies between spots and is summarised in Table A.1. The shift occurs gradually, starting on the 4th October and taking 4 days for the spots to reach their maximum deviation on the 7th. The spots then return to their previous positions on the 13th October around run 29700.

From run 29700 onwards the spots are less stable than before. The following observations were made concerning the nature of the shift:

- The spots are stable around run 26600 indicating that a VDET/ITC relative movement was not a possible explanation for the tracking distortions seen at that time.
- The start of the shift does not coincide with the ALEPH detector being closed on the 22nd September but starts 12 days afterwards.
- The fact that the shift occurred relatively slowly and the spots returned to their normal positions suggests that the movement is related to a gradual change, of temperature or pressure for example.
- The average cluster pulse heights were studied as a function of run number because if some of the strips were to saturate, the pulse height information would no longer be accurate for these strips<sup>1</sup> and this could cause an apparent shift in the cluster position. The pulse heights were seen to be stable for all spots hence this is not a possible explanation for the observed shift.

#### A.4.1 Possible Explanations for the Shift

Three possible explanations could account for the observed spot shifts :

- (a) The VDET moved.
- (b) The ITC inner wall moved and the laser system moved with it.
- (c) The laser system moved relative to the ITC inner wall.

Explanation (a) suggests that the VDET modules moved, perhaps due to a temperature change. If this was the case then a deterioration in tracking quality would be expected for runs between 29400 and 29700. In order to check this, the ALEPH tracking quality program, DQUAL [70], was used to independently analyse these runs. The DQUAL program uses di-muon events and analyses the residuals between the actual VDET hit and the expected hit position found by extrapolating a track back from the TPC and ITC. This program should be able to detect VDET movements of greater than  $30\ \mu\text{m}$ . Runs 29400-29700 were analysed using the tracking quality program and also a set of runs taken when the spots were stable. No significant differences were seen between the two sets of results. However, many of the spot shifts are less than  $30\ \mu\text{m}$  and therefore it is possible that the DQUAL analysis is not sensitive to them.

Explanations (b) and (c) appear to be more feasible. It was noted that atmospheric pressure rose from 970 mbar on October 4th to 990 mbar on October

---

<sup>1</sup>If a strip saturates then the strip pulse height is measured to be smaller than it really is.

Module Number	Z side		Approx. $\phi$	XY side	
	Spot	Max. shift ( $\mu\text{m}$ )		Spot	Max. shift ( $\mu\text{m}$ )
B013	1	+2	$290^\circ$	*	
	2	+4		26	-12
A013	*		$290^\circ$	*	
	4	+9		28	+70
B001	5	+17	$0^\circ$	29	+7
	6	+20		30	+12
A001	7	+12	$0^\circ$	*	
	*			32	-40
B004	9	+20	$70^\circ$	33	-85
	*			34	-50
A004	*		$70^\circ$	35	-10
	12	+14		36	+45
B006	13	+15	$120^\circ$	37	+3
	14	+16		38	+10
A006	*			*	
	*			*	
B009	17	+8	$195^\circ$	*	
	*			42	+17
A009	19	+5	$195^\circ$	43	-7
	20	+5		44	+4
B011	21	-11	$245^\circ$	45	+65
	*			46	+85
A011	*		$245^\circ$	47	-5
	24	+12		*	

Table A.1: Summary table of spot shifts. A positive shift indicates that the spot moved in the direction of increasing strip number (see Figures A.3, A.8). A \* indicates an absent spot.

7th. This latter pressure was the highest recorded around this time and coincides with the time of the maximum spot displacement. Since the gas pressure inside the ITC chamber follows the pressure outside, this pressure change should not have resulted in a movement of the walls of the ITC. A likely hypothesis is that small bubbles of air are trapped in the glue between the kapton foils of the laser system and the ITC walls. Changes in atmospheric pressure could cause such bubbles to expand or contract thus causing movements of the kapton foils and hence causing movements of the prisms which are attached to the kapton.

#### A.4.2 Interpretation of Spot Movements.

Adopting the assumption that it was the VDET which moved it is worthwhile trying to interpret the individual spot movements in terms of a global movement of the VDET. The first point to notice from Table A.1 is that all the spots, except

spot 21, move in the direction of increasing strip number in Z. Figure A.3 shows the way the strips are numbered and so the Z movements can be considered as suggestive of the VDET contracting along its length<sup>2</sup>. However, problems arise when trying to interpret the movements more accurately. This is because there is a two-fold ambiguity when matching the Z view of a spot with its corresponding XY view. For example, on module B006 spot 13 (Z) could be paired with either spot 37 or 38 (XY) (see Table A.1). This ambiguity is overcome during normal data taking by extrapolating tracks back from the TPC and ITC and looking for VDET hits within a region surrounding the extrapolated track. However for VDET laser events there are no hits in the other subdetectors and so this extrapolation can not be performed. An attempt was made to resolve the ambiguity by looking for correlations between the pulse heights of the Z and XY spots but this did not prove very successful since, for example, spot 20 was equally correlated with spots 43 and 44. Another way to resolve this problem is by obtaining a more detailed knowledge of the geometry of the system.

Despite these limitations, an idea of the sort of movement that took place can be obtained by making an assumption about the Z-XY pairing of spots. One possible movement is pictured in Figure A.8, where each face is drawn individually. It can be seen that the motion cannot be easily accounted for in terms of a simple rotation or translation. However, this strange combination of contractions and expansions would perhaps be expected if temperature fluctuations were the cause. However, the VDET temperatures were investigated in the period from the 4th to 14th of October and were found to be stable to within 2°C, thus reinforcing the hypothesis that it was the laser system which moved and not the VDET.

### A.4.3 Addition of Laser Spot Analysis into DQUAL Program

It was mentioned above that the tracking quality program was perhaps not sensitive to VDET movements of less than 30  $\mu\text{m}$ . In view of this it was decided to include some code in the DQUAL program to analyse the VDET laser events. This new code produces the following histograms :

- XY view spot deviation against  $\phi$ . (Side A)
- XY view spot deviation against  $\phi$ . (Side B)
- Z view spot deviation against  $\phi$ . (Side A)
- Z view spot deviation against  $\phi$ . (Side B)
- Distribution of XY deviations for all spots.
- Distribution of Z deviations for all spots.

---

<sup>2</sup>Note that the movement of a spot in one direction implies that the VDET module moved in the opposite direction.

Examples of these histograms are shown in Figures A.9 and A.10. The solid triangles correspond to data taken between runs 28496 and 28608 (before the shift) and the open triangles correspond to data taken between runs 29508 and 29540 (during the shift). The distributions in Figure A.10 should be Gaussian and the extent to which they are not Gaussian is an indication that some movement has taken place. Clearly these histograms are sensitive to the movements which took place.

## A.5 Improvements for LEP II

In view of the problems of spot pairing mentioned above and the possible instability of the laser system due to pressure changes, a new laser system has been designed for use with the upgraded VDET [71]. The new system has several improvements :

- The new laser system is matched to the longer length of the new VDET and light spots are incident on all but one of the outer VDET faces.
- The angles and positions of each light spot are precisely known.
- The prism cells are shaped to match the curvature of the ITC inner wall to avoid the problem of air bubbles being trapped behind the optics, which is a source of instability due to changes in atmospheric pressure.

With these improvements, the mechanical stability of the VDET can be monitored to an accuracy of better than one micron [72]. This is particularly useful for high energy running as the small event rate means that the number of di-muon events is reduced by a factor of the order of 100 and so monitoring of the VDET alignment using real data is difficult.

## A.6 Conclusions

The performance of the VDET Laser Alignment System has been studied using data from the 1994 ALEPH run. The original motivation for this work came when a deterioration of the tracking quality after the June 1994 detector opening suggested that the VDET had perhaps moved. The results show that the VDET did not move at this time. In general the stability of the system was better than  $3\ \mu\text{m}$  until 4th October. All the laser spots were then seen to move - the largest shift being  $85\ \mu\text{m}$ . This movement can be attributed to either a movement of the VDET or of the laser system or of its support (ITC inner wall). The spots returned to their nominal positions around October 13th suggesting that a pressure or temperature change had been the cause. This was investigated and movements of the laser system associated with changes in atmospheric pressure were found to be the most likely cause. The ALEPH tracking quality program,

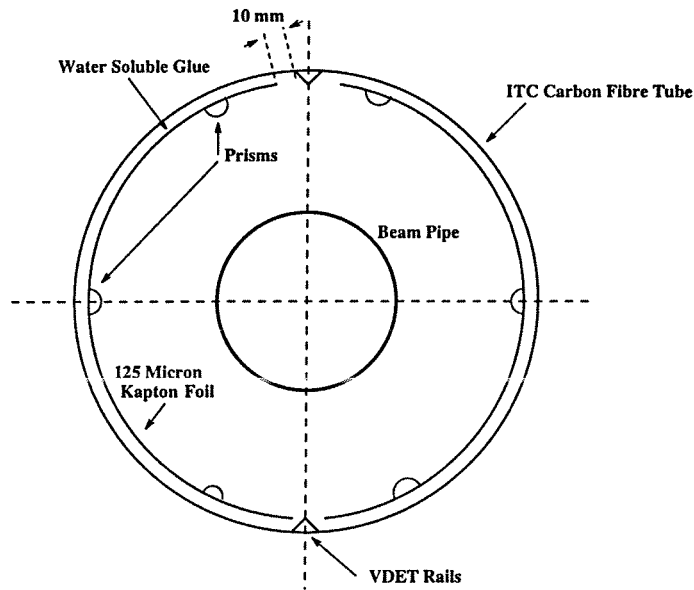
DQUAL did not show any differences in the results from di-muon events which occurred before and during the shift.

Code has been added to the tracking quality program to analyse the VDET laser events. It is hoped that this new code will be sensitive to relative movements between the ITC and VDET of less than  $10\ \mu\text{m}$ .

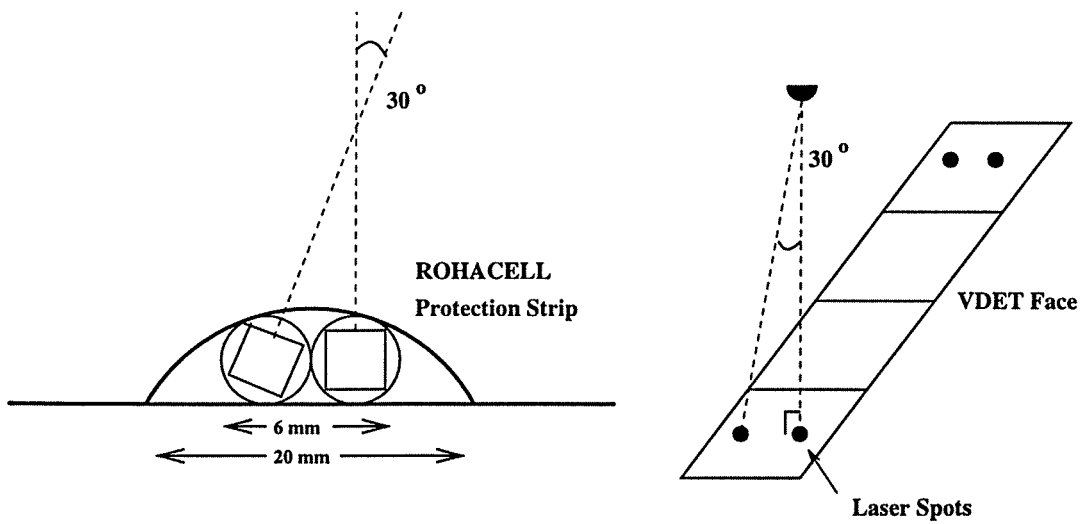
#### **Acknowledgements**

I would like to thank Paschal Coyle for advice regarding this analysis and Ian Tomalin for analysing the di-muon events for runs taken before, during and after the period when the shift was observed.





(a) Cross section of foil and prism arrangement.



(b) Close-up of one of the prism cells and a view of one of the VDET faces showing the angles of the two beams.

Figure A.1: Diagram of the VDET laser system.

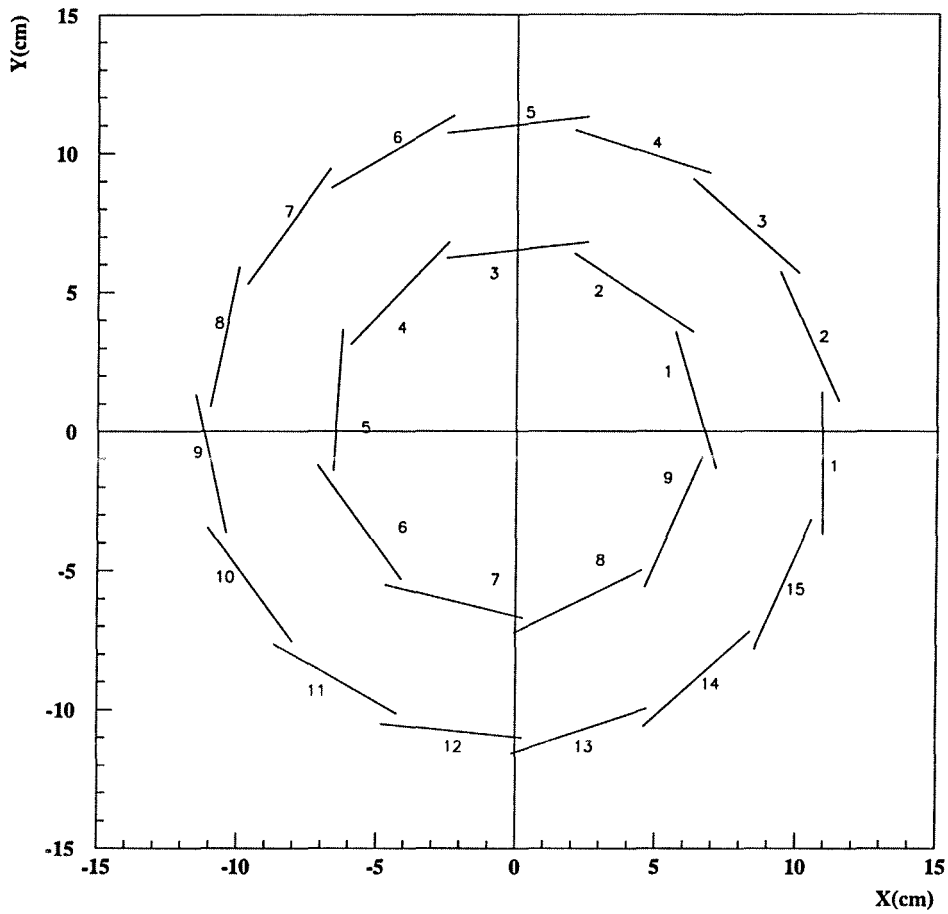


Figure A.2: VDET faces projected onto the ALEPH XY plane, as viewed from side A. The face numbers are shown. Laser light is incident on the end wafers of faces 1, 4, 6, 9, 11 and 13 of the outer layer.

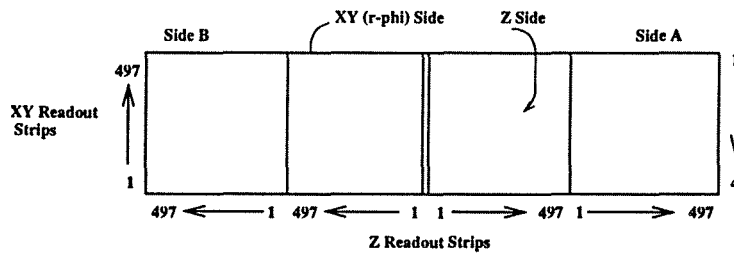
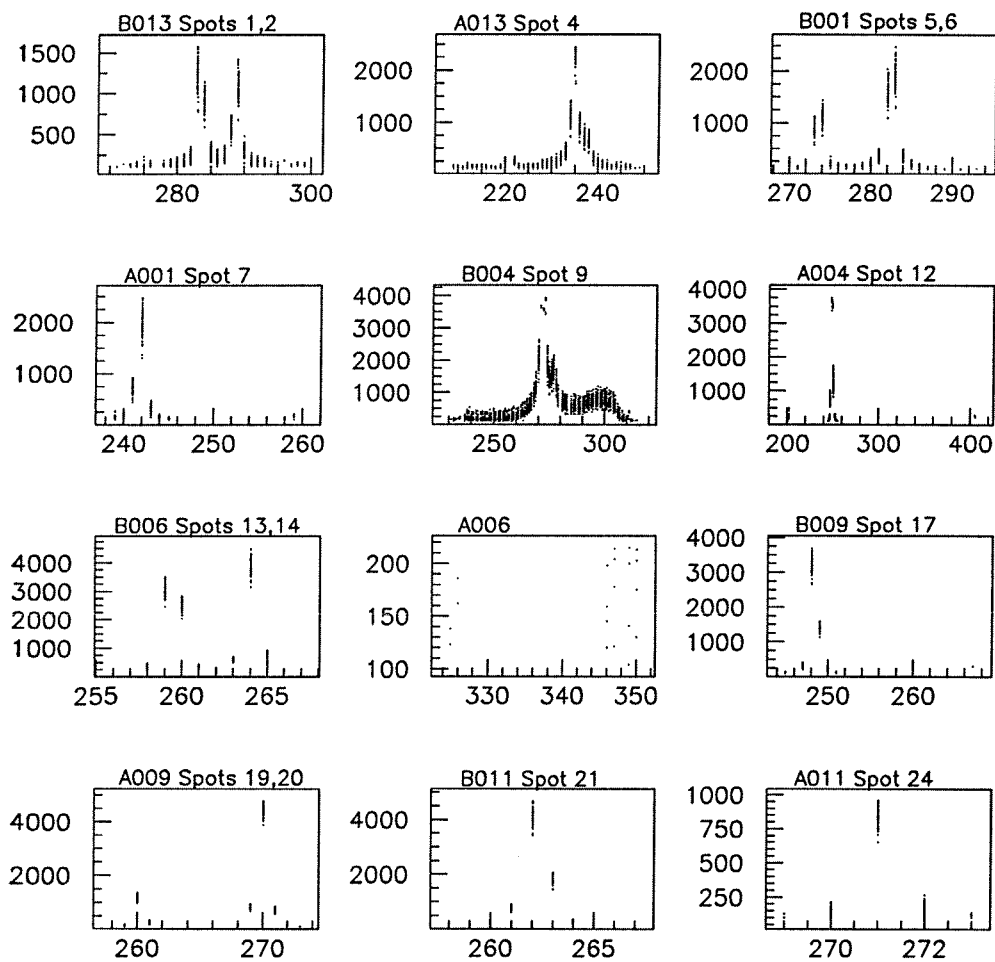


Figure A.3: Numbering of VDET strips.



**Figure A.4:** Pulse height against strip number for Z view spots. Note some spots are not seen, for example spot 8 on module A001.

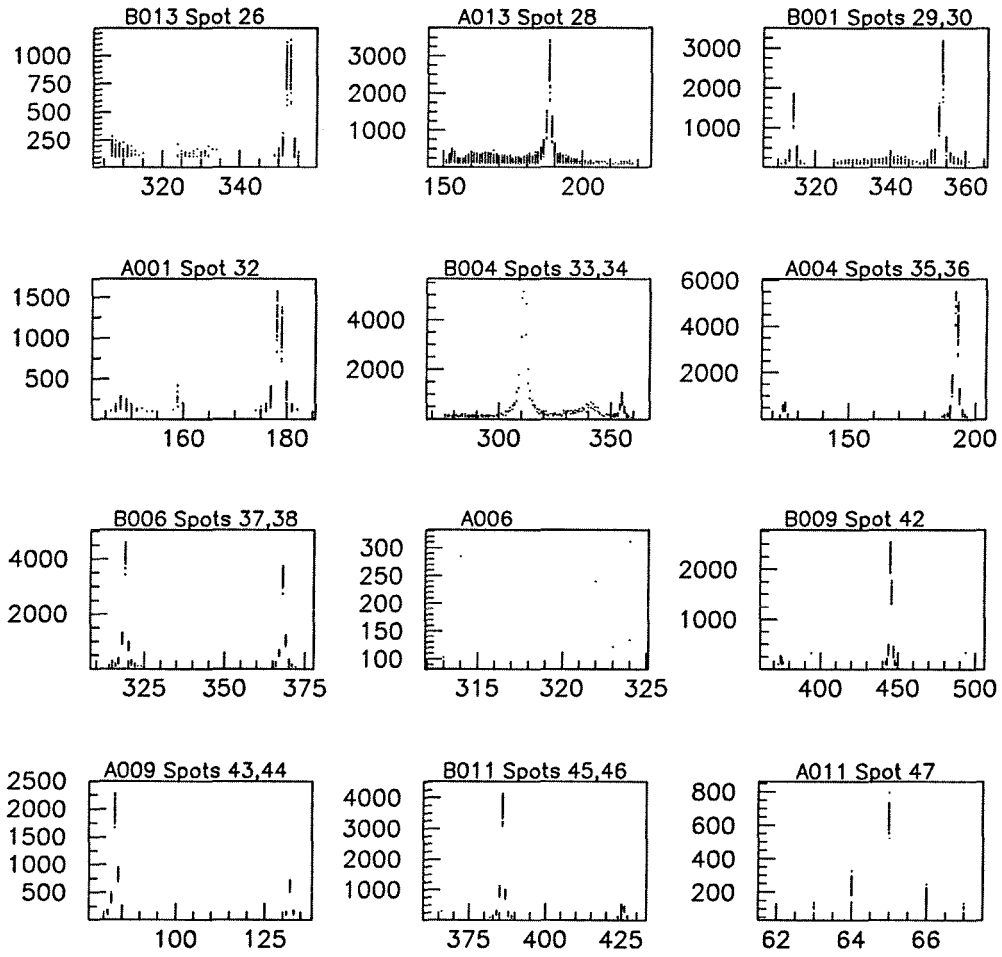
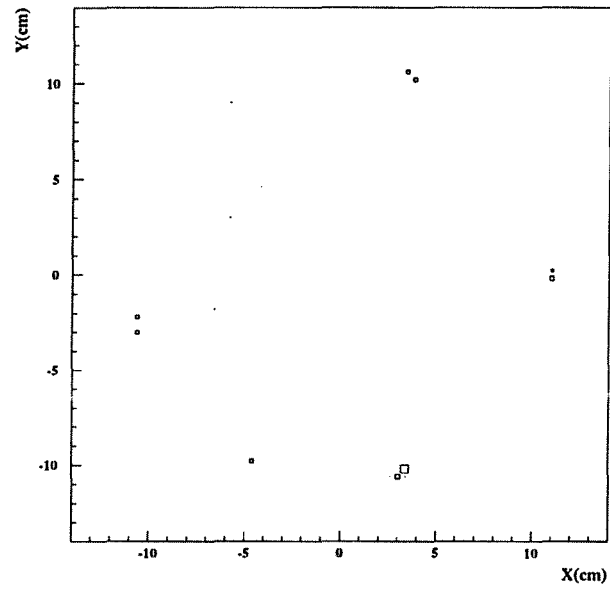
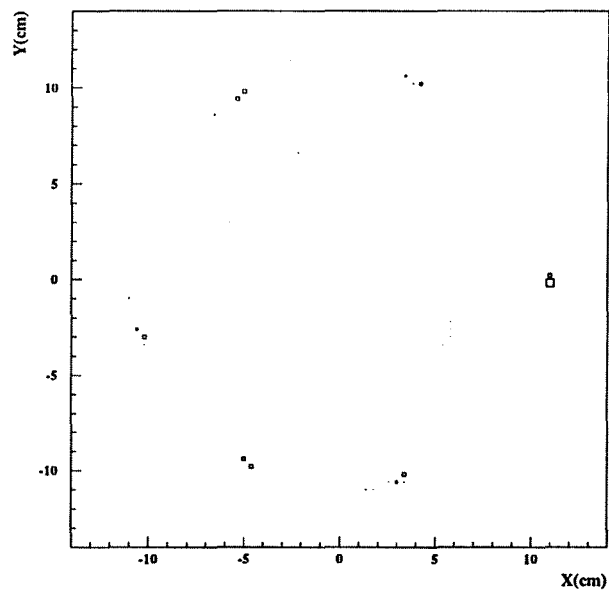


Figure A.5: Pulse height against strip number for XY view spots. Again note that some spots are not seen.

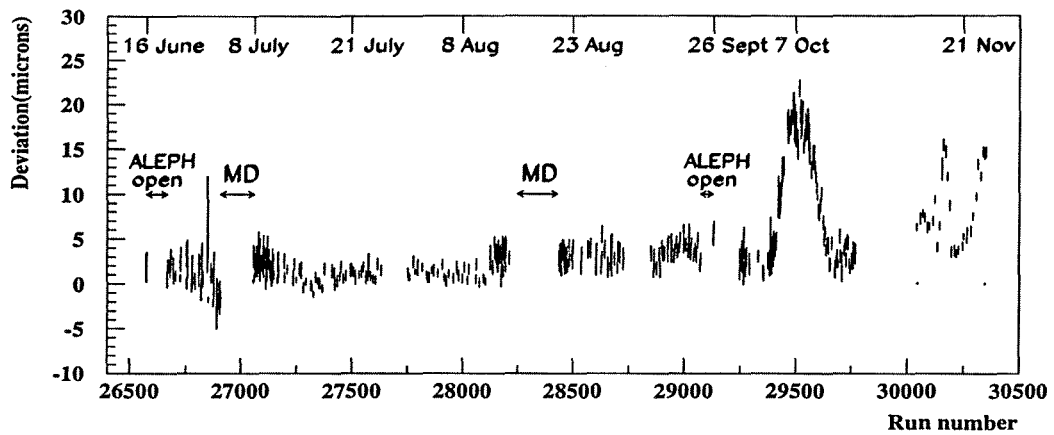


(a) Side A

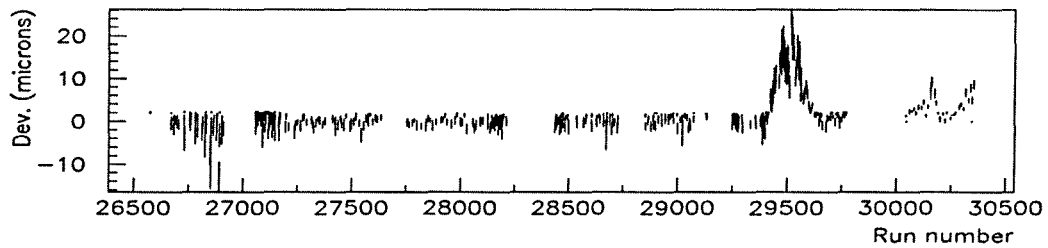


(b) Side B

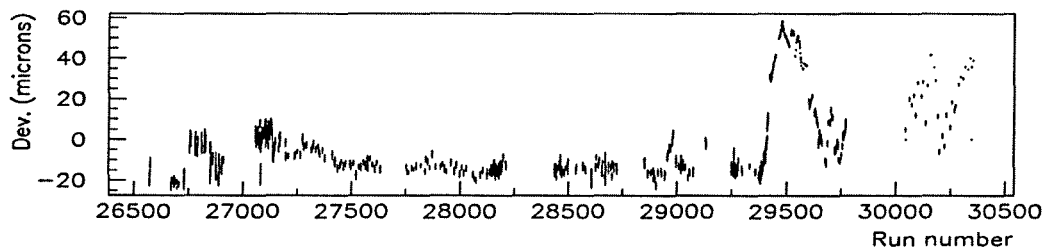
Figure A.6: XY distribution of laser hits.



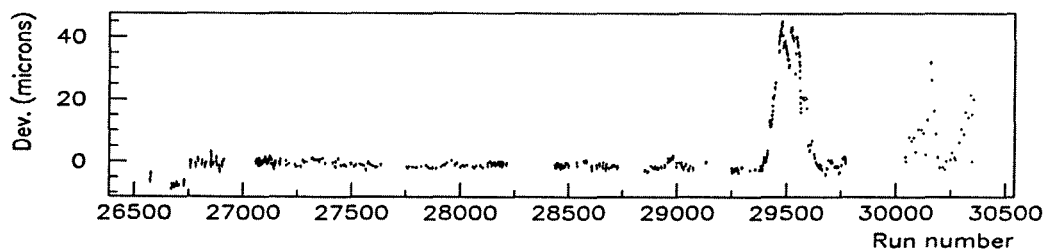
(a) B001 Spot 5



(b) B004 Spot 9



(c) A013 Spot 28



(d) A004 Spot 36

**Figure A.7:** Deviation against run number for representative spots. Plot (a) shows the periods when the ALEPH detector was open and 'MD' refers to periods of LEP machine development.

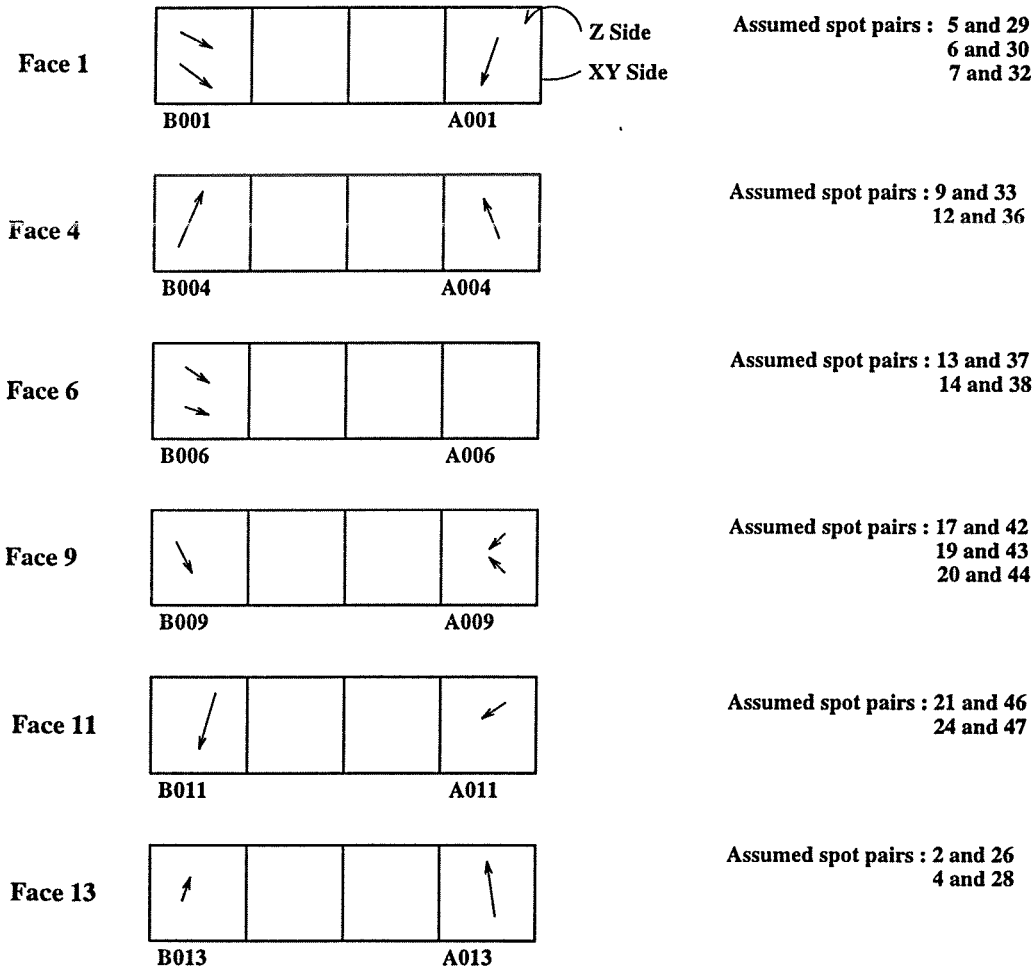
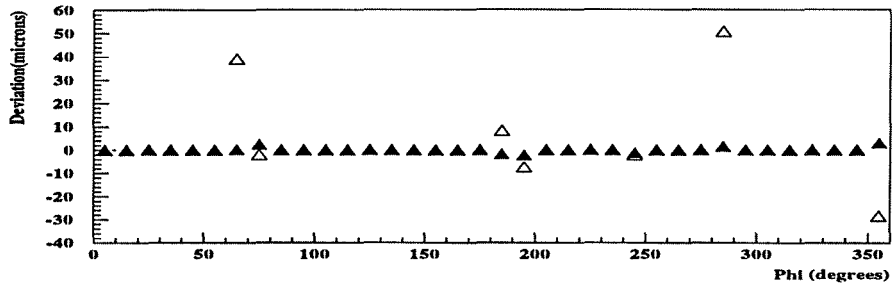
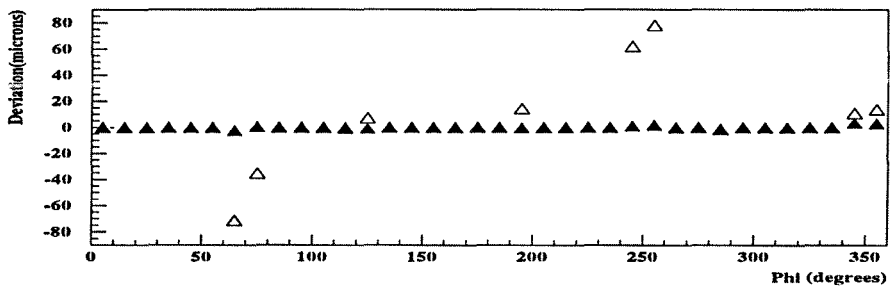


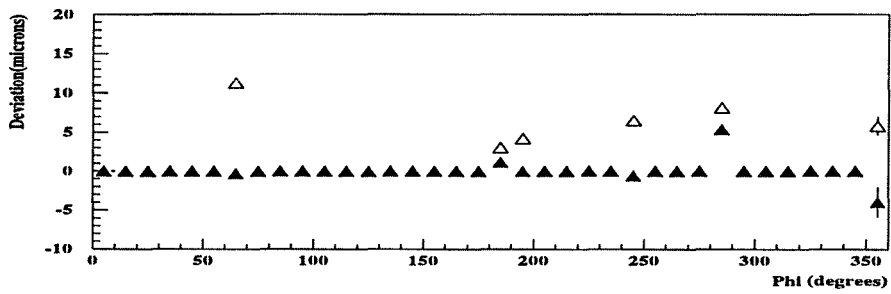
Figure A.8: Possible movements of VDET faces.



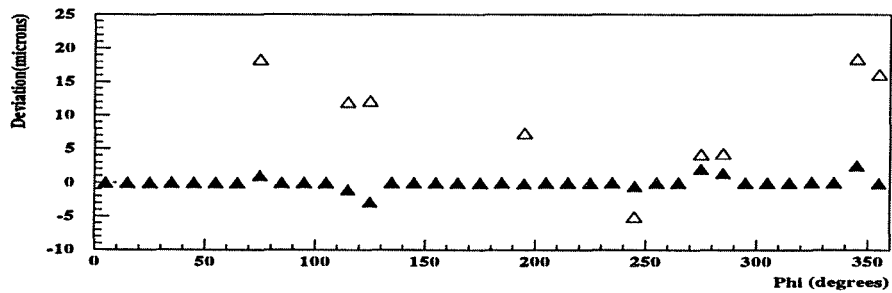
(a) XY deviation vs  $\phi$ , side A



(b) XY deviation vs  $\phi$ , side B



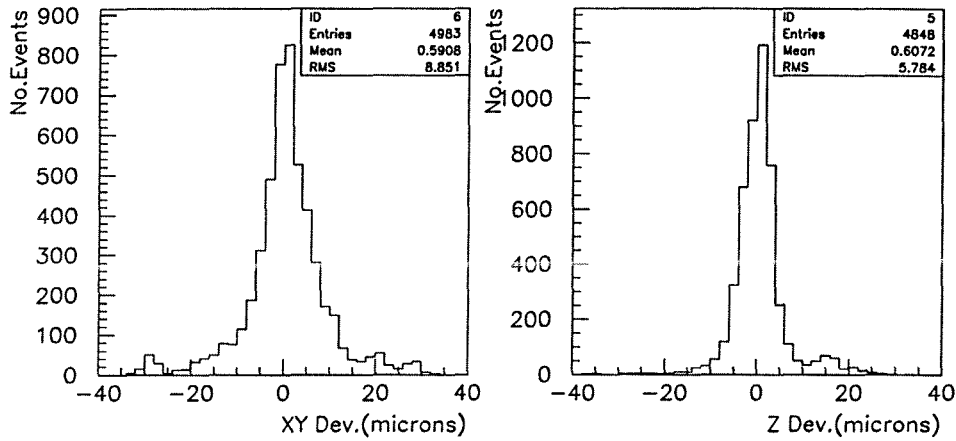
(c) Z deviation vs  $\phi$ , side A



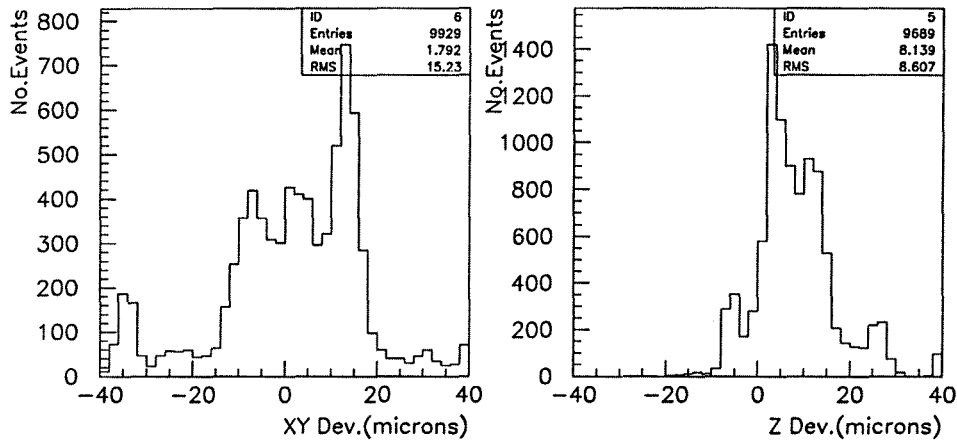
(d) Z deviation vs  $\phi$ , side B

Figure A.9: Laser plots of deviation vs.  $\phi$ (spot). (Solid triangles - runs 28496–28608, open triangles - runs 29508–29540).





(a) Distribution of deviations, runs 28496-28608



(b) Distribution of deviations, runs 29508-29540

Figure A.10: Laser plots of deviation distributions.

# Appendix B

## Multi-parameter Fit Correlation Matrix

The correlation coefficients between the parameters in the multi-parameter fit for  $\Delta m_d$  are given in Table B.1, where the parameters are given as follows :

1 = $\tau_b$	12 = $\langle Q_{B_d^{1.0}}^{1.0} \rangle$
2 = $\langle Q_{uds}^{0.5} \rangle$	13 = $\langle Q_{B_s^{1.0}}^{1.0} \rangle$
3 = $\langle Q_c^{0.5} \rangle$	14 = $\langle Q_{B_s^{1.0}}^{1.0} \rangle$
4 = $\langle Q_b^{0.5} \rangle$	15 = $\tau_\Lambda$
5 = $\langle Q_{uds}^{1.0} \rangle$	16 = $\tau_{B^+}$
6 = $\langle Q_c^{1.0} \rangle$	17 = $\tau_{B_d}$
7 = $\langle Q_b^{1.0} \rangle$	18 = $\tau_{B_s}$
8 = $\Delta m_d$	19 = $f_\Lambda$
9 = $\langle Q_\Lambda^{1.0} \rangle$	20 = $f_s$
10 = $\langle Q_{B^\pm}^{1.0} \rangle$	21 = $\mathcal{P}_b$
11 = $\langle Q_{B_d^{1.0}}^{1.0} \rangle$	22 = $\mathcal{P}_c$

Parameter	1	2	3	4	5	6	7	8	9	10	11	12	13	14	15	16	17	18	19	20	21	22
1	1.000	-0.043	0.052	-0.072	0.002	-0.002	-0.005	0.020	-0.015	-0.044	-0.033	0.001	-0.012	-0.001	0.143	0.624	0.570	0.238	-0.263	0.050	-0.012	0.045
2		1.000	-0.968	0.647	0.186	-0.128	0.014	0.034	-0.003	-0.022	-0.017	0.001	-0.006	-0.001	0.000	0.008	-0.026	-0.008	0.140	0.024	-0.034	-0.017
3			1.000	-0.762	-0.132	0.118	-0.012	-0.058	0.004	0.028	0.022	-0.001	0.008	0.001	0.000	-0.009	0.029	0.010	-0.172	-0.029	0.034	0.001
4				1.000	0.055	-0.051	0.084	0.141	-0.006	-0.041	-0.030	0.000	-0.012	-0.001	0.000	0.005	-0.032	-0.014	0.239	0.039	-0.020	0.088
5					1.000	-0.953	0.587	-0.172	0.009	0.044	0.029	0.003	0.012	0.001	0.003	0.004	-0.046	0.001	-0.104	-0.029	-0.080	-0.197
6						1.000	-0.713	0.180	-0.010	-0.051	-0.033	-0.004	-0.014	-0.002	-0.004	-0.003	0.052	-0.001	0.120	0.034	0.086	0.203
7							1.000	-0.117	0.011	0.055	0.037	0.003	0.015	0.002	0.005	-0.007	-0.056	0.001	-0.120	-0.041	-0.061	-0.089
8								1.000	0.010	0.191	0.076	0.042	0.056	0.006	-0.096	0.222	-0.217	-0.087	-0.210	-0.130	0.054	0.100
9									1.000	-0.012	-0.009	0.000	-0.003	0.000	-0.004	0.004	0.002	-0.002	0.074	0.010	0.006	0.017
10										1.000	-0.048	-0.003	-0.019	-0.002	-0.003	-0.007	0.030	-0.007	0.238	0.054	0.013	0.060
11											1.000	0.000	-0.013	-0.001	-0.004	0.018	-0.001	-0.007	0.176	0.040	0.009	0.049
12												1.000	-0.001	0.000	0.001	-0.006	0.008	0.001	0.001	0.001	0.001	-0.001
13													1.000	-0.001	-0.001	0.003	0.007	-0.008	0.069	0.022	0.003	0.017
14														1.000	0.000	0.000	0.001	-0.001	0.008	0.002	0.000	0.002
15															1.000	0.009	-0.005	-0.003	0.044	0.001	0.012	0.021
16																1.000	0.089	0.014	-0.099	-0.018	0.005	-0.031
17																	1.000	-0.010	0.007	0.002	-0.026	0.023
18																		1.000	0.040	0.005	0.003	0.021
19																			1.000	-0.235	0.017	-0.184
20																				1.000	0.000	-0.043
21																					1.000	-0.495
22																						1.000

Table B.1: Correlation coefficients for multi-parameter fit.

# References

- [1] J. Alcaraz *et al.* (LEP Electroweak Working Group), 'Combination of Preliminary LEP and SLD Electroweak Measurements and Constraints on the Standard Model', LEPEWWG/96-02 (1996).
- [2] Particle Data Group, Phys. Rev. **D 54** (1996).
- [3] S. Glashow, Nucl. Phys. **22** (1961) 579.
- [4] F. Halzen and A.D. Martin, 'Quarks and Leptons', John Wiley & Sons (1984).
- [5] A. Buras and M. Lindner, 'Heavy Flavours', Advanced Series on High Energy Physics, (World Scientific, Singapore, 1992), Vol. 10.
- [6] L. Wolfenstein, Phys. Rev. Lett. **51** (1983) 1945.
- [7] C. Jarlskog and R. Stora, Phys. Lett. **B 208** (1988) 268.
- [8] V. Barger and R. Phillips, 'Collider Physics', Frontiers in Physics Series (Vol. 71), Addison-wesley Publishing Company, (1987).
- [9] A.J. Buras *et al.*, Nucl. Phys. **B245** (1984) 369.
- [10] F.J. Gilman and M.B. Wise, Phys. Rev. **D 27** (1983) 1128.  
A.J. Buras *et al.*, Nucl. Phys. **B 238** (1984) 529.
- [11] Private communication with Owen Hayes (ALEPH).
- [12] D.Buskulic *et al.* (ALEPH Collaboration), Contribution to the 28th International Conference on High Energy Physics, Warsaw, Poland, July 1996, ICHEP96 PA08-020
- [13] A. Ali, DESY Preprint **96-106** (1996).
- [14] A. Buras *et al.*, Nucl. Phys. **B347** (1990) 491.
- [15] M. Neubert, Proceedings of the 1995 European School of High Energy Physics, Dubna, Russia (1995).
- [16] A. Ali and D. London, DESY Preprint **96-140** (1996).

- [17] H.-G. Moser, ALEPH Note **93-138** PHYSIC **93-119** (1993).
- [18] H.-G. Moser and A. Roussarie, 'Mathematical Methods for  $B^0 - \bar{B}^0$  Oscillation Analyses' (1996) (Submitted to Nucl. Inst. and Methods).
- [19] D. Buskulic *et al.* (ALEPH Collaboration), Phys. Lett. **B322** (1993) 441.
- [20] D. Buskulic *et al.* (ALEPH Collaboration), CERN Preprint **PPE/96-102** (1996) (Submitted to Z. Phys. C).
- [21] R. Akers *et al.* (OPAL Collaboration), Z. Phys. **C66** (1995) 555.
- [22] M. Acciarri *et al.* (L3 Collaboration), Phys. Lett. **B383** (1996) 487.
- [23] D. Buskulic *et al.* (ALEPH Collaboration), Phys. Lett. **B356** (1995) 409.
- [24] S. Emery, Ph.D. Thesis, DAPNIA, Saclay, France (1995).
- [25] P. Abreu *et al.* (DELPHI Collaboration), Z. Phys. **C72** (1996) 17.
- [26] D. Buskulic *et al.* (ALEPH Collaboration), Phys. Lett. **B313** (1993) 498.
- [27] P. Abreu *et al.* (DELPHI Collaboration), Phys. Lett. **B338** (1994) 409.
- [28] G. Alexander *et al.* (OPAL Collaboration), Z. Phys. **C72** (1996) 377.
- [29] D. Buskulic *et al.* (ALEPH Collaboration), Phys. Lett. **B377** (1996) 205.
- [30] G. Alexander *et al.* (OPAL Collaboration), Contribution to the 28th International Conference on High Energy Physics, Warsaw, Poland, July 1996, ICHEP96 PA08-14.
- [31] D. Buskulic *et al.* (ALEPH Collaboration), Contribution to the 28th International Conference on High Energy Physics, Warsaw, Poland, July 1996, ICHEP96 PA05-54.
- [32] R. Barate *et al.* (ALEPH Collaboration), CERN Preprint **PPE/97-025** (1997) (Submitted to Phys. Lett. B).
- [33] The ALEPH Handbook (Volumes 1 and 2), Editor C. Bowdery (1995).
- [34] D. Decamp *et al.* (ALEPH Collaboration), Nucl. Inst. and Methods **A294** (1990) 121.
- [35] H. Seywerd *et al.*, CERN Preprint **PPE/96-041** (1996) (Submitted to Nucl. Inst. and Methods)
- [36] D. Buskulic *et al.* (ALEPH Collaboration), Nucl. Inst. and Methods **A360** (1995) 481.
- [37] J. Knobloch and P. Norton, 'Status of Reconstruction Algorithms for ALEPH', ALEPH Internal Note (1991).

- [38] D. Brown and G. Redlinger, ALEPH Note **92-008** PHYSIC **92-008** (1992).
- [39] D. Brown, ALEPH Note **92-47** PHYSIC **92-42** (1992).
- [40] W. Bartel *et al.*, Z. Phys **C33** (1986) 23.
- [41] D. Brown *et al.*, ALEPH Note **92-171** PHYSIC **92-153** (1992).
- [42] T. Mattison, ALEPH Note **92-173** PHYSIC **92-155** (1992).
- [43] T. Sjöstrand, 'PYTHIA 5.7 and JETSET 7.4', CERN Report **TH 7112/93** (1993).
- [44] D. Buskulic *et al.* (ALEPH Collaboration), Z. Phys. C **55** (1992) 209.
- [45] R. Barate *et al.* (ALEPH Collaboration), CERN Preprint **PPE/97-017** (1997) (Submitted to Phys. Lett. B).
- [46] R. Barate *et al.* (ALEPH Collaboration), CERN Preprint **PPE/97-018** (1997) (Submitted to Phys. Lett. B).
- [47] K. Ackerstaff *et al.* (OPAL Collaboration), CERN Preprint **PPE/96-137** (1996) (Submitted to Z. Phys. C).
- [48] A. Halley and F. Thomson, ALEPH Note **97-016** PHYSIC **97-013** (1997).
- [49] W.T. Eadie *et al.*, 'Statistical Methods in Experimental Physics', North-Holland Publishing Company (1971).
- [50] G. Altarelli and G. Parisi, Nucl. Phys. **B126** (1977) 298.
- [51] 'Z Physics at LEP 1', Volume 3, editors G. Altarelli *et al.* CERN **89-08** (1989).
- [52] C. Peterson *et al.*, Phys. Rev. **D27** (1983) 105.
- [53] D. Buskulic *et al.* (ALEPH Collaboration), Z. Phys. **C71** (1996) 357.
- [54] D. Decamp *et al.* (ALEPH Collaboration), Phys. Lett **B284** (1992) 177.
- [55] R.D. Field and R.P. Feynman, Nucl. Phys. **B136** (1978) 1.
- [56] R.Erickson *et al.*, Phys. Rev. Lett. **42** (1979) 822.  
J.P. Berge *et al.*, Phys. Lett. **B91** (1980) 311.  
M. Derrick *et al.*, Phys. Lett. **B91** (1980) 470.  
J.P. Albanese *et al.*, Phys. Lett. **B144** (1984) 302.
- [57] A. Halley, Ph.D. Thesis, RALT-120, (1991).
- [58] M. Fernandez-Bosman *et al.*, ALEPH Note **91-132** Softwr **91-005** (1991).

- [59] D. Abbaneo *et al.* (Heavy Flavour sub-group of the LEP Electroweak Working Group), Presentation of LEP Electroweak Heavy Flavour Results for Summer 1996 Conferences, ALEPH Note **96-099** (1996).
- [60] D. Buskulic *et al.* (ALEPH Collaboration), Phys. Lett. **B357** (1995) 699.
- [61] F. James, 'MINUIT', CERN Program Library Long Writeup **D506** (1994).
- [62] H.-G. Moser, ALEPH Note **96-029** PHYSIC **96-026** (1996).
- [63] The LEP *B* Lifetime Working Group,  
<http://wwwcn.cern.ch/~claires/plots/bw>
- [64] R.J. Barlow, 'Statistics', Wiley (1989) 76.
- [65] Private communication with Olivier Schneider (ALEPH).
- [66] The LEP *B* Oscillations Working Group, Contribution to Moriond QCD, LEPBOSC **97/001.3** (1997).
- [67] F. Thomson and P. Coyle, ALEPH Note **95-39** MINIV **95-02** (1995)
- [68] I. R. Tomalin, Minutes of the Tracking Meeting of 22/9/94.
- [69] J. Rothberg *et al.*, ALEPH Note **94-174** SOFTWR **94-012** (1994).
- [70] I. R. Tomalin, ALEPH Note **94-159** SOFTWR **94-014** (1994).
- [71] A. Wagner and H. Dietl, ALEPH Note **97-006** MINIV **97-001** (1997).
- [72] A. Wagner, ALEPH Note **96-122** MINIV **96-001** (1996).





↑

↓



↑

↓

